UNIVERSITY OF OKLAHOMA

GRADUATE COLLEGE

ATTRIBUTE ASSISTED SEISMIC FACIES, FAULTS, KARST, AND ANISOTROPY ANALYSIS

A DISSERTATION

SUBMITTED TO THE GRADUATE FACULTY

in partial fulfillment of the requirements for the

Degree of

DOCTOR OF PHILOSOPHY

By

JIE QI
Norman, Oklahoma
2017

ATTRIBUTE ASSISTED SEISMIC FACIES, FAULTS, KARST, AND ANISOTROPY ANALYSIS

A DISSERTATION APPROVED FOR THE
CONOCOPHILLIPS SCHOOL OF GEOLOGY AND GEOPHYSICS

BY

_____
Dr. Kurt J. Marfurt, Chair

_____
Dr. S. Lakshmivarahan

_____
Dr. Roger M. Slatt

_____
Dr. Xiaowei Chen

_____
Dr. Jamie P. Rich

I would like to dedicate this dissertation to my family and friends whose support, patience, and persistent encouragement was instrumental in allowing me to complete this degree program.

Acknowledgements

To my wife, my family, my friends, and all people who I worked with in last four years, I would like to thank for their help and support throughout the time of my Ph.D. research.

I cannot express enough thanks to my committee members: Dr. Kurt J. Marfurt; Dr. S. Lakshmivarahan; Dr. Roger M. Slatt; Dr. Xiaowei Chen; Dr. Jamie P. Rich for their support and encouragement. First, I would like to thank my supervisor Dr. Kurt Marfurt, who provide this opportunity to know the fantastic world of geophysics. I am extremely grateful for your support for studying and doing research. Thank you for your guidance, I am sure without that, I could not finish this dissertation. I would like to thank Dr. Varahan for teaching me the computational science, which helps me improve my ability in the mathematical algorithm and programming skills. I would like to thank Dr. Slatt for providing me the geologic knowledge that helped me understand the geologic setting of the Woodford Shales used in my Ph.D. research. I would like to thank Dr. Chen for sharing knowledge in shear wave splitting and its application to anisotropy prediction. I would also like to thank Dr. Rich for teaching me unconventional geophysics course, helping me improve my ability in Matlab programming, and guiding me to do the prototype velocity variation with azimuth project.

I would like to express my thanks to all my Chinese teammates, Bo Zhang, Shiguang Guo, Fangyu Li, Tao Zhao, Tengfei Lin, Bin Lyu, and Xuan Qi, for helping me survive all the stress during my studies. I would like to thank all AASPI colleagues and co-authors Dr. Sumit Verma, Dr. Bradley Wallet, Marcus Cahoj, Gabriel Machado, Abdulmohsen AlAli, Lennon Infante, Thang Ha, Bryce Hutchinson, Oluwatobi

Olorunsola, Murphy Cassel, Megan Gunther, Robert Hardisty, David Lubo Robles, Rafael Pires de Lima, Saurabh Sinha, Swetal Patel, Yuji Kim, and many others whose name are not listed.

Finally, I extended my deepest thanks to my wife Qinglu Cheng and my parents for everything that they have done for me. All of this would have been impossible without their constant support.

Table of Contents

List of Figures

Abstract

Seismic attributes provide quantitative measures of key statistical, geometric, or kinematic components of the 3D seismic volume. These measures can thus be subsequently used in 3D visualization, interactive crossplotting, or computer-assisted facies analysis. In this dissertation, I evaluate the attribute expression of seismic facies including karst collapse features, mass transport complexes, turbidites, and salt using 3D visualization and 3D pattern recognition.

One of the more common and more important seismic facies is salt. Salt segmentation is critical for accelerating velocity modeling, which in turn is necessary for seismic depth migration. In general, geophysicists need to pick the high velocity salt interface manually. In the first chapter of the dissertation, I present a semi-supervised multiattribute clustering method, and apply it not only to salt segmentation, but also to mass transport complex, shale, and sand segmentation in the Gulf of Mexico. I develop a 3D Kuwahara filtering algorithm, and smooth the interior attribute response and sharpen the attribute contrast between one face with neighboring facies. Then, I manually paint target facies to evaluate the ability of candidate attributes to discriminate each seismic facies from the other. Crosscorrelating their histogram, candidate attributes with low correlation coefficients provide good facies discrimination. Kuwahara filtering significantly increases this discrimination. Kuwahara filtered attributes corresponding to interpreter-defined facies are then projected against a Generative Topological Mapping (GTM) manifold, resulting in a suite of *n* probability density functions (PDFs). The

Bhattacharyya distance between the PDF of each unlabeled voxel to each facies PDF results in a probability volume of each interpreter-defined facies.

In the second chapter, I introduce a 3D fault enhancement and skeletonization workflow. For large datasets, interpreter hand-picking of faults can be very time-consuming. This process can be accelerated by generating high resolution edge detecting attributes. Coherence is an algorithm that measures both stratigraphic and structural discontinuities. Application of a directional Laplacian of a Gaussian (LoG) filter to coherence volumes provides more continuous and sharper faults. To further increase fault resolution and preserve stratigraphic discontinuities, I skeletonize the filtered coherence volumes perpendicular to the discontinuities with the goal of providing subvoxel resolution. "Fault" points doesn't fall on the geometric grid suggesting the distribution of the value onto eight neighboring grid points. I demonstrate this fault enhancement and skeletonization workflow through application to two datasets from New Zealand and the Gulf of Mexico.

With the advent of shale resource plays, wide azimuth acquisition has become quite common. Migrating seismic gathers into different azimuthal bins provides a means to estimate horizontal stress and natural fractures. Different azimuths preferentially illustrate faults perpendicular to them. However, coherence applied to the lower fold azimuthally limited seismic volumes is contaminated by noise. In the third chapter, I improve the energy ratio coherence algorithm and extend it to map more subtle discontinuities, which can only be seen in different azimuthally limited seismic volumes. The main modification compared to the original energy ratio coherence algorithm is that I add the weighted covariance matrices of each azimuthal sectors together to form a single

covariance matrix, thereby improving the signal-to-noise ratio. I apply this multi-azimuth coherence algorithm to two datasets from the Fort Worth Basin.

In the fourth chapter, I summarize attribute-assisted interpretation in the Barnett Shale and the Ellenburger Group. Karst, faults, and joints are known to form geologic hazards for most Barnett Shale wells in the Fort Worth Basin. In the best cases, these drilling-related geohazards form conductive features that draw off expensive hydraulic fracturing fluid from the targeted shale formation. In the worst cases, the completed wells are hydraulically connected to the underlying Ellenburger aquifer and produce large amounts of water that must be disposed. Karst collapse generates a distinct morphologic pattern on 3D seismic data. I show that multiple attributes delineate different components of the same geologic features, thereby confirming my interpretation.

Chapter 1 : Semi-supervised multiattribute seismic facies analysis

Jie Qi, Tengfei Lin, Tao Zhao, Fangyu Li, and Kurt Marfurt

The University of Oklahoma, ConocoPhillips School of Geology and Geophysics.

This paper was published by SEG and AAPG journal Interpretation in 2016

Title: Semi-supervised multiattribute seismic facies analysis

ABSTRACT

One of the key components of traditional seismic interpretation is to associate or "label" a specific seismic amplitude package of reflectors with an appropriate seismic or geologic facies. The object of seismic clustering algorithms is to use the computer to accelerate this process, allowing one to generate interpreted facies for large 3D volumes. Determining which attributes best quantify a specific amplitude or morphology component seen by the human interpreter is critical to successful clustering. Unfortunately, many patterns, such as coherence images of salt domes, result in "salt and pepper" classification. Application of 3D Kuwahara median filters smooth the interior attribute response and sharpens the contrast between neighboring facies, thereby preconditioning the attribute volumes for subsequent clustering. In our workflow, the interpreter manually paints *n* target facies using traditional interpretation techniques, resulting in attribute training data for each facies. Candidate attributes are evaluated by crosscorrelating their histogram for each facies, with low correlation implying good facies discrimination. Kuwahara filtering significantly increases this discrimination. Multiattribute voxels for the *n* interpreter-painted facies are projected against a Generative Topological Mapping (GTM) manifold, resulting in *n* probability density functions (PDFs). The Bhattacharyya distance between the PDF of each unlabeled voxel to each of *n* facies PDFs results in a probability volume of each user-defined facies. We demonstrate the effectiveness of this workflow to a large 3D seismic volume acquired offshore Louisiana, USA.

INTRODUCTION

Seismic stratigraphy plays a key role in the interpretation of many Gulf of Mexico (GOM) seismic surveys. While many geologic features are represented by a specific geometric pattern, such as channel incisement, angular unconformities against erosional surfaces and onlap onto smooth horizons, some geologic features are more chaotic and more difficult to describe. Salt domes and mass transport complexes (MTCs) are often seen in offshore data of the Gulf of Mexico. Salt can form seals while MTCs can be seals or drilling hazards. Seismic geomorphology coupled with an appropriate depositional model allows prediction of lithology distribution, deformation features, and overall reservoir heterogeneity. Salt holds an additional interest in the processing shop, where the accurate definition of high velocity salt is critical to prestack depth migration. Defining the limits of salt domes in offshore seismic data consumes hours of interpreter time. MTCs often exhibit similar textures to salt in 3D coherence volumes. Both features are difficult to autopick, while geobody tools often perform poorly.

The published literature on salt segmentation exceeds that of any other computer-aided facies identification workflow, and can be divided into two methods. The first method is based on image segmentation. Lomask et al. (2007) applied a modified version of a "Normalized cuts image segmentation" (NCIS) algorithm, which was first introduced to seismic interpretation as an atomic meshing of a seismic image (Hale and Emanuel, 2002). NCIS was adapted from the eigenvector-based method proposed by Shi and Malik (2002), and it provides a globally optimized solution to the problem of seismic salt-boundary picking. Lomask et al.'s (2007) workflow build a weighting function, which indicates the presence of a boundary between pairs of voxels in the image. In related

work, Halpert et al. (2014) modified a pairwise region comparison (PRC) algorithm, based on human-interpreted supervision on one or more 2D slices to guide a 3D segmentation process.

The second method is based on pattern recognition and texture attribute classification. Gao (2003) applied a gray-level co-occurrence matrix (GLCM) to detect a salt dome, and found that one GLCM attribute was insufficient to automatic define the salt boundary. Berthelot (2013) combined several GLCM attributes, spectral components, dip, and coherence, and used a supervised Bayesian classification method to delineate salt. They focused on texture to characterize the change of seismic character between the salt and surrounding geology. Wallet and Pepper (2013) applied mathematical morphology to a single attribute to constrain texture boundaries, thereby reducing the variance of seismic attributes for improved salt delineation.

3D computer-assisted seismic facies classification is based on attributes. West et al. (2002), Meldahl et al (1999), and Corradi et al. (2009) used interpreter-provided seed points or polygons to train neural network classifiers. Coleou et al. (2003), Gao (2007), Matos et al. (2009), and Roy et al. (2013) used 3D self-organizing maps to compute unsupervised facies volumes that were later calibrated with well control and principles of geomorphology. Roy et al. (2014) used generative topographic mapping to cluster multiattribute data volumes, which were then compared to well control using the Bhattacharyya distance.

Unlike photographic images, seismic textures are 3D and contain many voxels. On vertical slices, seismic facies span the continuum from conformal sands and shales, to more complex turbidites, to highly deformed MTCs, to chaotic salt. To segment such

facies it is necessary to quantify the differences in their seismic attribute expression. Barnes and Laughlin (2002) found that the choice of attributes was critical to effective classification.

Skilled human interpreters have little difficulty in differentiating seismic facies such as salt and MTCs from each other. Teaching a computer to do the same is more difficult, requiring careful psychological analysis of the human process. How does a human interpreter differentiate these two "chaotic" textures? How to we quantify different degrees of chaos?

Figure 1.1 indicates our seismic facies classification workflow. We begin our paper with a summary of candidate attributes that appear to differentiate the seismic facies of interest. Next, we precondition the attribute volumes through Kuwahara filtering, resulting in a smoother facies response and sharper edges. We then introduce a degree of supervision by computing histograms for each candidate attribute for a suite of user-defined facies. Cross-multiplying these histograms quantifies which attributes best differentiate a given facies pair. The selected attributes are then used as input to a generative topographic mapping (GTM) classification algorithm. The probability of a given facies at each voxel is estimated using the Bhattacharyya distance. We conclude by validating the predicted facies on seismic vertical lines and time slices that were not used in the training, and generating a suite of geobodies.

ATTRIBUTE EXPRESSION OF SEISMIC FACIES

Seismic amplitude is the most common "attribute" used in seismic interpretation. If a geologic feature is not measurable by the spatial variation in seismic amplitude and phase, no derivative attributes will enable identification. Much of seismic interpretation

is based on pattern recognition. Seismic attributes provide quantitative measures of statistical, geometric, or kinematic patterns seen in the 3D seismic amplitude volume. Our initial choice of candidate attributes to differentiate the target seismic facies is based on experience. However, the final choice will be determined through quantitative attribute histogram analysis of manually picked seismic facies.

Figure 1.2 shows a summary of seismic attribute anomalies associated with different facies seen in the GOM data volume described in this paper. Coherence is sensitive to lateral discontinuities such as faults, channel edges and karst (Qi et al., 2014), as well as chaotic zones such as salt and MTCs. We use vector dip as input for principal-component structure-oriented filtering (SOF) in the most coherent window to suppress random and cross-cutting coherent noise and improve vertical resolution (Marfurt, 2006). We estimate the coherent part of the data using a Karhunen-Loève filter; coherent energy is the energy of the Karhunen-Loève filtered data, with stronger reflectors exhibiting higher energy than weaker reflectors. Incoherent events internal to salt exhibit the lowest coherent energy. Coherent energy can use to separate a strong reflectivity sand/shale package from a weaker reflectivity shale/shale package.

While coherence response to MTCs and salt may be similar, gray-level co-occurrence attributes can help differentiate different kinds of chaotic textures. Texture analysis holds significant promise in computer-aided interpretation and is often used in interpreter-driven or computer-assisted facies analysis (West et al., 2002; Gao, 2007; Corradi et al., 2009). We calculate the gray-level co-occurrence matrices (GLCM) along structural dip, which quantifies the spatial repeatability (co-occurrence) of voxel amplitude values (gray levels) at a distance within an analysis window. GLCM entropy

is a statistical measure of randomness of the seismic amplitude. GLCM dissimilarity highlights regions having strict stationary statistics (invariant mean and variance).

The structural curvature is computed by taking the derivatives of the dip components. Reflections that exhibit similar waveforms, which having small offsets (<1/4 wavelength) and subtle changes in dip across faults, will generate curvature, but not coherence anomalies (Al-Dossary and Marfurt, 2006). Reflector convergence (Marfurt and Rich, 2010) also differentiates eroded zones from more conformal stratigraphy.

We select five attributes that quantify a specific amplitude or morphology component exhibited by the target. Coherence and reflector convergence can differentiate chaotic zone, such as salt dome, or an MTC, from sediment, but not from each of them. Furthermore, local high coherence zones occur within salt and MTCs given their observation. Texture attributes, such as GLCM-entropy, and –dissimilarity differentiates chaotic zones, but are relatively insensitive to seismic facies boundaries. Coherent energy differentiates a strong reflectivity sand/shale package from a weaker reflectivity shale/shale package, but it MTCs exhibit both low and high energy elements. Our final task is therefore to precondition the attribute data to provide piecewise smooth images amenable to computer classification algorithms.

KUWAHARA FILTERING

Kuwahara (1976) filtering is commonly used in structure—oriented filtering. Kuwahara filters adapt to the variability of the data within overlapping analysis windows, where Luo et al. (2002) used standard deviation followed by a mean filter and Marfurt (2006) used 3D coherence followed by a 3D Karhunen-Loève filter to generate edge-

preserving structure-oriented filters. Kuwahara filter as an edge-preserving filter is widely used in image processing. Applied to photographs, Kuwahara filters result in piecewise monochromatic features separated by sharp boundaries (Figure 1.3). By localizing the smoothing, the Kuwahara filter properly removes detail, even such as "salt and pepper" noise in high-contrast regions while preserving shape boundaries in low-contrast regions. Kyprianidis et al. (2009) find that the Kuwahara filter "maintains a roughly uniform level of abstraction across the image while providing an overall painting-style look". In our work, we use the same concept to define edges between different types of incoherent zones. Equally important, the Kuwahara filter will smooth rapidly varying attribute anomalies within salt and MTCs to facilitate subsequent clustering.

The Kuwahara filter (Figure 1.4) searches all windows containing a given voxel. In our workflow, the analysis windows are oblique cylinders with radius = 50 m and height of ±20 ms containing L=143 voxels whose top and bottom faces are aligned with the local dip magnitude and dip azimuth. L overlapping windows contain any given voxel. For a given attribute, one computes the standard deviation, σ, the mean μ, and the median, m, in each of the L overlapping analysis windows. The filtered attribute will then be the value of m associated with the window having the minimum value of normalized standard deviation, σ/μ. The smoothness and noise suppression of an image is controlled by the size of the analysis window. If the analysis window length is large, the image will be smoother, but somewhat blocky. If the analysis window is small, the image will be smoothed less, and blockiness reduced. Numerical experiments showed that a single large window L=500 filters provided superior results to cascading two small window L=143 filters at reduced computation cost.

INTERPRETER SUPERVISION AND ATTRIBUTE HISTOGRAM ANALYSIS

Clustering

The use of classification algorithms to detect natural clusters of attribute responses to geologic facies is referred to as unsupervised classification. On contrast, supervised classification is based on a set of training data, in our case is composed of a suite of attribute vectors corresponding to interpreters picked voxels within a given seismic facies. There are many interpreter-supervised machine-learning methods used in seismic facies classification including artificial neural networks (ANN), support vectors machines (SVM), self-organizing maps (SOM), and generative topographical mapping (GTM). SOM and GTM both fit the *N*-attribute residing in *N*-dimensional space with a lower dimensional manifold (in our application, a 2-dimensional manifold).

Attribute Histograms

A histogram is a graphical representation of the probability distribution of a quantitative variable. The relationship to geologic events is best understood by examining the data histogram, with Sheffield et al. (2008) finding that effective 3D visualization requires the mapped feature be near a histogram extremum. The correlation coefficient between voxel value histograms of images can be used to detect image content from a large database.

We represent the distribution of attribute values associated with the voxels that fall within an interpreter-painted facies by its histogram. The voxel histogram represents the amplitude distribution of a given attribute, and represents a probability density function (PDF). Zero-mean seismic amplitude usually has a Gaussian distribution centered about zero. The inclusion of dead traces and mute zones in the histogram

calculation results in a spike at value zero, and should be avoided. Correlation of histograms is sensitive to their PDF, and insensitive to the geometric rotation and scaling in seismic data. Luo et al. (2001) introduced a scheme based on histogram equalization to scale seismic data for optimum display. We begin by generating a matrix of histograms for each of the *F* facies and each of the *N* candidate attributes. Then for each facies pair (salt vs. MTC, MTC vs. sediment, or sediment vs. salt), we generate a vector of *N* crosscorrelation coefficients. The histograms from the seismic amplitude and seismic attributes contain noise, such that their histograms poorly cross-correlate. Furthermore, the edges between the different facies may be fuzzy, and difficult to identify. Kuwahara filtering of the seismic attributes followed by histogram smoothing addresses these issues. The correlation coefficient, r_{fgn}, between histogram for facies *f*, h_f, and the histogram for facies *g*, h_g, for attribute *n* is simply:

$$r_{fgn} = \frac{\sum_{j=0}^{100}\left[\left(h_{fj} - \bar{h}_f\right)\left(h_{gj} - \bar{h}_g\right)\right]}{\left\{\left[\sum_{j=0}^{100}\left(h_{fj} - \bar{h}_f\right)^2\right]\sum_{j=0}^{100}\left(h_{gj} - \bar{h}_g\right)^2\right\}^{1/2}}, \tag{1.1}$$

where the $\bar{h}_f$ and $\bar{h}_g$ are the average of the histogram and where we have constructed our histogram to span 101 bins.

APPLICATION

The 3D seismic data cover an area of 8000 sq. km (3089 sq. mi) along the current offshore Louisiana shelf edge. The seismic data were acquired by PGS using towed streamer acquisition with two sources and three receiver cables with a maximum offset of 6000 m. We start with a minibasin bound by two salt diapirs to the west and east (Figure 1.5). The uplift of the western salt dome is contemporaneous with the upper

minibasin fill and occurred earlier than the eastern salt dome rise. We interpret (paint) three seismic facies of interest: salt dome, mass transport complexes (MTCs), and relatively undeformed sediment that includes both strong (an interbedded sand and shale package) reflectors, and weak (a thick predominantly shale package) reflectors. The human eye can easily recognize the edge of salt and the limit of the MTCs. Salt exhibits lower amplitude, lower frequencies, and appears to be internally highly chaotic. The MTC generally exhibits higher amplitude, broadband frequencies, and laterally chaotic and vertically moderately conformal. The sedimentary packages exhibit alternatively high or low amplitude, broadband frequencies, coherent, and highly conformal.

Although a human interpreter can easily recognize them, mapping salt domes and MTCs using voxel-based classifiers are quite difficult. Within the chaotic salt, there may be coherent multiples or coherent migration aliasing artifacts. Within an MTC, there will be a jumble of coherent and incoherent reflectors cut by slump surfaces and small listric and toe-thrust faults.

Seismic attributes

We calculate coherence, coherent energy, the magnitude of reflector convergence, GLCM-entropy, and GLCM-dissimilarity along structural dip (Figure 1.6). Examination of Figure 1.6a shows that layered sediments exhibit high coherence. Faults, stratigraphic boundaries, and other discontinuities exhibit low coherence. Salt domes have high coherence inclusions (displayed as white) within a low coherence (black) background, while MTCs will have coherent (white), often rotated, reflectors embedded in a relatively incoherent (black) matrix. Thus, in these data, both salt and MTC exhibit a "salt and pepper" appearance in coherence volumes. Reflector convergence (Figure 1.6b) is a 2D

vector and shows the magnitude and azimuth of convergence, such as occurs at pinch-outs and angular unconformities. Those attributes help differentiate more "fumbled" internal salt dome and mass transport complex reflectors from conformably layered stratigraphy. GLCM-entropy (Figure 1.6c), and GLCM-dissimilarity (Figure 1.6d) show salt domes and MTCs to have high dissimilarity and high entropy while sediments have low entropy and dissimilarity. Coherent energy (Figure 1.6e) highlights high reflection coefficient reflectors (the deeper sand/shale package) from low reflectivity, shallower shale/shale package. Salt appears as low energy, with some high energy inclusions. The MTC is more heterogeneous, with high energy reflectors embedded in a low energy matrix.

Kuwahara-filtered attributes

While our preliminary analysis of seismic attributes differentiates the three target facies in this GOM survey, two challenges reduce the accuracy of computer-assisted facies classification. The first challenge is the mixed high- and low-value ("salt and pepper") anomalies seen in the salt and the MTC. The second challenge is that of additional facies. We have already suggested that the "sediments" facies can be broken into a sand/shale vs. shale/shale facies. In addition, faults may also be misclassified as one of our three facies. Specifically, the faults in this survey give rise to low coherence, the high magnitude of reflector convergence, high GLCM-entropy and high GLCM-dissimilarity anomalies. In Figure 1.6, around the right salt dome, there are three faults (indicated by red arrows) cutting through the salt dome and neighboring sand that exhibit to similar attribute response through salt and the MTC.

We address the first (heterogeneity) problem by applying a Kuwahara filter to smooth rapidly varying attribute anomalies to facilitate subsequent clustering. Figure 1.7 shows the Kuwahara filtering workflow. One computes three sub-attributes from each seismic attribute: the standard deviation, σ, the mean μ, and the median, m, in each of the overlapping analysis windows. Figure 1.8 shows the median, m, of each candidate attribute, computed within a 100 m by 100 m by ±12 ms rectangular window resulting in a much smoother, less detailed image. The "salt and pepper" features in the salt and MTC are now more continuous, while the thin anomalies associated with the faults are eliminated.

Unfortunately, the median filtering has smoothed the edges of seismic facies from rapidly varying to smoothly varying. To apply a Kuwahara filter, we find window k of the L non-centered overlapping windows that contain a target voxel that has the smallest normalized standard deviation, σ/μ. Kuwahara filtering then assigns the median of window k to be the output value for the target voxel. In this example, we cascaded two small 50 m radius by ±8 ms Kuwahara filters. Compared with the median-filtered attributes shown in Figure 1.8, the Kuwahara-filtered attributes shown in Figure 1.9 better preserve the boundaries between different seismic facies, preconditioning them for subsequent classification. Figure 1.10 compares time slices through several attributes before and after Kuwahara filtering where we note that the Kuwahara-filtered attributes have smoothed seismic facies (Figure 1.10). Like the median filter, the Kuwahara filter eliminates thin anomalies such as faults (red arrows) and channels (blue arrow).

To more clearly see the detailed improvements by Kuwahara filtering, we examine the attributes before and after filtering along two different traces. In Figure

1.11a, trace 1 intersects a top salt boundary, while trace 2 intersects both the top and bottom boundaries of MTC. Before filtering (Figure 1.11b), values within the salt dome vary rapidly, making it difficult to detect the top salt boundary. Likewise, the discrimination of the edges of the MTC is also difficult. In contrast, the Kuwahara filtered trace in Figure 1.11c, shows piecewise smooth values, producing a sharp boundary of the salt dome and MTC.

Attribute selection to separate painted facies

Given these filtered attributes, the next task shown in Figure 1.1 is to paint the target facies of interest on vertical or time slices and generate histograms for each facies. Figure 1.12 shows histograms for the three seismic facies: sediment (blue), MTC (green), and salt (red). Histograms of picked facies are normalized to range between 0 and 1 for easy comparison and do not change the correlation coefficient of any histogram pair. Note that Kuwahara filtering both narrows and further separates the distribution of the attribute histograms. Coherence and GLCM-dissimilarity attributes now have significantly greater discrimination between the three target facies, allowing the facies to be separated. Reflector convergence and GLCM-entropy attributes have poor separation between salt and MTC, but good separation of these two facies from the sediments.

Figures 1.13 compares the correlation coefficients r_{fg} between the original seismic attribute painted facies with those between the Kuwahara-filtered attribute painted facies. For the original attributes (Figure 1.13a), the histogram correlation coefficients r_{fg} of sediment vs. salt are all less than 0.5 for most attributes. In the salt vs. the MTC facies, only coherence has a low value of r_{fg}, while coherence and GLCM-dissimilarity attributes have low values of r_{fg} for the MTC vs. the sediment facies. After Kuwahara filtering

(Figure 1.13b), the correlation is significantly reduced, suggesting that our classifier will be better able to discriminate one facies from the other where green boxes indicate correlation coefficients less than a threshold of 0.5. Coupled with the improved edge enhancement of the Kuwahara filter, we expect improved results. Figure 1.14 shows overlays of the filtered attributes on the vertical seismic slice and time slices at t=1172ms. Such threshold discrimination between facies is limited to one attribute at a time although one can sequentially reject larger and larger areas of examination through cascading thresholding of additional attributes.

Crossplotting of two attributes

Crossplotting of seismic attributes is used to highlight the relationship of input attributes. In seismic facies analysis, the interpreter picks polygons on the crossplot and display the result, providing a degree of supervision. Figure 1.15a and b show a vertical section and time slice of original coherence and GLCM dissimilarity crossplot co-rendered with seismic amplitude. Figure 1.15c and d show the same images after by Kuwahara filtering. The crossplotted Kuwahara filtered images show better facies boundaries, and have less internal "salt and pepper" behavior. Unfortunately, crossplotting become difficult with three attributes, and intractable for more than three facies. Gao (2007) addressed this problem by crossplotting principal components of the attributes, which projects the data onto a plane. Thus, we propose using GTM analysis, which maps data onto a deformed manifold.

GTM interactive clustering and Bhattacharyya distance

We apply generative topographical mapping (GTM) (e.g. Roy et al., 2014) to obtain vector projections of multiple attributes onto a 2D latent space. On this example,

GTM represents a 5-dimensional (5-attribute) data by a lower 2-dimensional deformed manifold. GTM starts with an initial 2D plane, defined by the first two eigenvectors of the 5×5 attribute covariance matrix (i.e. principal component analysis). This plane is uniformly populated with clusters each of which describes a Gaussian PDF. The plane is deformed onto a curved manifold by moving the center of a Gaussians to better fit the data. At each iteration, the variance of the Gaussian is decreased. The process continues until convergence providing a maximum likelihood estimation of the Gaussian centers. At the end, all vectors are projected onto a 2D latent space.

From our histogram analysis, the five attribute volumes used in the GTM are coherence, magnitude of reflector convergence, GLCM-entropy, GLCM-dissimilarity, and coherent energy, representing the depositional features seen in the seismic facies volume. After training, the 5D attribute vectors at each voxel is projected onto the 2D latent space.

Figure 1.16a and b show slices through the unsupervised GTM volume computed using the original attribute co-rendered with seismic amplitude. Figure 1.16c and d show the slices through the GTM volume computed by Kuwahara filtered attributes co-rendered with seismic amplitude. Each voxel is projected onto the 2D latent space that is mapped against a 2D colorbar. The users can then define polygons about hypothesized clusters on display then using commercial crossplotting tools. Salt, MTC and sediment can be nearly differentiated, where purple color indicates salt, the red color MTCs, the green color the low amplitude conformal shale packages, and the blue color the high amplitude conformal water bottom and sand/shale packages. Figure 1.17a shows vertical slice BB’ and time slice at t= 1172 ms, through seismic amplitude. By drawing polygons

on the GTM 2D histogram, we define geobodies of salt (Figure 1.17b), MTCs (Figure 1.17c), and sediment (Figure 1.17d). To more quantitatively introduce supervision, we project each painted face onto the previously trained 2D manifold, generating average PDFs for each facies. We then project each 5D data voxel onto the same manifold, generating its own PDF. The Bhattacharyya distance (e.g. Roy et al., 2014), which measures the similarity between two PDFs, is then calculated between the voxel PDF with each facies PDF. We firstly run our method on a few seismic lines. At the paint, the clustering is "unsupervised". We add supervision by projecting the voxels painted in Figure 1.5b onto the latent space, generating PDFs for salt, MTC, and sediment facies (Figure 1.18a-c). To validate these PDFs, we pick single voxels for each facies on a line in a different part of the survey, and project them on the latent space (Figure 1.18d-f). Note that the PDF of the single voxel fall with the PDF of the supervision data. Cross multiplying the PDF of a given voxel and the PDF of the supervision given the square of the Bhattacharyya distance. The Bhattacharyya distance says how likely the voxel belongs to each facies.

Figure 1.19 show seismic amplitude co-rendered with Bhattacharyya distance volumes for each of the supervised facies. The Bhattacharyya distance provides a probability measurement of how likely a facies to appear at a certain spatial location. A Bhattacharyya distance value of 0.8 against salt means the analysis point is 80% likely to be salt. Such probability estimation is especially useful when there is no clear separation within a transition zone among multiple facies.

CONCLUSIONS

We have developed a workflow to automate the volumetric delineation of seismic facies, with a focus on chaotic facies such as salt diapirs and mass transport complexes common in the Gulf of Mexico. Key to such classification is the choice of attributes that capture patterns seen by the human interpreter that help identify the target facies. Human interpreters see patterns and facies boundaries at scales larger than a few voxels. We approximate this pattern recognition by applying 3D Kuwahara filtering to each attribute volume. Generative topological mapping not only allows "clustering" of the attribute data, but also facilitates the introduction of interpreter provided supervision, resulting in a probabilistic volume of each desired facies. The Bhattacharyya distance between the PDF of each unlabeled voxel to each of *n* facies PDFs results in a probability volume of each user-defined facies.

ACKNOWLEDGEMENTS

We would like to thank the PGS for providing a license to their data for use in research and education. We also thank the sponsors of the OU Attribute-Assisted Processing and Interpretation Consortium for their guidance and their financial support.

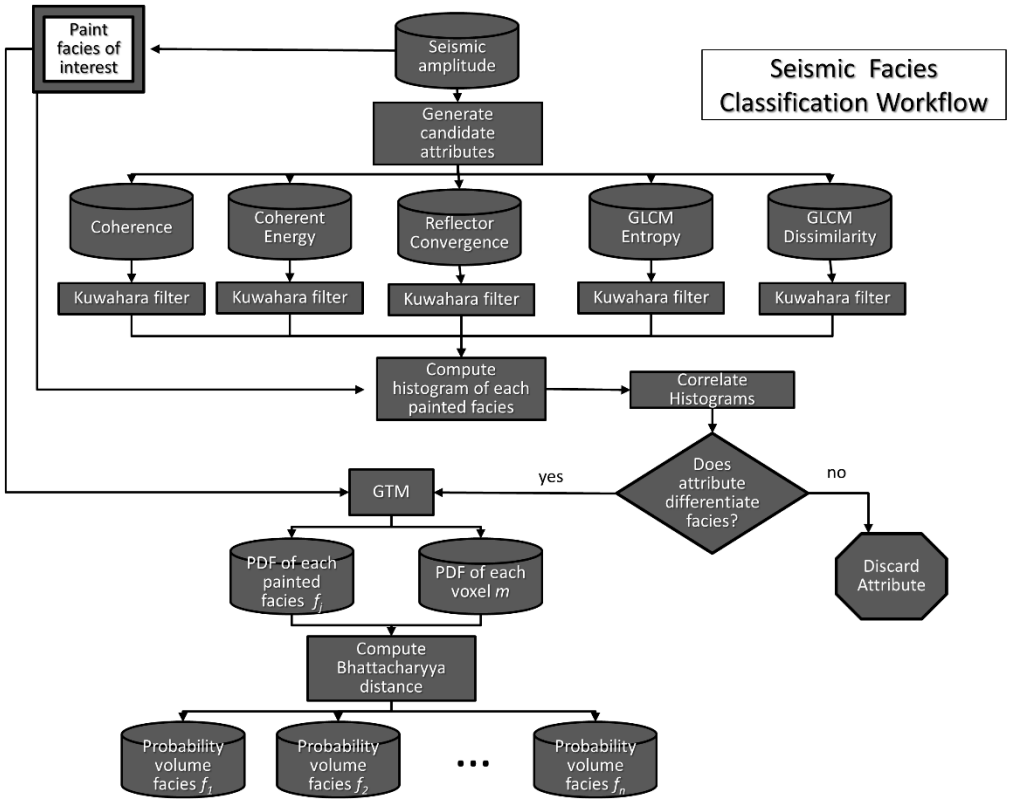

Figure 1.1 Workflow illustrates the steps used in our multiattribute seismic facies analysis workflow. The interpreter begins by painting target facies of interest on either seismic amplitude or attribute data. After Kuwahara filtering, histograms are computed for each facies and each candidate attribute. Attributes that do not differentiate facies are rejected, while those that do are kept and mapped onto a latent space using GTM. Next, the pdf for each facies f is mapped onto the latent space generating a suite of PDFs. Next, the attribute vector at each voxel, m, is projected onto the latent space, generating an additional PDF. Finally, the probability that a given voxel m belongs to facies f is computed using the Bhattacharyya distance.

Facies name	Seismic expression	Coherence	Coherent energy	Reflector convergence	GLCM entropy	GLCM dissimilarity
Salt	Low energy, incoherent, vertically and laterally chaotic	"salt and pepper"	Low	Low	High	High
MTC	Mixed energy, incoherent, mixed frequency, piecewise conformal	"salt and pepper"	"salt and pepper"	Low	High	High
Turbidite	Low energy, coherent, piecewise conformal	High	Low	Moderate	Moderate	High
Sand/shale package	High energy, coherent, modern frequency, conformal	High	High	High	Low	Moderate
Shale package	Low energy, coherent, conformal	High	Moderate	High	Low	Moderate

Figure 1.2 Table of five seismic facies, their seismic expression, and their attribute response seen in this data volume. The recognition of features that allow discrimination between seismic facies is critical. If this can be done, the next most important task is to select attributes that quantitatively measure these features.

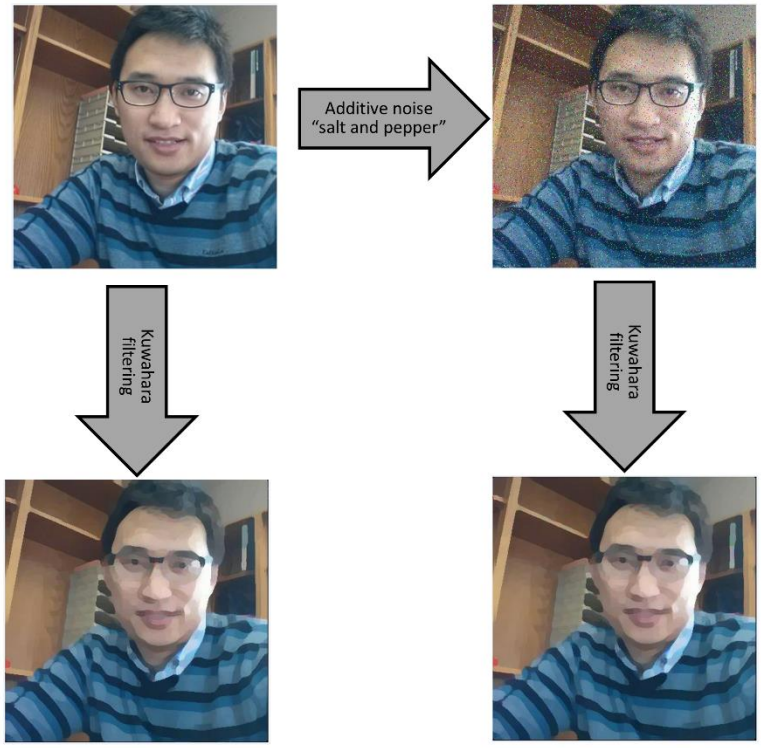

Figure 1.3 A photo of the first author with and without additive noise before and after Kuwahara filtering applied to each of the R, G, and B components. Note that noise type is "salt and pepper". Kuwahara filtering smooth as internal details of the image, but preserves edges.

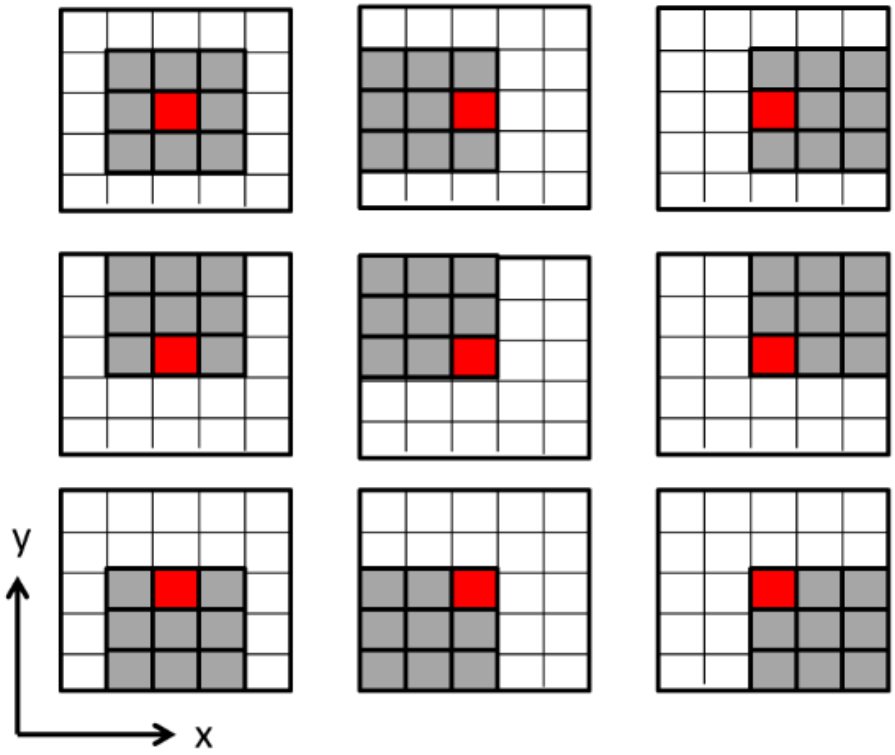

Figure 1.4 Cartoon of 2D Kuwahara filtering. The input data include 25 samples centered about the red square. Gray squares indicate voxels used in the nine laterally shifted 9-sample analysis windows, each of which contains the output location indicated by the red square. The output is the mean as median of that gray window that has the smallest standard deviation. In 3D, we evaluate 125 neighboring voxels, and compute the mean, the median, and, standard deviation, σ/μ, in 27 overlapping 3 by 3 by 3 analysis window.

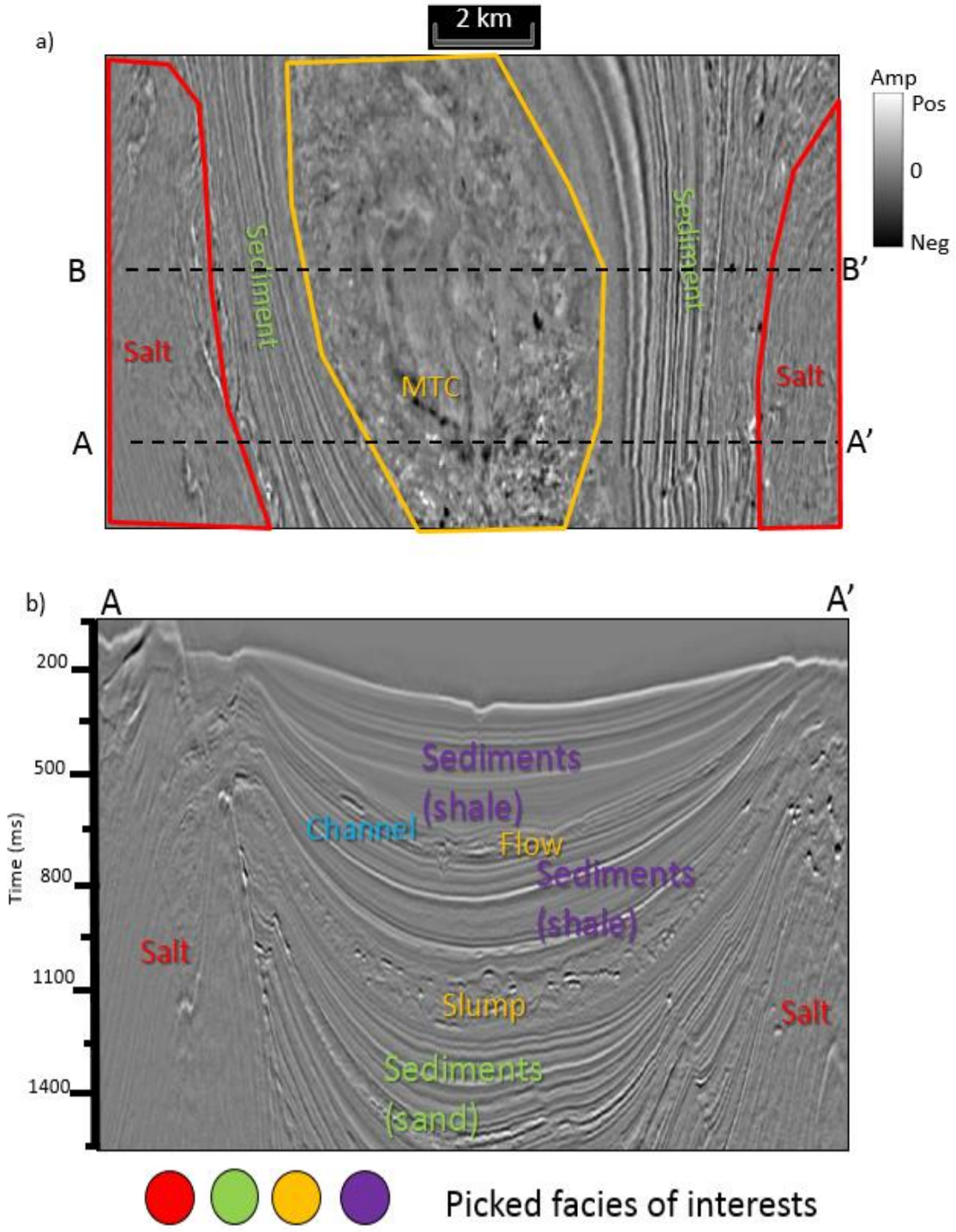

Figure 1.5 (a) Time slice at t=1144 ms, and (b) vertical slice along line AA' through the seismic amplitude volume. In these images, we have painted two seismic facies of interest: a red salt facies and a yellow MTC facies. Two other facies of interest are a suite of weak reflectors, which we interpret to be shale on shale package, and areas of stronger reflectors that we interpret to be a mixed sand-shale package. Line BB' has not been interpreted and will be shown in later figures.

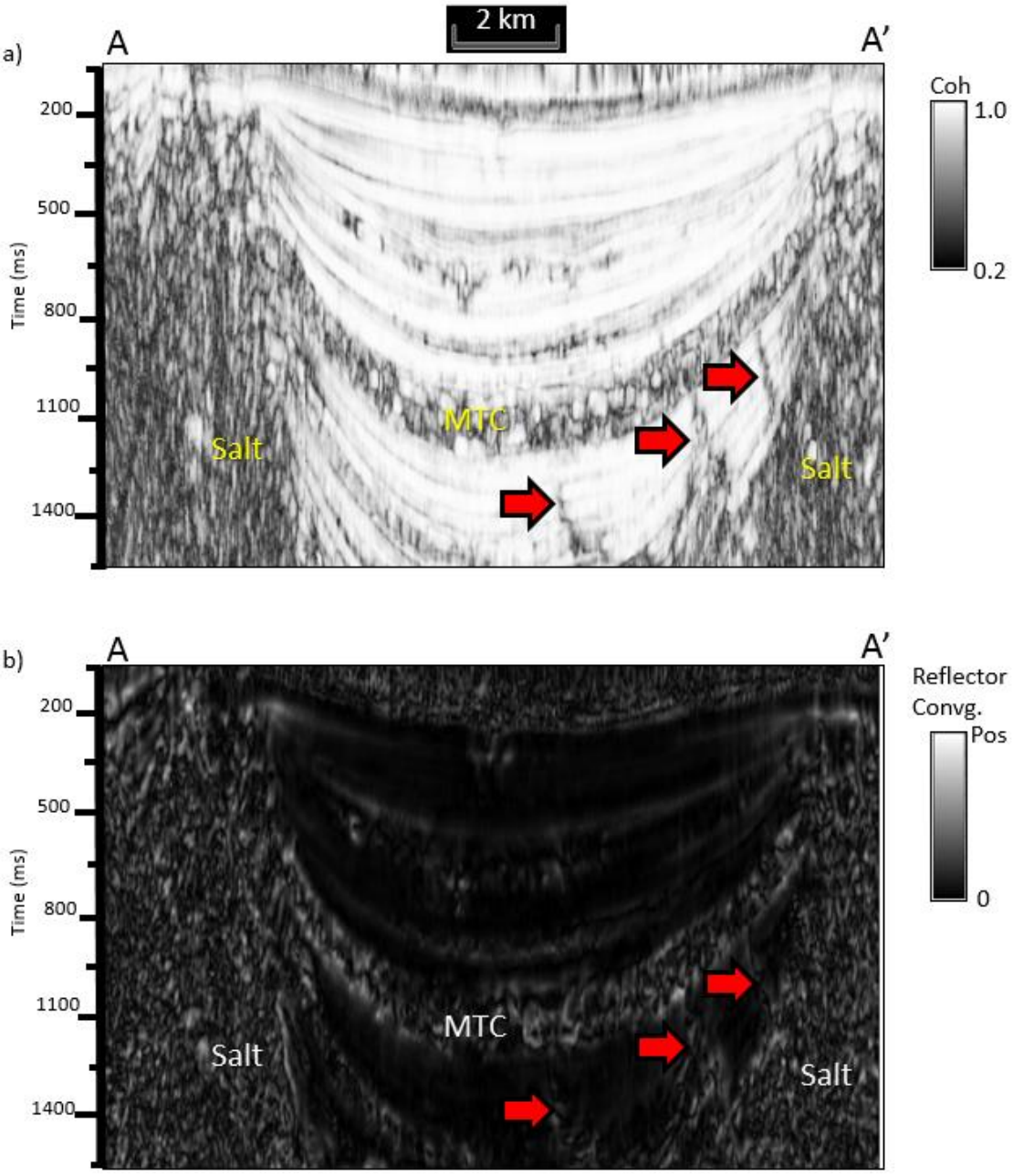
a)
A
2 km
A'
Time (ms)
200
500
800
1100
1400
Salt
MTC
Salt
Coh
1.0
0.2
b)
A
A'
Time (ms)
200
500
800
1100
1400
Salt
MTC
Salt
Reflector
Convg.
Pos
0

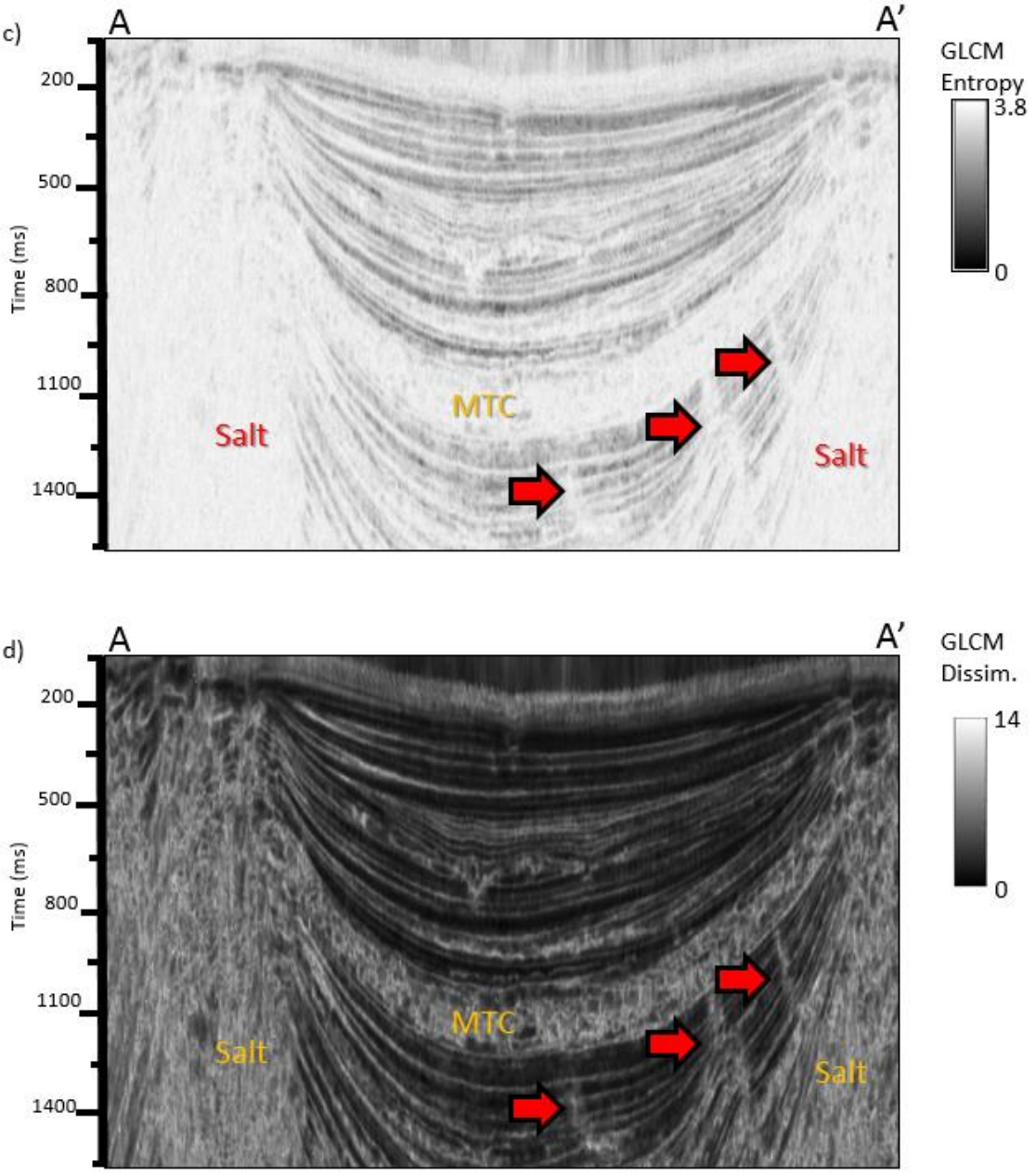
c)
A
A'
200
500
800
1100
1400
Time (ms)
Salt
MTC
Salt
GLCM
Entropy
3.8
0
d)
A
A'
200
500
800
1100
1400
Time (ms)
Salt
MTC
Salt
GLCM
Dissim.
14
0

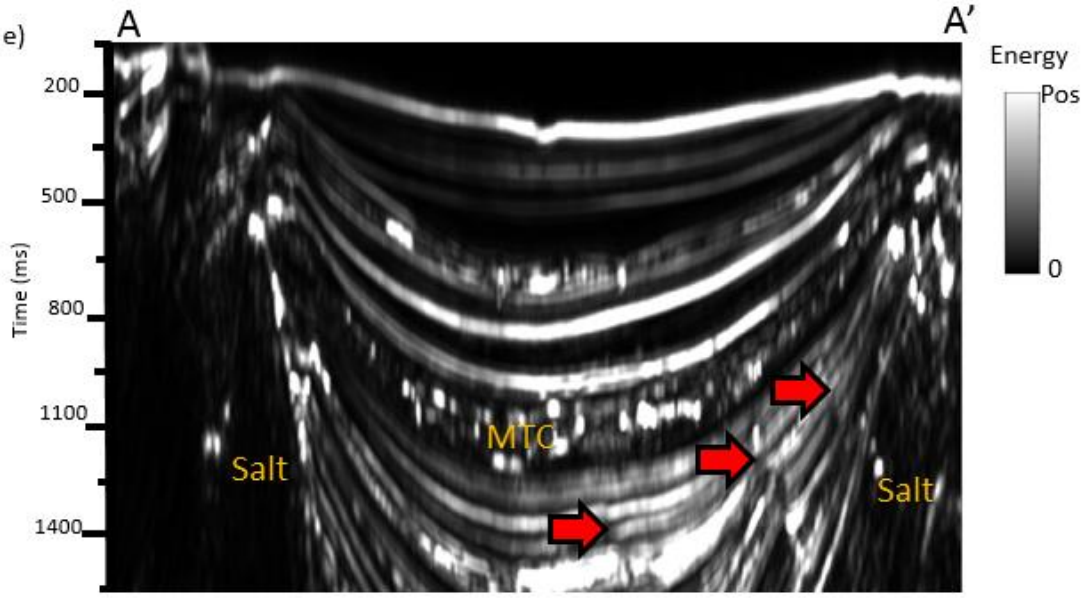

Figure 1.6 Vertical slices along line AA' through, (a) coherence, (b) magnitude of reflector convergence, (c) GLCM-entropy, (d) GLCM-dissimilarity and (e) coherence energy volumes. Note the "salt and pepper" expression of coherence and the magnitude of reflector convergence. Red arrows indicate faults, which will either be a separate facies or be misclassified in our attribute-based seismic facies analysis.

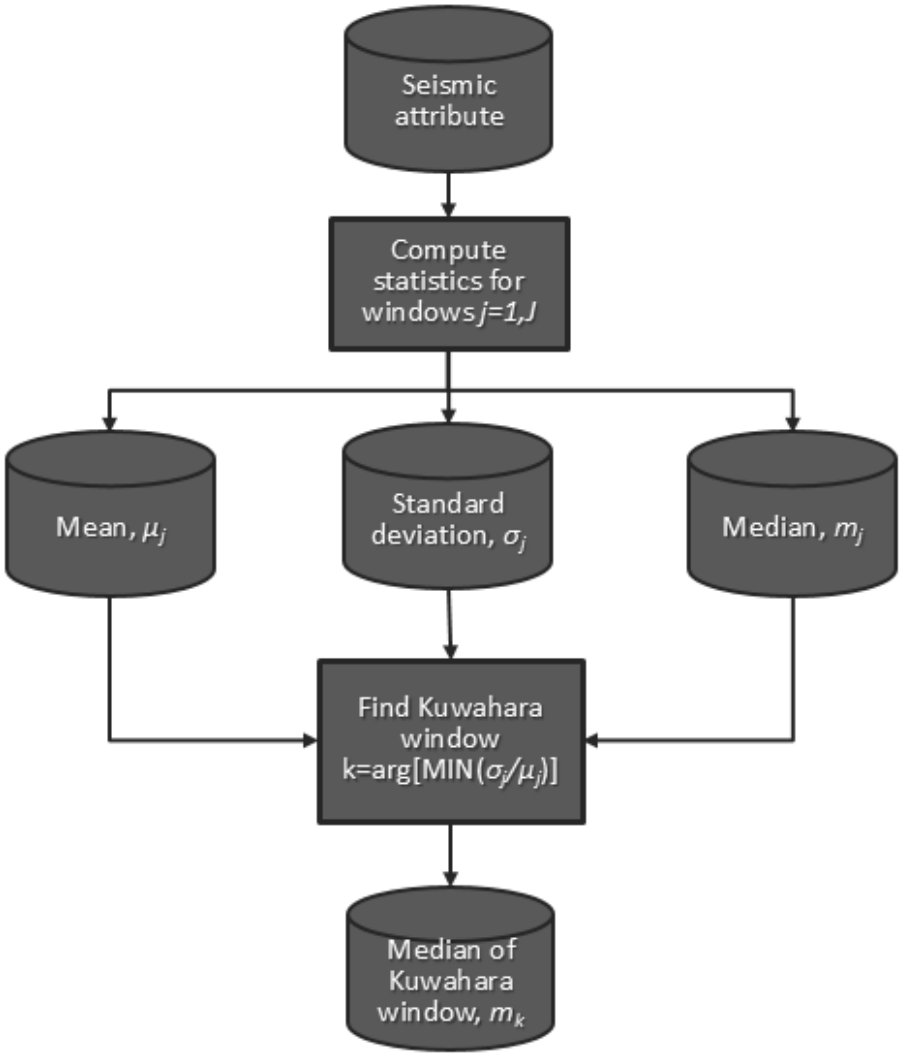

Figure 1.7 Workflow showing the input to Kuwahara filtering. For each attribute, first compute the mean, standard deviation, and median for every voxel using a centered *J*-sample analysis window. Then find the window *k* of *J* non-centered windows containing the target voxel that has the smallest normalized standard deviation, σ/μ. Finally, output the median, *m*, of window *k* as the filtered value at the target voxel.

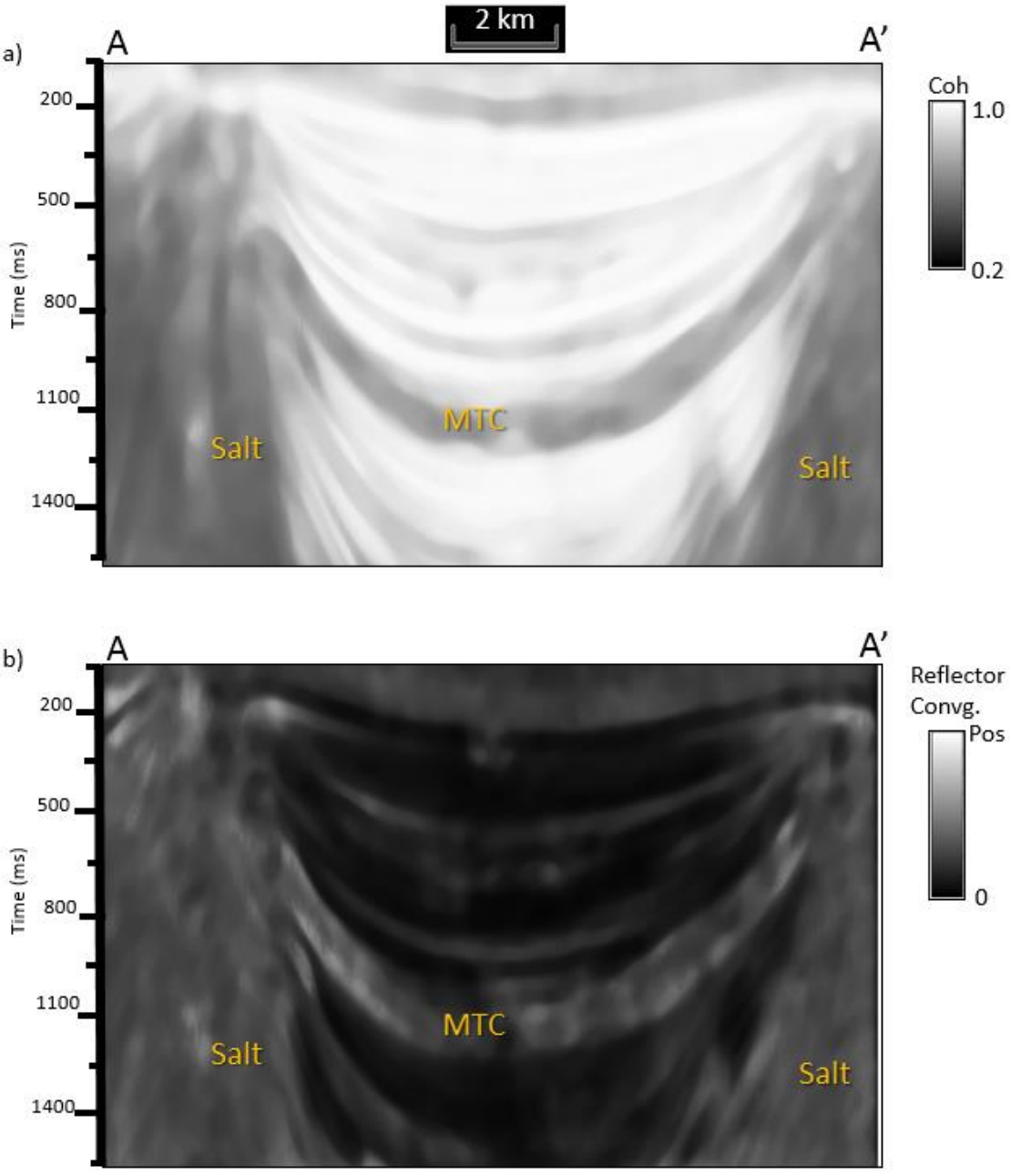
a)
A
2 km
A'
200
500
800
1100
1400
Time (ms)
Salt
MTC
Salt
Coh
1.0
0.2
b)
A
A'
200
500
800
1100
1400
Time (ms)
Salt
MTC
Salt
Reflector
Convg.
Pos
0

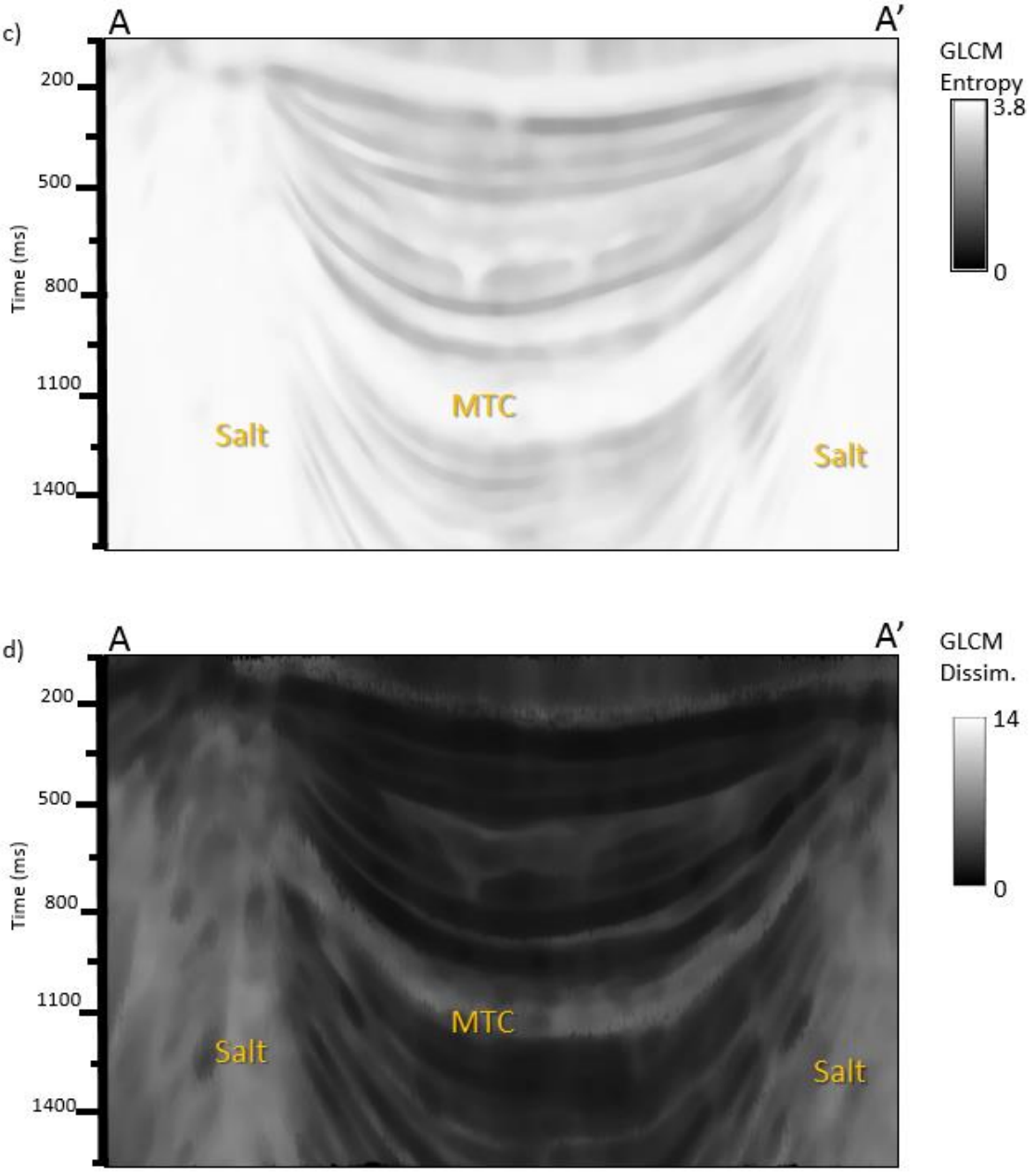
c)
A
A'
200
500
800
1100
1400
Time (ms)
Salt
MTC
Salt
GLCM
Entropy
3.8
0
d)
A
A'
200
500
800
1100
1400
Time (ms)
Salt
MTC
Salt
GLCM
Dissim.
14
0

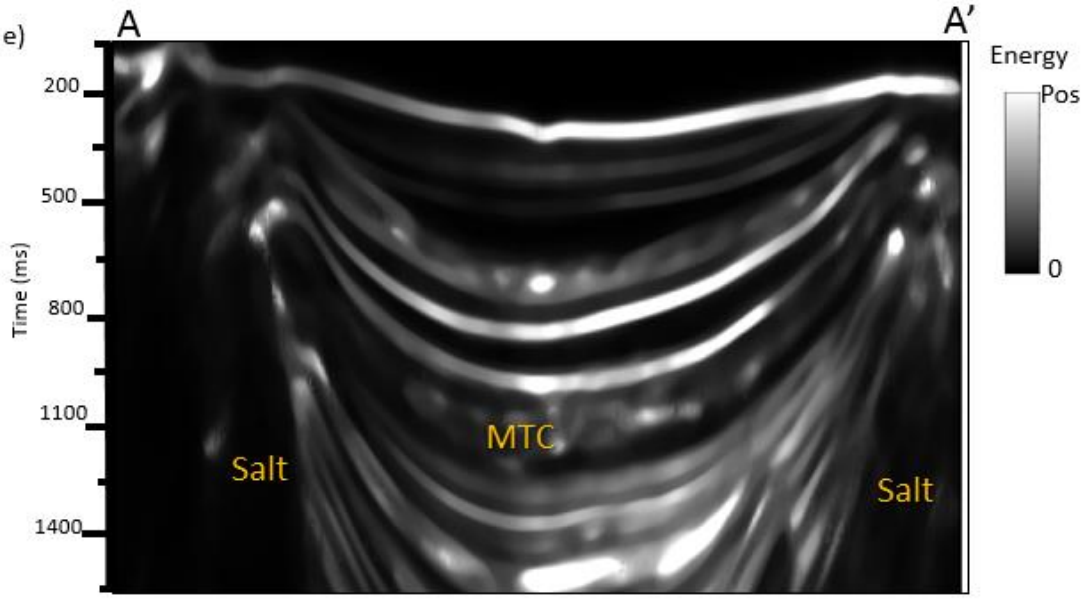

Figure 1.8 Vertical slices along line AA' through median-filtered (a) coherence, (b) magnitude of reflector convergence, (c) GLCM-entropy, (d) GLCM-dissimilarity and (e) coherent energy. Note that the "salt and pepper" expression of coherence and the magnitude of reflector convergence have been suppressed.

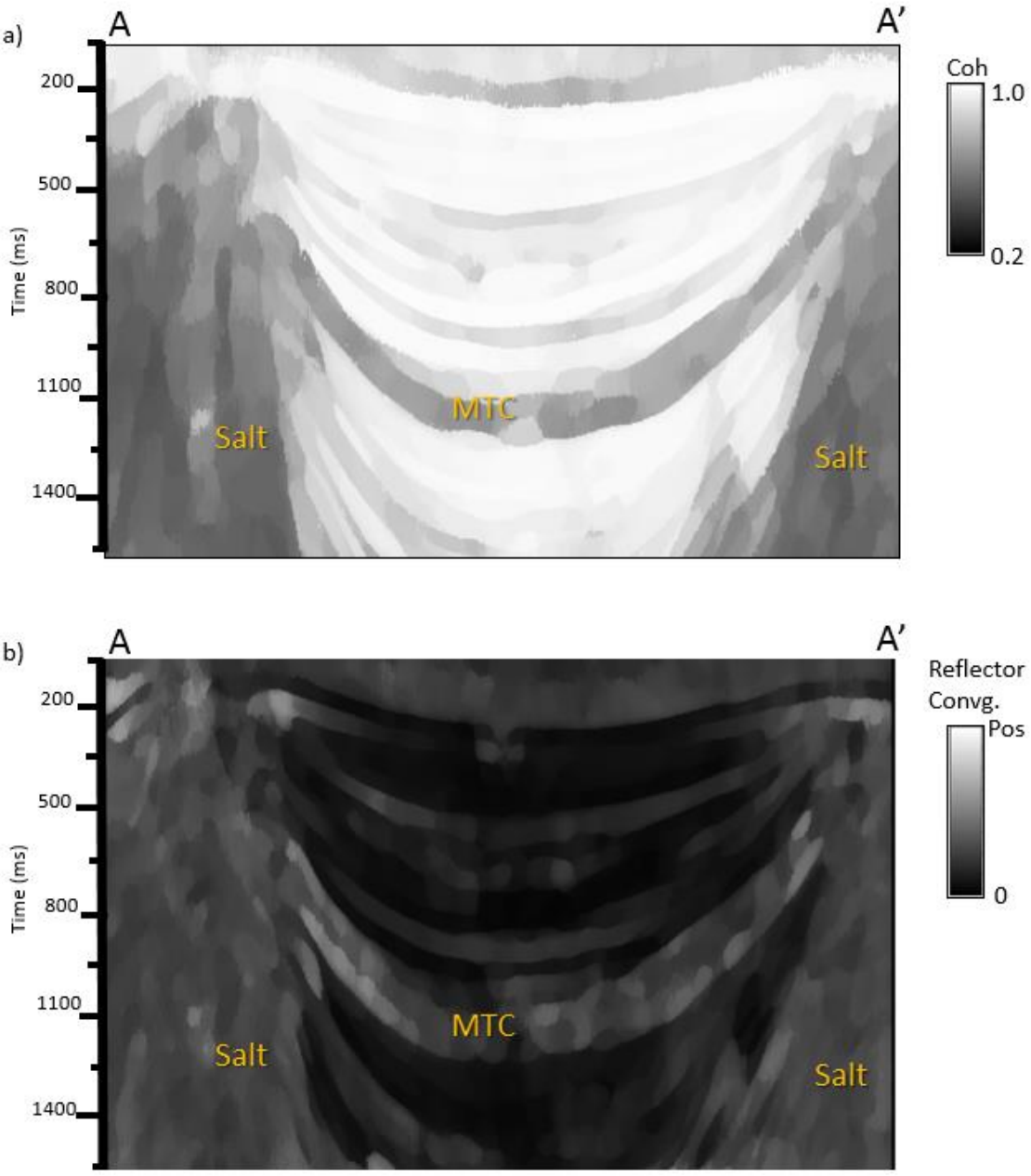
a)
A
A'
200
500
800
1100
1400
Time (ms)
Salt
MTC
Salt
Coh
1.0
0.2
b)
A
A'
200
500
800
1100
1400
Time (ms)
Salt
MTC
Salt
Reflector
Convg.
Pos
0

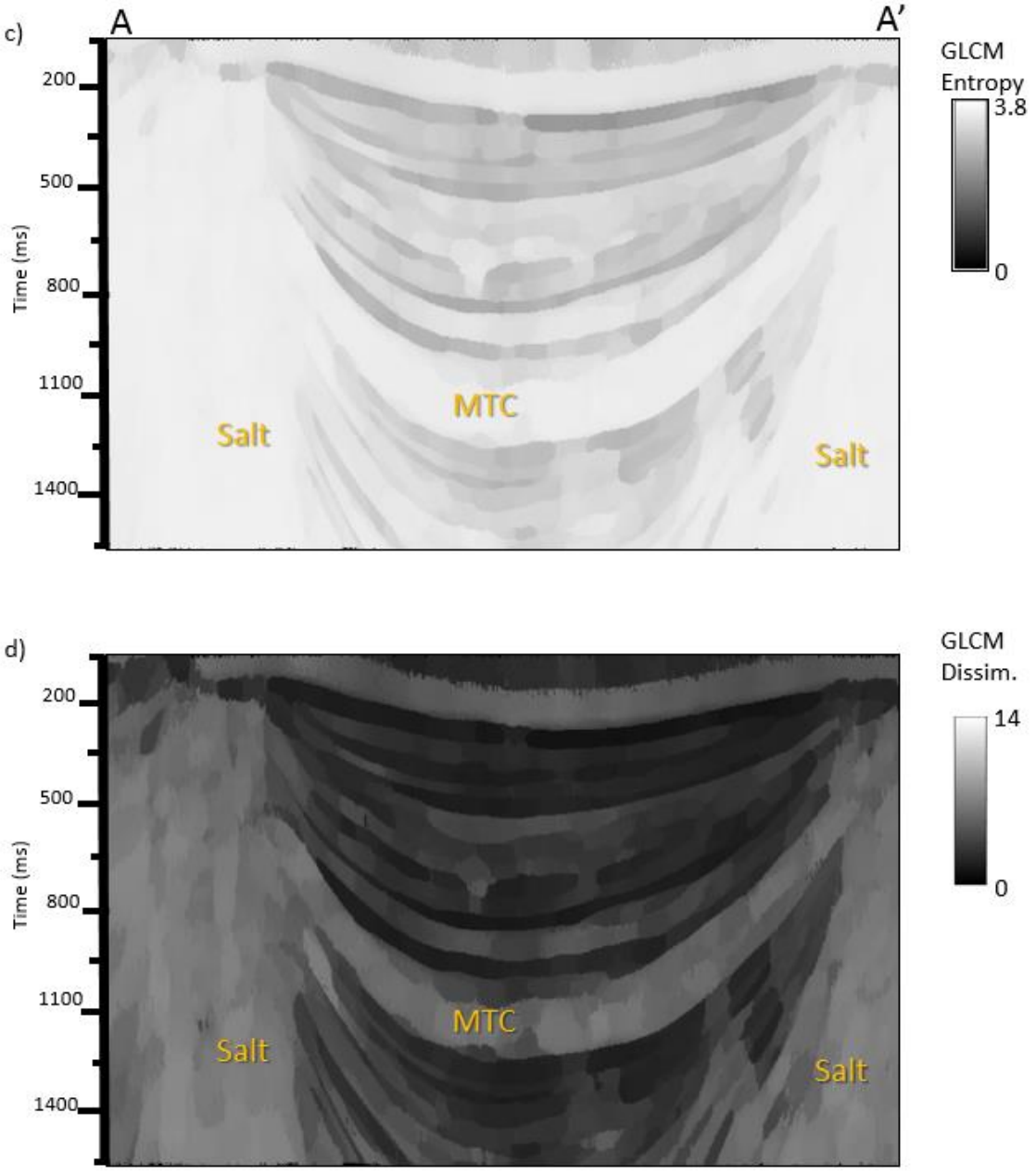
c)
A
A'
200
500
800
1100
1400
Time (ms)
Salt
MTC
Salt
GLCM
Entropy
3.8
0
d)
200
500
800
1100
1400
Time (ms)
Salt
MTC
Salt
GLCM
Dissim.
14
0

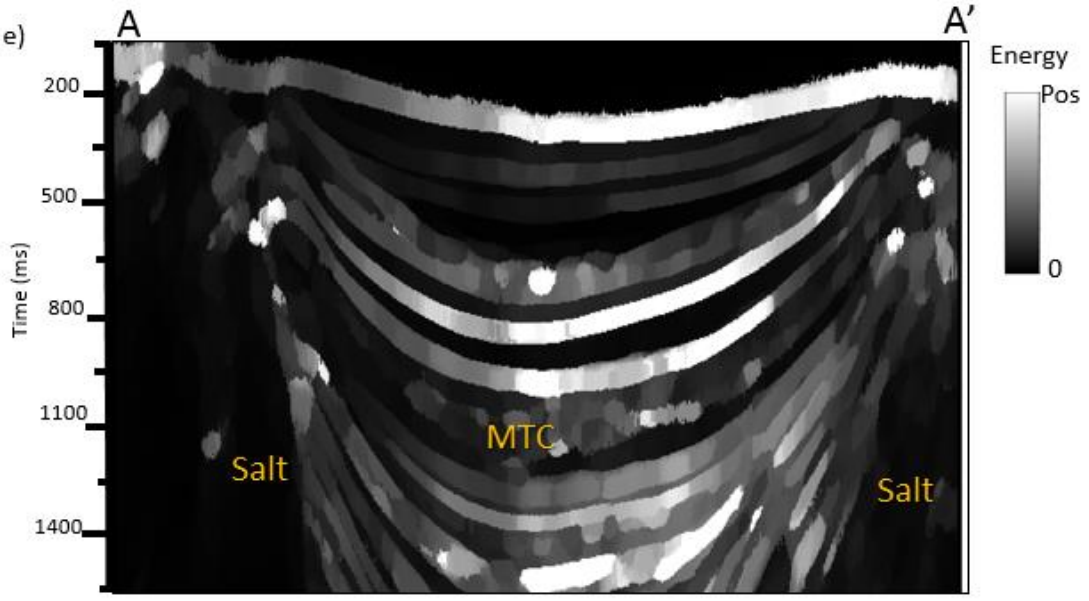

Figure 1.9 Vertical slices along line AA' through Kuwahara-filtered (a) coherence, (b) magnitude of reflector convergence, (c) GLCM-entropy, (d) GLCM-dissimilarity, and (e) coherent energy. Compared with the median-filtered attributes; the Kuwahara-filtered attributes have much clearer edges between any facies.

a)

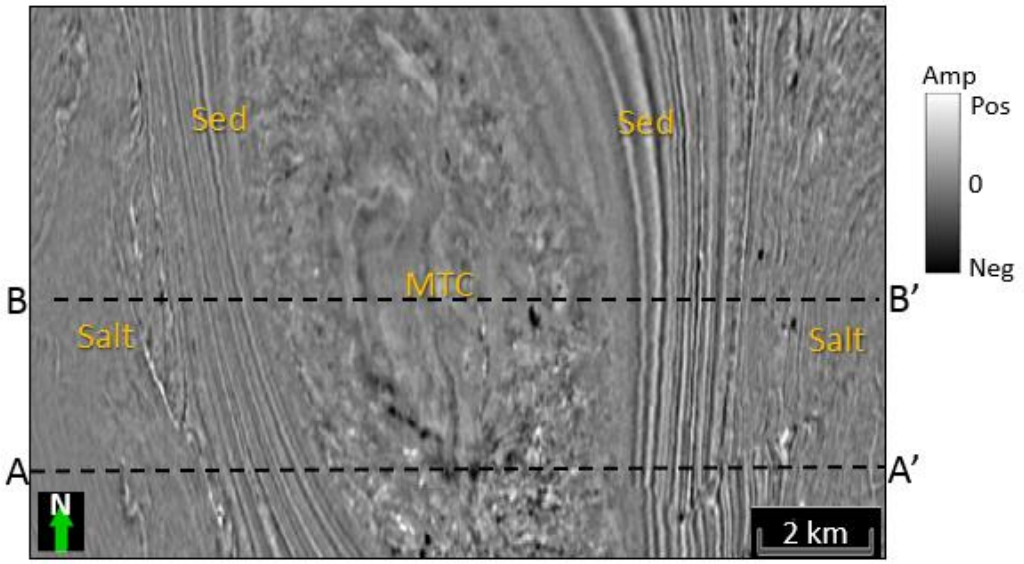
Sed
Sed
MTC
B
B'
Salt
Salt
A
A'
N
2 km
Amp
Pos
0
Neg

b)

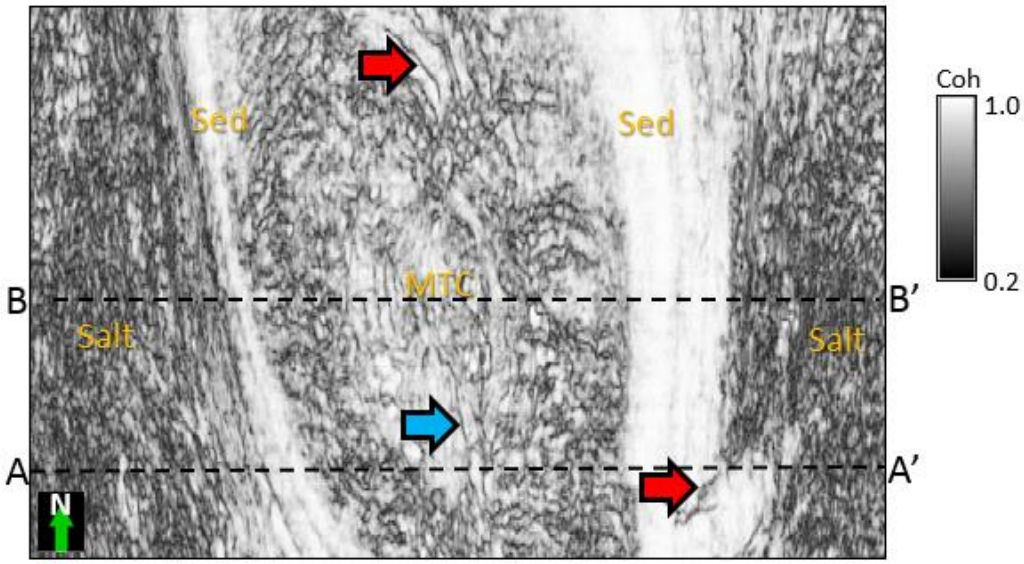
Sed
Sed
MTC
B
B'
Salt
Salt
A
A'
N
Coh
1.0
0.2

c)

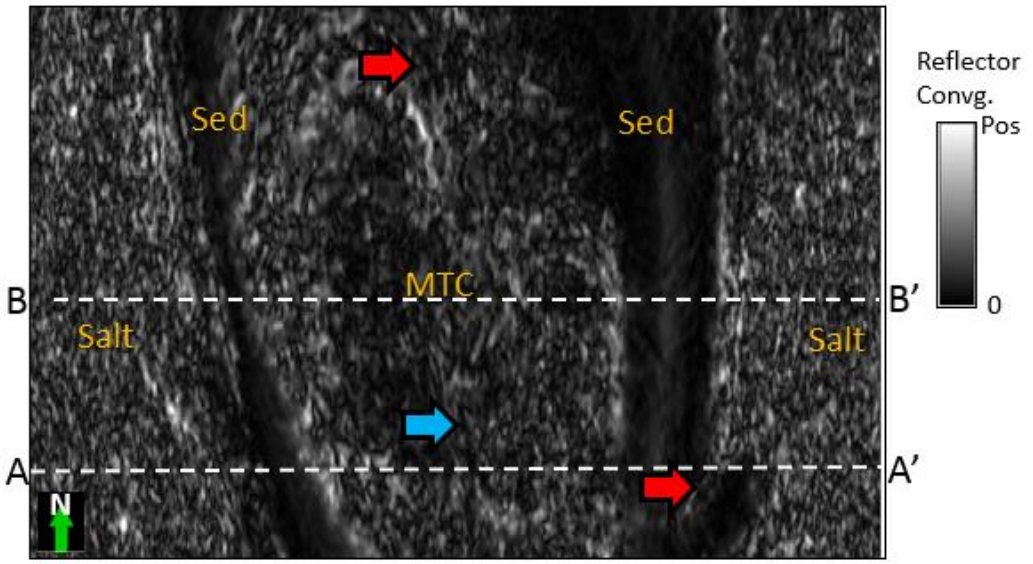
Sed
Sed
MTC
B
B'
Salt
Salt
A
A'
N
Reflector
Convg.
Pos
0

d)

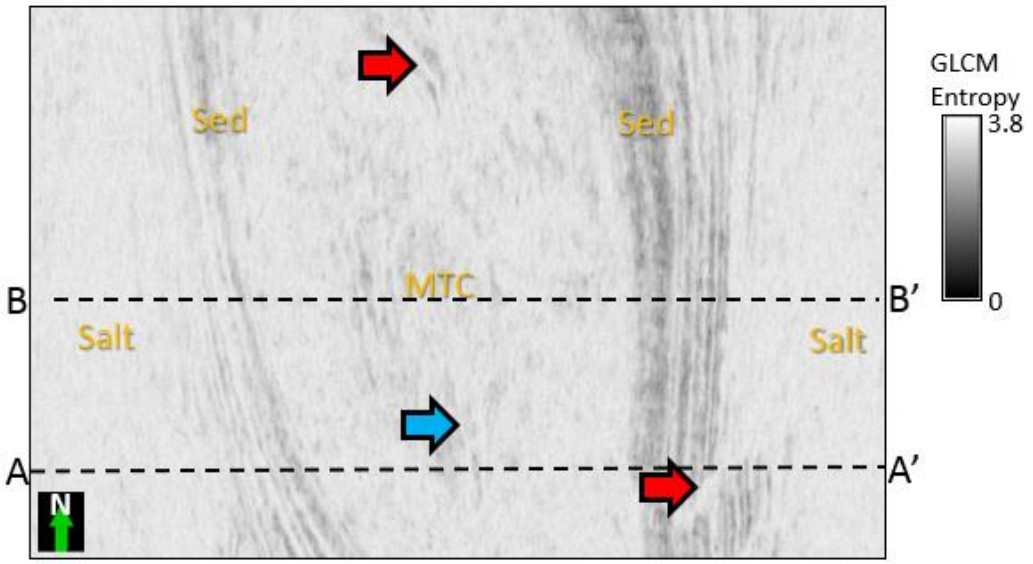
Sed
Sed
MTC
B
B'
Salt
Salt
A
A'
N
GLCM
Entropy
3.8
0

e)

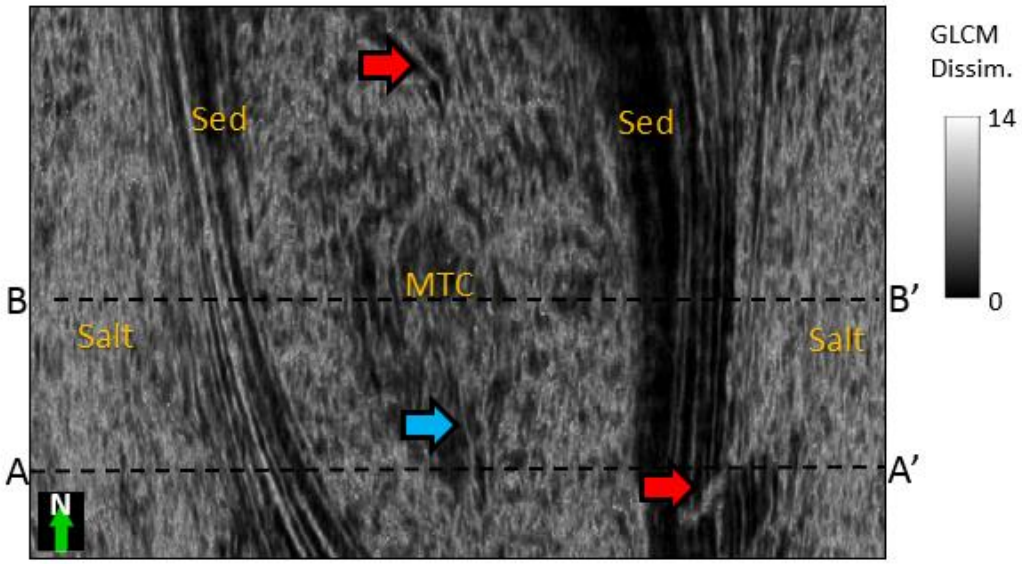
Sed
Sed
MTC
B
B'
Salt
Salt
A
A'
N
GLCM
Dissim.
14
0

f)

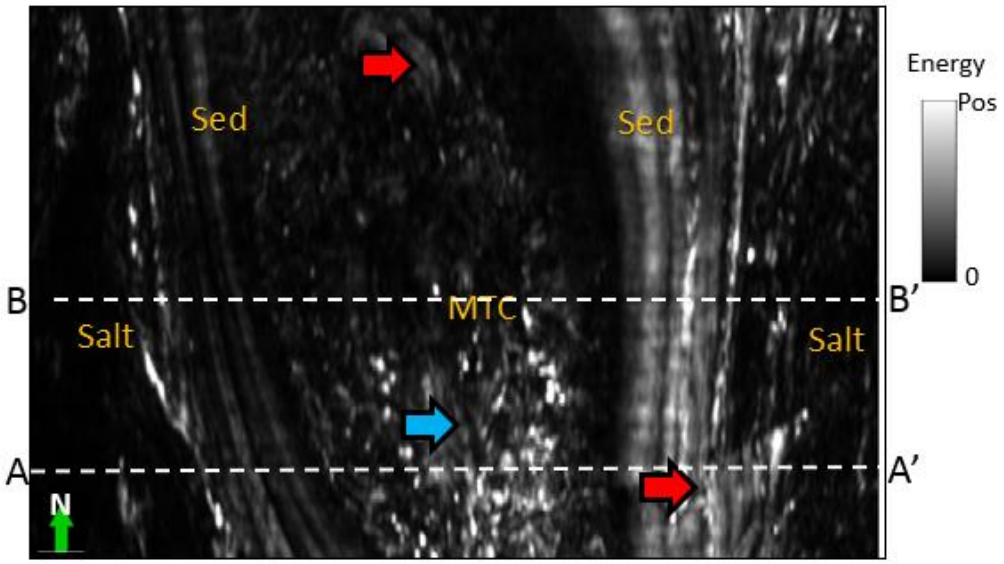
Sed
Sed
B
MTC
B'
Salt
Salt
A
A'
N
Energy
Pos
0

g)

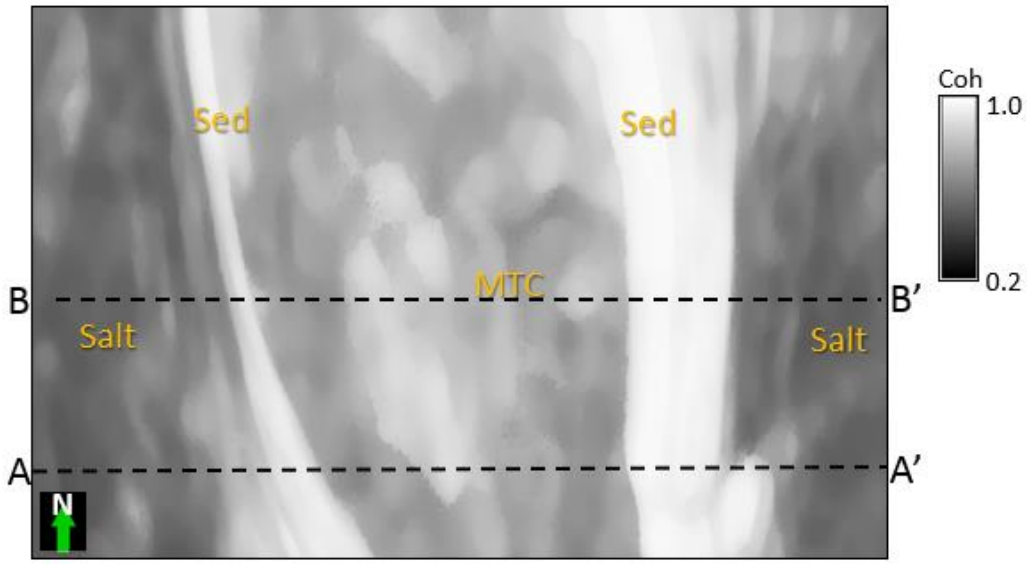
Sed
Sed
MTC
B
B'
Salt
Salt
A
A'
N
Coh
1.0
0.2

h)

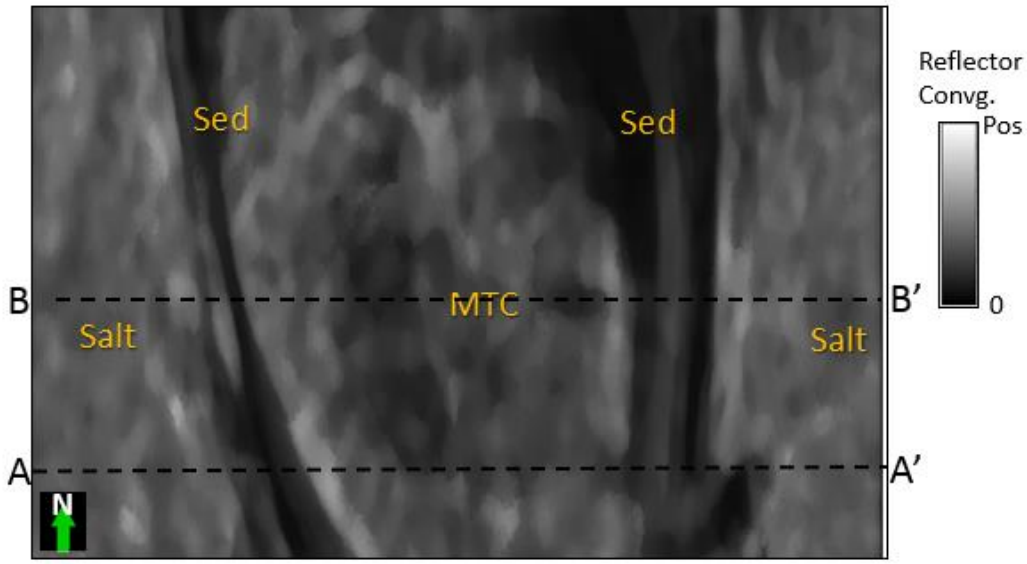
Sed
Sed
MTC
B
B'
Salt
Salt
A
A'
N
Reflector
Convg.
Pos
0

i)

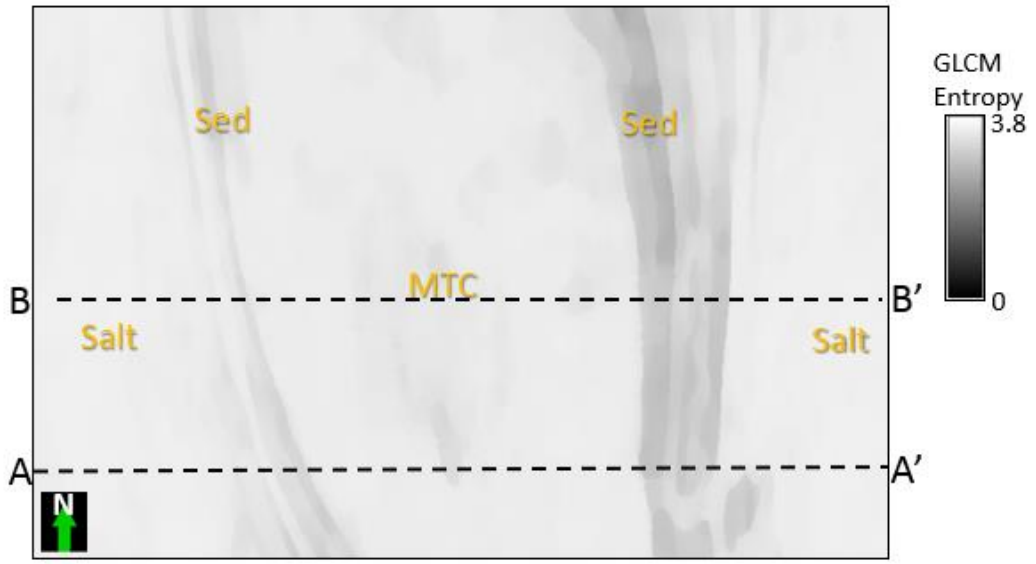
Sed
Sed
MTC
B
B'
Salt
Salt
A
A'
N
GLCM
Entropy
3.8
0

j)

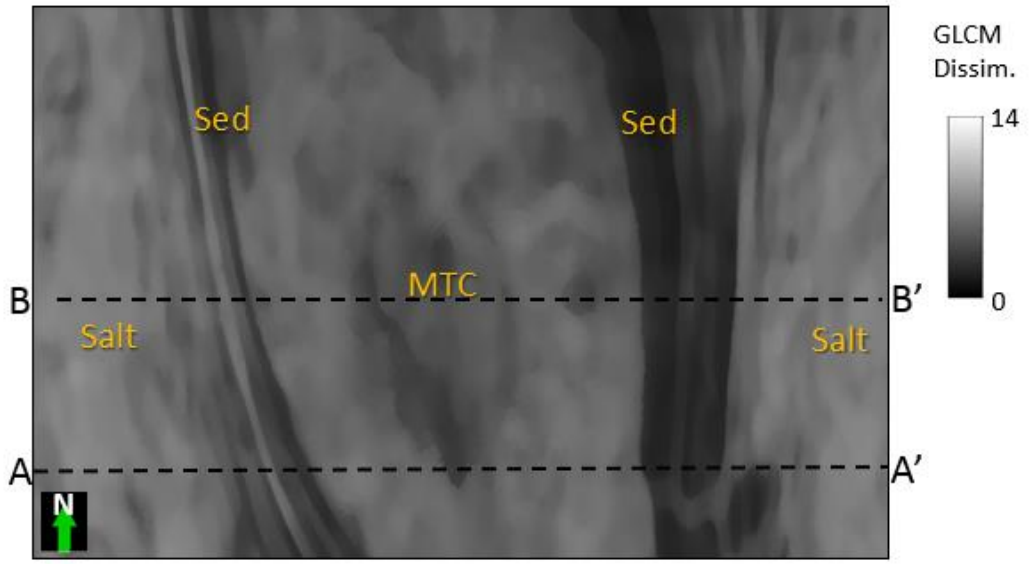
Sed
Sed
MTC
B
B'
Salt
Salt
A
A'
N
GLCM
Dissim.
14
0

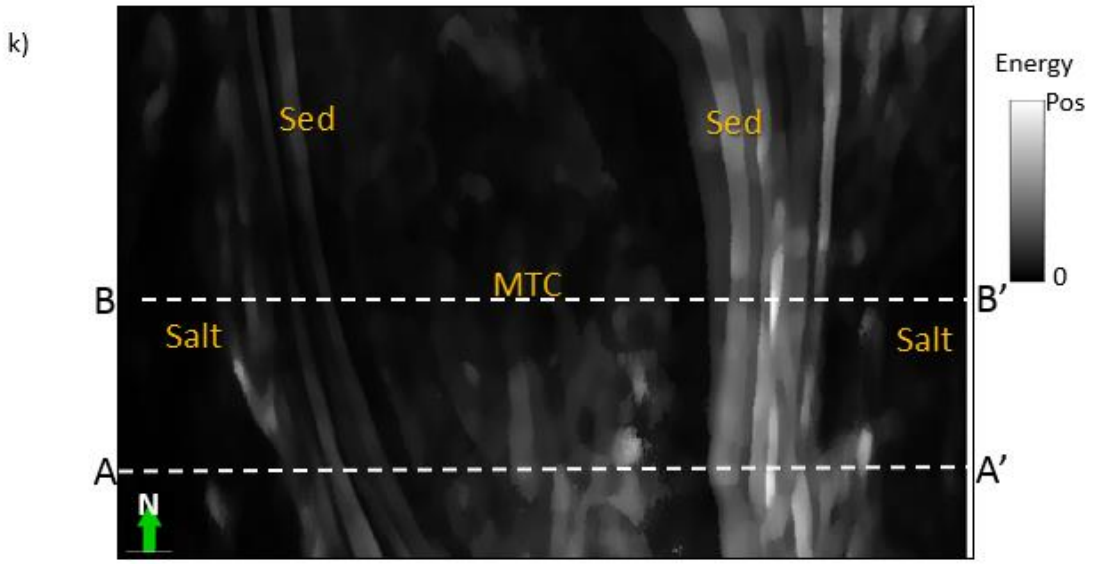

Figure 1.10 Time slices at t=1144ms through, (a) seismic amplitude, (b) coherence, (c) magnitude of reflector convergence, (d) GLCM-entropy, (e) GLCM-dissimilarity, and (f) coherent energy, and Kuwahara-filtered attributes (g) – (k). The Kuwahara-filtered attributes suppress the "salt and pepper"; these are much clearer boundaries between any two seismic facies. Patterns are easy for human interpreters, but difficult for classifiers to identify as a single face.

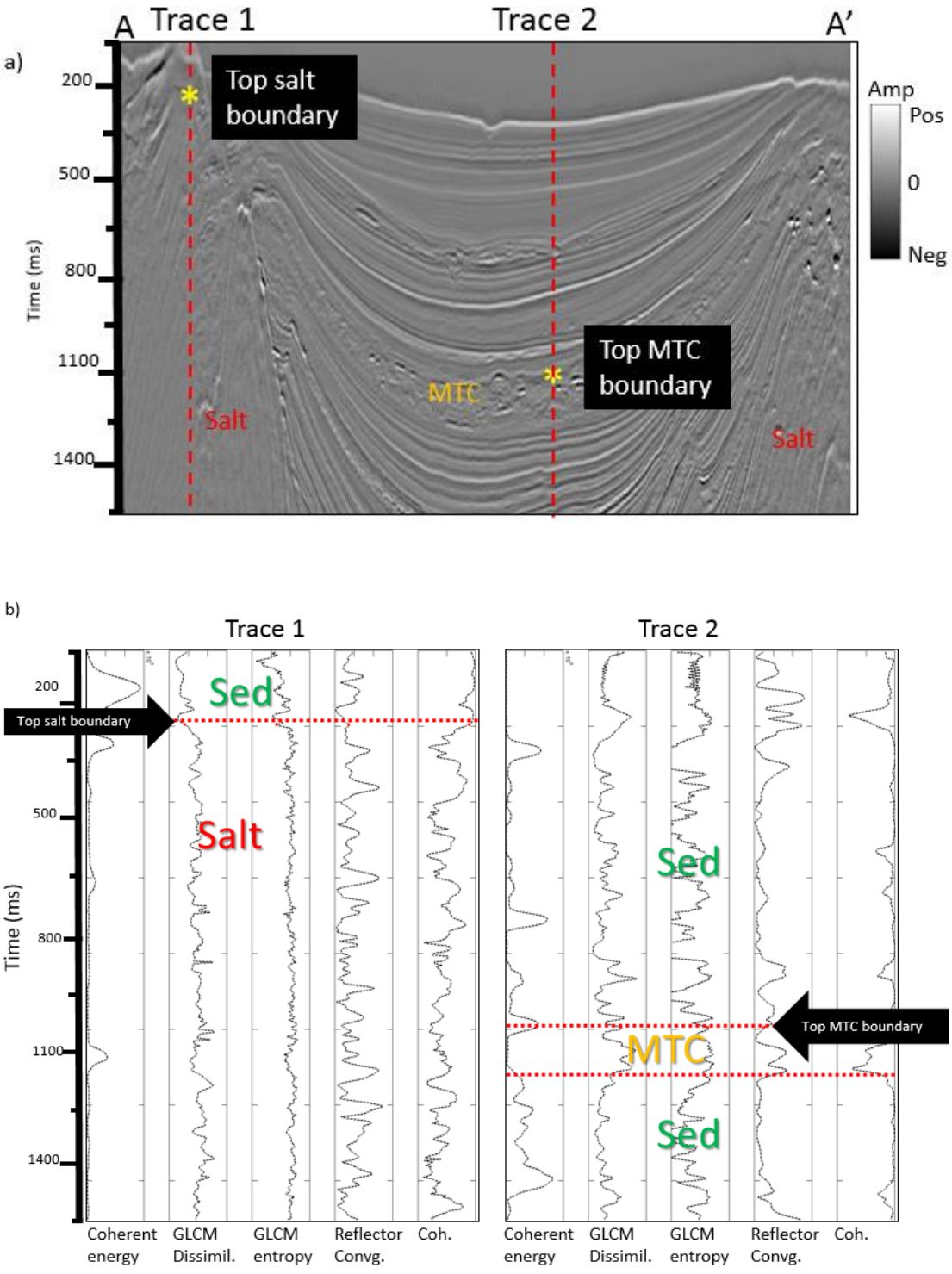
a)
A
Trace 1
Trace 2
A'
Top salt boundary
Top MTC boundary
MTC
Salt
Salt
Time (ms)
200
500
800
1100
1400
Amp
Pos
0
Neg
b)
Trace 1
Trace 2
Top salt boundary
Top MTC boundary
Sed
Salt
Sed
MTC
Sed
Time (ms)
200
500
800
1100
1400
Coherent energy
GLCM Dissimil.
GLCM entropy
Reflector Convg.
Coh.
Coherent energy
GLCM Dissimil.
GLCM entropy
Reflector Convg.
Coh.

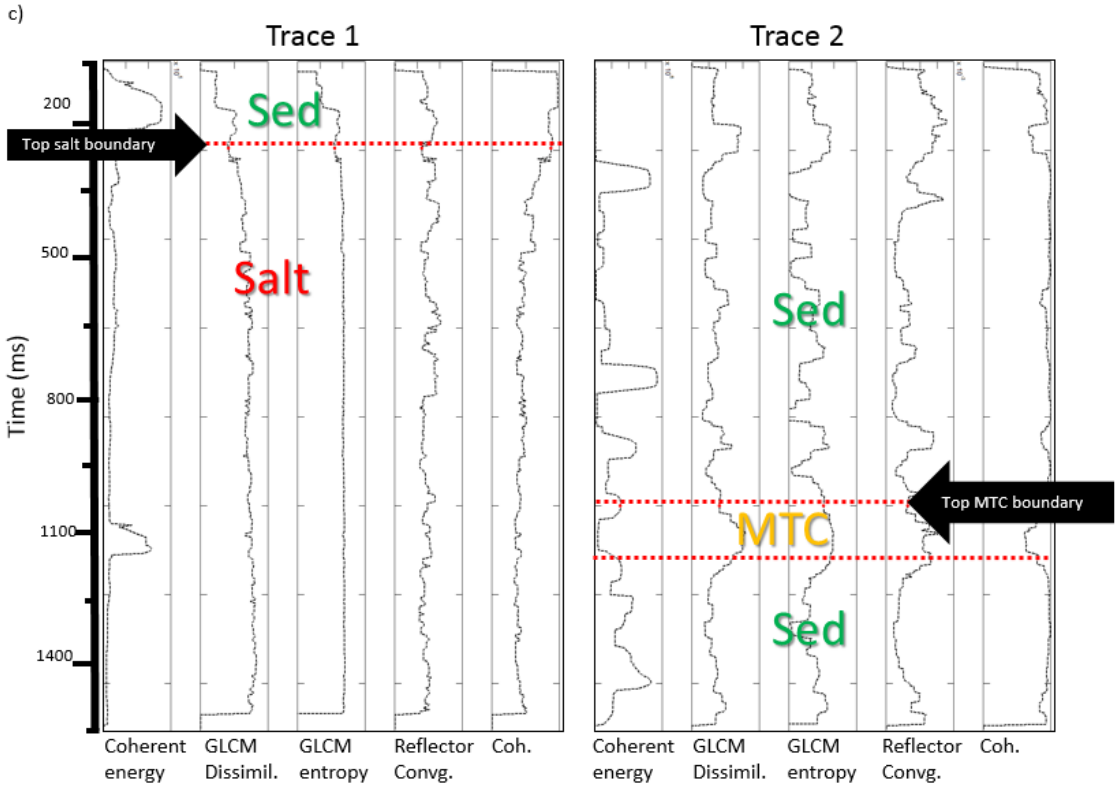

Figure 1.11(a) A vertical slice along line AA' through seismic amplitude, (b) original attribute values along the trace 1 and the trace 2, and (c) Kuwahara-filtered attribute. Before Kuwahara filtering, values within the salt dome vary rapidly, making it difficult to detect the top salt boundary. In contrast, the Kuwahara filtered trace shows piecewise smooth values, producing a sharp boundary at the top of the salt dome and MTC.

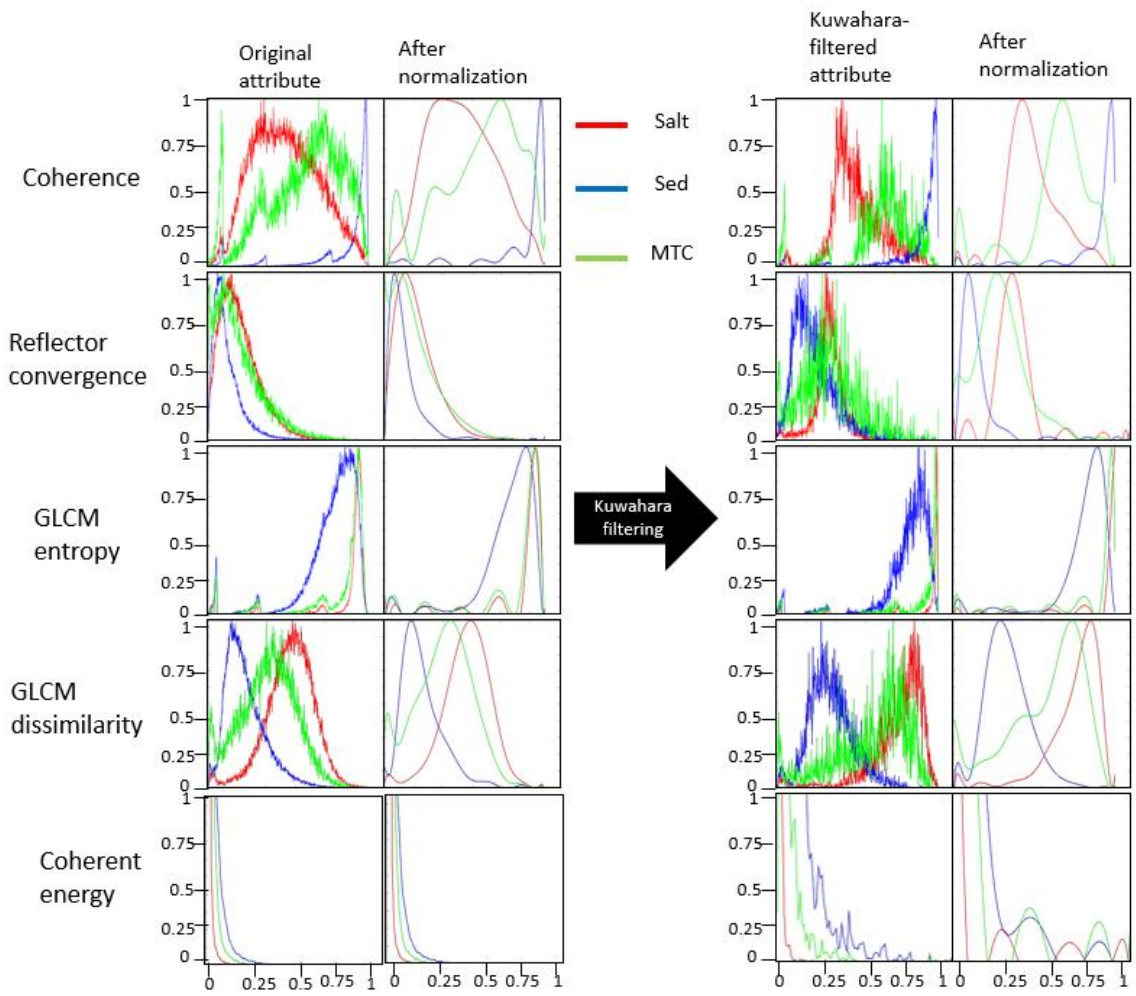

Figure 1.12 Histograms of picked facies are normalized for easy comparison and do not change the correlation coefficient of any histogram pair. Note that Kuwahara filtering both narrows and further separates the distribution of the attribute histograms.

a)

Original Attribute	Salt vs. MTC	MTC vs. Sediment	Sediment vs.Salt
Coherence	0.2871	0.1645	0.4526
Reflector convergence	0.8945	0.7385	0.4581
GLCM entropy	0.9336	0.5369	0.3163
GLCM dissimilarity	0.6476	0.3399	0.2612
Coherent energy	0.9546	0.9946	0.9209

b)

Kuwahara-filtered attribute	Salt vs. MTC	MTC vs. Sediment	Sediment vs. Salt
Coherence	0.0434	0.1593	0.2933
Reflector convergence	0.6579	0.2714	0.1363
GLCM entropy	0.6085	0.182	0.0684
GLCM dissimilarity	0.1414	0.1501	0.2435
Coherent energy	0.7362	0.9718	0.6606

Figure 1.13 Histogram correlation coefficient $r_{fg} < 0.5$ are highlighted in green between (a) original seismic attributes pairs, and (b) Kuwahara-filtered attributes pairs.

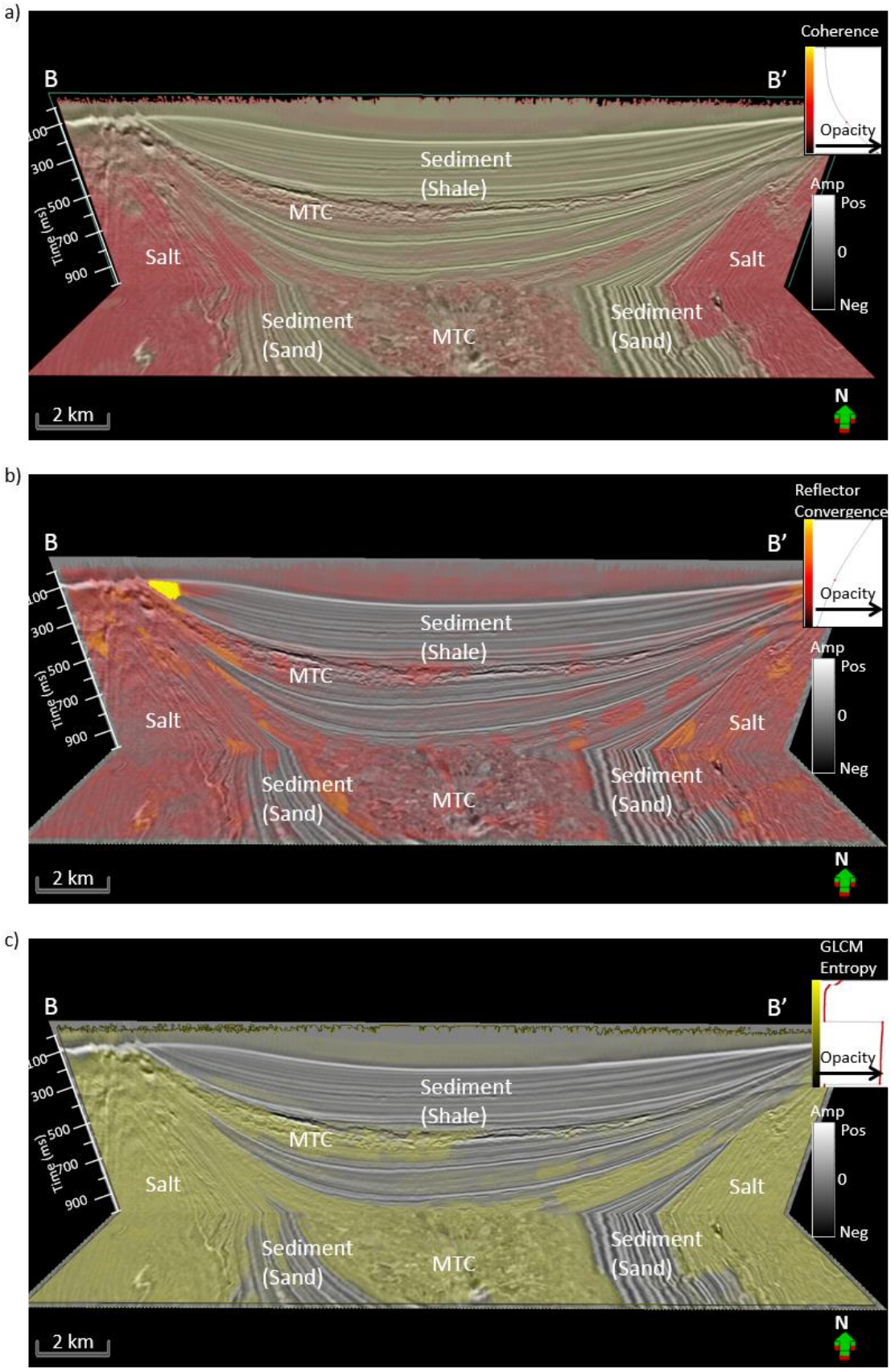
a)
B
B'
Coherence
Opacity
Amp
Pos
0
Neg
Time (ms)
100
300
500
700
900
Sediment
(Shale)
MTC
Salt
Salt
Sediment
(Sand)
MTC
Sediment
(Sand)
2 km
N
b)
B
B'
Reflector
Convergence
Opacity
Amp
Pos
0
Neg
Time (ms)
100
300
500
700
900
Sediment
(Shale)
MTC
Salt
Salt
Sediment
(Sand)
MTC
Sediment
(Sand)
2 km
N
c)
B
B'
GLCM
Entropy
Opacity
Amp
Pos
0
Neg
Time (ms)
100
300
500
700
900
Sediment
(Shale)
MTC
Salt
Salt
Sediment
(Sand)
MTC
Sediment
(Sand)
2 km
N

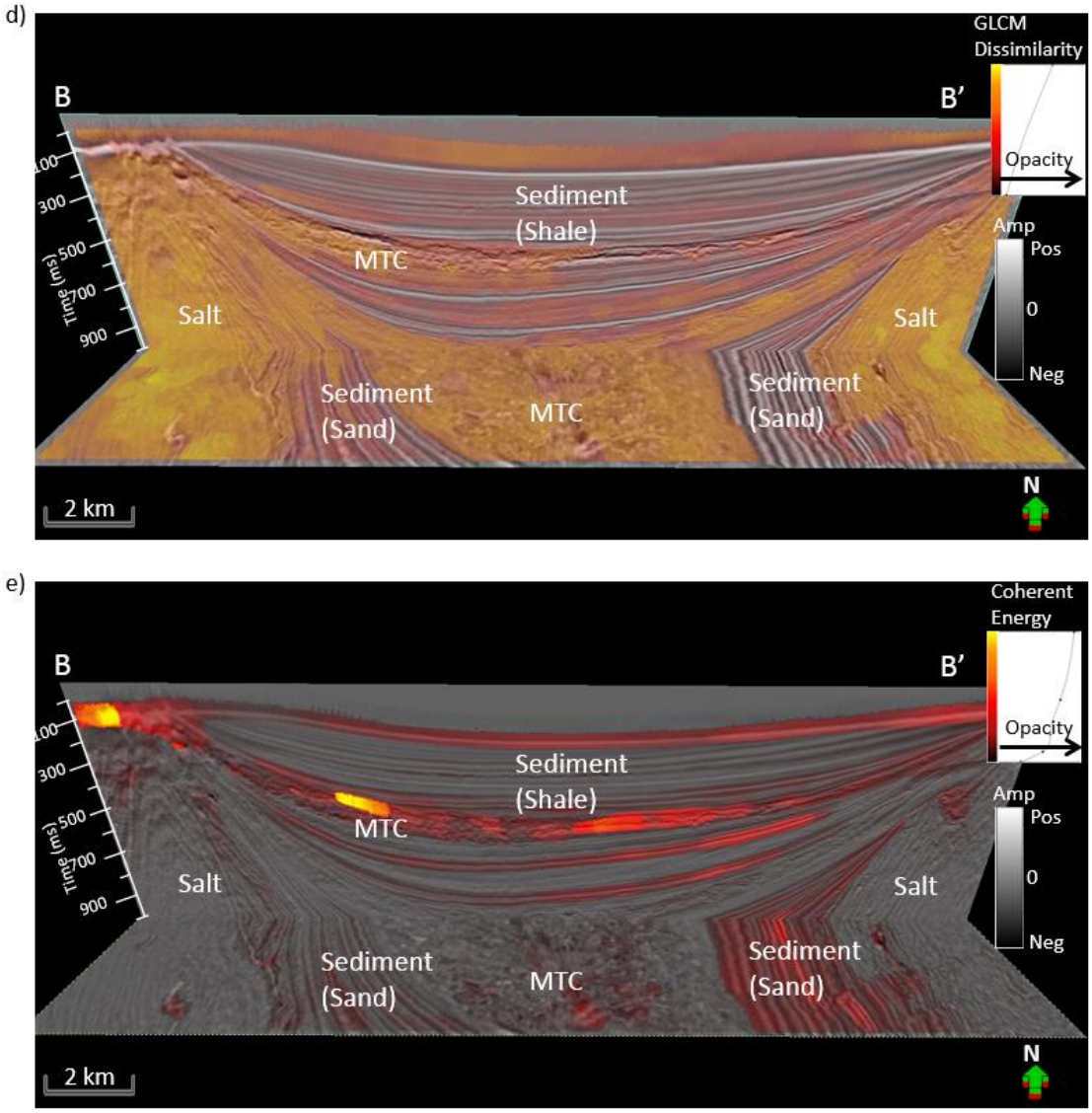

Figure 1.14 Vertical slices along line BB' and time slices at t=1172 ms through seismic amplitude co-rendered with Kuwahara-filtered and using threshold attributes, (a) coherence, (b) magnitude of reflector convergence, (c) GLCM-entropy, (d) GLCM-dissimilarity, and (e) coherent energy. Note that the Kuwahara-filtered attributes, with the low facies histogram correlation coefficient (Figure 1.13b), more clearly blocks the desired facies. Location of line BB' shows in Figure 1.5.

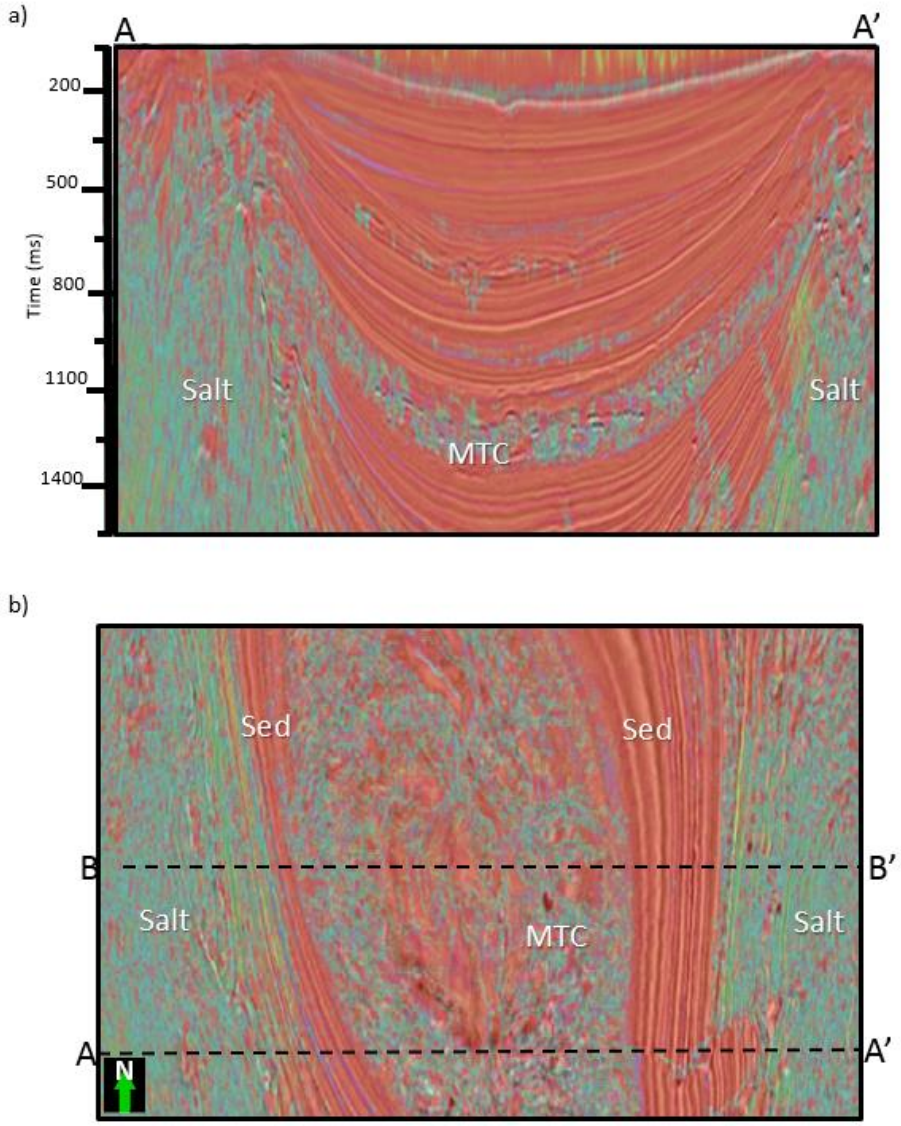
a)
A
A'
200
500
Time (ms)
800
1100
1400
Salt
MTC
Salt
b)
Sed
Sed
B
B'
Salt
MTC
Salt
A
A'
N

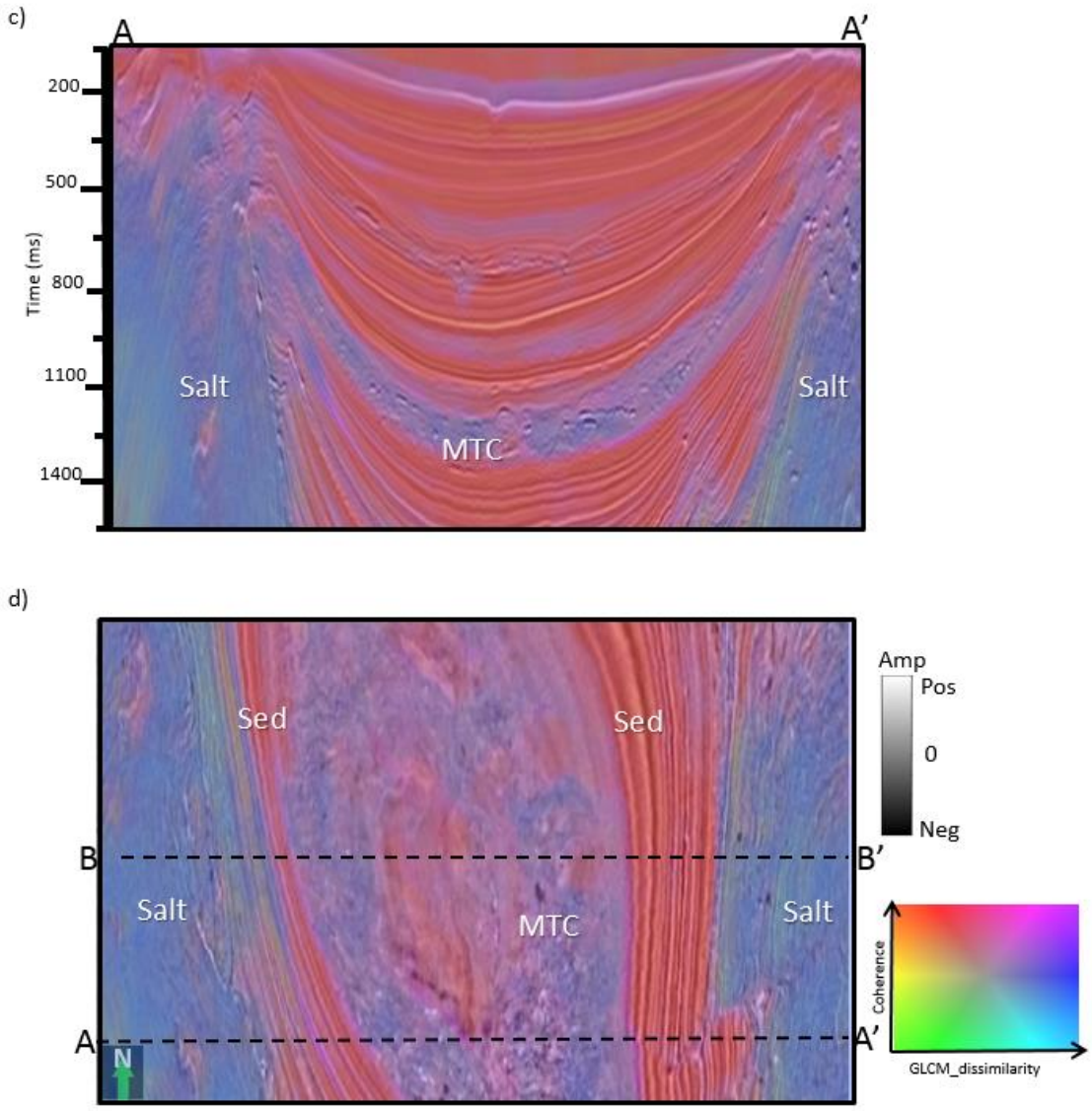

Figure 1.15 Vertical slices along line AA' and time slice at t=1144 ms through crossplotted coherence and GLCM-dissimilarity, before (a) and (b), and after (c) and (d) Kuwahara filtering. Note that the Kuwahara filtered crossplot shows sharper edges and less internal variation.

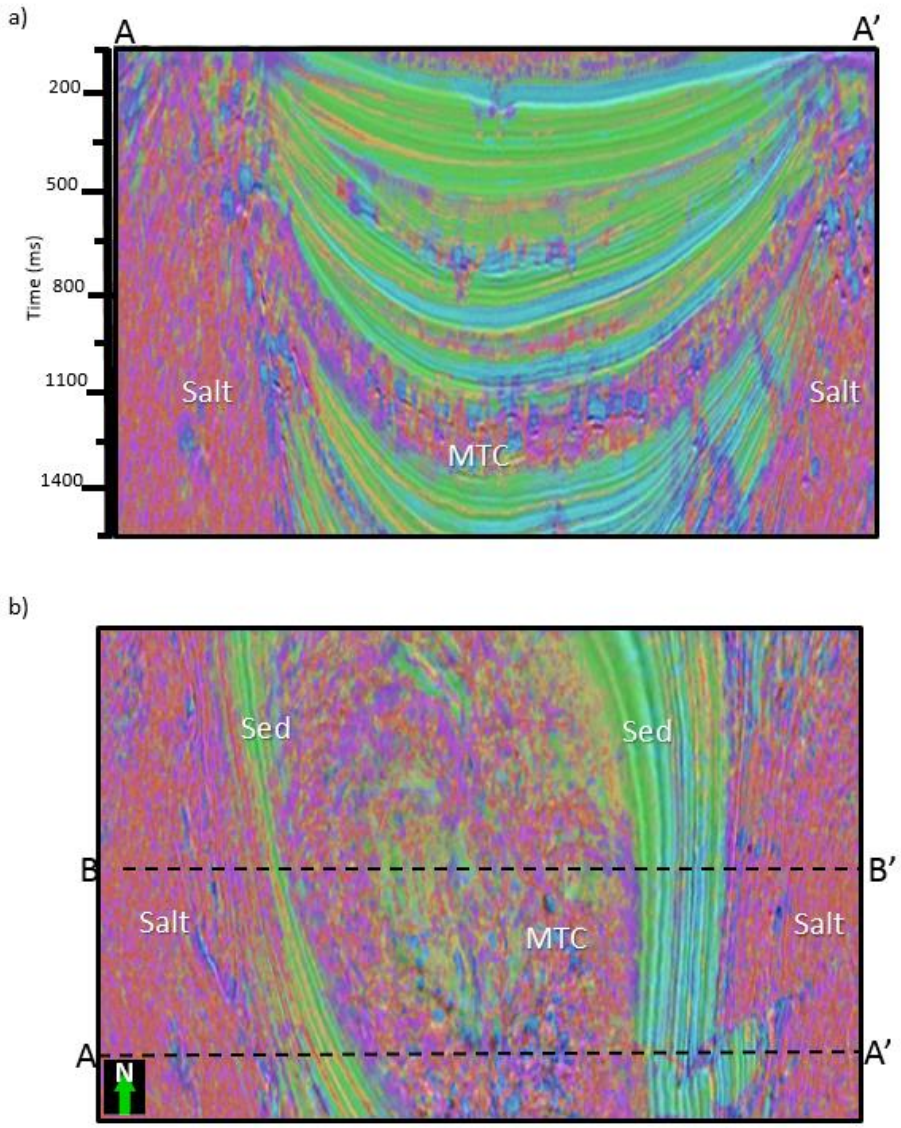
a)
A
A'
200
500
Time (ms)
800
1100
1400
Salt
MTC
Salt
b)
Sed
Sed
B
B'
Salt
MTC
Salt
A
A'
N

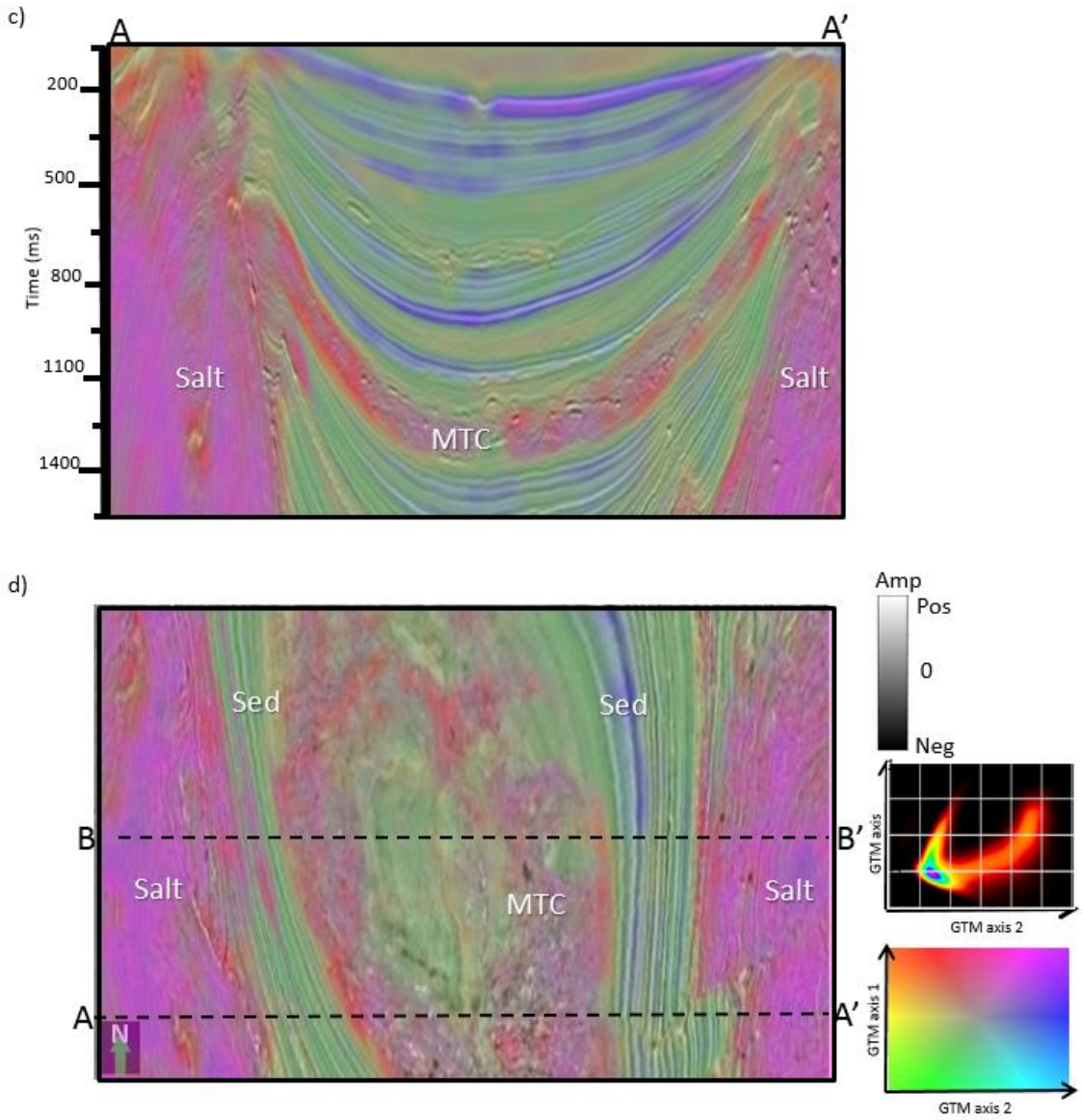

Figure 1.16 (a) Vertical slices along line AA' and (b) time slice at t=1144 ms through gtm classification with original attributes use a 2D latent space mapped against; (c) vertical slices along line AA' and (d) time slice at t=1144 ms through gtm classification with Kuwahara filtered attributes.

a)

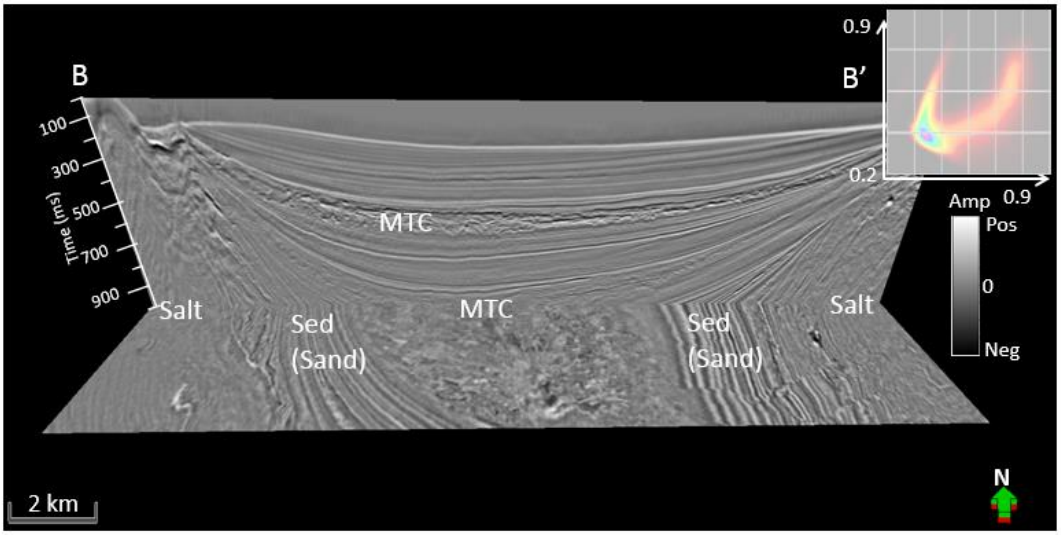
B
B'
100
300
500
700
900
Time (ms)
MTC
MTC
Salt
Sed
(Sand)
Sed
(Sand)
Salt
0.9
0.2
0.9
Amp
Pos
0
Neg
N
2 km

b)

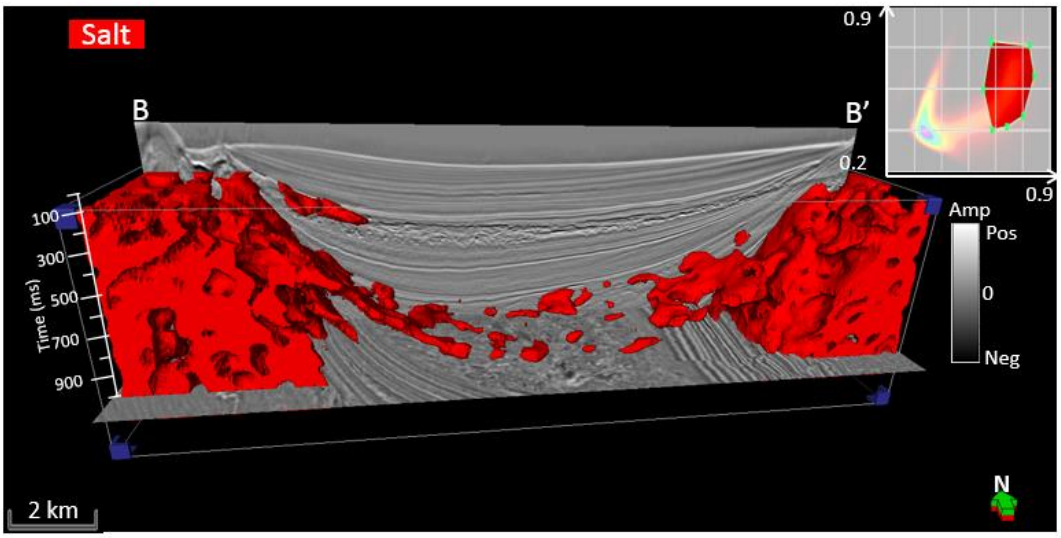
Salt
B
B'
100
300
500
700
900
Time (ms)
0.9
0.2
0.9
Amp
Pos
0
Neg
N
2 km

c)

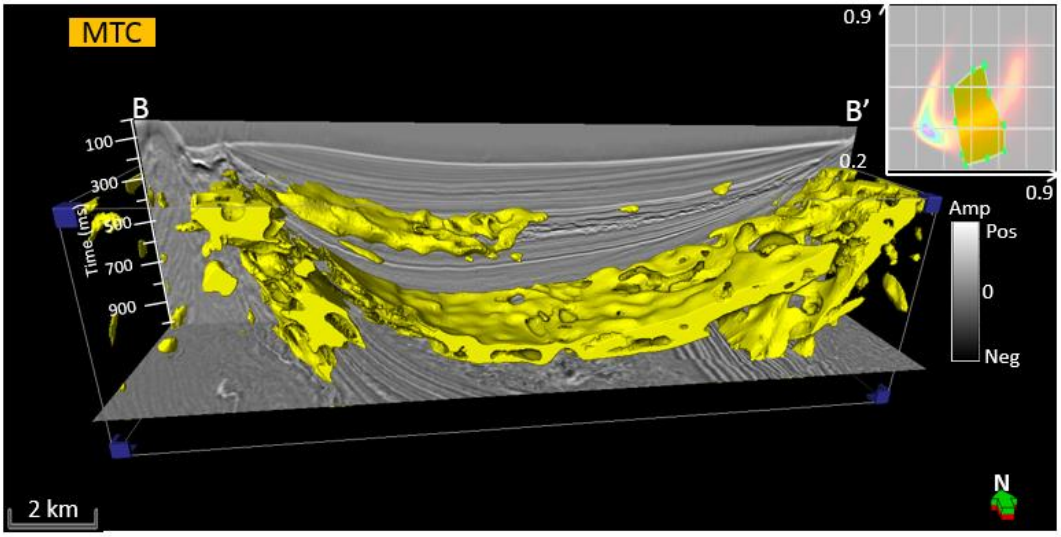
MTC
B
B′
100
300
500
700
900
Time (ms)
0.9
0.2
0.9
Amp
Pos
0
Neg
N
2 km

d)

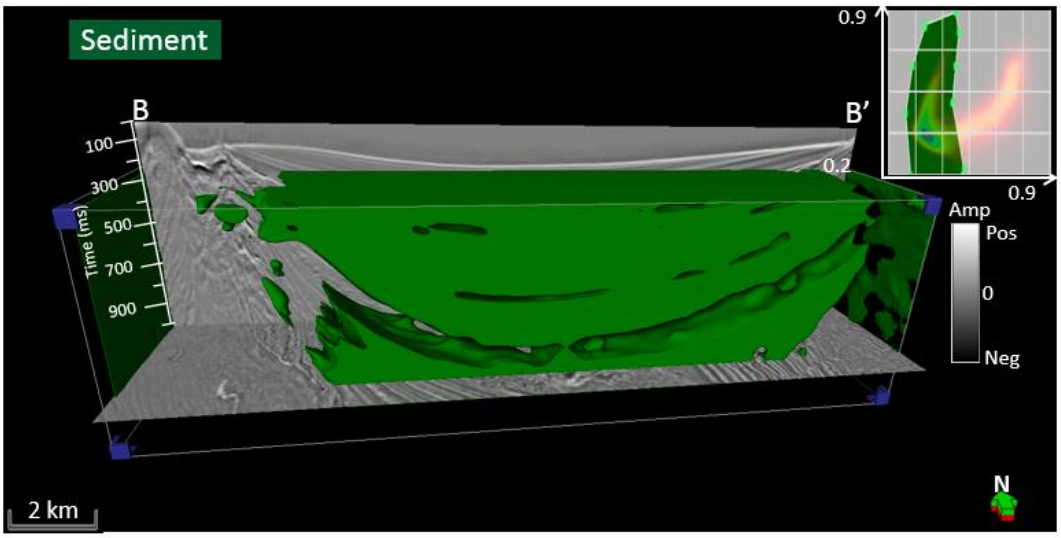
Sediment
B
B′
100
300
500
700
900
Time (ms)
0.9
0.2
0.9
Amp
Pos
0
Neg
N
2 km

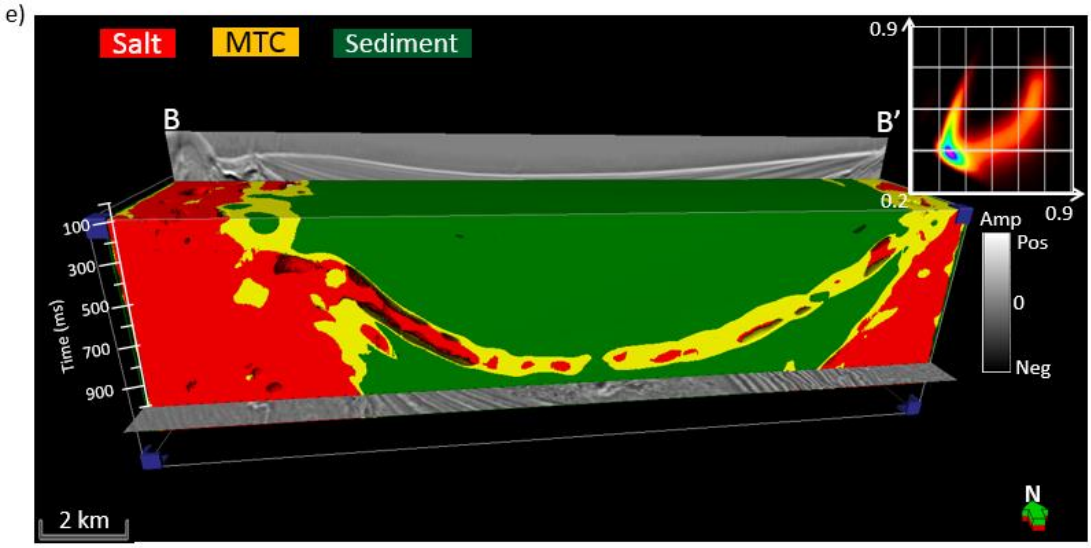

Figure 1.17 Vertical slices along line BB' and time slices at t=1172 ms through (a) seismic amplitude, and co-rendered with, (b) with salt facies (in red), (c) MTC facies (in yellow), (d) sediment facies (in green), and (e) with all three facies obtained by manually drawing a polygon on the GTM histogram.

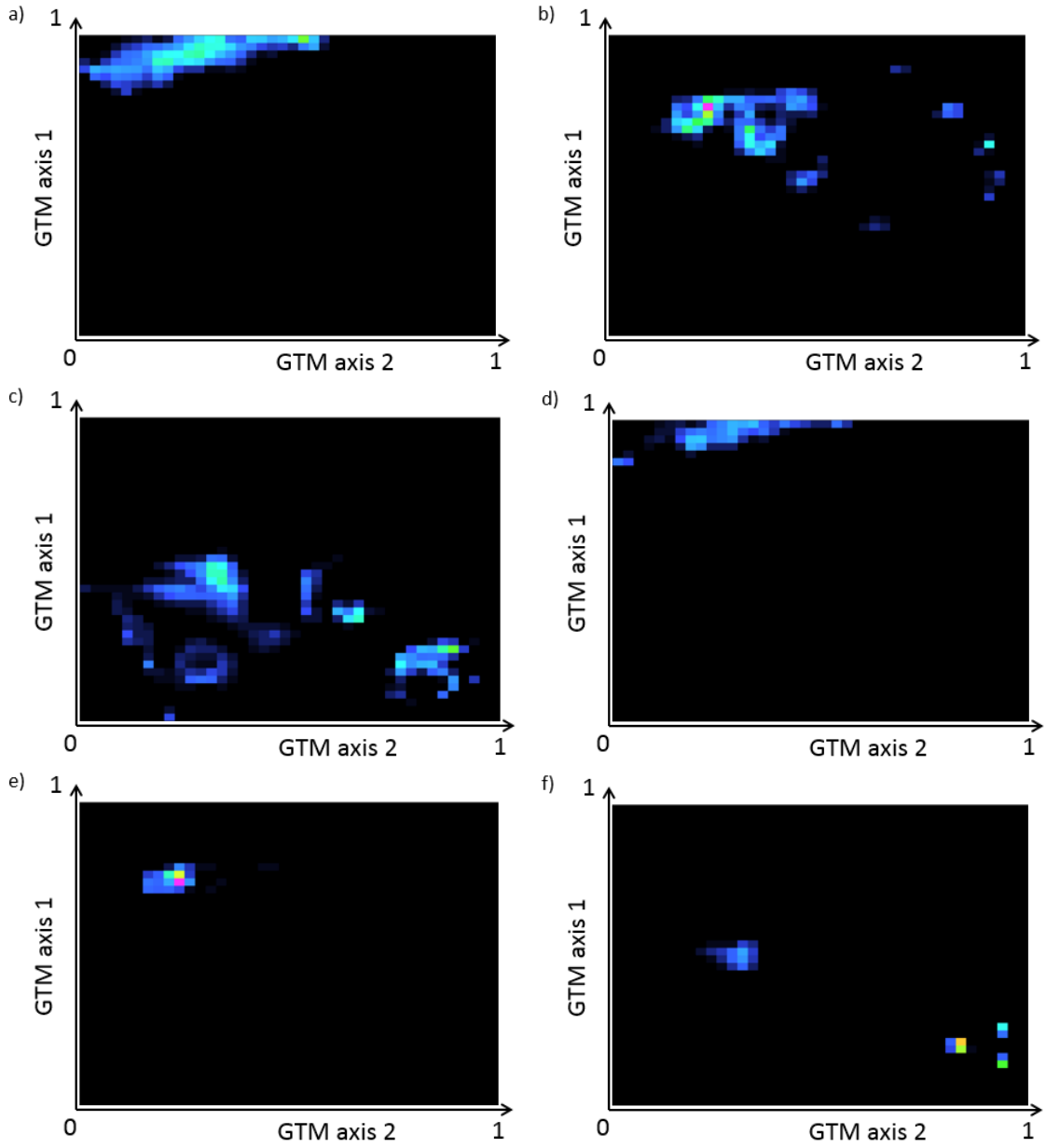

Figure 1.18 The voxels painted in Figure 1.5b onto the latent space, generating PDFs for (a) salt, (b) MTC, and (c) sediment, and the single voxels painted in Figure 1.5b, generating PDSs for (d) salt, (e) MTC, and (f) sediment.

a)

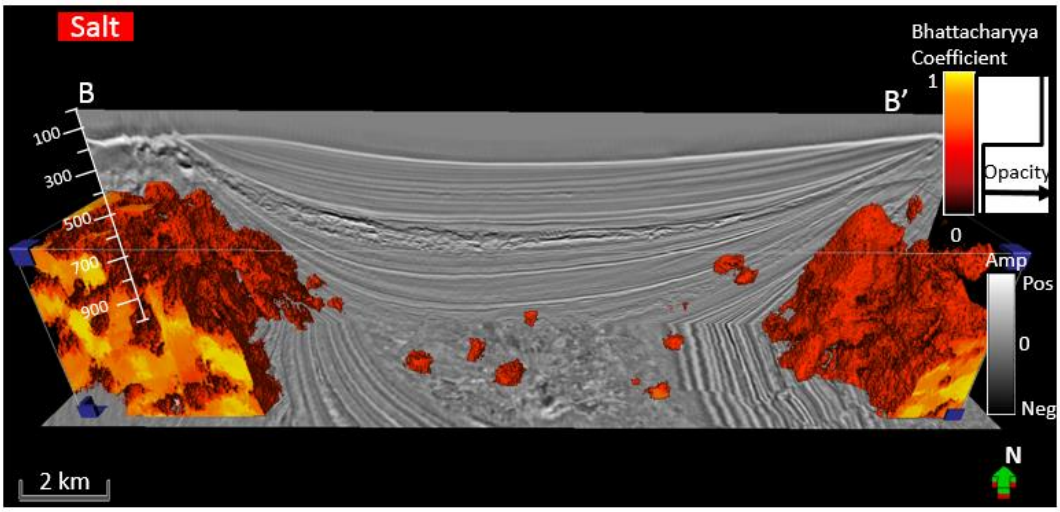
Salt
Bhattacharyya
Coefficient
1
0
Opacity
B
B'
100
300
500
700
900
Amp
Pos
0
Neg
N
2 km

b)

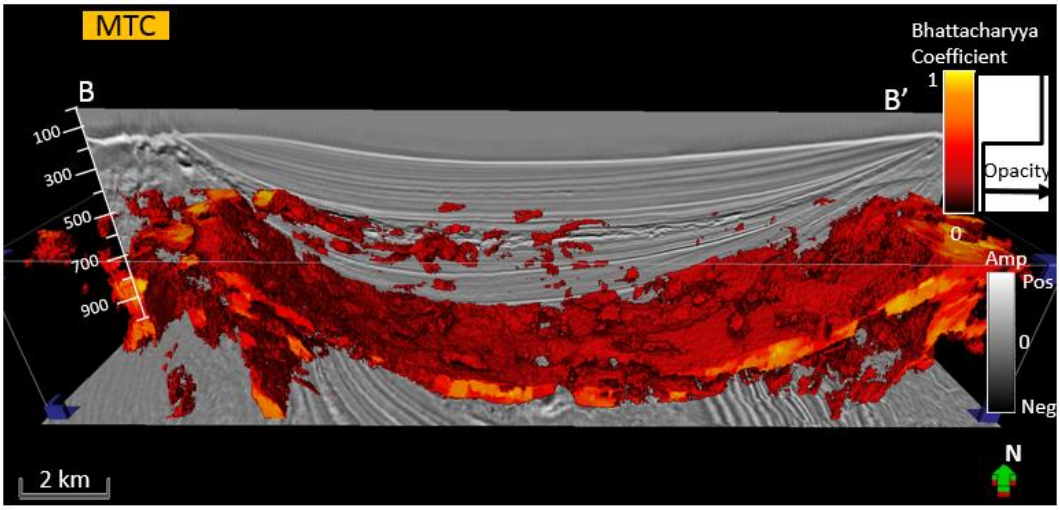
MTC
Bhattacharyya
Coefficient
1
0
Opacity
B
B'
100
300
500
700
900
Amp
Pos
0
Neg
N
2 km

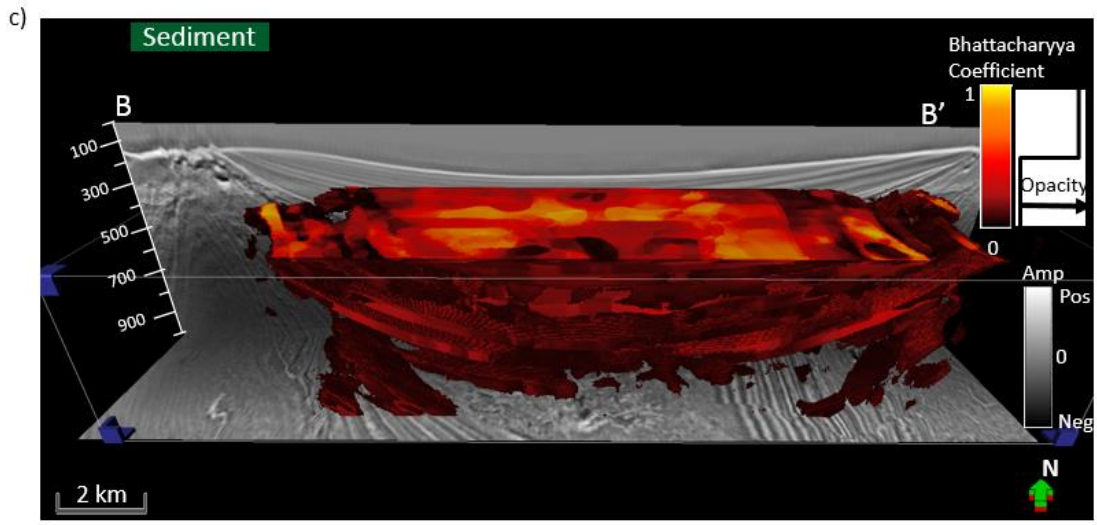

Figure 1.19 Vertical slice along line BB' and time slice at t=1172 ms through seismic amplitude, and co-rendered with Bhattacharyya Coefficient associated with (a) salt, (b) MTC, and (c) sediment facies.

REFERENCES

Al-Dossary, S., and K. J. Marfurt, 2006, 3D volumetric multispectral estimates of reflector curvature and rotation: Geophysics, **71**, 41–51,

Barnes, A. E., and K. J. Laughlin, 2002, Investigation of methods for unsupervised classification of seismic data: 72th Annual International Meeting, SEG, Expanded Abstracts, 2221-2224.

Berthelot, A., A. H. S. Solberg, E. Morisbak, and L. J. Gelius, 2013, Texture attributes for detection of salt: Journal of Applied Geophysics, **88**, 52-69.

Borgos, H. G., T. Skov, and L. Sonneland, 2005: Automated Structural Interpretation Through Classification of Seismic Horizons, Mathematical Methods and Modelling in Hydrocarbon Exploration and Production, Springer Verlag, 89-106.

Coleou, T., M. Poupon, and K. Azbel, 2003, Unsupervised seismic facies classification: A review and comparison of techniques and implementation: The Leading Edge, **22**, 942–953.

Corradi, A., P. Ruffo, A. Corrao, and C. Visentin, 2009, 3D hydrocarbon migration by percolation technique in an alternative sand-shale environment described by a seismic facies classification volume: Marine and Petroleum Geology, **26**, 495–503.

Gao, D., 2003, Volume texture extraction for 3D seismic visualization and interpretation: Geophysics, **68**, 1294–1302.

Gao, D., 2007, Application of three-dimensional seismic texture analysis with special reference to deep-marine facies discrimination and interpretation: An example from offshore Angola, West Africa: AAPG Bulletin, **91**, 1665–1683.

Hale, D., and Emanuel, J., 2002, Atomic meshes of seismic images: 72nd Annual International Meeting, SEG, Expanded Abstract, 2126-2129.

Halpert, A. D., R. G. Clapp, B. Biondi, 2014, Salt delineation via interpreter-guided 3D seismic image segmentation: Interpretation, **2**, 79-88.

Kuwahara, M., K. Hachimura, S. Eiho, and M. Kinoshita, 1976, Digital processing of biomedical images: Plenum Press, 187–203.

Kyprianidis, J. E., H. Kang, and J. Döllner, 2009, Image and Video Abstraction by Anisotropic Kuwahara Filtering: Computer Graphics Forum 28, 7, 1955–1963.

Lomask, J., R. G. Clapp, and B. Biondi, 2007, Application of image segmentation to tracking 3d salt boundaries: Geophysics, **72**, 47–56.

Luo, Y., K. P. Gunaratnam, A. H. Wu, and M. Alfaraj, 2001, Histogram Equalization and Its Application in Seismic Exploration: 71th Annual International Meeting, SEG, Expanded Abstracts, 1835-1840.

Luo, Y., S. al-Dossary, and M. Marhoon, 2002, Edge-preserving smoothing and applications: The Leading Edge, **21**, 136–158.

Marfurt, K. J., 2006, Robust estimates of 3D reflector dip and azimuth: Geophysics, **71**, 29–40.

Marfurt, K. J., and J. R. Rich, 2010, Beyond curvature: Volumetric estimates of reflector rotation and convergence: 80th Annual International Meeting, SEG, Expanded Abstracts, 1467–1472.

Matos, M. C., K. J. Marfurt, and P. R. S. Johann, 2009, Seismic color self-organizing maps: Presented at the11th International Congress of the Brazilian Geophysical Society.

Meldahl, P., R. Heggland, B. Bril, and P. de Groot, 1999, The chimney cube, an example of semi-automated detection of seismic objects by directive attributes and neural networks: Part I — Methodology: 69th Annual International Meeting, SEG, Expanded Abstracts, 931–934.

Roy, A., B. L. Dowdell, and K. J. Marfurt, 2013, Characterizing a Mississippian tripolitic chert reservoir using 3D unsupervised and supervised multiattribute seismic facies analysis: An example from Osage County, Oklahoma: Interpretation, **1**, 109-124.

Roy, A., A. S. Romero-Pelaez, T. J. Kwiatkowski, and K. J. Marfurt, 2014, Generative topographic mapping for seismic facies estimation of a carbonate wash, Veracruz Basin, southern Mexico: Interpretation, **2**, 31-47.

Qi, J., B. Zhang, H. Zhou, and K. J. Marfurt, 2014, Attribute expression of Fault-controlled karst – Fort Worth Basin, TX: Interpretation, **2**, 91-110.

Sheffield, T. M., and B. A. Parne, 2008, Geovolume Visualization and Interpretation: What makes a useful visualization seismic attribute?: 78rd Annual international Meeting, SEG, Expanded Abstract, 849-853.

Shi, J. and J. Malik, 2000, Normalized cuts and image segmentation: Institute of Electrical and Electronics Engineers Transactions on Pattern Analysis and Machine Intelligence, 22, 838–905.

Wallet, B., R. E. F. Pepper, 2013, Using mathematical morphology in an attribute workflow to improve the interpretability of salt bodies in the Gulf of Mexico: 83rd Annual international Meeting, SEG, Expanded Abstract, 1324-1328.

West, P. B., R. S. May, E. J. Eastwood, and C. Rossen, 2002, Interactive seismic facies classification using textural attributes and neural networks: The Leading Edge, **21**, 1042-1049.

Chapter 2 : Workflow to skeletonize faults and stratigraphic features

Jie Qi, Gabriel Machado, and Kurt Marfurt

The University of Oklahoma, ConocoPhillips School of Geology and Geophysics.

This paper was accepted by SEG journal Geophysics in 2017

Title: A workflow to skeletonize faults and stratigraphic features

ABSTRACT

Improving the accuracy and completeness of subtle discontinuities in noisy seismic data is useful for mapping faults, fractures, unconformities and stratigraphic edges. In this paper, we propose a workflow to improve the quality of coherence attributes. First, we apply principal component structure-oriented filtering to reject random noise and sharpen the lateral edges of seismic amplitude data. Next, we compute eigenstructure coherence, which highlights both stratigraphic and structural discontinuities. We apply a Laplacian of a Gaussian filter to the coherence attribute that sharpens the steeply dipping faults, attenuates the stratigraphic features parallel to the seismic reflectors, and skeletonizes unconformity features subparallel to reflectors. Finally, we skeletonize the filtered coherence attribute along with the fault plane. The filtered and skeletonized seismic coherence highlight the geological discontinuities more clearly and precisely. These discontinuous features can be color-coded by their dipping orientation, or as a suite of independent, azimuthally limited volumes, providing the interpreter a means of isolating fault sets that are either problematic or especially productive. We validate the effectiveness of our workflow by applying it to seismic surveys acquired from the Gulf of Mexico, USA and the Great South Basin, New Zealand. The skeletonized result rejects noise and enhances discontinuities seen in both the vertical and lateral direction. The co-rendering of the "fault" azimuth and the "fault" dip magnitude exhibits both strengths of the discontinuities and their orientation. Finally, we compare our workflow to the results generated from the swarm intelligence and find our method to be better at tracking short faults and stratigraphic discontinuities.

INTRODUCTION

Identification and mapping faults are one of the most important steps in seismic data interpretation in conventional plays, while fault identification is critical to identifying potential drilling hazards and characterizing natural fractures in unconventional resource plays. While major faults seen in seismic amplitude volume can be easily identified and picked by experienced interpreters, the process is still time-consuming particularly in picking more subtle faults masked by noise. A huge effort has been made to accelerate the procedure of seismic interpretation. In this paper, we introduce a 3D workflow that minimizes coherence artifacts, links disconnected faults and stratigraphic edges, and skeletonizes the results.

Coherence (Marfurt et al., 1998; Gersztenkorn and Marfurt, 1999) is routinely used to detect structural discontinuities in 3D seismic data. Other edge-detection algorithms (e.g., Dorn et al., 2012; Al-Dossary and Marfurt, 2003; Luo et al., 1996; Wang et al., 2016) provide similar results. Unfortunately, coherence measures all lateral discontinuities, including where steeply dipping coherent noise interferes with more gently dipping reflectors. Coherence also delineates channel edges, carbonate build-ups, slumps, collapse features and angular unconformities. Also, coherence can be used to detect chaotic textures in multiattribute seismic facies analysis (Qi et al., 2016).

Automatic fault extraction in most commercial software packages requires that the seismic attribute is first smoothed prior to skeletonization. Seismic data conditioning for fault interpretation includes removing incoherent noise, sharpening the edges between the hanging wall and footwall, and flattening the spectrum of the seismic data. Fehmers and Höcher (2003) proposed an edge-preserving structure-oriented filtering workflow

that uses anisotropic diffusion to reject cross-cutting noise in 3D seismic data. Marfurt (2006) generalized an algorithm developed by Luo et al. (2002) based on overlapping Kuwahara windows. Davogustto and Marfurt (2011) combined these two approaches into one algorithm and cascaded them with k_x-k_y footprint suppression. Zhang et al. (2015) applied the structure-oriented filtering workflow to prestack time migrated data that improves prestack seismic inversion results. Spectral balancing also improves the coherence image and partially diminished the stairstep artifacts commonly seen on vertical slices. All these processes are applied to the seismic amplitude data and can be thought to be seismic data processing.

However, one can also filter the coherence image which we call "image processing". One of the more popular algorithms is based on swarm intelligence (Randen et al., 2001 and Pedersen et al., 2002). Some automated fault extraction algorithms need human supervision to select appropriate pilot samples or traces. Other innovations include an edge-detection algorithm described by Zhang et al. (2014) that generates skeletonized fault sticks on time slices. The local-fault-extraction method can result in a suite of one-pixel thick-labeled fault surfaces from seismic data (Cohen et al., 2006). Wu and Hale (2015) describe a method that maps intersecting faults based on Hale (2013)'s fault construction technique. AlBinHassan and Marfurt (2003) and Boe (2012) applied Radon transforms to improve fault images, while Kadlec et al. (2008) used level sets to address the same objective. Barnes (2006) constructed a second moment tensor of coherence values falling with an analysis window about each voxel to determine the fault orientation, rejecting anomalies parallel to stratigraphy. He then dilated the images to connect disjoint fault segments, followed by skeletonization to reduce their thickness.

Other 3D attribute-based visualization techniques (Marfurt, 2016; Qi et al., 2014; Wallet et al., 2011; Wu and Hale, 2016) are also useful for fault and discontinuity interpretation. Faults illuminated by different geometric attributes can be co-rendered using RGB or CMY to co-render multiple coherence volumes computed from spectral components (Li and Lu (2014); Henderson et al., 2011). Dewett and Henza (2016) extended this approach beyond these coherence images using self-organizing maps to combine the results. These combined fault images were subsequently enhanced using swarm intelligence.

In this paper, we introduce a 3D fault directional skeletonization workflow (Figure 2.1) that uses the dip magnitude and azimuth of a directional Laplacian of a Gaussian (LoG) enhanced discontinuities image. We begin our paper by using principal-component structure-oriented filtering to suppress both random and steeply dipping coherent noise on the seismic amplitude data. Then, we compute the coherence attribute from the original and filtered seismic amplitude volumes and compare the results. Next, we apply a directional LoG filter resulting in a smooth but somewhat blurred image. Finally, we skeletonize the LoG filtered image perpendicular to sharpen locally planar features.

METHOD

Post-stack data conditioning:

Seismic attributes quantify patterns seen among neighboring seismic samples and traces to extract subtle features valuable for interpretation. For this reason, minor improvements of post-stack amplitude data can significantly improve subsequent attribute images. In this workflow, we use a Karhunen-Loève (principal-component) filter aligned with a structure to suppress random and any crosscutting coherent noise. Each

voxel has an estimate of coherence. Of all the overlapping windows that contain our analysis point, we choose the window that is most coherent (Davogustto and Marfurt, 2011). Within this window about an analysis point u_l at time *t*, we compute the covariance matrix ***C*:**

$$\boldsymbol{C}_{ij}(t) = \sum_{k=-K}^{K} [u_i(t + k\Delta t - px_i - qy_i)u_j\big(t + k\Delta t - px_j - qy_j\big)$$

$$+u_i^H(t + k\Delta t - px_i - qy_i)u_j^H\big(t + k\Delta t - px_j - qy_j\big)], \tag{2.1}$$

where u_i and u_j indicate the i^{th} *and* j^{th} trace, x_i and y_i (x_j and y_j) the distance along the *x*-axis and *y*-axis of the i^{th} (j^{th}) trace from the analysis point, p and q are the apparent dip in the *x* and *y* direction measured in *s/m*, and superscript H denotes the Hilbert transform. The samples along structural dip for a fixed value of *k* form what is called a sample vector. The first eigenvector $\mathbf{v}^1$ of the matrix ***C*** best represents the lateral variation in each of the sample vectors. Cross correlating this eigenvector with the sample vector that includes the analysis point gives a cross-correlation coefficient, β:

$$\beta = \sum_{j=1}^{J} u\big(t + k\Delta t - px_j - qy_j\big)v_j^1(t), \tag{2.2}$$

and the KL-filtered (or first principal component) of the data u_{KL} at time *t* is then a scaled version of the eigenvector $\mathbf{v}^1$:

$$u_{KL} = \beta\mathbf{v}^1. \tag{2.3}$$

The "Kuwahara" window is in general laterally and vertically not centered about the analysis point u_l. An analysis window of five traces and seven interpolated sample vectors, $u(t\pm k\Delta t)$ is shown in Figure 2.2. Note that in this cartoon, the wavelet amplitude of the three left most traces are about two times larger than that of the two right-most traces. Each sample vector approximately reflects a scaled version of the pattern (2, 2, 2,

1, 1), where the scaling factor can be positive for a peak, negative for a trough, or zero for a zero crossing. The first eigenvector for this cartoon will be a unit length vector representing this pattern:

$$\mathbf{v}^1 = \left(\frac{2}{\sqrt{14}}\ \frac{2}{\sqrt{14}}\ \frac{2}{\sqrt{14}}\ \frac{1}{\sqrt{14}}\ \frac{1}{\sqrt{14}}\right). \tag{2.4}$$

Projecting the central sample vector at time t against the eigenvector $\mathbf{v}^1$, gives a cross correlation coefficient β. For structure-oriented filtering, one scales $\mathbf{v}^1$ by β giving the KL-filtered version of the seismic data. Note that since the covariance matrix used to compute the first eigenvector used seven sample vectors, that the statistical analysis involves seven times as much input data as for a simple mean filter. Furthermore, by using the laterally varying eigenvector, one better preserves the lateral change in amplitude in the original data.

Coherence

Coherence is an edge-detection attribute and measures lateral changes in the seismic waveform and amplitude. There are several popular coherence algorithms, including those based on semblance (Marfurt et al., 1998), eigenstructure (Gersztenkorn and Marfurt, 1999), the gradient structure tensor method (Bakker et al., 1999), and the Sobel filter (Luo et al., 1996 & Luo, 2002). In our workflow, we use an energy ratio coherence of J traces in a $\pm K$ sample analysis window defined as the ratio between the energy of the coherent (KL-filtered data, u_{KL}) to the energy of the unfiltered (or total data, u) within the analysis window centered about the analysis point:

$$C = \frac{E_{coh}}{E_{total}+\varepsilon}, \tag{2.5}$$

where the coherent energy E_{coh} (the energy of the KL-filtered data) is:

$$E_{coh} = \sum_{k=-K}^{+K} \left\{ \left[u_{KL}\left(t + k\Delta t - px_j - qy_j\right) \right]^2 + \left[u_{KL}^H\left(t + k\Delta t - px_j - qy_j\right) \right]^2 \right\},$$

(2.6)

the total energy E_{total} of unfiltered data in the analysis window is:

$$E_{total} = \sum_{k=-K}^{+K} \left\{ \left[u\left(t + k\Delta t - px_j - qy_j\right) \right]^2 + \left[u^H\left(t + k\Delta t - px_j - qy_j\right) \right]^2 \right\},$$

(2.7)

and where a small positive value, ε, prevents division by zero, and superscript H denotes the Hilbert transform. Application of Hilbert transform of seismic data avoids unstable estimates of the covariance matrix for small vertical windows centered about a trace zero crossing (Marfurt, 2006). We applied the technique to volumes using a semblance and Sobel filter algorithm, as well as the energy ratio coherence algorithm all of which are computed along structural dip. There is no significant difference for the larger, through-going faults. As expected, small discontinuities that are better delineated by energy-ratio coherence provide greater details. In contrast, if there is a footprint in the coherence images, skeletonization will sharpen it.

Fault enhancement:

The goal of fault enhancement is to suppress incoherent noise and enhance faults trends. While coherence highlight faults and channel edges, these fault images may be broken. A normal fault plane defines the surface between the footwall and the hanging wall (Figure 2.3). Following Barnes (2006) and Machado et al. (2016), in an N-voxel (α_n) spherical analysis window, the second-order moment tensor **A** of the discontinuity data $\alpha_n(x_1, x_2, x_3)$ is

$$\mathbf{A} = \begin{bmatrix} A_{11} & A_{12} & A_{13} \\ A_{12} & A_{22} & A_{23} \\ A_{13} & A_{23} & A_{33} \end{bmatrix}, \quad (2.8)$$

where the elements A_{ij}:

$$A_{ij} = \sum_{n=1}^{N} x_{in} x_{jn} \alpha_n, \tag{2.9}$$

where x_{in} are the distances from the center of the analysis window. If the input coherence data is computed from time-migrated data, axis z should be stretched to depth. For planar coherence anomalies, the three eigenvalues λ_i of the second moment tensor **A** will have $\lambda_1 \geq \lambda_2 \gg \lambda_3$. The eigenvectors $\mathbf{v_1}$and $\mathbf{v_2}$ of the second-order moment tensor represent the planar surface, while the eigenvector $\mathbf{v_3}$ represents the normal to the planar surface. The eigenvector $\mathbf{v_3}$ has three components with v_{31} positive to the north, $\mathbf{v_{32}}$ positive to the east, and v_{33} positive down (Figure 2.3). Machado et al. (2016) applied a directional Laplacian of Gaussian (LoG) operator to 3D seismic data to smooth along and sharpen the faults perpendicular to locally planar events. The Gaussian smoother is elongated along the plane (defined by the eigenvectors $\mathbf{v_1}$ and $\mathbf{v_2}$):

$$G_{mn} = exp[-a_m^T \boldsymbol{R}^T \Lambda^{-1} \boldsymbol{R} a_n], \tag{2.10}$$

where $\boldsymbol{R}$ is the rotation matrix and defined as $[\mathbf{v_1}\ \mathbf{v_2}\ \mathbf{v_3}]$. Λ is a diagonal matrix is defined as:

$$\Lambda = \begin{pmatrix} \sigma_1^2 & 0 & 0 \\ 0 & \sigma_2^2 & 0 \\ 0 & 0 & \sigma_3^2 \end{pmatrix}, \tag{2.11}$$

where the value of $\sigma_1$and σ_2 is 3 times of the bin size, and σ_3 is the bin size. The rotation matrix $\boldsymbol{R}$ is aligned with the eigenvector $\mathbf{v_3}$. Thus, the second derivative of the Gaussian in the eigenvector $\mathbf{v_3}$ direction (ξ_3) is:

$$\frac{d^2 G}{d\xi_3} = \gamma \left[\frac{-2}{\lambda_3} + 4\xi_3^2\right] exp\left[-\frac{1}{2}\left(\frac{\xi_1^2}{\sigma_1^2} + \frac{\xi_2^2}{\sigma_2^2} + \frac{\xi_3^2}{\sigma_3^2}\right)\right], \tag{2.12}$$

where ξ_1, ξ_2, and ξ_3 are aligned along the eigenvector $\mathbf{v_1}$, $\mathbf{v_2}$, and $\mathbf{v_3}$, respectively, and γ is a normalization factor. Since the directional LoG filter is based on a Gaussian distribution function, we call our filtered result a "fault probability" image.

Fault skeletonization:

Finding eigenvector $\mathbf{v_3}$ is key to directionally skeletonize planar anomalies in coherence images (Qi et al., 2016). For each voxel, we extract 26 neighboring samples of fault probability that fall within a $\pm dx * \pm dy * \pm dz$ gridded window (Figure 2.4). Figure 2.4a shows a hypothesized plane in green, intersecting the center of the window at point U_{14}. The intersection of $\mathbf{v_3}$ with this window gives the locations (U_{left}, U_{right}) which fall in the 2D red and blue rectangles, and are then interpolated from the neighboring grid points. We assume the center analysis point U_{14} is at (*0,0,0*) and the point U_1 is at *(-dx,-dy,-dz*). Values of interpolated points U_{left} and U_{right} in the analysis window (Figure 2.4) are:

$$U_{left} \approx \begin{bmatrix} \frac{dx - x_{left}}{dx} & \frac{x_{left}}{dx} \end{bmatrix} \begin{bmatrix} U_{11} & U_{20} \\ U_{12} & U_{21} \end{bmatrix} \begin{bmatrix} \frac{dz - z_{left}}{dz} \\ \frac{z_{left}}{dz} \end{bmatrix}, \text{ and} \tag{2.13}$$

$$U_{right} \approx \begin{bmatrix} \frac{dx - x_{right}}{dx} & \frac{x_{right}}{dx} \end{bmatrix} \begin{bmatrix} U_{7} & U_{16} \\ U_{8} & U_{17} \end{bmatrix} \begin{bmatrix} \frac{dz - z_{right}}{dz} \\ \frac{z_{right}}{dz} \end{bmatrix}. \tag{2.14}$$

If the value at the center of the analysis window, $U_{14} < U_{left}$ or $U_{14} < U_{right}$, no fault maximum occurs and we set the skeletonized value to be zero. If the value at the center of the analysis window, $U_{14} \geq U_{left}$ and $U_{14} \geq U_{right}$, a fault anomaly falls within the window. We fit a parabola of the form:

$$u(\xi) = a\xi^2 + b\xi + c, \tag{2.15}$$

to the value U_{left}, U_{14}, and U_{right} (Figure 2.4b). The maximum value U_{max} and distance ξ_{max} between U_{14} and location of U_{max} projection on the eigenvector $\mathbf{v_3}$ is:

$$U_{max} = -\frac{b^2}{4a} + U_{14}, \tag{2.16}$$

$$\xi_{max} = -\frac{b}{2a}, \tag{2.17}$$

where a and b are defined as:

$$a = (U_{left} + U_{right} - 2U_{14})/2d^2, \tag{2.18}$$

$$b = (U_{left} - U_{right})/d^2, \tag{2.19}$$

where d is the half-length between U_{left} and U_{right}. In general, U_{max} does not fall on the grid point U_{14}, such that we need to distribute the U_{max} value into the eight neighboring grid points and the weights functions w_k are based on their distance between the U_{max} and eight neighboring grid points:

$$U_k = \frac{w_k}{\sum w_j} U_{max}. \tag{2.20}$$

In Figure 2.5, U_{max} falls with a sub-cube of the grid analysis window, indicated by the red dashed line. We compute skeletonized values on 8 neighboring grid points whose weighted average produces the fault probability at the maximum location. Finally, all skeletonized values on grid points will be output to the skeletonized image. Figure 2.6 show a normal fault before and after our directional skeletonization workflow. Coherence fault anomalies appear broken on the time slice (Figure 2.6b). While "stairstep" artifacts appear on the vertical slice. "Fault" dip azimuth φ and "fault" dip magnitude θ, which are computed from the eigenvector $\mathbf{v_3}$ indicate the direction of skeletonization, with the result shown in Figure. After this workflow, faults become sharper and more continuous. Stratigraphic features are also preserved, and these can be used to estimate fault throws that are indicated by blue arrows in Figure 2.6c. Lateral discontinuities such

as shale dewatering syneresis are enhanced after our workflow that is indicated by yellow arrow.

APPLICATION

Gulf of Mexico (GOM3D):

We first apply our workflow to a 3D seismic dataset in the Gulf of Mexico (GOM3D). The seismic data were acquired by PGS using towed streamer acquisition with two sources and three receiver cables with a maximum offset of 6000 m. The dataset within the inline and crossline spacing of 123.1ft * 39.4ft (37.5m * 12.5m), covers over 2723.27 ft^2 (253 km^2), and has been prestack time migrated. The uplift of the western salt dome is contemporaneous with the upper minibasin fill, and it occurred earlier than the eastern salt dome rise. Structural and stratigraphic features such as salt domes, mass transport complexes, and undeformed sediment and shale, are major seismic facies in this area. Figure 2.7 displays a time slice at 1s and a vertical slice AA' through the seismic amplitude volume. Random and coherent noise overprint reflectors in the migrated dataset. After principal-component structure-oriented filtering (Figures 2.7c and 2.7d), the signal-to-noise ratio of lateral and vertical discontinuities has increased as seen in both clearer faults and block delineation within the mass transport complexes. Figures 2.7e and 2.7f shows the rejected noise. Figure 2.8 shows the comparison of coherence before and after principal component structure-oriented filtering. Salt domes and mass transport complexes exhibit a "salt and pepper" pattern in the coherence volume. Figure 2.8c and 2.8d show that coherence computed after filtering preserves lateral and vertical discontinuities, and suppresses random and coherent noises. Coherence computed from the structure-oriented filtered seismic amplitude volume exhibits a better signal-to-noise

ratio. Small cross faults and other discontinuities within the mass transport complexes are clearly imaged at the time (Figure 2.8c) and vertical slices (Figure 2.8d) through coherence. However, fault anomalies still exhibit the "stairstep" artifacts. Figures 2.9a and 2.9b show directionally skeletonized coherence images. Fault anomalies are now more continuous, exhibit higher contrast, with reduced "stairstep" artifacts. Salt edges, MTC edges, and many subtle faults (indicated by green arrows in Figure 2.9) are enhanced in both time and vertical slices. The noise that does not represent locally planar discontinuities is suppressed during the skeletonization step. In Figure 2.10, we use Hue-Lightness-Saturation (HLS) color model to co-render the fault dip magnitude (against S), the skeletonized fault probability (against L), and the fault dip azimuth (against H). In Figure 2.10, the fault orientation is readily seen. Numerical computation of fault probability and orientation at each voxel provide an easy way to identify fault sets, either visibly or through statistical analysis. Note that the coherent noise within the salt has been organized and should be interpreted as noise. More sophisticated processing produces homogeneous reflection salt images in this part of the Gulf of Mexico.

The signal-to-noise ratio of this dataset was very low, and the dataset was time-migrated. We applied the workflow to this dataset, and found significant improvement after applying our skeletonized fault probability workflow. However, there are still some spikes and are poorly displayed. In terms of spikes, coherence values will always range between 0 and 1. For this reason, isolated spikes do not cause problems so long as they do not align with other spikes. The biggest limitation in applying attributes and skeletonization to this kind of data is those interference phenomena corresponding to overlapping, poorly migrated events will give rise to discontinuities, which of course will

then be sharpened. Such data limitations, including issues as basic as fault shadows, need to be properly addressed in the imaging algorithm, and cannot be corrected by any data conditioning or image processing.

Great South Basin (GSB3D):

Our second test data is from the Great South Basin, New Zealand. The intracontinental rift basin formed during the mid-Cretaceous and is divided into several highly faulted sub-basins that contain very thick sedimentary fill. A polygonal fault system is very developed in the area, and its genetic mechanisms include gravity collapse, density inversion, syneresis and compactional loading (Cartwright et al., 2003), while syneresis is also seen in the dataset. The inline and crossline spaces are both 12.5m, and the time sample rate is 2ms. Figure 2.11 shows the original seismic amplitude. We compute coherence from the seismic amplitude volume. In Figure 2.12a, polygonal faults are well delineated. However, the well-known "stairstep" artifacts are exhibited on the vertical slice (Figure 2.12c). The syneresis pattern (Figure 2.12b and 2.12c) is too chaotic to be interpreted. Fault trends in coherence are disconnected, especially on curved faults. After our workflow (Figure 2.13), polygonal faults are sharper and more continuous, and "stairstep" artifacts have been suppressed. Syneresis, and other stratigraphic features, are also enhanced after skeletonization. The "thick" black smears correspond to faults subparallel to the vertical slices. Figure 2.14 shows a 3D view of skeletonized fault probability co-rendered with fault dip azimuth and seismic amplitude data. Note that polygonal fault planes and syneresis are both preserved after directional skeletonization in the 3D volume, and fault planes associated with fault dip azimuth are readily identified. Lateral discontinuities such as syneresis are also seen.

Comparison of directional skeletonization with swarm intelligence:

We apply our directional skeletonization method and swarm intelligence to the GSB3D survey, and compare these results in fault and syneresis enhancement. Figure 2.15a shows a time slice at 1.72s through the coherence volume that is used as the input for comparison of the two different methods. The polygonal faults (green rectangular) and syneresis (orange arrow) are both present in this time slice. Figure 2.15b shows the directional skeletonization result, and Figure 2.15c shows the result of swarm intelligence, both computed from coherence. Note that, directional skeletonization shows more details (subtle faults) than swarm intelligence in the polygonal fault zone. Swarm intelligence generates linear artifacts, but directional skeletonization does not, as indicated by the red arrows in Figures 2.15c and 2.15d. Figure 2.15d shows the swarm intelligence result with the directionally skeletonized volume as input. The results obtained by applying swarm intelligence to the directionally skeletonized data are better than that those obtained from coherence, preserving more subtle discontinuities in the polygonal faults zone. However, despite applying many different combinations of parameters for swarm intelligence, the syneresis area could not be preserved (orange arrow). We conclude with Figure 2.16 showing same volumes as in Figure 2.15 but on vertical slices. The swarm intelligence result with directional skeletonization volume as input shows more continuous and sharper fault images than the one computed directly from coherence. The directional skeletonization workflow in Figure 2.16 exhibit fewer "stairstep" artifacts than those in Figure 2.16 (red arrows). Blue arrows indicate faults better mapped by swarm intelligence than by directional skeletonization, at the expense of organizing other features that are probably noise. Stratigraphic features are preserved

and enhanced using the directional skeletonization workflow. Comparing Figure 2.16c with 2.16d, we can see that swarm intelligence with directional skeletonization as input created fewer artifacts. Swarm intelligence and the skeletonization workflow both need edge-detection attribute as input. These two methods are sample-by-sample analysis, and computation cost of these two methods are similar. For the dataset GSB3D with 500 by 280 traces and 750 time samples, the enhancement and skeletonization take around 200s. Applying the same dataset to swarm intelligence, the computation time is around 220s.

CONCLUSIONS

We have developed a 3D fault directional skeletonization workflow to skeletonize and segment fault images. First, we applied structure-oriented filtering to suppress random and coherent noise. Next, we computed coherence as our edge-detection attribute to detect discontinuous features. Coherence computed after data conditioning using structure-oriented filtering (SOF), followed by iterative application of a LoG filter and directional skeletonization rejects noise, enhances faults in both vertical and lateral direction. We skeletonize the results perpendicular to the "fault" dip azimuth and dip magnitude, resulting in sharper, more continuous fault and stratigraphic edges. These discontinuous features can be color-coded by their dip azimuth and magnitude, or as a suite of independent, azimuthally limited fault sets that may be found to have a greater risk of communicating with adjacent aquifers, or on the positive side, to be better correlated with open fractures. Subtle, stratigraphically limited features such as faults within mass transport complexes and syneresis in shales are also enhanced. Multiattribute display of the skeletonized faults and its dip magnitude and azimuth readily display interfault relationships. Comparing our directional skeletonization workflow with swarm

intelligence, we find the swarm intelligence has the danger of enhancing small artifacts, which are not present in our skeletonization results. Swarm intelligence and directional skeletonization both reduce “stairstep” artifacts, and connect previously discontinuous fault segments. Our skeletonization workflow preserves stratigraphic features, such as dewatering syneresis, which swarm intelligence smears. Cascading directional skeletonization with the swarm intelligence results in more continuous and sharper fault imaging than with coherence as input.

ACKOWNLEDGEMENTS

We thank the sponsors of the OU Attribute-Assisted Processing and Interpretation Consortium for their guidance and their financial support.

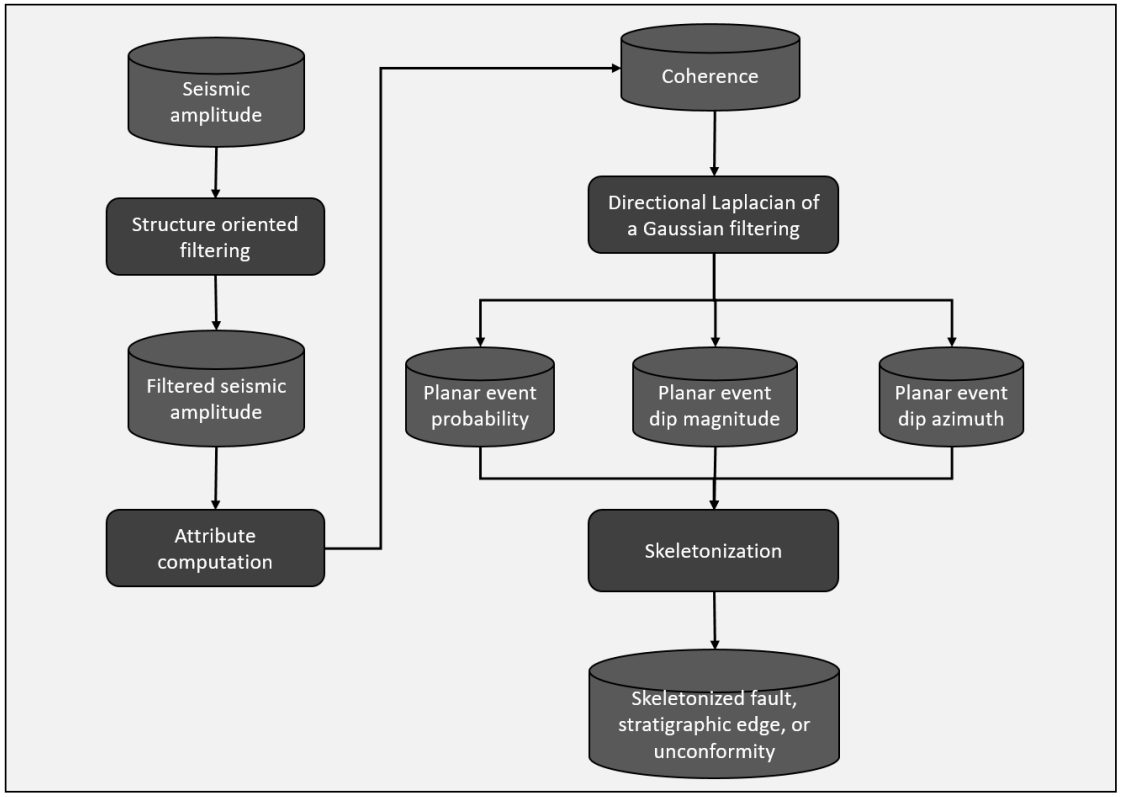

Figure 2.1 Workflow illustrating the steps used in our directional skeletonization workflow. The interpreter begins with post-stack data conditioning by applying structure-oriented filtering on seismic amplitude data. After filtering, coherence or other edge-detection attribute is computed. A directional LoG filter produces volume estimates of the probability, dip magnitude, and dip azimuth of locally planar events. These events are then skeletonized to produce sharper images.

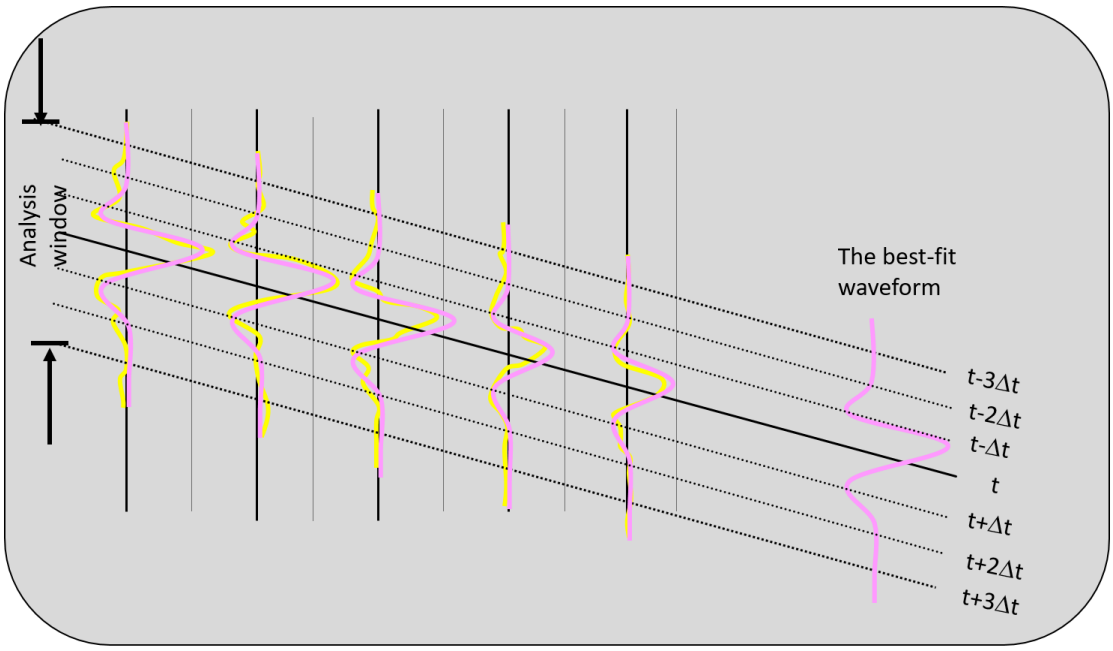

Figure 2.2 Cartoon of an analysis window with five traces and seven samples. Note that the wavelet amplitude of the three left most traces is about two times larger than that of the two right-most traces.

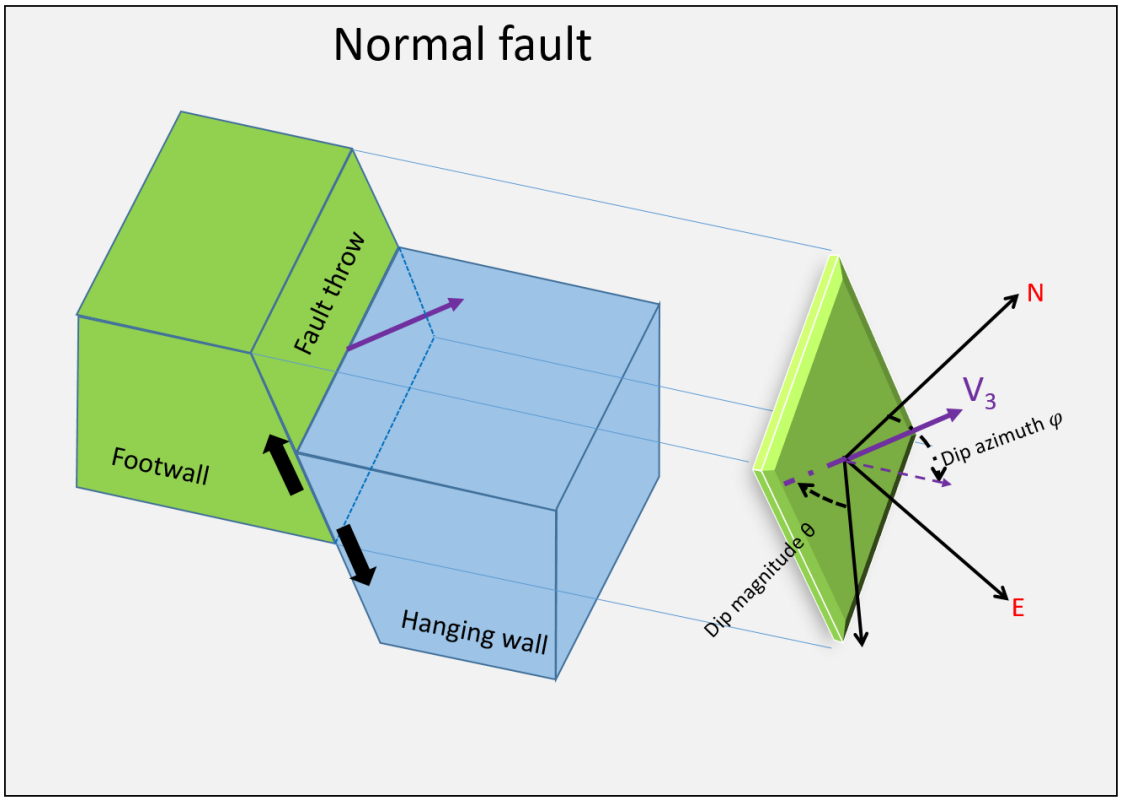

Figure 2.3 Cartoon of a normal fault defined by the eigenvector $\mathbf{v_3}$ perpendicular to the fault plane. The projection of $\mathbf{v_3}$ on the horizontal plane defines the "fault" dip azimuth φ, and the angle between $\mathbf{v_3}$ and the z-axis defines the "fault" dip magnitude.

a)

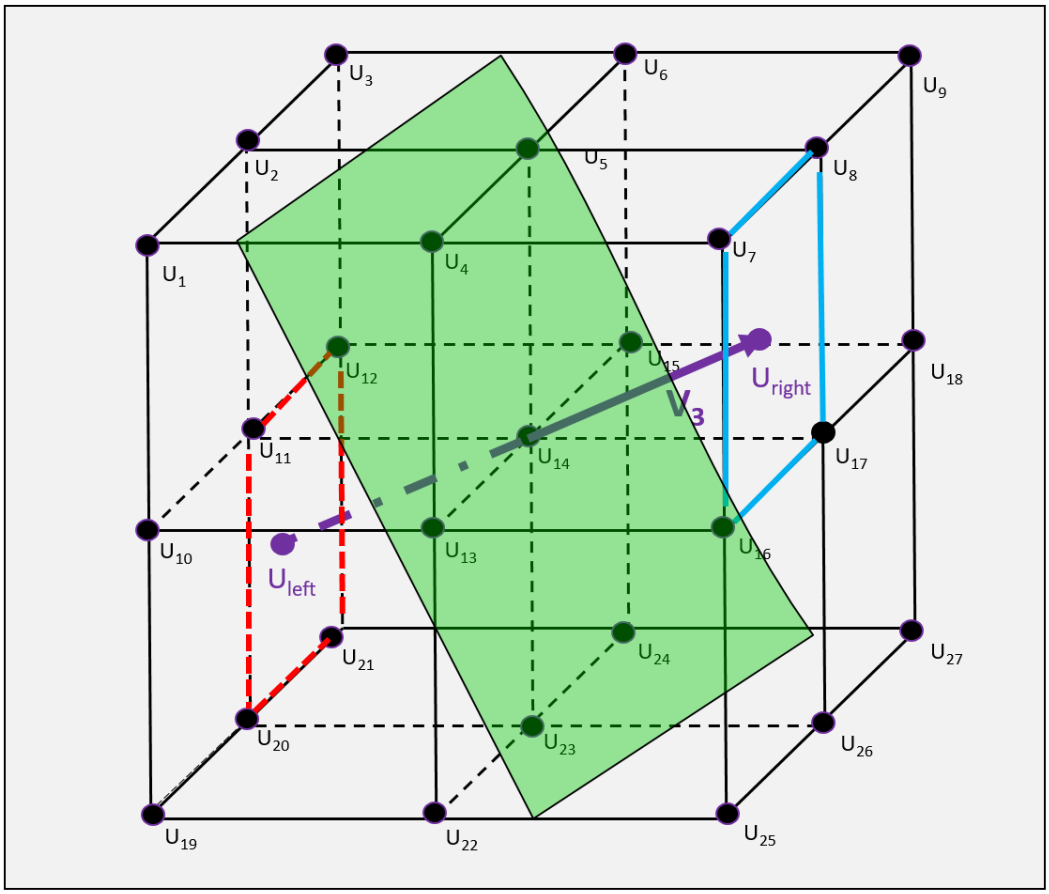
U1
U2
U3
U4
U5
U6
U7
U8
U9
U10
U11
U12
U13
U14
U15
U16
U17
U18
U19
U20
U21
U22
U23
U24
U25
U26
U27
U left
U right
V3

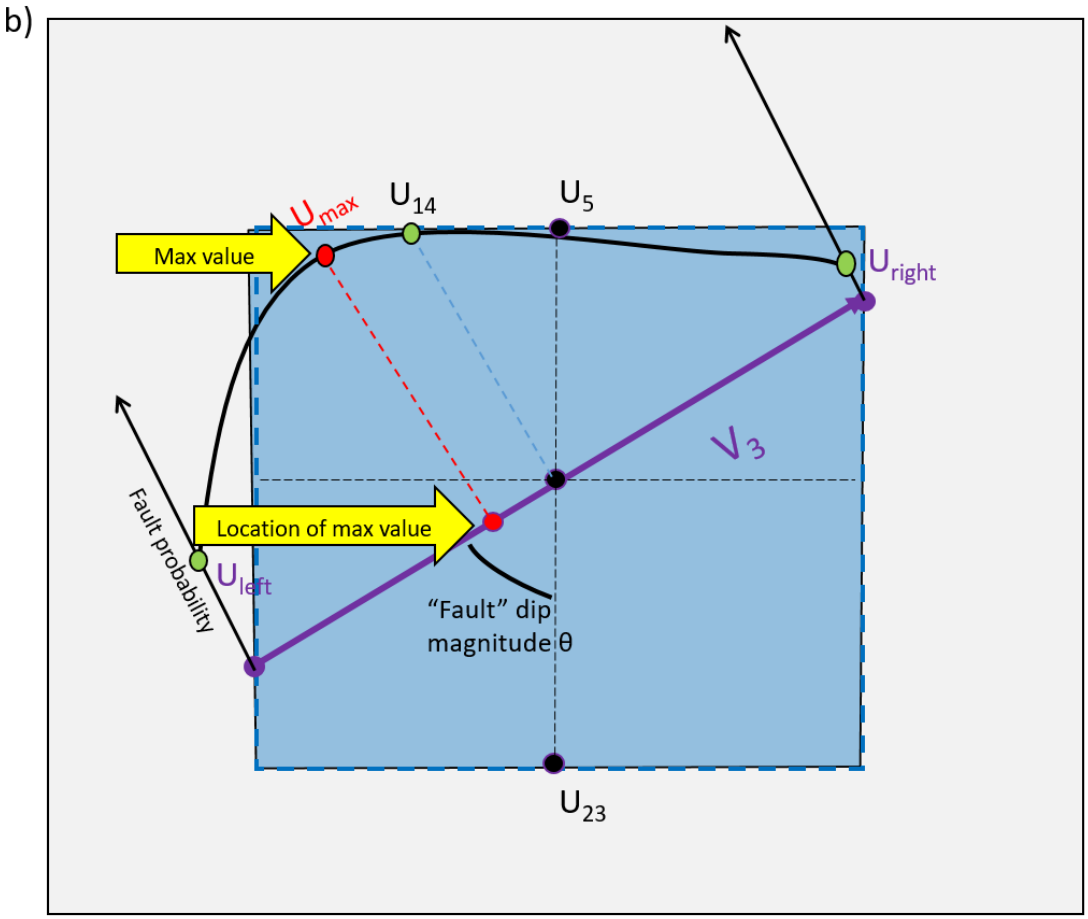

Figure 2.4 Cartoon showing details of directional skeletonization. (a) The analysis window about each voxel consisting of eight subcubes and 26 neighboring voxels. The green plane indicates a locally planar event with center point U_{14}. U_{left} and U_{right} define points where the eigenvector $\mathbf{v_3}$ intersects the analysis window**.** The attribute value at U_{left} is interpolated from the corner values of the red square U_{11}, U_{12}, U_{20}, and U_{21}. The attribute value at U_{right} is interpolated from the corner values of the blue square U_7, U_8, U_{16}, and U_{17}. (b) Further interpolation along axis $\mathbf{v_3}$ by fitting the parabola to U_{14}. U_{left} and U_{right} to estimate the maximum value U_{max} and its location.

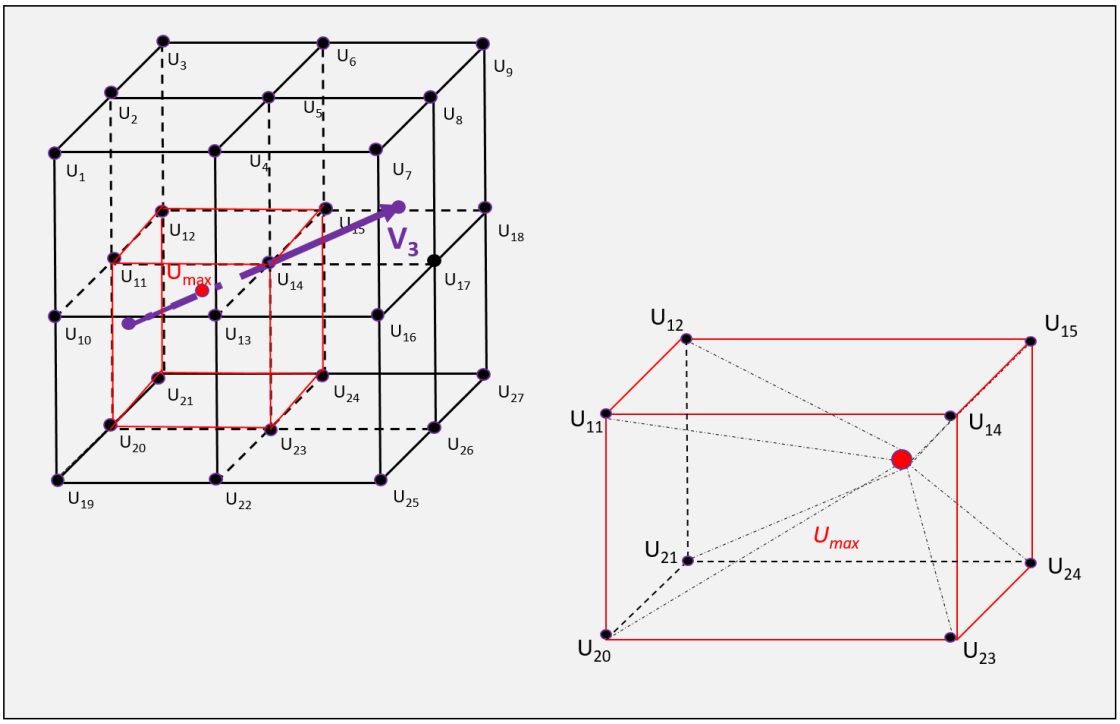

Figure 2.5 Cartoon showing the location of U_{max} in 3D. In general, U_{max} does not fall on a voxel, such that U_{max} needs to be distributed to its eight neighboring grid points for subsequent display.

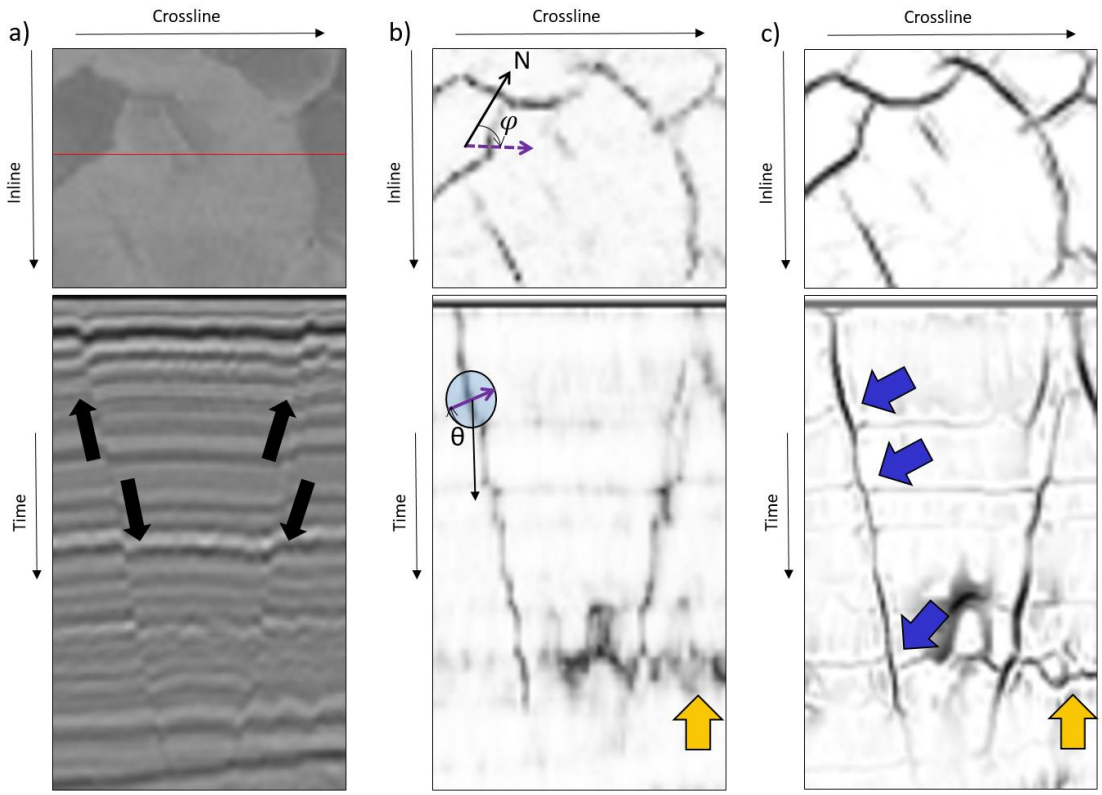

Figure 2.6 Examples of two normal faults seen on a time and vertical slice through (a) the original seismic amplitude volume, (b) the coherence volume, and (c) directional skeletonization volume. Purple arrow indicates the eigenvector $\mathbf{v_3}$ in the vertical slice, whereas purple dashed arrow indicates its projection on the time slice. "Fault" dip azimuth φ and "fault" dip magnitude θ are illustrated in (b). Fault anomalies exhibit the well-known "stairstep" artifacts, such that fault planes are disconnected. After our directional skeletonization workflow, faults become sharper and more continuous. Stratigraphic features are preserved, which can be used to estimate fault throws that are indicated by blue arrows in (c). Lateral discontinuities are also enhanced after our workflow those are indicated by the yellow arrow in (c).

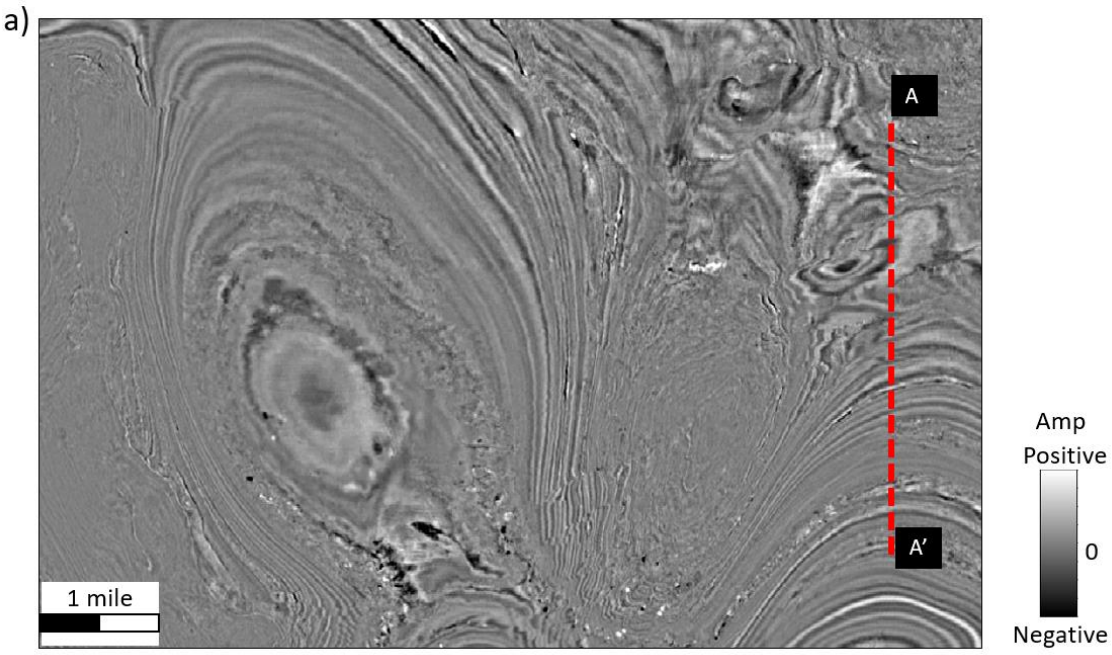
a)
A
A'
1 mile
Amp
Positive
0
Negative

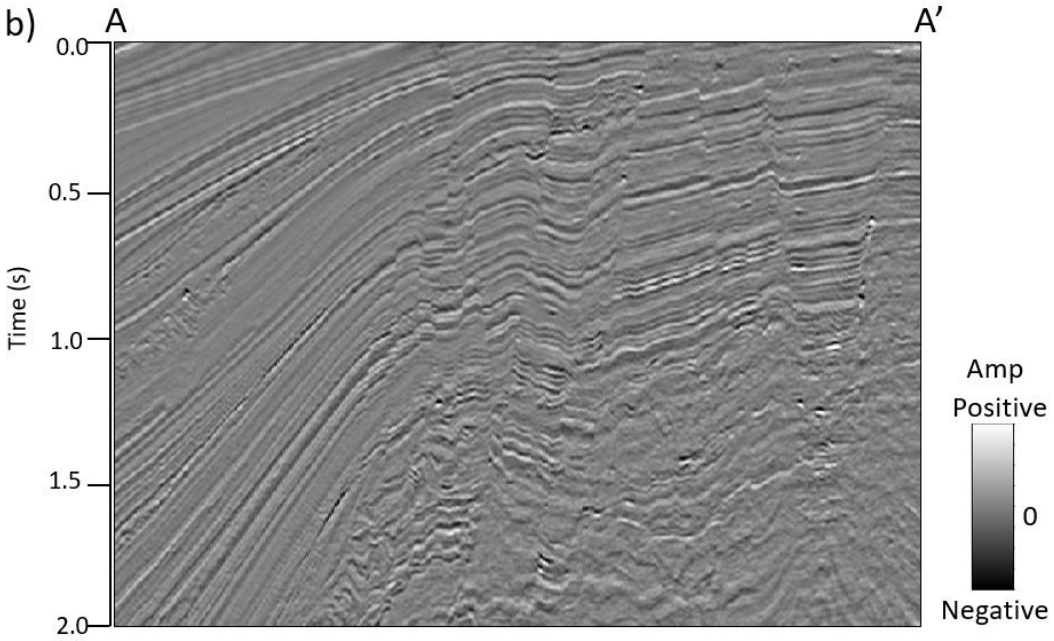
b)
A
A'
0.0
0.5
1.0
1.5
2.0
Time (s)
Amp
Positive
0
Negative

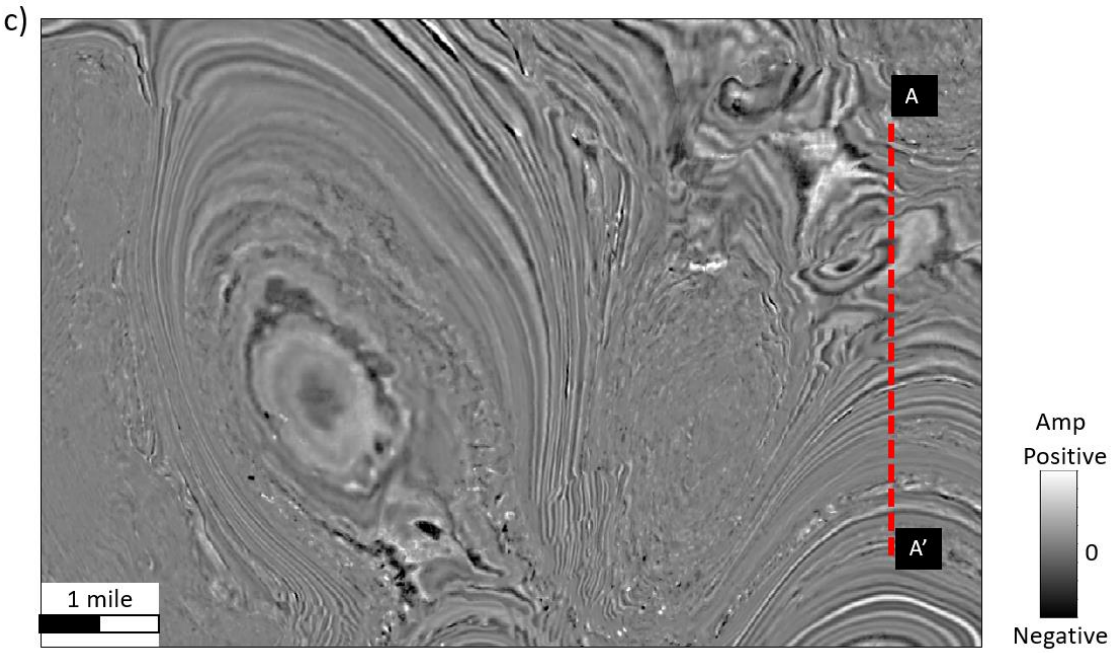
c)
A
A'
1 mile
Amp
Positive
0
Negative

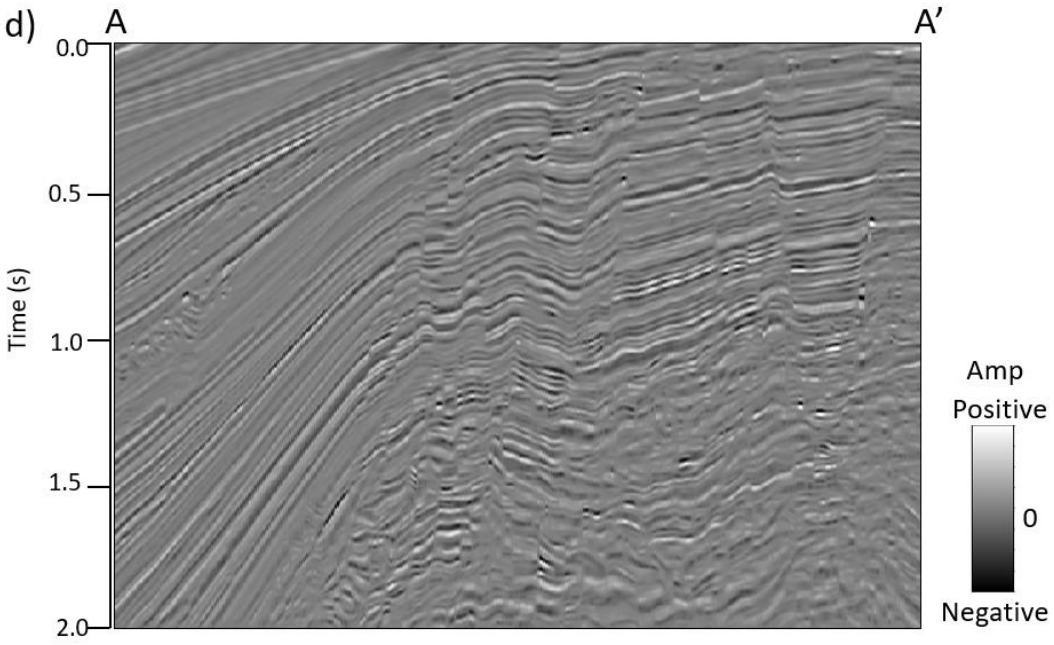
d)
A
A'
0.0
0.5
1.0
1.5
2.0
Time (s)
Amp
Positive
0
Negative

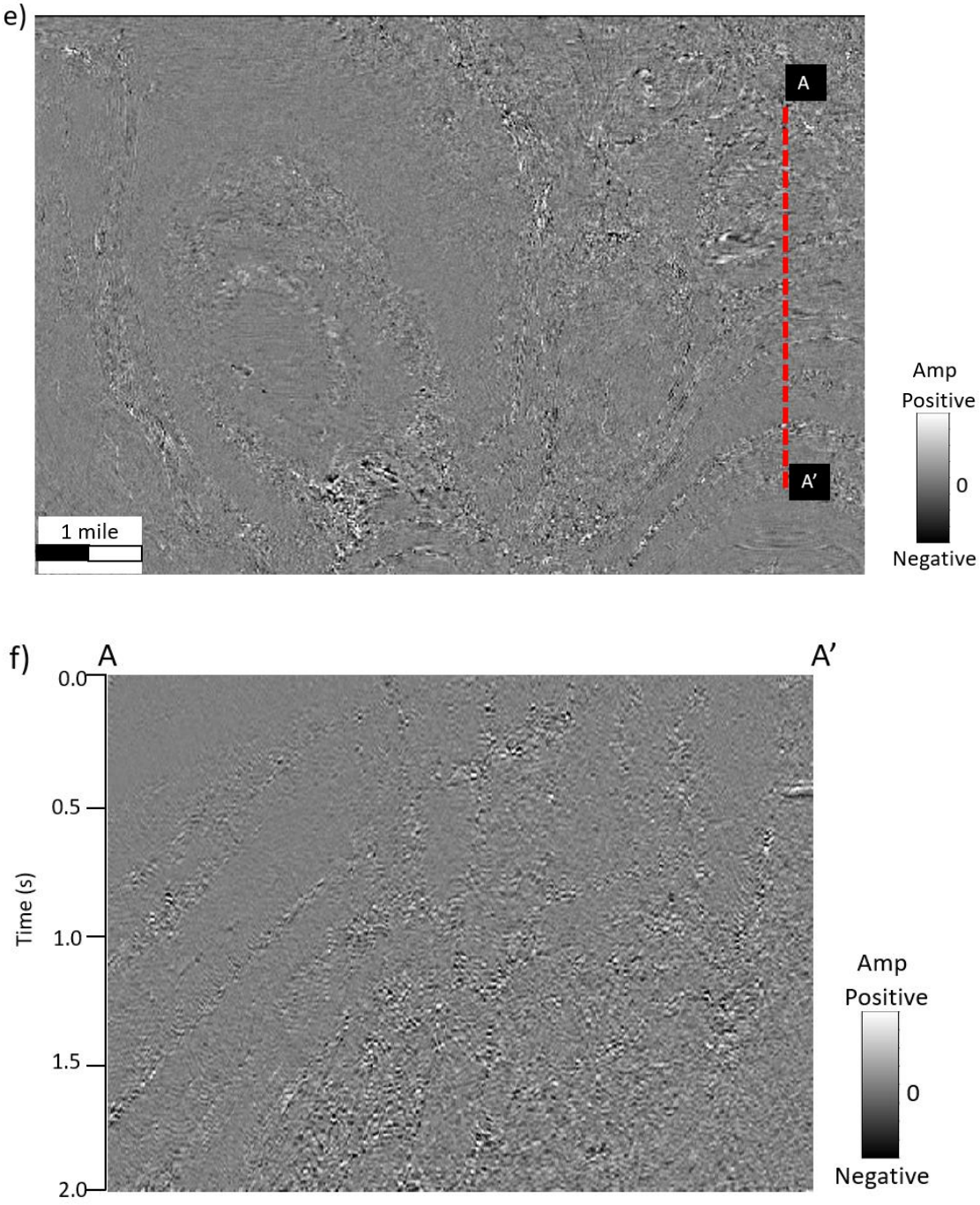

Figure 2.7 (a) Time slice at t=1s and (b) vertical slice along line AA' through the original seismic amplitude volume in the GOM3D survey. (c) Time slice at t=1s and (d) vertical slice along line AA' through the seismic amplitude volume after structure-oriented filtering. (e) Time slice at t=1s and (f) vertical slice along line AA' through the rejected "noise" volume. Note that the seismic amplitude volume after structure-oriented filtering shows a better signal-to-noise ratio. All images are at the same scale amplitude.

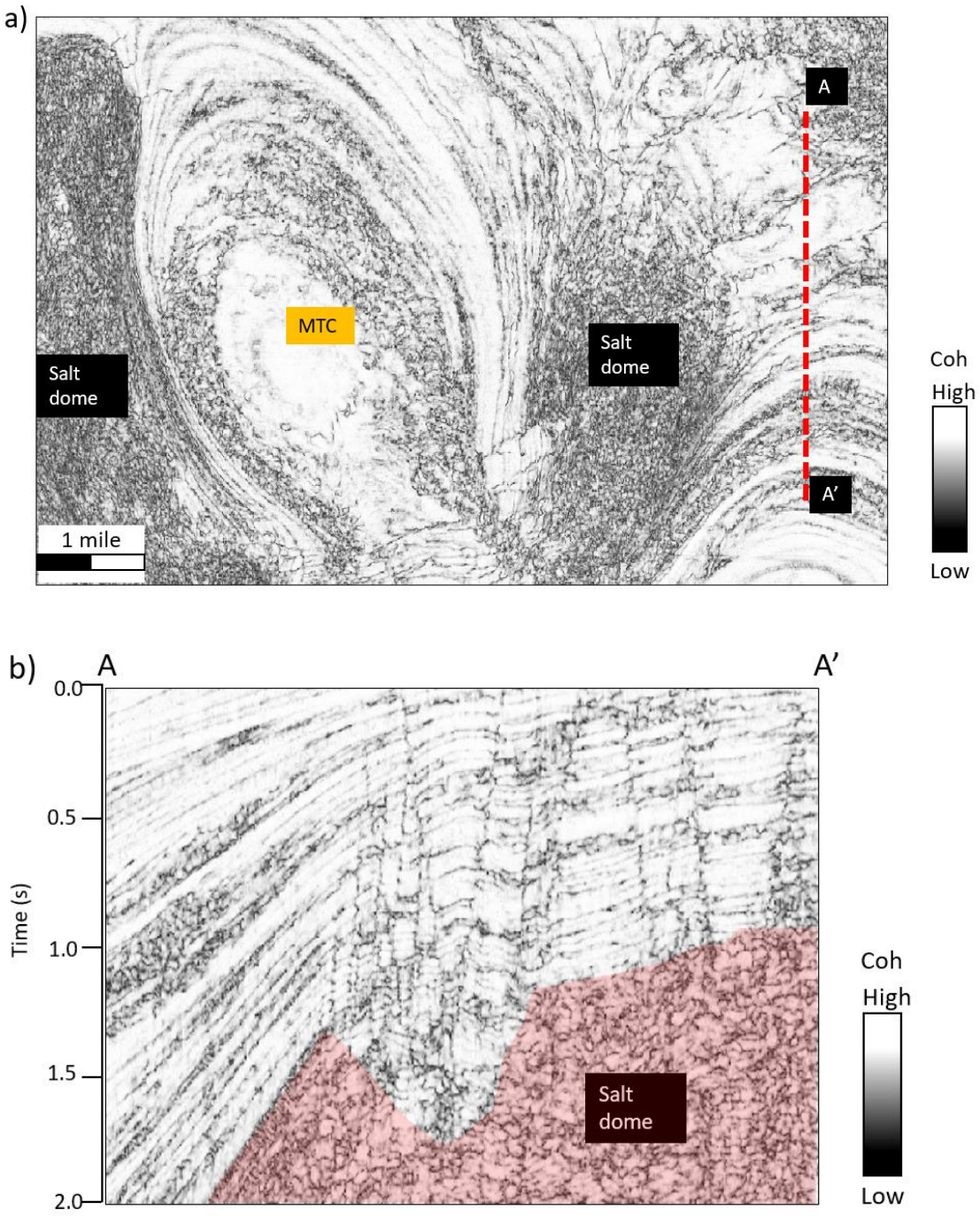
a)
A
MTC
Salt dome
Salt dome
A'
1 mile
Coh
High
Low
b)
A
A'
0.0
0.5
1.0
1.5
2.0
Time (s)
Salt dome
Coh
High
Low

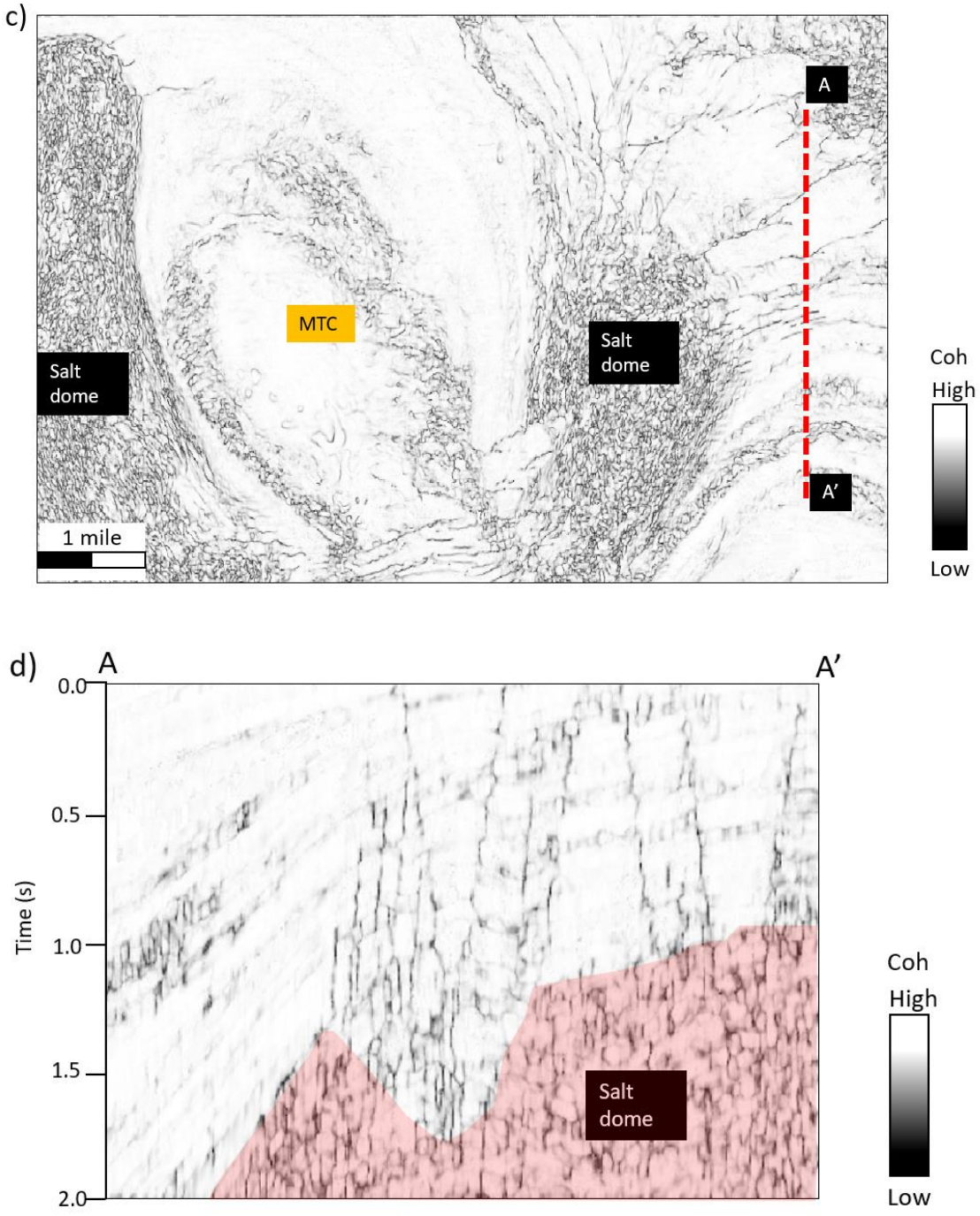

Figure 2.8 (a) Time slice at t=1s and (b) vertical slice along line AA' through coherence computed from the original seismic amplitude volume. (c) Time slice and (d) vertical slice through coherence computed from the structure oriented filtered seismic amplitude volume. Note that low coherence values parallel to weak low signal-to-noise ratio reflectors are suppressed. Thoroughgoing normal faults and localized discontinuities internal to the mass transport complexes (MTCs) are slightly enhanced. Red polygon indicates a salt dome.

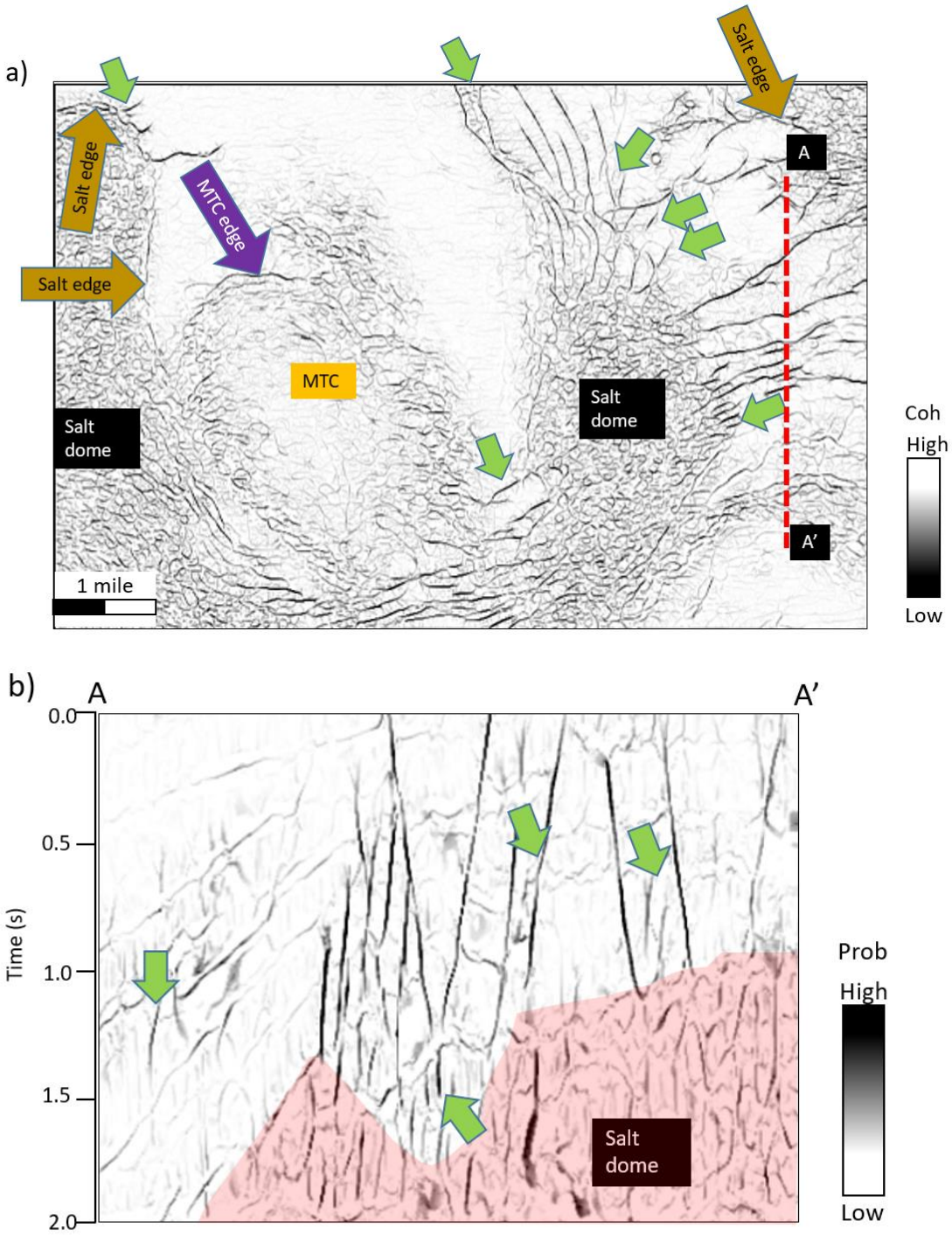

Figure 2.9 (a) Time slice at t=1s and (b) vertical slice along line AA' through the directionally skeletonized fault probability attribute. Note that faults after our workflow are more continuous, with higher contracts. Subtle features within the mass transport complexes are also enhanced. "Stairstep" artifacts in the faults have been reduced, and anomalies parallel to stratigraphy suppressed.

a)

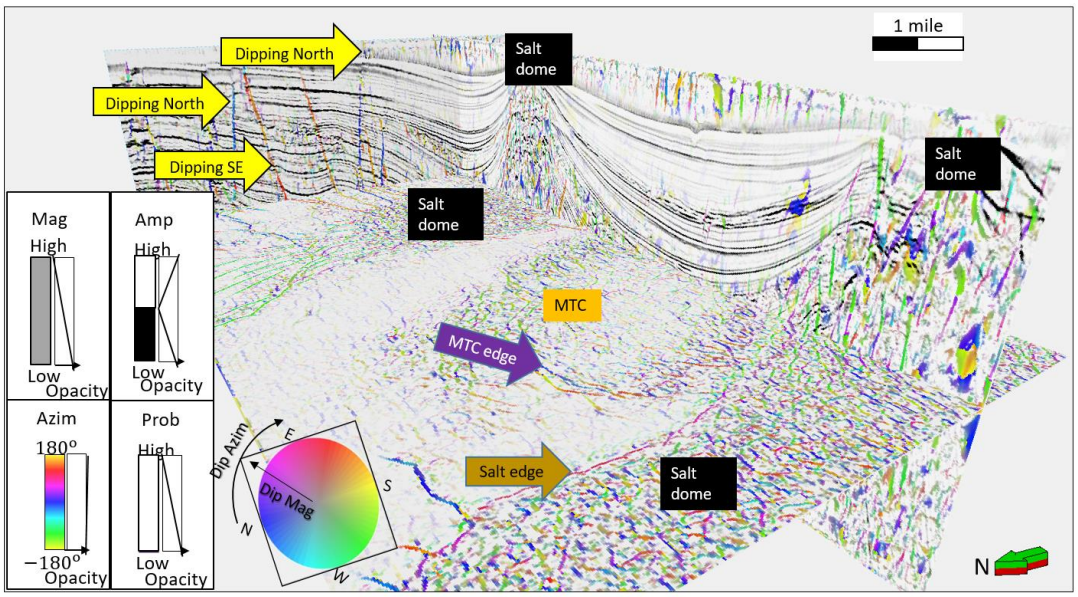
1 mile
Dipping North
Dipping North
Dipping SE
Salt dome
Salt dome
Salt dome
Salt dome
Salt dome
MTC
MTC edge
Salt edge
Mag
High
Low Opacity
Amp
High
Low Opacity
Azim
180°
−180°
Opacity
Prob
High
Low Opacity
Dip Azim
Dip Mag
E
S
N
W
N

b)

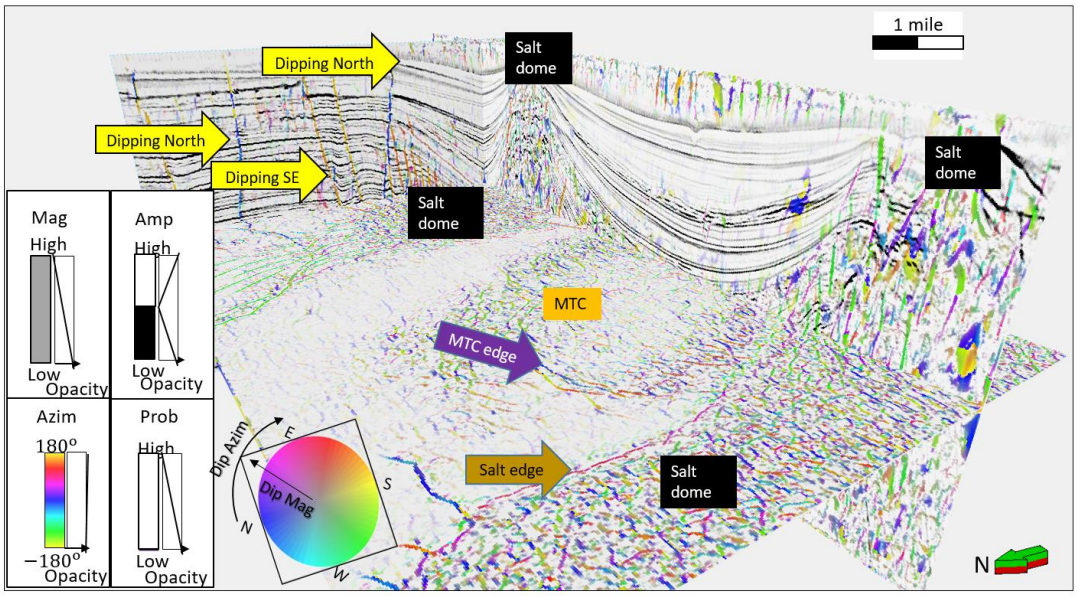
1 mile
Dipping North
Dipping North
Dipping SE
Salt dome
Salt dome
Salt dome
Salt dome
Salt dome
MTC
MTC edge
Salt edge
Mag
High
Low Opacity
Amp
High
Low Opacity
Azim
180°
−180°
Opacity
Prob
High
Low Opacity
Dip Azim
Dip Mag
E
S
N
W
N

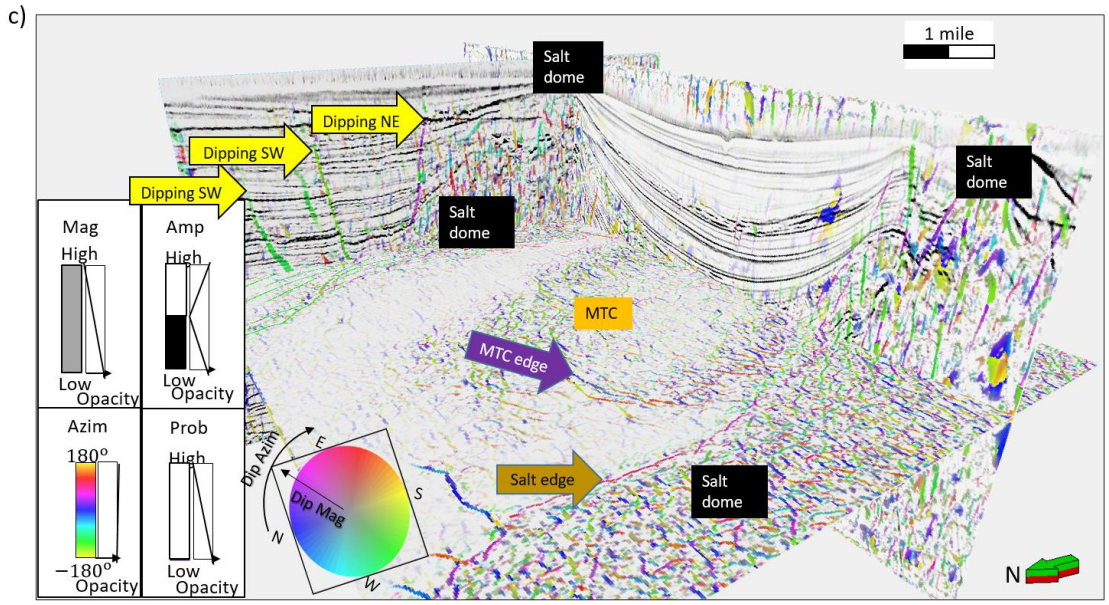

Figure 2.10 3D view showing several inlines of the directional skeletonization result co-rendered with seismic amplitude against the Hue-Lightness-Saturation. Faults orientation is readily seen. More organized artifacts now appear within the salt and should be ignored.

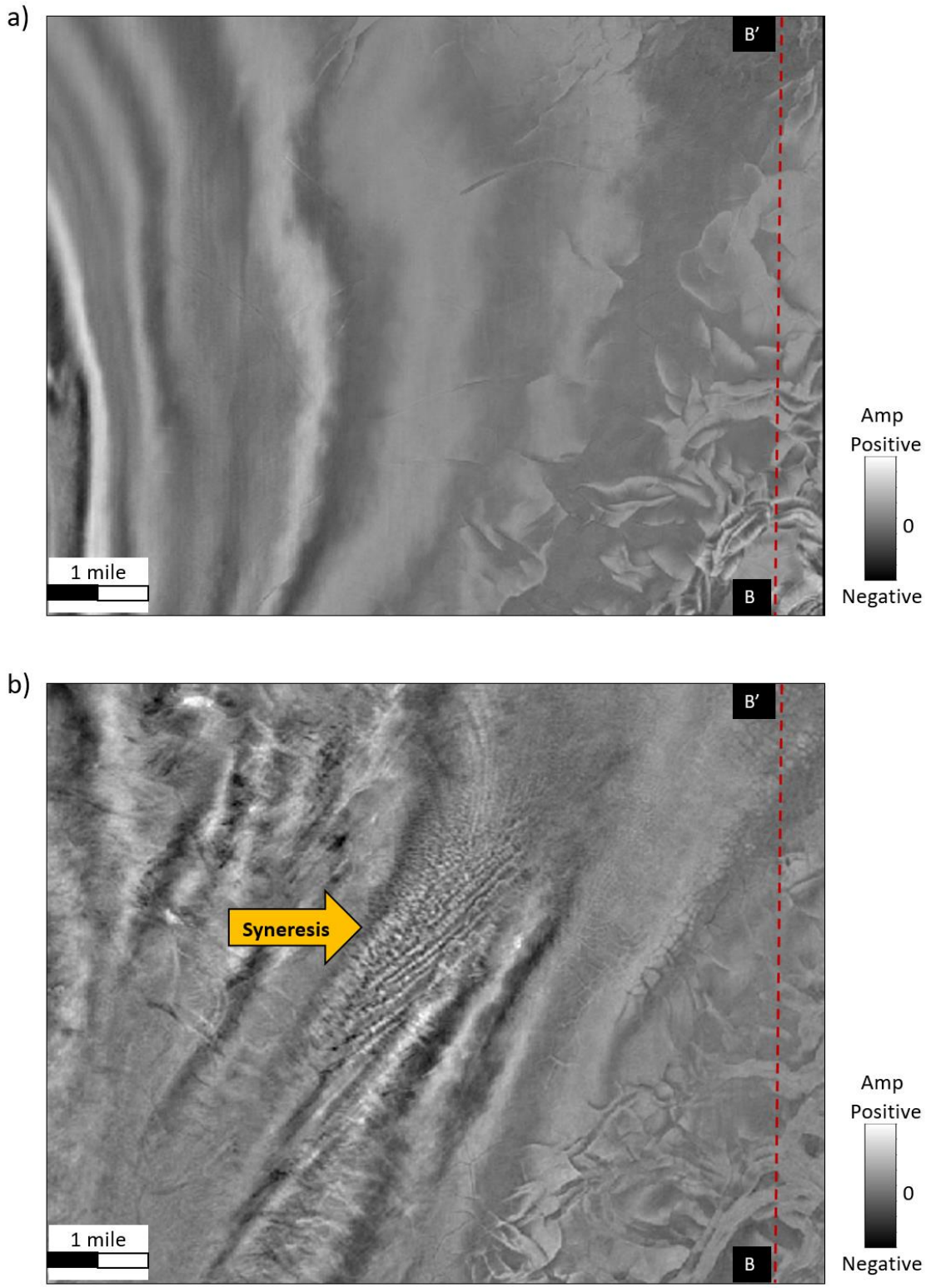
a)
B′
B
1 mile
Amp
Positive
0
Negative
b)
B′
B
Syneresis
1 mile
Amp
Positive
0
Negative

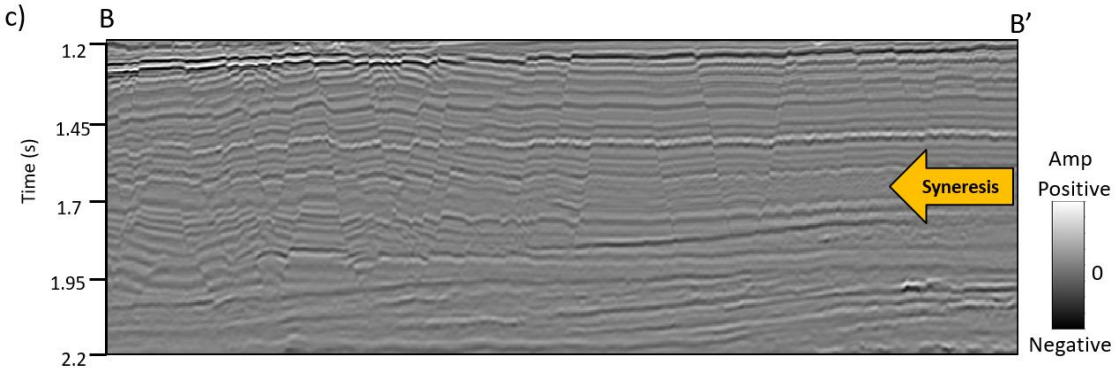

Figure 2.11 Time slice at (a) t=1.3s, and at (b) t=1.72s, and (c) a vertical slice along BB' through the original seismic amplitude volume in GSB3D survey. Polygonal faults developed in this area, as well as syneresis features (less accurately referred to as shale dewatering) appeared at t=1.72s.

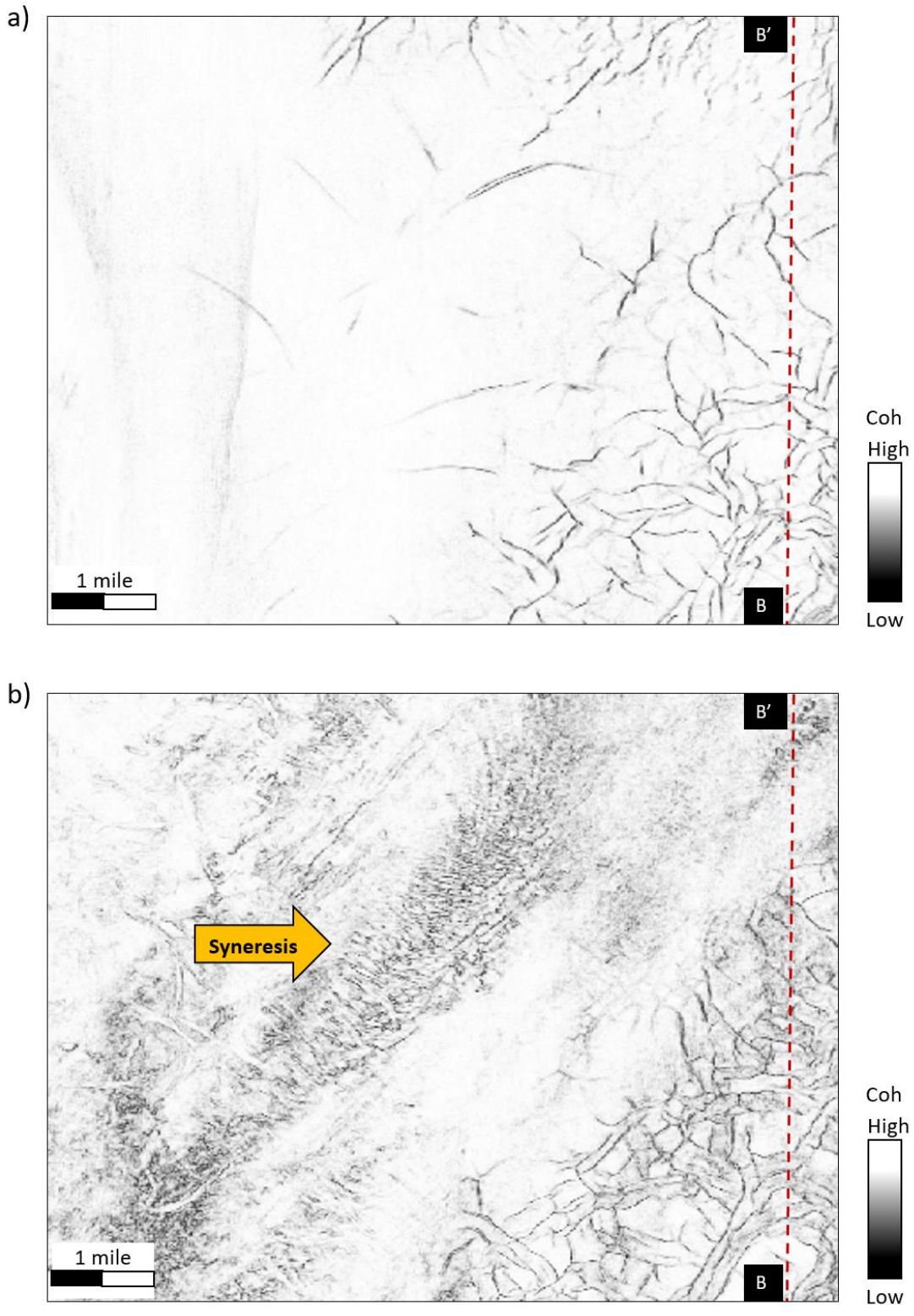
a)
B'
B
1 mile
Coh
High
Low
b)
B'
B
Syneresis
1 mile
Coh
High
Low

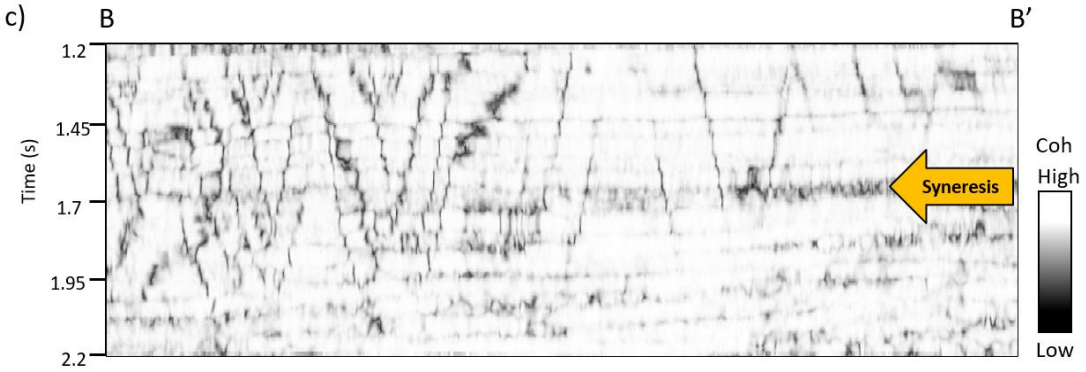

Figure 2.12 The same slices are shown in the previous figure through the coherence volume. Polygonal faults are well delineated. Faults in (b) exhibit the well-known "stairstep" artifacts on the vertical slices. The syneresis pattern in (b) is too chaotic to be interpreted.

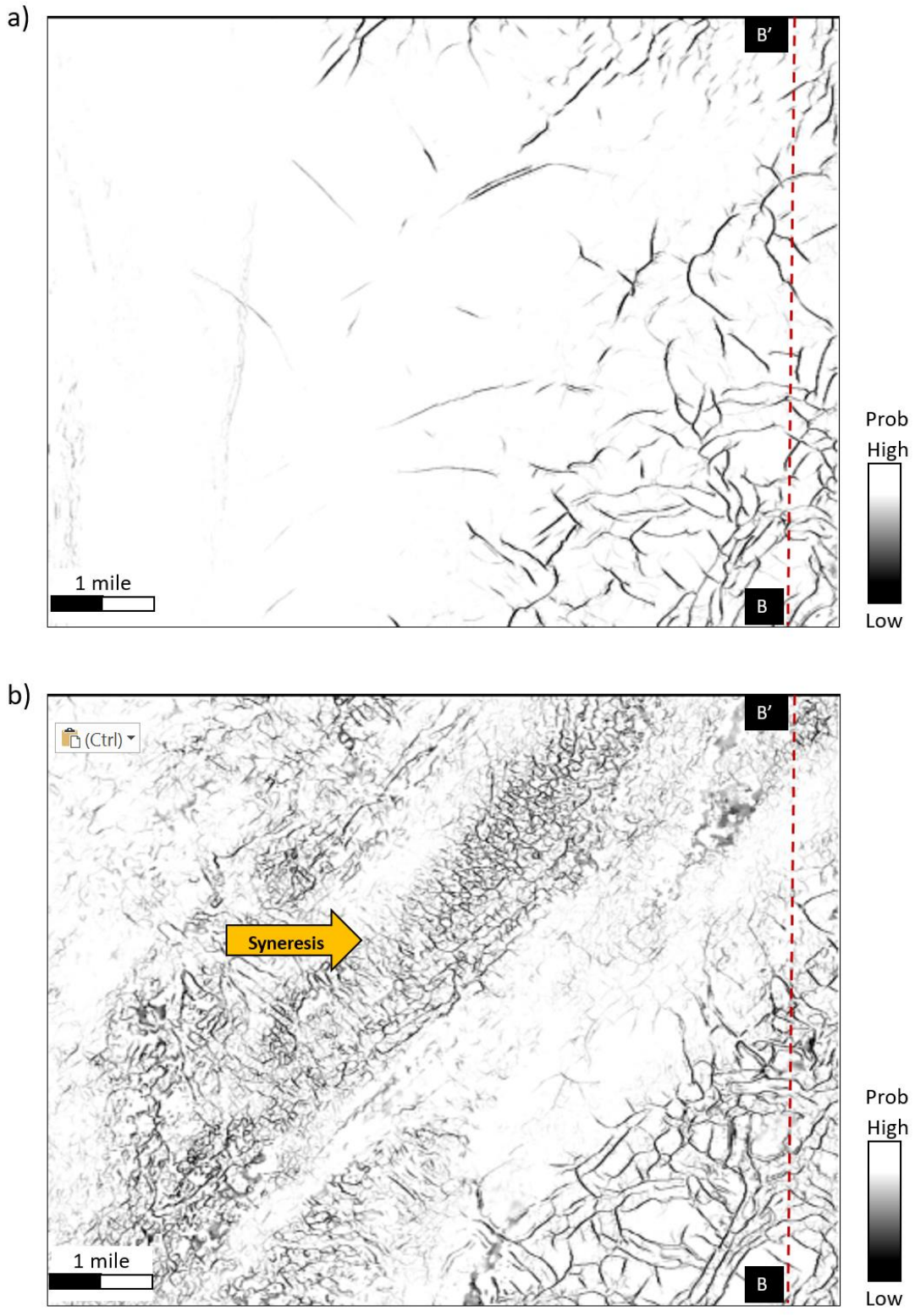
a)
B′
B
1 mile
Prob
High
Low
b)
B′
B
(Ctrl)
Syneresis
1 mile
Prob
High
Low

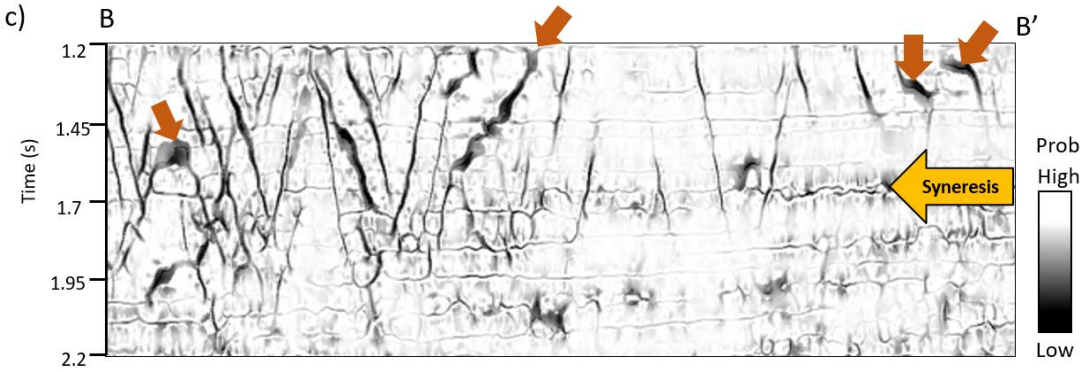

Figure 2.13 The same slices shown in the previous figure through the directionally skeletonized coherence volume. Compared with the original coherence images in the previous figure, polygonal faults are sharper, and more continuous. Random noise is suppressed, and subtle faults and other discontinuities are enhanced. In the vertical slice, the fault "stairstep" artifacts have been attenuated while syneresis discontinuities are enhanced. "Thick" black smears (orange arrows) correspond to faults subparallel to the vertical slice.

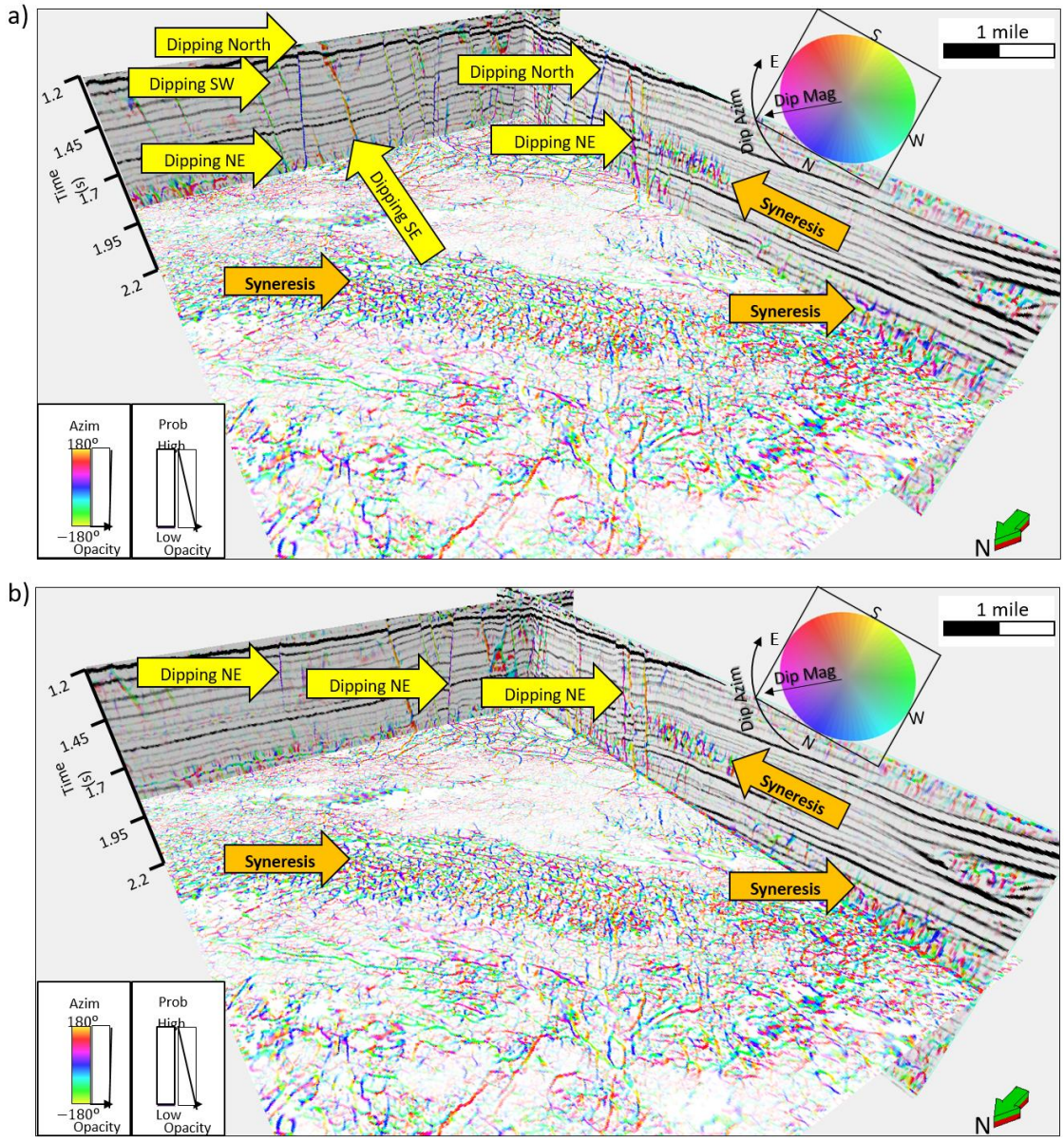

Figure 2.14 3D view showing several inlines and crosslines of the directional skeletonization result co-rendered with seismic amplitude using the Hue-Lightness-Saturation. Note that fault planes after directional skeletonization become sharper, and are readily identified.

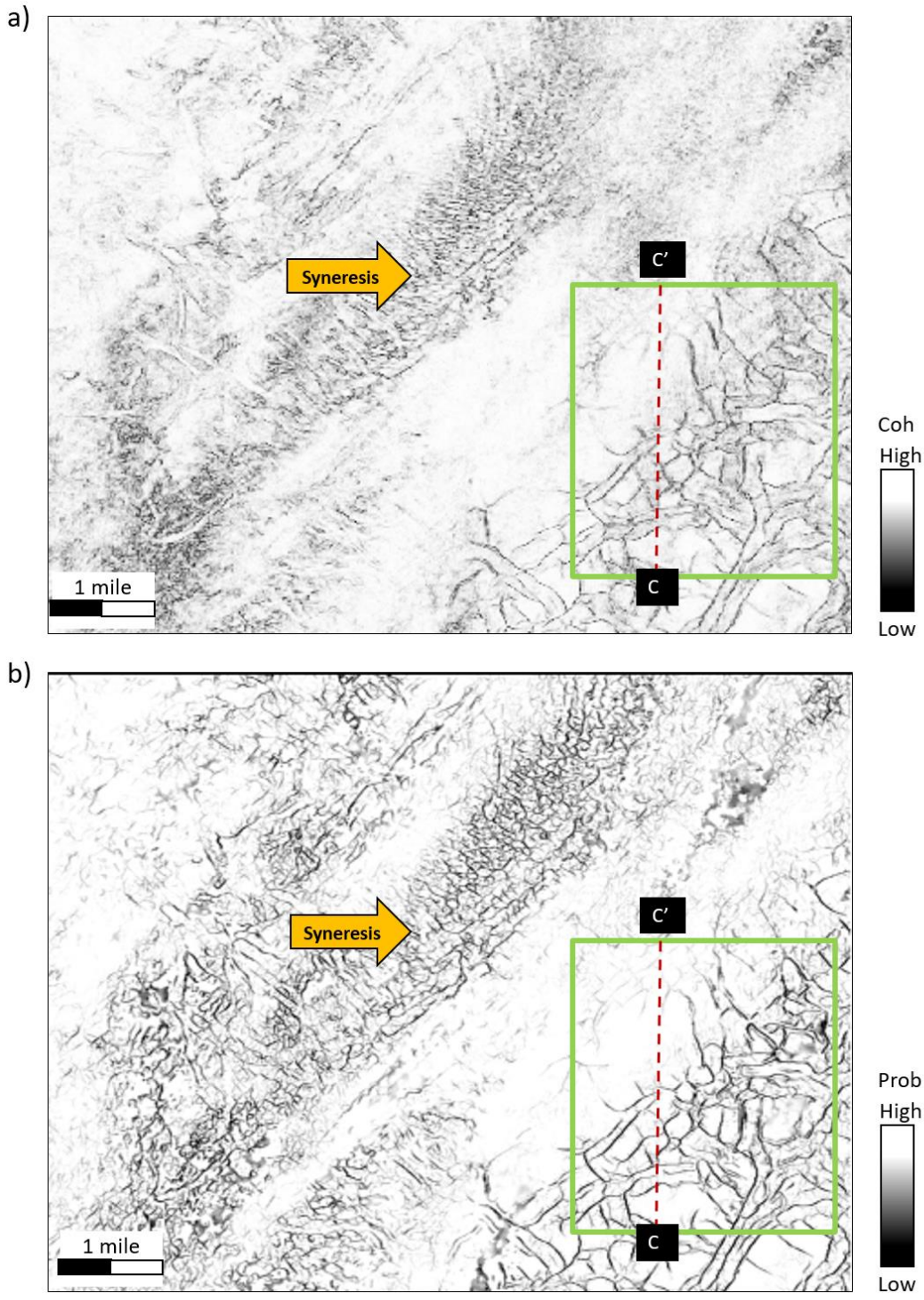
a)
Syneresis
C'
C
1 mile
Coh
High
Low
b)
Syneresis
C'
C
1 mile
Prob
High
Low

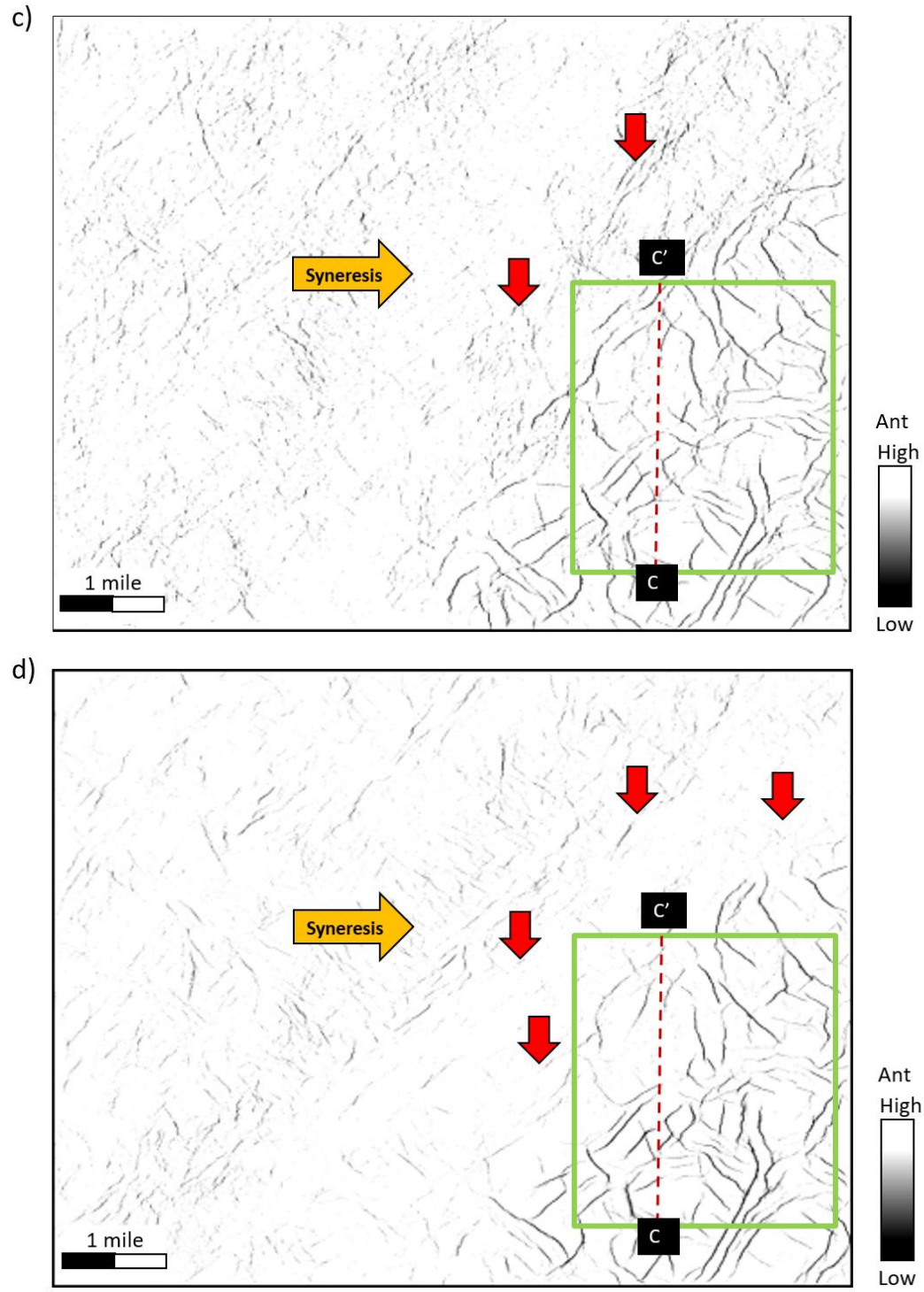

Figure 2.15 Time slice at t= 1.72s through (a) coherence, (b) directional skeletonization, (c) swarm intelligence volumes computed with coherence as input and, (d) with directional skeletonization volumes as input. Note that, skeletonization shows more subtle faults, has fewer artifacts, and preserves syneresis. Applying swarm intelligence to the skeletonized LoG image is better than that applied to coherence. Red arrows indicate artifacts generated by swarm intelligence.

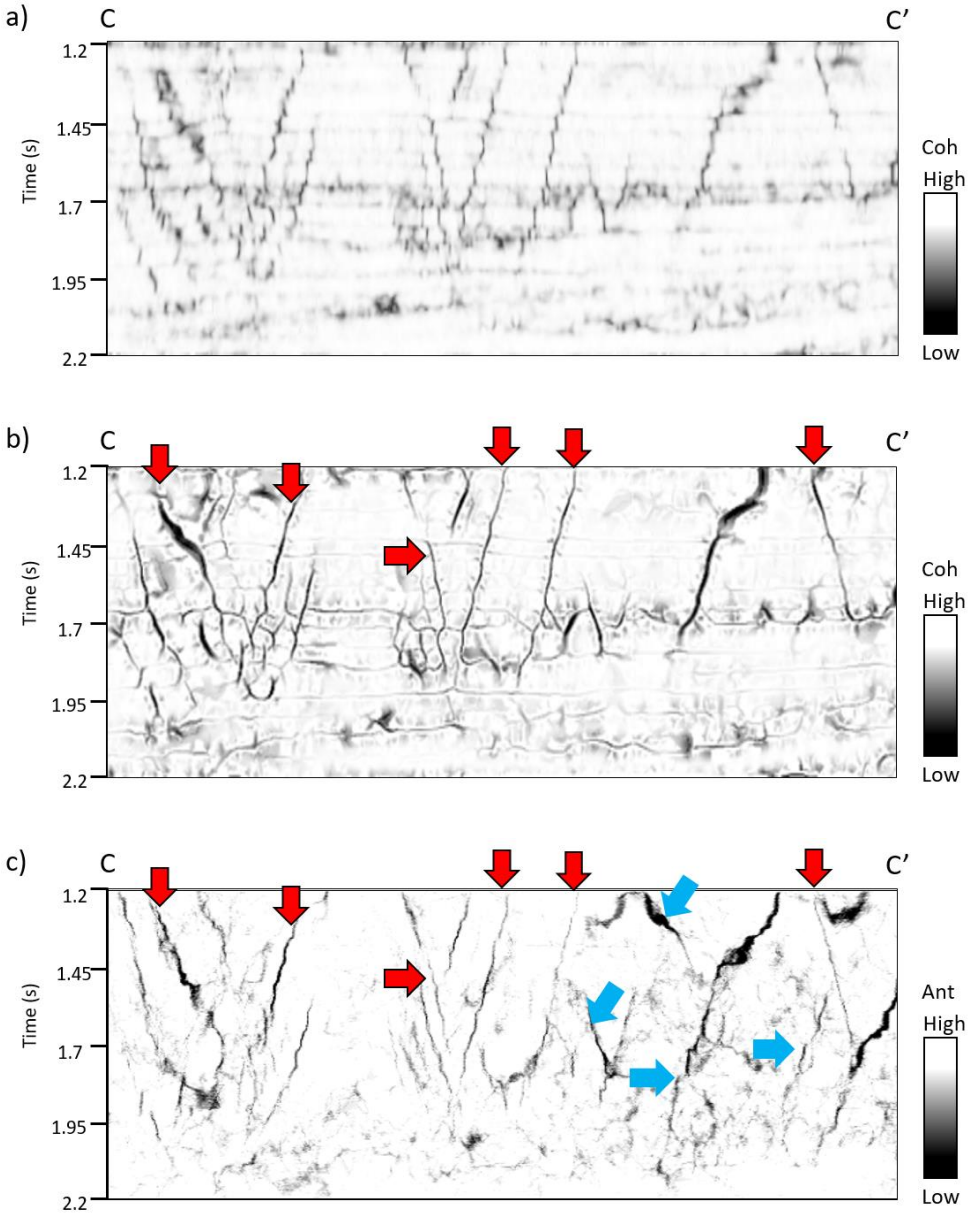
a)
C
C'
1.2
1.45
1.7
1.95
2.2
Time (s)
Coh
High
Low
b)
C
C'
1.2
1.45
1.7
1.95
2.2
Time (s)
Coh
High
Low
c)
C
C'
1.2
1.45
1.7
1.95
2.2
Time (s)
Ant
High
Low

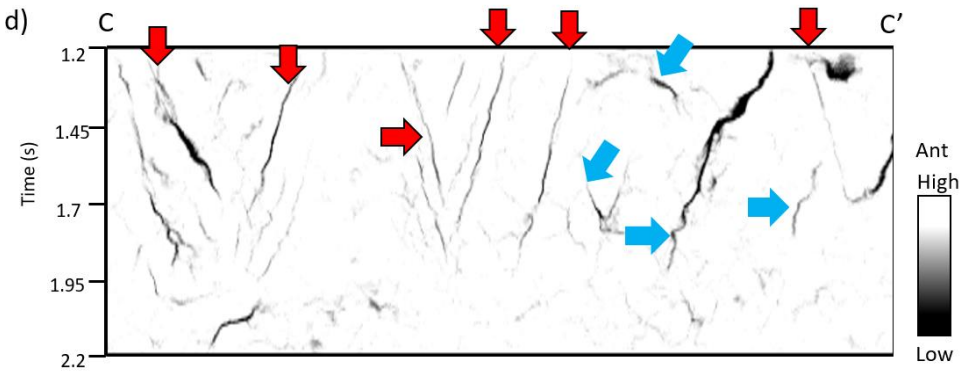

Figure 2.16 Vertical slices through (a) coherence, (b) directional skeletonization, and swarm intelligence volumes with (c) coherence as input, and (d) directional skeletonization volume as coherence as input. The skeletonization workflow in (b) exhibits fewer "stairstep" artifacts (red arrows) than those in (c) and (d). Blue arrows indicate that swarm intelligence maps faults to a greater extent than our directional skeletonization, at the expense of organizing other features that may be noise.

REFERENCES

AlBinHassan, N. M., and K. J. Marfurt, 2003, Fault detection using Hough transforms: 73rd Annual International Meeting, SEG, Expanded Abstracts, 1719-1721.

Bakker, P., L. J. van Vliet, and P. W. Verbeek, 1999, Edge-preserving orientation adaptive filtering: Conference on Computer Vision and Pattern Recognition, IEEE-CS, Proceedings, 535–540.

Boe, T. H., 2012, Enhancement of large faults with a windowed 3D Radon transform filter: 82nd Annual International Meeting, SEG, Expanded Abstracts, 1-5.

Cartwright, J.A., D. James, and A. Bolton, 2003, The genesis of polygonal fault systems: a review, in P. Van Rensbergen, RR. Hillis, A.J. Maltman, and C.K. Morley, (eds.), Subsurface Sediment Mobilization: Geological Society, London, Special Publications 216, 223- 242.

Barnes, A. E., 2006, A filter to improve seismic discontinuity data for fault interpretation: Geophysics, **71**, 1-4.

Cohen, I.m N. Coult, and A. A. Vassiliou, 2006, Detection and extraction of fault surfaces in 3D seismic data: Geophysics, **71**, 21-27.

Davogustto, O., and k. J. Marfurt, 2011, Removing acquisition footprint from legacy data volumes: 81st Annual International Meeting, SEG, Expanded Abstracts, 1025-1029.

Dewett, D. T., and A. A. Henza, 2016, Spectral similarity fault enhancement: Interpretation, **4**, 149-159.

Dorn, G. A., B. Kadlec, and P. Murtha, 2012, Imaging faults in 3D seismic volumes: 82nd Annual International Meeting, SEG, Expanded Abstracts, 1-5.

Fehmers, G, and C. F. W. Höcher, 2003, Fast structural interpretation with structure-oriented fultering: Geophysics, **68**, 1286-1293.

Gersztenkorn, A., and K. J. Marfurt, 1999, Eigenstructure based coherence computations as an aid to 3D structural and stratigraphic mapping: Geophysics, **64**, 1468–1479.

Hale, 2013, Methods to compute fault images, extract fault surfaces, and estimate fault throws from 3D seismic images: Geophysics, **78**, 33-43.

Henderson, J., S. J. Purves, and G. Fisher, 2008, Delineation of geological elements from RGB color blending of seismic attributes using a semblance-based coherency algorithm: Geophysics, **63**, 1150-1165.

Kadlec, B., G. Dorn, H. Tufo, and D. Yuen, 2008, Interactive 3-D computation of fault surfaces using level sets: Visual Geoscience, **13**, 133–138.

Li, F., and W. Lu, 2014, Coherence attribute at different spectral scales: Interpretation, **2**, 1-8.

Luo, Y., 2002, Edge-preserving smoothing and applications: The Leading Edge, **21**, 136–158.

Luo, Y., W. G. Higgs, and W. S. Kowalik, 1996, Edge detection and stratigraphic analysis using 3D seismic data: 66th Annual International Meeting, SEG, Expanded Abstracts, 324–327.

Machado, G., A. Alali, B. Hutchinson, O. Olorunsola, and k. J. Marfurt, 2016, Display and enhancement of volumetric fault image: Interpretation, **4**, SB51-SB61.

Marfurt, K. J., 2015, Techniques and best practices in multiattribute display: Interpretation, **3**, 1-23.

Marfurt, K. J., 2006, Robust estimates of 3D reflector dip and azimuth: Geophysics, **71**, 29-40.

Marfurt, K. J., R. L. Kirlin, S. H. Farmer, and M. S. Bahorich, 1998, 3D seismic attributes using a running window semblance-based algorithm: Geophysics, **63**, 1150–1165.

Pedersen, S., T. Randen, L. Sonneland, and O. Steen, 2002, Automatic 3D fault interpretation by artificial ants: 72nd Annual International Meeting, SEG, Expanded Abstracts, 512-515.

Randen, T., S. Pedersen, and L. Sønneland, 2001, Automatic extraction of fault surfaces from three-dimensional seismic data: 71st Annual International Meeting, SEG, Expanded Abstracts, 551–554.

Qi, J., T. Lin, T. Zhao, F. Li, and K. J. Marfurt, 2016, Semisupervised multiattribute seismic facies analysis: Interpretation, **4**, SB91-SB106.

Qi, J., F. Li, B. Lyu, O. Olorunsola, K. J. Marfurt, and B. Zhang, 2016, Seismic fault enhancement and skeletonization: 86th Annual International Meeting, SEG, Expanded Abstracts, 1966-1970.

Qi, J., B. Zhang, H. Zhou, and K. J. Marfurt, 2014, Attribute expression of fault-controlled karst — Fort Worth Basin, TX: Interpretation, **2**, SF91–SF110.

Wallet, B., and V. Aarre, A. Davids, T. Dao, and K. J. Marfurt, 2011, Using a hue-saturation color map to visualize dewatering faults in the overburden of the Hod Field, North Sea: 81st Annual International Meeting, SEG, Expanded Abstracts, 946-950.

Wang, X., J. Gao, C. Chen, C. Yang, and Z. Zhu, 2016, Detecting method of seismic discontinuities based on high dimensional continuous wavelet transform: Chinese J. Geophys. (in Chinese), **29**, 3394-3407.

Wu, X., and D. Hale, 2015, 3D seismic image processing for faults: Geophysics, **81**, 1-11.

Wu, X., and D. Hale, 2016, Automatically interpreting all faults, unconformities, and horizons from 3D seismic images, **4**, 227-237.

Zhang, B., Y. liu, M. Pelissier, and N. Hemstra, 2014, Semiautomated fault interpretation based on seismic attributes: Interpretation, **2**, SA11-SA19.

Zhang, B., D. Chang, T. Lin, and K. J. Marfurt, 2015, Improving the quality of prestack inversion by prestack data conditioning, Interpretation, **3**, 5-12.

Chapter 3 : Multi-azimuth coherence

Jie Qi, Fangyu Li, and Kurt Marfurt

The University of Oklahoma, ConocoPhillips School of Geology and Geophysics.

This paper was submitted to SEG journal Geophysics in 2017

ABSTRACT

Since its introduction two decades ago, coherence has been widely used to map structural and stratigraphic discontinuities including faults, cracks, karst collapse features, channels, stratigraphic edges, and unconformities. With the interest to map azimuthal variations of horizontal stress as well as to improve the signal-to-noise ratio (SNR) of unconventional resource plays, wide/full azimuth seismic data acquisition has become common. Migrating seismic traces into different azimuthal bins costs no more than migrating them into one bin. If velocity anisotropy is not taken into account by the migration algorithm, subtle discontinuities and some major faults may exhibit lateral shifts, resulting in a smeared image after stacking. Based on these two issues, we introduce a new way to compute the coherence for azimuthally limited data volumes. Like multi-spectral coherence, we modify the covariance matrix to be the sum of the covariance matrices, each belonging to an azimuthally limited volume, then use the summed covariance matrix to compute the coherent energy. We validate the effectiveness of our multi-azimuth coherence by applying it to two seismic surveys acquired over the Fort Worth Basin, Texas. Not surprisingly, the multi-azimuth coherence exhibits less incoherent noise than coherence computed from azimuthally limited amplitude volumes. If the data have been migrated using an azimuthally variable velocity, multi-azimuth coherence exhibits higher lateral resolution than that computed from the stacked data. In contrast, if the data have not been migrated using an actual azimuthally variable velocity model, the misalignment of each image results in a blurring of both the multi-azimuth coherence and the coherence computed from the stacked data. This suggests that the proposed method promises a future tool for azimuthal velocity analysis.

INTRODUCTION

Seismic attributes are routinely used to quantify changes in amplitude, dip, and reflector continuity in seismic amplitude volumes. Coherence is an edge-detection attribute that maps lateral changes in the waveform, which may be due to structural discontinuities, stratigraphic discontinuities, pinchouts, or steeply dipping coherent noise cutting more gently dipping reflectors. Several generations of coherence algorithm have been introduced and applied to geological discontinuity detection, including the cross-correlation (Bahorich and Farmer, 1995), the semblance (Marfurt et al., 1998), the eigenstructure method (Gersztenkorn and Marfurt, 1999), the gradient structure tensor (Bakker, 2002), and the predictive error filtering (Bednar, 1998) algorithms. All those algorithms operate on a spatial window of neighboring traces (Chopra and Marfurt, 2007).

Bahorich and Farmer's (1995) cross-correlation algorithm searches along candidate dips for the highest positive normalized cross-correlation coefficient between the pilot trace and the nearest two or four neighboring traces in the inline and crossline directions resulting in values between 0 (incoherent) and 1 (coherent). Marfurt et al.'s (1998) semblance algorithm computes the ratio of the energy of the average trace to the average energy of all the traces in an analysis window. Gersztenkorn and Marfurt's (1999) eigenstructure-based coherence algorithm first computes a covariance matrix from a window of trace segments oriented along structural dip. In this algorithm, the coherence is computed as the ratio of the first eigenvalue to the sum of the all the eigenvalues of the covariance matrix. The energy ratio coherence algorithm (Chopra and Marfurt, 2007) also used a covariance matrix, but now computed from windowed analytic traces (the original

data and its Hilbert transform), and estimates the coherent component of the data using a Karhunen-Loeve filter. Like semblance, in this algorithm, the coherence is the ratio of the energy of the coherent (KL-filtered) analytic traces to that of the original analytic traces. Bakker (2002) computed a version of coherence called "chaos" by computing eigenvalues of the gradient structure tensor. The 3x3 gradient structure tensor is computed by cross-correlating derivatives of the seismic amplitude in the *x, y,* and *z* directions. The first eigenvalue represents the energy of the data variability (or gradient) perpendicular to reflector dip. If the data can be represented by a constant amplitude planar event, the chaos = -1.0. In contrast, if the data are totally random, the chaos = +1.0. Closely related to coherence is Luo et al.'s (1996) filter algorithm, generalized to work at longer wavelength's as a generalized Hilbert transform (Luo et al., 2003). Kington (2015) compared different coherence algorithms and exhibited the trade-offs among different implementations.

After picking faults directly on vertical slices through the seismic amplitude volume, the coherence family of attributes is the most popular tool to map faults on seismic time, horizon, and stratal slices. Coherence also delineates channel edges, carbonate build-ups, slumps, collapse features and angular unconformities (e.g. Sullivan et al., 2006; Schuelke, 2011; Qi et al., 2014). In addition, coherence can also be applied to detect seismic textures in multiattribute seismic facies analysis (Qi et al., 2016).

With the focus on shale resource plays, wide azimuth surveys are commonly acquired to orient horizontal wells perpendicular to the maximum horizontal stress direction for optimum completion. The signal-to-noise ratio of wide azimuth surveys can be significantly improved through improved statics and leverage against ground roll and

interbed multiples, and also amenable anisotropy analysis. The axes of azimuthal anisotropy are commonly aligned with open fractures and micro cracks. In contrast, the ones being opened perpendicular to the axis have minimum azimuthal anisotropy. Several authors have applied coherence azimuthally limited volumes with limited results. Chopra and Marfurt (2007) found coherence computed from such lower fold data to exhibit higher later resolution but also to be noisy. Al-Dossary et al. (2003) attempted perhaps the first interazimuth coherence algorithm, but found it provided greater sensitivity to data quality than to geology.

A somewhat related problem is the computation of coherence from spectrally limited data volumes. Li and Lu (2014), and Li et al. (2015), computed coherence from different spectral components and co-rendered them using an RGB color model. Sui et al. (2015) added a covariance matrices computed from a suite of spectral magnitude components, obtaining a coherence image superior to that of the original broadband data. Marfurt (2017) expanded on this idea, but added coherence matrices computed from analytic spectral components (the spectral voices and their Hilbert transforms) along structural dip and found improved suppression of random noise and enhancement of small faults and karst collapse features.

In this paper, we build on this last piece of work, but now generalize it to sum a covariance matrices computed from a suite of azimuthally limited rather than frequency limited volumes. We begin our paper with a review of the energy ratio coherence algorithm. We show the improved lateral resolution but reduced signal-to-noise of coherence images generated from azimuthally limited seismic data. We then show how the multi-azimuth coherence computation provides superior results when applied to a data

volume that has been properly migrated using an azimuthally varying velocity model. Next, we apply the multi-azimuth coherence algorithm to a data volume that has not been properly corrected for azimuthal anisotropy. We conclude with a summary of our findings and a short list of recommendations.

METHOD

Energy Ratio Coherence

Coherence is an edge-detection attribute, and measures lateral changes in the seismic waveform and amplitude. The covariance matrix is constructed from a suite of sample vectors, each parallel to structural dip. Figure 3.1 shows $2K+1=7$ sample vectors of length $M=5$, or one sample for each trace. The covariance matrix for this data window is

$$C_{mn} = \sum_{k=-K}^{+K} (d_{km} d_{kn} + d_{km}^{H} d_{kn}^{H}), \qquad (3-1)$$

where the superscript H denotes the Hilbert transform, and the subscripts *m* and *n* are indices of input traces. The Hilbert transformed (90^{o} phase rotated) sample vectors don't modify the vertical resolution, but improve areas of low signal-to-noise ratio about zero crossing (Gersztenkorn and Marfurt, 1999; Marfurt, 2006). The first eigenvector $\mathbf{v}^{(1)}$ of the matrix **C** best represents the lateral variation of each of the sample vectors. In Figure 3.1, each sample vector is an approximate reflects a scaled version of the pattern (2, 2, 2, 1, 1), where the scaling factor can be positive for a peak, negative for a trough, or zero for a zero crossing. The first eigenvector for this cartoon will be a unit length vector representing this pattern:

$$\mathbf{v}^{(1)} = \left(\frac{2}{\sqrt{14}}\ \frac{2}{\sqrt{14}}\ \frac{2}{\sqrt{14}}\ \frac{1}{\sqrt{14}}\ \frac{1}{\sqrt{14}}\right). \qquad (3-2)$$

Crosscorrelating this eigenvector with the k^{th} sample vector that includes the analysis point gives a cross-correlation coefficient, β_k:

$$\beta_k = \sum_{m=1}^{M} d_{km} v_m^{(1)}, \qquad (3-3)$$

The Karhunen-Loève filtered data within the analysis window are then

$$d_{km}^{KL} = \beta_k v_m^{(1)}. \qquad (3-4)$$

Note that in Figure 3.1 that the wavelet amplitude of the three left most traces is about two times larger than that of the two right-most traces.

Energy ratio coherence computes the ratio of coherent energy and total energy in an analysis window:

$$C_{ER} = \frac{E_{coh}}{E_{tot} + \varepsilon^2}, \qquad (3-5)$$

where the coherent energy E_{coh} (the energy of the KL-filtered data) is:

$$E_{coh} = \sum_{k=-K}^{+K} \sum_{m=1}^{M} [(d_{km}^{KL})^2 + (d_{km}^{H\,KL})^2], \qquad (3-6)$$

while the total energy E_{tot} of unfiltered data in the analysis window is:

$$E_{tot} = \sum_{k=-K}^{+K} \sum_{m=1}^{M} [(d_{km})^2 + (d_{km}^{H})^2], \qquad (3-7)$$

and where a small positive value, ε, prevents division by zero.

Multi-azimuth Coherence

We generalize the concept of energy ratio coherence by summing J covariance matrices $\mathbf{C}(\varphi_j)$ computed from each of the J azimuthally-sectored data volumes:

$$\mathbf{C}_{multi-\varphi} = \sum_{j=1}^{J} \mathbf{C}(\varphi_j). \qquad (3-8)$$

The summed covariance matrix is the same *M* by *M* size as the original single azimuth covariance matrix but is now composed of *J* time as many sample vectors. Eigen-decomposition of the covariance matrix is a nonlinear process, such that the first eigenvector of the summed covariance matrix is not a linear combination of the first eigenvectors computed for the azimuthally limited covariance matrix, in which case the resulting coherence would be the average of the azimuthally limited coherence computations. To minimize the volume of data to be analyzed, azimuths are commonly binned into six 30^0 or eight 22.5^0 sectors, although finer binning is common in large processing shops.

APPLICATION

Our two examples are both from the Fort Worth Basin, Texas. The survey A was acquired in 2006 using 16 live receiver lines forming a wide-azimuth survey with a nominal 55×55 ft CDP bin size. The data were preprocessed and binned into six azimuths, preserving amplitude fidelity at each step before prestack time migration (Roende et al., 2008). Figure 3.2 shows time slices at t=0.74 s through the six different azimuthally limited seismic amplitude volumes. Figure 3.3 shows time slices through the six corresponding coherence volumes. Because the signal-to-noise ratio of each azimuthal sector seismic amplitude is low, the signal-to-noise ratio of the resulting coherence images is also low. Those differences between the azimuthally limited coherence images include the shape and size of karst features (indicated by green arrows), the continuity of subtle faults (indicated by yellow arrows), and level of incoherent noise. As recognized by Perez and Marfurt (2008) faults are best delineated by the azimuths perpendicular to them (e.g. Figure 3.3a at 00 vs. Figure 3.3c at 600)

Stacking the six seismic amplitude volumes and then compute coherence (the conventional analysis workflow) gives the result shown in Figure 3.4a which exhibits greater signal-to-noise but slightly lower lateral resolution than the azimuthally limited coherence time slices shown in Figure 3.3. Figure 3.4b shows the result of stacking the six images shown in Figure 3.3. The signal-to-noise ratio on Figure 3.4b is lower than that of Figure 3.4a, however edges of the karst features become appear more pronounced than on the traditional coherence computation. Figure 3.4c shows the multi-azimuth coherence result computed using the covariance matrix described by equation 8. Note that the multi-azimuth coherence displays the higher lateral resolution rather than either traditional coherence or the stacked azimuthal coherence, especially in areas with high anisotropic effects (indicated in Figure 3.4d). Karst features (indicated by green arrows) exhibit highly incoherent anomalies and subtle faults (indicated by yellow arrows) appear as strong as major faults. Multi-azimuth coherence not only preserves most of the discontinuities seen in each of the azimuthally limited coherence volumes in Figure 3.3, but also suppresses incoherent noise.

The survey B is also from the Fort Worth Basin, Texas. The data was prestack time migrated into eight azimuthal sectors, with the 22.5^{o} azimuthal interval. Figure 3.5 shows time slices at t=1.36 s through four of the coherence volumes 0^{o}-22.5^{o}, 45^{o}-67.5^{o}, 90^{o}-112.5^{o}, and 135^{o}-157.5^{o}. These data were migrated using an isotropic velocity model, such that anisotropy gives rise to lateral shifts (indicated by yellow arrows) in the coherence anomalies. Perez and Marfurt (2008) applied a spatial cross-correlation technique to the coherence slices to measure lateral shifts of discontinuities and then correct them using a data warping algorithm. Figure 3.6a illustrates traditional coherence

attribute computed from the stacked seismic amplitude volume. Note the signal-to-noise ratio in Figure 3.6a is higher than that in Figure 3.5, because random noise is suppressed after stacking azimuthally limited seismic amplitude volumes. However, Figure 3.5 exhibits the higher lateral resolution than Figure 3.6a. Lateral shifts (indicated by yellow arrows) of discontinuities observed from different azimuthally limited coherence volumes, have been smeared after the stacking step. In general, applied isotropic velocity to the areas with anisotropic effects (aligned nature fractures), or hydraulically induced fractures, will give rise to azimuthal variations of discontinuities. Guo et al. (2016) compared this data (before hydraulic fracturing) with adjacent data (after hydraulic fracturing), and found that this data exhibits strong anisotropic effects along faults by correlating most-positive curvature and amplitude variation with azimuth (AVAz) anisotropy. Figure 3.6b shows the co-rendered RGB plot of azimuthally limited coherence volumes 0^o-22.5^o (red), 45^o-67.5^o (green), 90^o-112.5^o (blue). If the three input azimuthal coherence volumes were perfectly aligned, the coherent part of the co-rendered RGB image would be white and aligned faults would be black. However, in the co-rendered RGB image, combining three colors of those azimuthal coherence volumes, the two major faults in Figure 3.6b are displayed more continuous by different color rather than in Figure 3.6a, which indicates that faults are more continuous after stacking all azimuthally limited coherence volumes like in Figure 3.4b. Areas that appear to be magenta indicate that the azimuthal coherence volume 0^o-22.5^o is less coherent to other two volumes, whereas areas that appear to be blue indicate that the azimuth coherence volume 90^o-112.5^o is less coherent. Figure 3.6c shows the multi-azimuth coherence attribute. Compared with figure 3.6a and b, Figure 3.6c illustrates significant

improvements in the delineation of areas with lateral shifts (indicated by yellow arrows). Two major faults exhibit highly incoherent anomalies. Figure 3.6b and Figure 3.6c indicate similar discontinuous anomalies, but Figure 3.6c exhibits higher signal-to-noise ratio. Also, lateral resolution, especially in less coherent areas, has been increased.

CONCLUSIONS

We have introduced a new way to compute coherence of azimuthal sectors that preserves subtle discontinuities seen on the individual azimuthal volumes. The new multi-azimuth coherence can avoid smearing lateral variations and suppress incoherent noise. The algorithm consists of computing a covariance matrix for each azimuthal sectors and summing the results. Eigen-decomposition of the summed covariance matrix of all azimuthally limited volumes is a nonlinear process, such that the first eigenvector of the summed covariance matrix is not a linear combination of the first eigenvectors computed for the azimuthally limited covariance matrix. The summed covariance matrix provides a superior image to those provided by stacking the data and computing coherence, or by stacking the coherence computed from each azimuthally limited seismic volume. Comparing to traditional coherence or the stacked azimuthal coherence, the multi-azimuth coherence displays the higher lateral resolution, and exhibit karst collapse features and subtle faults that appear as clear as the major faults. Although RGB blending can only co-render these attribute volumes at a time, it provides a powerful tool that measures imaging problems associated with anisotropy. Survey A from the southwest part of the Fort Worth Basin exhibits only moderate azimuthal anisotropy. Fault images at different azimuths align in the RGB images and appear as black, while the elliptical collapse features express a color that favors the azimuth perpendicular to the orientation

of the edge. Survey B from the northeast part of the Fort Worth Basin straddles the mineral wells fault and exhibits considerate anisotropy. Therefore, the fault images are misaligned and appear as a suit of red, green, and blue anomalies. Summing the corresponding misaligned covariance matrices results in a blurred coherence image. While the improvement over coherence computed from the stacked data is minimal, we hypothesize that addressing these misalignment issues may provide a future anisotropic velocity analysis tool and quality control measure.

ACKNOWLEDGEMENTS

The authors would like to thank Marathon Oil and Devon Energy for providing the data. We also thank all financial support by the University of Oklahoma Attribute-Assisted Seismic Processing and Interpretation (consortium).

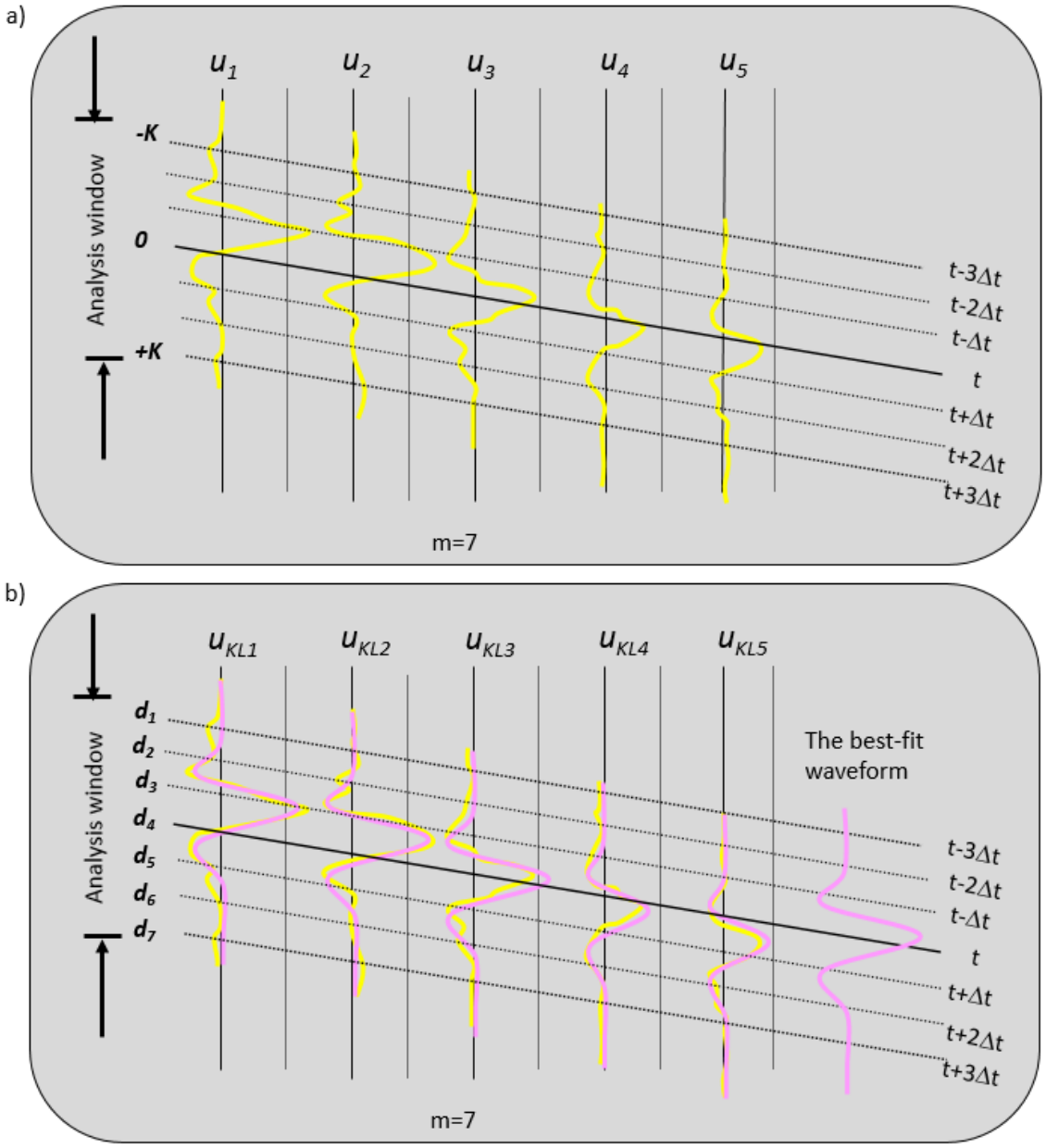

Figure 3.1 Cartoon of an analysis window with five traces and seven samples. Note that the wavelet amplitude of the three left most traces is about two times larger than that of the two right-most traces.

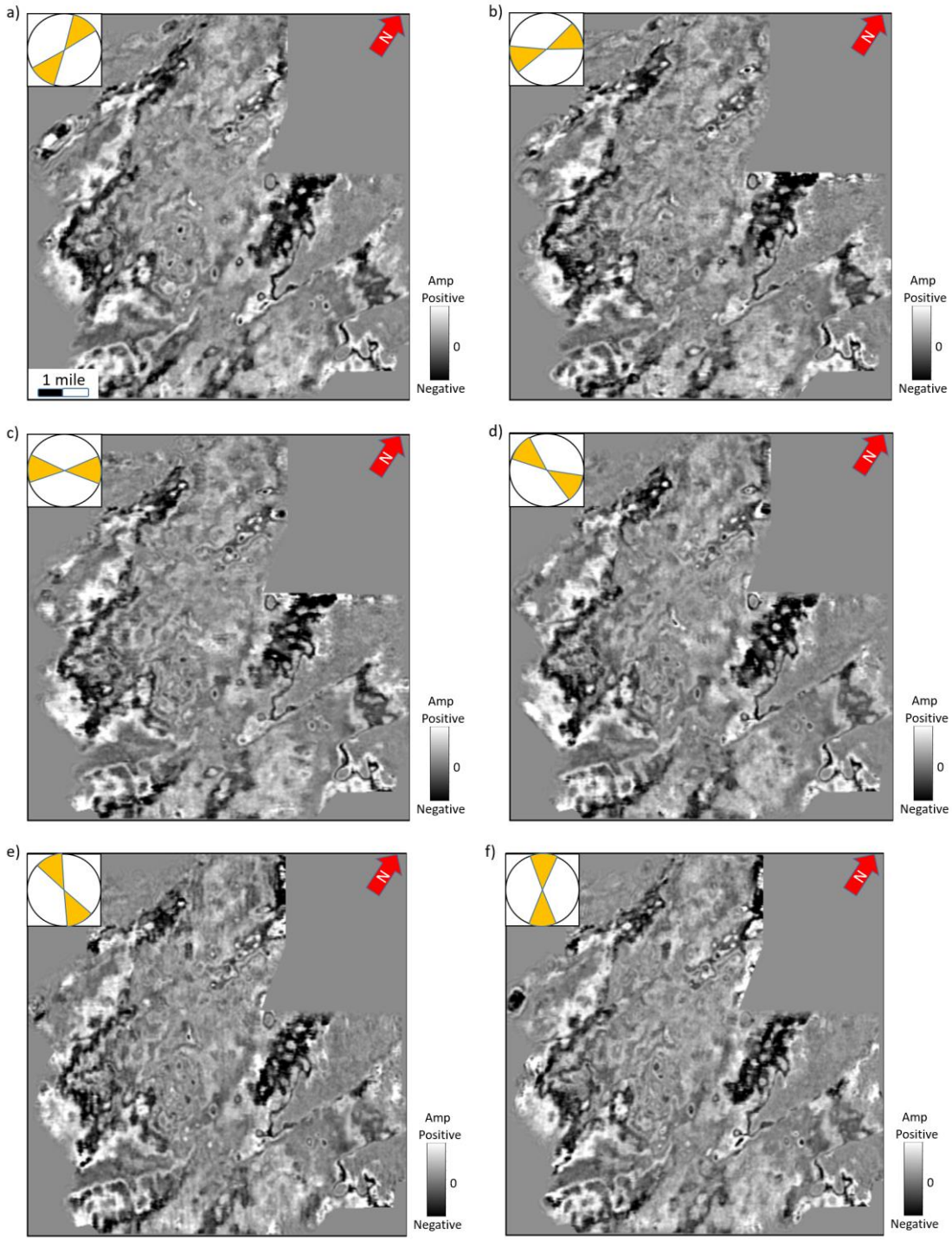

Figure 3.2 Time slices at t=0.74s through azimuthally limited migrated seismic amplitude volumes: (a) 165° to 15°, (b) 15° to 45°, (c) 45° to 75°, (d) 75° to 105°, (e) 105° to 135°, and (f) 135° to 165°. Note azimuthal variations and that although the signal-to-noise ratio of each azimuthal sector is low, one can identify faults and karst features.

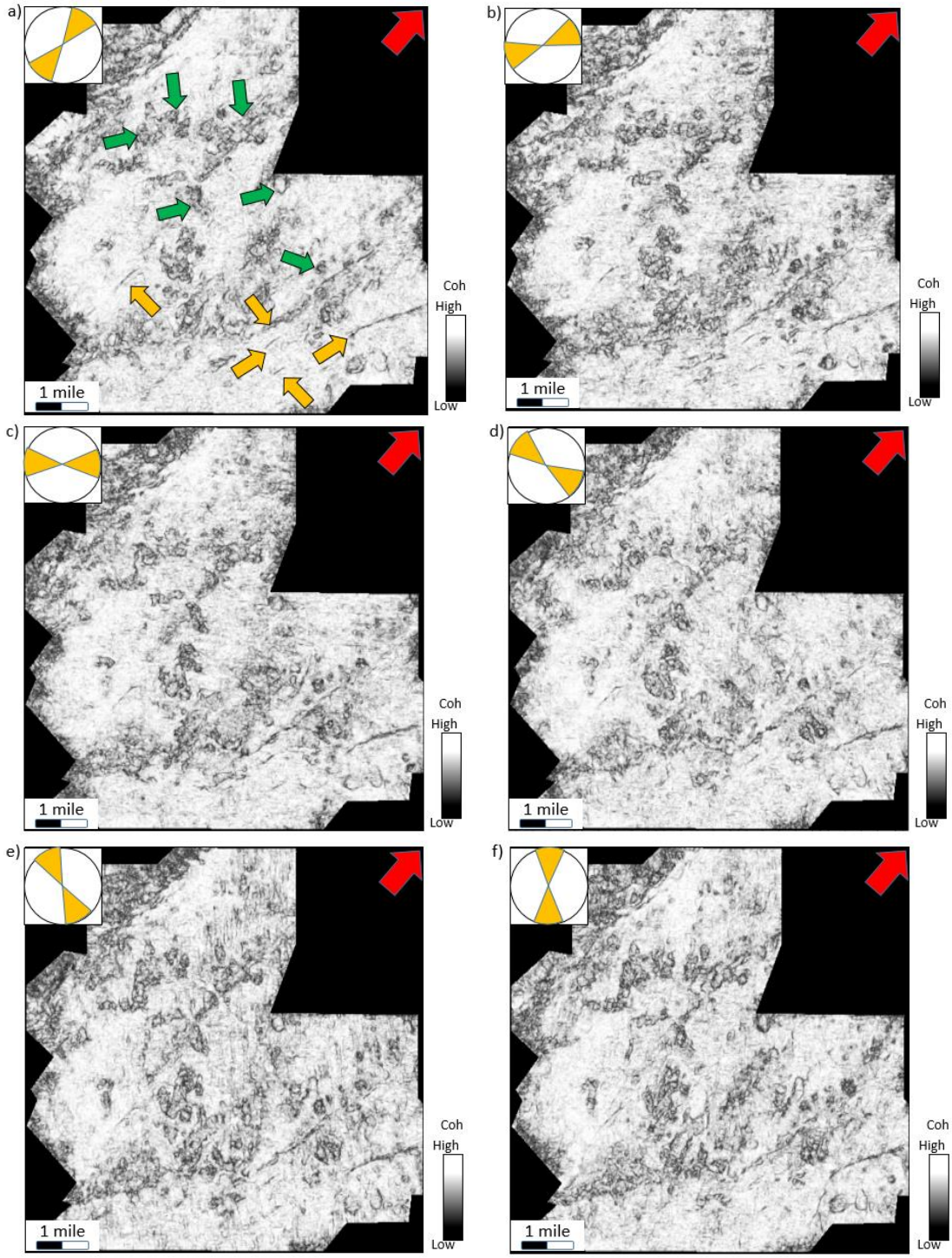

Figure 3.3 Time slices at t=0.74s through coherence volumes computed from the azimuthally limited data shown in Figure 3.1: (a) 165º to 15º, (b) 15º to 45º, (c) 45º to 75º, (d) 75º to 105º, (e) 105º to 135º, and (f) 135º to 165º. Although one can identify faults (yellow arrows) and karst collapse features (green arrows), the images are quite noisy.

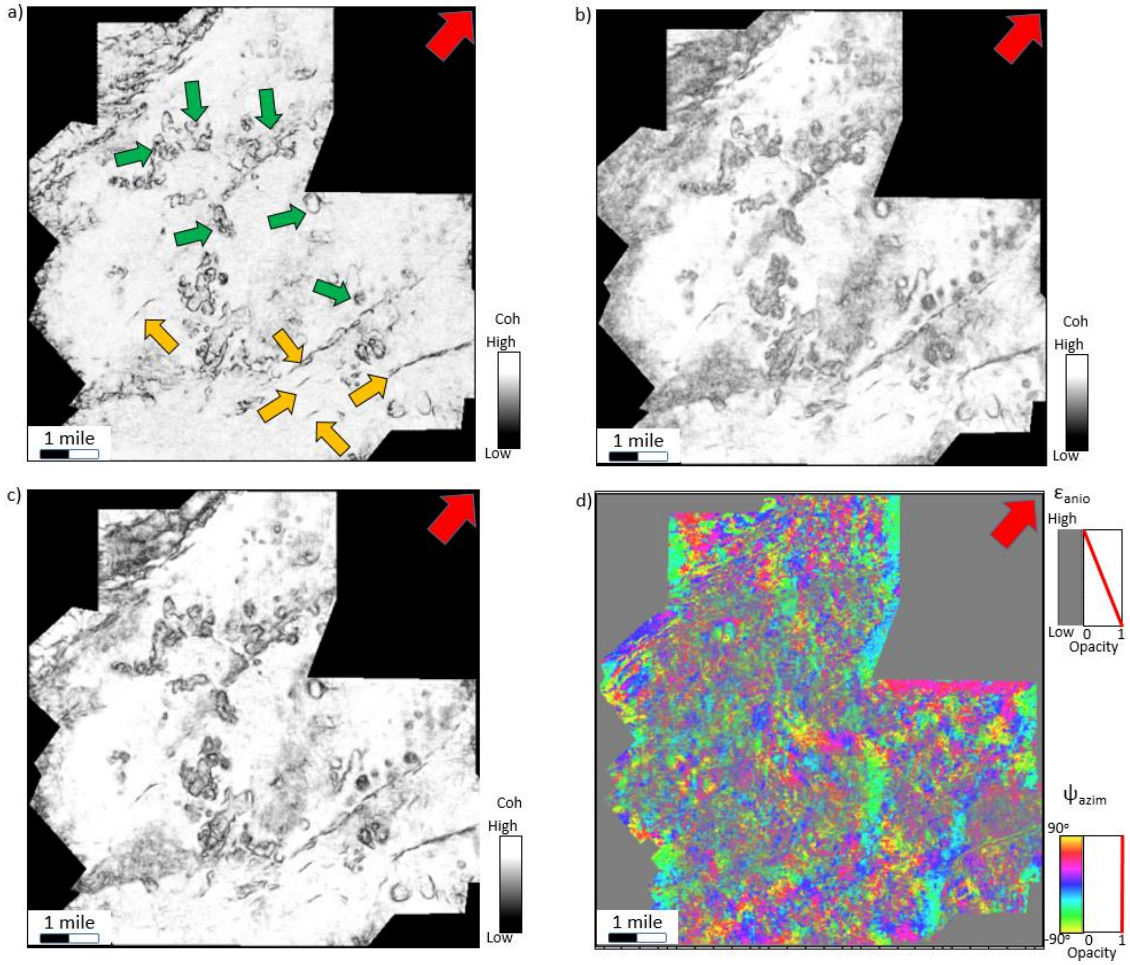

Figure 3.4 Time slices at t=0.74s through coherence volume computed from (a) the poststack seismic amplitude data, (b) the sum of the coherence shown in Figure 3.2, (c) the multi-azimuth coherence, and (d) the top Marble Fall limestone through the co-rendered anisotropic intensity ε_{anis} and azimuth ψ_{azim}. Note there is the improved lateral resolution of the multi-azimuth coherence. Edges of karst features (indicated by green arrows) are better delineated, and subtle discontinuities (indicated by yellow arrows) are as strong as major faults. The result obtained by stacking the azimuthal coherence volumes is as same places noisy and in other slices. The co-rendered anisotropic intensity ε_{anis} and azimuth ψ_{azim} image indicates the areas with high anisotropic effects, where also correspond to lateral variation areas.

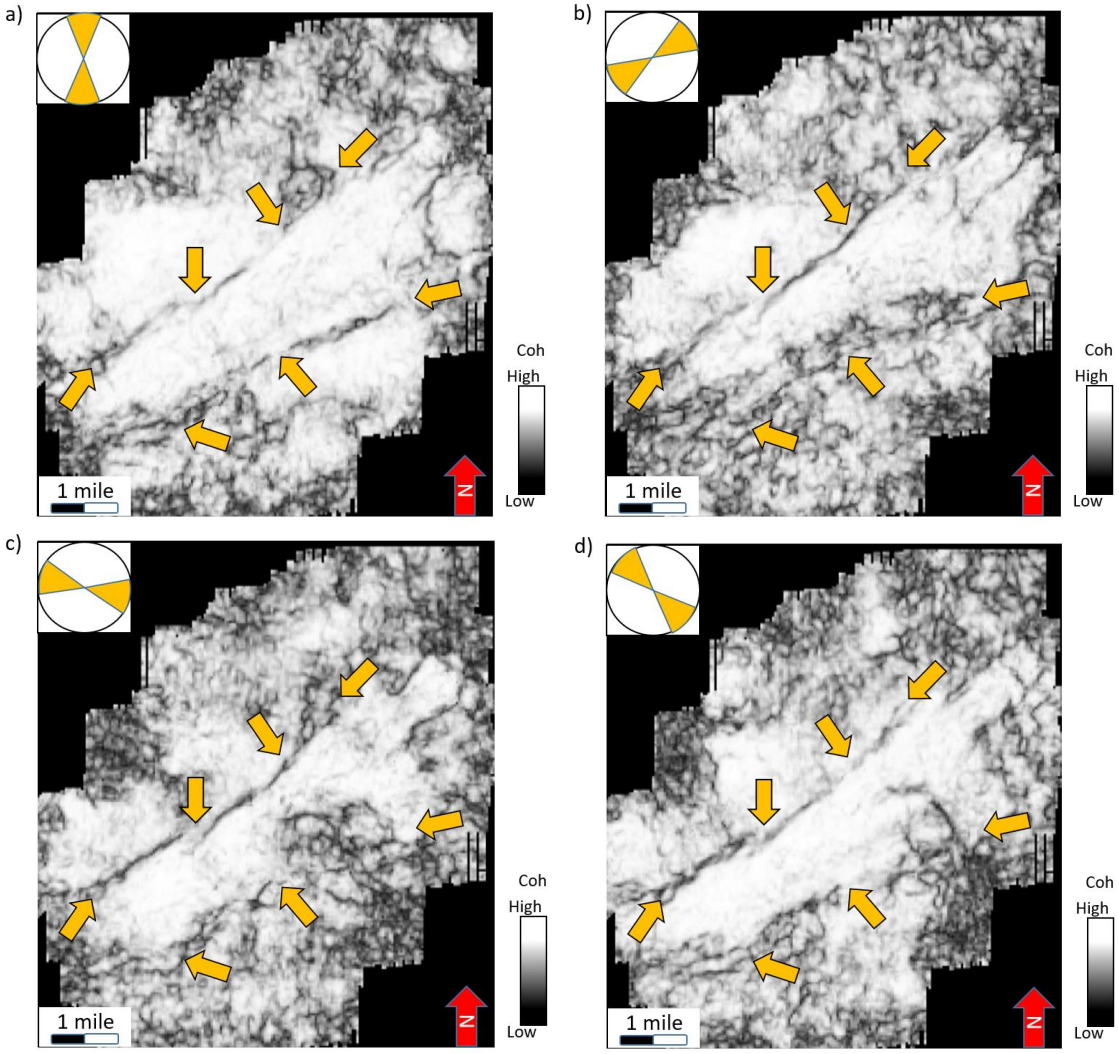

Figure 3.5 Time slices at t=1.36s through coherence volume computed from the azimuthal sector (a) 0º-22.5º, (b) 45º-67.5º, (c) 90º-112.5º, and (d) 135º-157.5º in the second dataset. Note that, there are significant differences between each azimuthal coherence. Lateral shifts of discontinuities are indicated by yellow arrows.

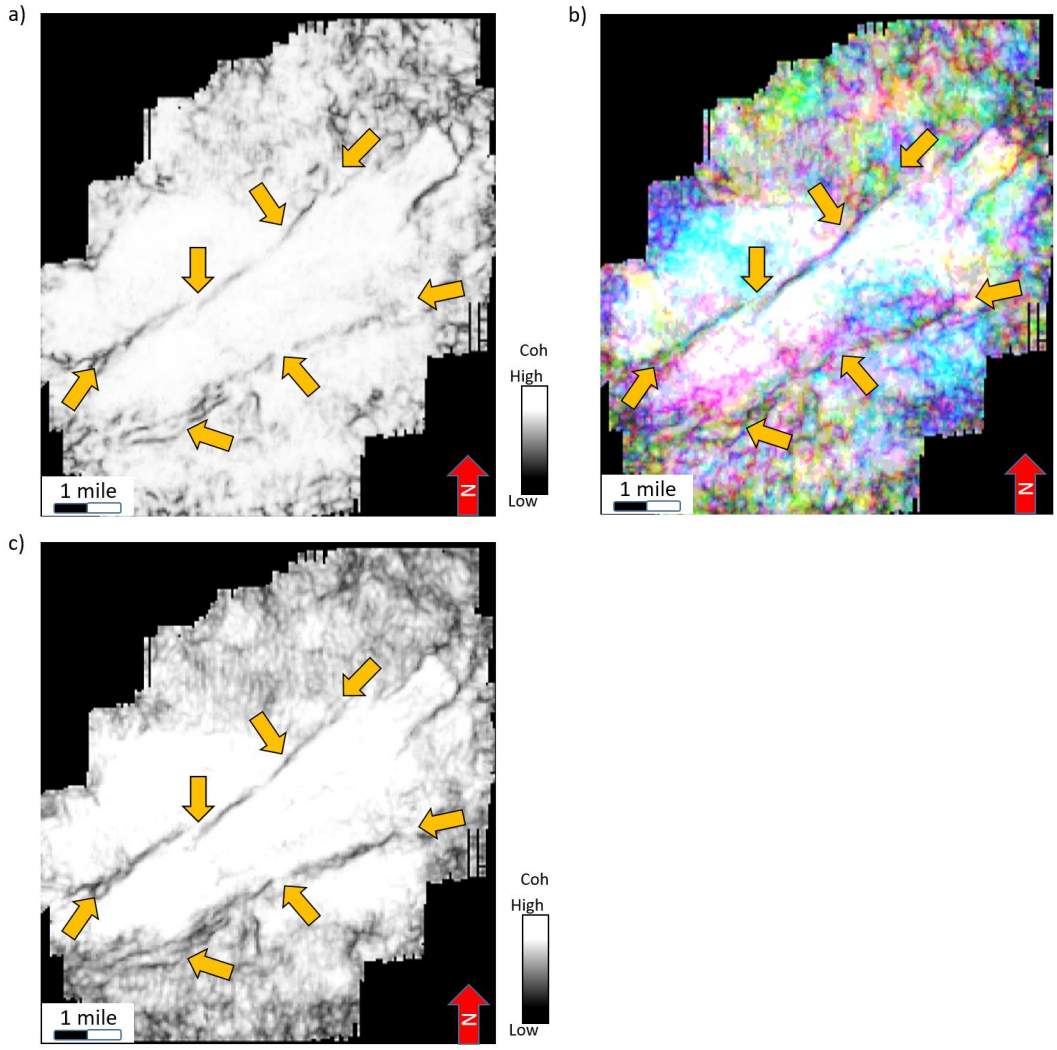

Figure 3.6 Time slices at t=1.36s through (a) the poststack coherence volume, (b) the RGB image computed by azimuthal sectors 0º-22.5º, 45º-67.5º, 90º-112.5º, and (c) the new multi-azimuth coherence. Note that, there are significant improvements in delineation of lateral shifted faults (indicated by yellow arrows) in the multi-azimuth coherence. Lateral resolution especially in less coherent areas has been better delineated.

REFERENCES

Al-Dossary, S., Y. Simon, and K. J. Marfurt, 2004, Interazimuth coherence attributes for fracture detection: 74th Annual International Meeting, SEG, Expanded Abstracts, 183–186.

Bahorich, M. S., and Farmer, S. L., 1995, 3-D seismic discontinuity for faults and stratigraphic features: The Leading Edge, **14**, 1053–1058.

Bakker, P., 2002, Image structure analysis for seismic interpretation: PhD thesis, Delft University of Technology.

Bednar, J. B., 1998, Least-squares dip and coherency attributes: The Leading Edge, **17**, 775–776.

Chopra, S., K. J. Marfurt, 2007, Seismic attributes for prospect identification and reservoir characterization: Book, SEG.

Gersztenkorn, A., and K. J. Marfurt, 1999, Eigenstructure based coherence computations as an aid to 3D structural and stratigraphic mapping: Geophysics, **64**, 1468–1479.

Guo, S., S. Verma, Q. Wang, B. Zhang, and K. J. Marfurt, 2016, Vector correlation of amplitude variation with azimuth and curvature in a post-hydraulic-fracture Barnett Shale survey: Interpretation, **4**, SB23-SB35.

Kington, J., 2015, Semblance, coherence, and other discontinuity attributes: The Leading Edge, **34**, 1510-1512.

Li, F., J. Qi, and K.J. Marfurt, 2015, Attribute mapping of variable thickness incised valley-fill systems: The Leading Edge, **34**, 48-52.

Li, F., and W. Lu, 2014, Coherence attribute at different spectral scales. Interpretation, **2**, 1-8.

Luo, Y., S. al-Dossary, M. Marhoon, and M. Alfaraj, 2003, Generalized Hilbert transform and its application in geophysics: The Leading Edge, **22**, 198-202.

Marfurt, K., J., 2017, Interpretational value of multispectral coherence: EAGE Technique Expanded Abstracts.

Marfurt, K. J., 2006, Robust estimates of 3D reflector dip and azimuth: Geophysics, **71**, 29-40.

Marfurt, K. J., R. L. Kirlin, S. H. Farmer, and M. S. Bahorich, 1998, 3D seismic attributes using a running window semblance-based algorithm: Geophysics, **63**, 1150–1165.

Perez, G., and K. J. Marfurt, 2008, Warping prestack imaged data to improve stack quality and resolution, Geophysics, **73**, 1-7.

Qi, J., T. Lin, T. Zhao, F. Li, and K. J. Marfurt, 2016, Semisupervised multiattribute seismic facies analysis: Interpretation, **4**, SB91-SB106.

Qi, J., B. Zhang, H. Zhou, and K. J. Marfurt, 2014, Attribute expression of fault-controlled karst — Fort Worth Basin, TX: Interpretation, **2**, SF91–SF110.

Roende, H., C. Meeder, J. Allen, S. Peterson, and D. Eubanks, 2008, Estimating subsurface stress direction and intensity from subsurface full-azimuth land data: 78th Annual International Meeting, SEG, Expanded Abstracts, 217–220.

Schuelke, J. S., 2011, Overview of seismic attribute analysis in shale play: Attributes: New views on seismic imaging-Their use in exploration and production, Presented at 31st Annual GCSSEPM Foundation Bob F. Perkins Research Conference.

Sui, J.-K., X. Zheng, and Y. Li, 2015, A seismic coherency method using spectral attributes: Applied Geophysics, **12**, no. 3, 353-361.

Sullivan, E. C., K. J. Marfurt, A. Lacazette, and M. Ammerman, 2006, Application of new seismic attributes to collapse chimneys in the Fort Worth basin: Geophysics, 71, 111-119.

Zhang, B., T. Zhao, J. Qi, and K. J. Marfurt, 2014, Horizon-based semiautomated nonhyperbolic velocity analysis: Geophysics, **79**, 15-23.

Chapter 4 : Attribute expression of fault-controlled karst – Fort Worth Basin, TX – A tutorial

Jie Qi, Bo Zhang, Huailai Zhou and Kurt Marfurt

The University of Oklahoma, ConocoPhillips School of Geology and Geophysics.

This paper was published by SEG and AAPG journal Interpretation in 2014

ABSTRACT

Much of seismic interpretation is based on pattern recognition, such that experienced interpreters are able to extract subtle geologic features that a new interpreter may easily overlook. Seismic pattern recognition is based on the identification of changes in 1) amplitude, 2) phase, 3) frequency, 4) dip, 5) continuity, and 6) reflector configuration. Seismic attributes, which providing quantitative measures that can be subsequently used in risk analysis and data mining, partially automate the pattern recognition problem by extracting key statistical, geometric, or kinematic components of the 3D seismic volume. Early attribute analysis began with recognition of bright spots and quickly moved into the mapping of folds, faults, and channels. While a novice interpreter may quickly recognize faults and channels on attribute time slices, karst terrains provide more complex patterns. The goal of this tutorial is to instruct the attribute expression of a karst terrain in the western part of the Fort Worth Basin, Texas, United States of America. Karst provides a specific expression on almost every attribute. Specifically, karst in the Fort Worth Basin Ellenburger Group exhibits strong dip, negative curvature, low coherence, and a shift to lower frequencies. Geomorphologically, the inferred karst geometries seen in our study areas (Harris 3D, Texas) indicate strong structural control, whereby large-scale karst collapses is associated with faults and where karst lineaments are aligned perpendicularly to faults associated with reflector rotation anomalies.

INTRODUCTION

The word ‘karst’ is a German word which denotes the area of modern Slovenia known as Kras and to the ancient Roman as Carso. The well drained limestone terrain and extensive system of natural caverns makes Kras an important wine producing area. The word karst is now used to describe a carbonate terrain that has undergone significant diagenetic alteration which give rise to enhanced joints, caves, and collapse features. Paleo-karst play many roles in oil and gas reservoirs. Ordovician paleo-karst is a main oil and gas reservoir in the Tarim Basin, China where reservoir depth can reach 6 to 7 km (Chen et al., 2010). Across the Central Basin Platform of west Texas, karst-processes are responsible for the vuggy reservoir rock, and also the anhydrite-plugged updip seal (Duo, 2011). In shale resource plays, such as the Barnett Shale unconformably lying upon the Ellenburger in many areas of the Fort Worth Basin, karst can form ‘geohazards’. Wells that intersected collapse features and diagenetically altered faults and joints, will produce so much water from the underlying aquifer, which should be abandoned. In the Barnett and Eagle Ford shale, such hazards are often fault controlled, and many interpreters call this ‘a string of pearls’ (Schuelke, 2011). In the Mississippi lime play of northern Oklahoma and southern Kansas where the average pay cutoff is a 5% water cut, the deeper Ordovician-age karst Arbuckle (Ellenburger equivalent) formation provides the capacity to dispose of the 95% water (Elebiju et al., 2009).

The Fort Worth Basin Texas Barnett Shale was the first successfully exploited shale resource play in North America. Like most resource plays, the low permeability Barnett Shale serves as source rock, reservoir rock, trap, and seal. Production is most often achieved through the use of horizontal wells and hydraulic fracturing. In the “core”

producing area of the Fort Worth Basin, the Barnett Shale lies below the Marble Falls Limestone and above the Viola Limestone (Figure 4.1). In general, quartz- and dolomite-rich rocks are brittle, while calcite-rich rocks are ductile (Wang and Gale, 2009). In our study area, the Barnett Shale lies unconformably on top of the relatively brittle, dolomitic Ellenburger Group (Holtz and Kerans, 1992). Here, elsewhere, the extensively karst-modified Ellenburger presents numerous drilling-related risks.

Faults and fractures, associated with Ellenburger collapse, often propagate through the overlying Barnett Shale. Sullivan et al. (2006) and Roth and Thompson (2009) describe fault-controlled collapse features in a survey without a Viola hydraulic fracture barrier in western Wise Co., TX (Figure 4.1). Khatamadi et al. (2013) described basement control of karst using the same survey described in this paper. Hardage et al. (1996) and McDonnell et al. (2007) describe how these deeper collapse features locally enhanced accommodation and provided depocenters for Pennsylvanian-age Bend Conglomerates.

Seismic attributes are routinely used to map geologic features of interest. Coherence (e.g. Bahorich and Farmer, 1995) is routinely used to identify faults and channel edges. Curvature (e.g. al-Dossary and Marfurt, 2006) is used to map folds and flexures. Spectral components (e.g. Partyka et al., 1999) are used to constrain lateral variations in channel thickness. Qi and Castagna (2013) illuminate faults and karst detection using amplitude and phase spectrum and PCA fault-detection attribute which calculates the first principal component of most positive curvature, coherence, variance and phase spectrum. Often, interpreters want to know "which attribute is best for illuminating a particular geologic feature". In this tutorial, we illustrate the value of using multiple seismic attributes to illuminate paleo-karst terrain features common within the Fort Worth Basin. We will

argue that the integrative use of mathematically independent attributes can illuminate kinematically related deformation thereby reducing the risk of interpreter error.

We begin our tutorial with a brief summary of the geology of the study area. Next we describe post-stack data conditioning that suppresses migration artifacts and improves spectral bandwidth. Then we introduce a suite of seismic attributes, first displaying them as time slices through attribute volumes, then as horizon slices along the upper Ellenburger. As we discuss each attribute, we attempt to link the attribute expression to a specific component of the geology (e.g. the structural dip of collapse features). We will also address potential interpretation pitfalls when mathematically coupling attributes. We conclude by providing insights into the geology of the Fort Worth Basin and showing the value of multiattribute visualization.

GEOLOGICAL BACKGROUND

The Fort Worth Basin is one of several basins that formed during the late Paleozoic Ouachita Orogeny, generated by convergence of Laurasia and Gondwana (Bruner and Smosna, 2011). The Mississippian-age organic-rich Barnett Shale gas reservoir is a major resource play in the Fort Worth Basin. It extends over 28,000 mi^2 with most production coming from a limited area where the shale is relatively thick and isolated between effective hydraulic fracture barriers. Conformably overlying the Barnett Shale is the Marble Falls Formation. The lower Marble Falls consists of a lower member of interbedded dark limestone and gray-black shale. Underlying the Barnett Shale are the Ordovician Viola-Simpson Formations, which dominantly consist of dense limestone, and dolomitic Lower Ordovician Ellenburger Group.

The upper surface of the Ellenburger records the 2nd-order Sauk-Tippecanoe erosional unconformity which is characterized by extensive karst and solution-collapse (Loucks, 2003). Lucia (1971) first recognized the genetic relationship between karst dissolution and breccias seen in the Ellenburger Group. Kerans (1989, 1990) established the karst and cave models (Figure 4.2) and their development in the Ellenburger Group. This paleocave model forms the basis of the paleo-karst model which includes a paleocave floor, fill, and roof. Faulting and local subsidence may also be associated with karst and solution-collapse features on the top of the Ellenburger Group (Gale et al., 2007). Pore networks in the Ellenburger Group are complex because of the amount of brecciation and fracturing associated with karst. In the Fort Worth Basin, the Ellenburger Group is almost always a water-bearing formation. Faults and karst in the Ellenburger Group provide vertical conduits into the overlying Barnett Shale. Hydraulic fracturing may open these zones of weakness resulting in a well that produces large quantities of water. For this reason, mapping karst, joints, and fault "geohazards" in the Ellenburger Group is an important precursor to successful Barnett Shale completion.

Karst-related fractures are common in the upper Ellenburger (Kerans, 1989). Tectonic faults can serve as conduits for meteoric fluids that water circulation which favor subsequent dissolution (Loucks, 2008). Preferential dissolution along intersecting joints and faults, give rise to elliptical collapse features (Sullivan et al., 2006). Although karst is usually associated with meteoric waters, "bottoms-up" karst (i.e. hydrothermal alteration) can also occur (Sullivan et al., 2003). Operators have found copper mineralization in at least one Wise Co. well. Mineralization of Mississippi lime fractures are common in Osage Co., OK, and commercial exploitable Mississippi Valley Type

lead-zinc deposits occur further east in the tri-state area of Oklahoma, Kansas, and Missouri (Leach, et al., 1993). Sullivan et al., 2006; Elibiju et al., 2009; Khatamadi et al., 2013 provide evidence of basement-controlled faulting, hydrothermal mineralization, and collapse chimneys in the Fort Worth Basin. We expect similar mineralization and bottoms-up karst within our study area.

DATA CONDITIONING

A 3D seismic acquisition program was undertaken in 2006 by Marathon Oil Co. using 16 live receiver lines forming a wide-azimuth survey with a nominal 55 by 55 ft CDP bin size to image the Barnett Shale at approximately 3000 ft TVDSS or 0.7 s TWT (Roende et al., 2008). Although data quality is excellent, minor improvements through post stack data conditioning can significantly facilitate and improve subsequent interpretation. Our post-stack data conditioning workflow is shown in Figure 4.3a. This workflow contains two major steps: the first step is application of principal-component structure oriented filtering (SOF), and the second step is spectral balancing. Figure 4.3b indicates general steps of principal-component structure oriented filtering (SOF). We can create a single waveform which best fits with each original seismic trace (step 1-2, Figure 4.3b). The waveform is best coherent wavelet that fix each trace by the approximate scale which calculates from the best fit waveform and each trace. The lateral variation of the amplitude along structural dip is called the eigenvector $v^{(1)}$. One can take derivatives of this eigenmap. Such derivatives will be the input for subsequent calculations of "amplitude curvature". Figure 4.4 shows the spectrum for the entire survey before (a) and after (b) and a representative seismic line before (c) and after (d) the data conditioning workflow. A common spectral balancing approach is to estimate the coherent (signal)

part of the seismic trace as that which cross-correlates with neighboring traces. We estimate the coherent part of the seismic trace using two passes of a 9-trace structure-oriented filter. To minimize the risk of impact of removing geology, we then apply a single time-variant spectral balancing operator to the entire volume. Note that low amplitude but "annoying" cross-cutting migration noise is suppressed, fault and karst edges are preserved. This data conditioning routine, which focuses on spectrum broadened so that improve the resolution within the thin Barnett Shale.

KARST ON ATTRIBUTE TIME SLICES

Seismic amplitude

Seismic amplitude is the most common "attribute" used in seismic interpretation. If a geologic feature is not measurable by seismic amplitude and phase, no derivative attributes will enable identification. In Figure 4.4 (c) and (d) we see two strong reflections representing the top of Marble Fall and the top of Ellenburger. The organic-rich Barnett Shale is located between these two units (Figure 4.1). Three karst collapse features are recognizable on this section. The largest karst doline is visible along the margins of a fault, and two smaller compaction-induced sagging are situated some distance away from any faults. Below the top of the collapses, within the Ellenburger, and below collapse features, rapid changes in reflector dip, a decrease in continuity, and a decrease in frequency are seen. Figure 4.5 shows a time slice at t=0.750 s from the seismic amplitude volume. Red arrows indicate faults that are better delineated by attribute processing. However, note that the larger karst dolines features indicated by the yellow arrows are clearly seen within the traditional amplitude volume. This appearance is our first example of "mixed" attribute response. That is, the elliptical features are not a function of lateral

changes, but rather lateral change in reflection time, or dip, resulting in the onion-ring. The green arrow marks a smaller karst features that is to be seen in seismic amplitude slices.

Structural dip

A major characteristic of karst collapse is their bowl-shape appearance with strongly dipping sides. Figures 4.6a-d show time slices at t=0.750 s for apparent dip components at 0°, 45°, 90° and 135° from north. Figure 4.7 shows mathematical model in defining reflector dip. Figure 4.8a shows their corresponding dip magnitude while Figure 4.8b illustrates the dip azimuth modulated by dip magnitude using a 2D color bar. The larger karst collapses (yellow arrows) and the major faults (red arrows) exhibit high dip anomalies. Very subtle flexures and joints are best illuminated by the apparent dip component perpendicular to them. As observed on Figure 4.6a-d, large bowl-shape karst collapses features are coincident with large faults with laterally extensive damage zones. The red dashed lines in Figure 4.8a and b, suggest that these large karst collapse features are structurally laterally linked by faults or joints, giving rise to what many interpreters refer to as a 'string of pearls' (Schuelke, 2011). We interpret the features indicated by the blue arrows to be eroded valleys or cave collapses depended on Kerans paleocave models (Kerans, 1988, 1989, 1990). Other low magnitude anomalies (green arrows) are likely smaller scale karst features that are relatively distal to the major fault zones. Orange arrows indicate a relatively rugose surface that is free of large collapse. This rugose area is south way extension while karst collapse features are north way extension (it will be shown on Figure 4.17) and the interface between the top Ellenburger and the lower Barnett Shale is shallow at south way.

Correlating the dip magnitude, azimuth attribute time slice (figure 4.8) to apparent dip components (figure 4.6), reveals collapse features that are expressed as steeply dipping edges which in this image appear as black ellipses. While the components of vector dip are useful for interpretation, they also serve as input for other attributes. Reflector curvature, rotation, and convergence are directly computed from vector dip, while coherence, amplitude gradients, textures, and structure-oriented filtering are computed along vector dip.

When reflectors are horizontal, displays of azimuth calculations are understandably fruitless. However, to overcome this limitation we propose modulating dip azimuth by dip magnitude using a 2D color bar as shown in Figure 4.8b. Here, the broad magenta (NE) and green (SW) bands indicate rotation about the major normal faults cutting the survey. The dissolutional caves are "brighter" with a radial pattern mimicking the 2D color bar indicating the reflections are dipping into the collapse features.

Additionally, although these faults (no. 1-4) exhibit a similar orientation, they are of different scales in dip magnitude (figure 4.8a), and they are of different anomalies in apparent dip (figure 4.6a-d) and dip azimuth (figure 4.8b). That is because the fault (no. 4) has opposite hanging wall and footwall position (this difference can be proved by time-structure map in figure 4.20). We interpret these faults to have been caused by the same normal geologic stress, but perhaps cutting different lithologies, giving rise to different patterns on the left and right areas of the time slice.

We zoom in on two zones of interest seen on the dip magnitude time slice in Figure 4.9a and display them in Figures 4.9b and 4.9e. We then draw two profiles that cut the collapse and fault features of interest and display line BB' in Figure 4.9c and line

CC’ in Figure 4.9d. Line BB’ (Figure 4.9c) crosses a major fault (red arrow), two large scale karst collapse features (yellow arrow) and a channel-like collapse feature (blue arrow). Line CC’ (Figure 4.9d) crosses three large scale karst collapse features and a major fault. The karst and channel-like collapse features exhibit synclinal cross sections at both the Top Marble Fall and the Top Ellenburger. Light green arrows indicate a bright spot anomaly under the largest karst collapse feature, which we interpret to be due to infill with lower impedance, perhaps fractured or brecciated material. Green arrows in Figure 9e indicate small scale karst collapse features which exhibit less bright basal reflections in Figure 4.9g. Not all karst collapse features exhibit bright bottom reflections, suggesting heterogeneity in their fill.

Coherence

Karst not only gives rise to changes in reflector dip and azimuth, but also to changes in the seismic waveform continuity. We use vector dip as input for principal-component (structure-oriented) filtering in the most coherent window, which represent lateral amplitude variation, to constrain random and coherent noise and improve vertical resolution (Marfurt, 2006). Figure 4.10 shows a time slice through a coherence volume computed by taking the ratio of the energy of a principal-component (structural-oriented) filtered data based on the workflow shown on figure 4.3b to the energy of the original data. Comparing this image to the previous image of reflector dip we note that the faults (red arrows) and large collapse features (yellow arrows) do appear somewhat weaker. Since coherence is computed along structural dip, this implies that there is small offset ($< \frac{1}{4} \lambda$) and only small changes in waveform across the edges of the collapse. Low coherence and high dip magnitude at yellow arrows indicates that this incised valley has

little offset along its flanks. Where examining vertical slices time through the amplitude data (Figure 4.4c and 4.4d), note the dissolution within the Ellenburger is significantly less at *t*=0.7 s at the Barnett Shale level, with the shale layers simply draped over the collapse feature. Similarly, the blue arrows indicates karst valleys, which are not as well-defined as those observed in the dip magnitude volume. We conclude that these large collapse features are coherent in lateral amplitude or waveform however their laterally variable dip is best imaged using coherence. Orange arrows indicate incoherent, rugose eroded surfaces that are free of large collapse features which suggests lithology changes from southwest to northeast. These incoherent surfaces do not appear to be fault controlled. Green arrows indicate small karst features.

Spectral decomposition

Lateral changes in layer thickness and impedance produce lateral variation in spectral components. Karst related diagenetic products generate lateral changes in porosity, and from limestone to dolomite (Lucia, 1995). In our study area, dissolutional collapse features within the underlying Ellenburger Group generate small faults (< ¼ λ) and fractures in the overlying Barnett Shale, reducing velocity and acoustic impedance and in turn can resulting lateral changes in tuning thickness. Chaotic collapse features and rugose surfaces give rise to nonspecular scattering, with constructive interference at low frequencies and destructive interference and at high frequencies, thereby shifting the spectra lower. Figures 4.11a shows a time slice at t=0.750 s through the peak spectral magnitude volumes computed using a matching pursuit algorithm described by Liu et al. (2007). Peak frequency magnitude attribute is highest energy level shown as magenta part on figure 4.4a and 4.4b. Note the improved resolution of the peak spectral magnitude in

illuminating the dissolutional cave edges and internal discontinuities. Blue arrows indicate suspect paleo-valleys or collapsed paleocaverns that are revealed low spectral magnitude. Orange arrows indicate large karst features which were identifiable using previously described routines (Figure 4.10).

Peak frequency and peak phase are meaningful if the corresponding magnitude is above the noise level. If so, we suggest using magnitude to modulate these images (Figure 4.11b). Note the shift to low values of peak frequency (magenta to red) above collapse features, which represents the destructive interference at the higher frequencies. The high frequencies (cyan to blue) record thinner layers in the Barnett Shale (low magnitude). In figure 4.11b, the orange arrows point to low frequency features which correspond to rugose surfaces as shown in coherence attributes (figure 4.10) and peak magnitude attributes (figure 4.11a). Given the rugose nature of this surface, time slices through the peak phase spectrum provide only limited interpretational value.

Structural curvature, reflector rotation and reflector convergence

Structural curvature is computed by taking the derivatives of the dip components as shown in Figure 4.6. As such, we expect curvature to highlight joints and fractures characterized by more subtle, longer wavelength joints and flexures. Reflections that exhibit similar waveforms, that is, those having small offset ($< \frac{1}{4} \lambda$), and subtle changes in dip across faults will generate curvature, but not coherence anomalies (Al-Dossary and Marfurt, 2006). The amplitude of the curvature anomaly is inversely proportional to the radius of curvature at each voxel, with negative values indicating synclinal, and positive values anticlinal deformation (Figure 4.12).

Figures 4.13a and b contrast the most-positive and most-negative structural curvature along the same time slice. In this survey, the major faults are expressed by a positive curvature anomaly across the footwall which is laterally offset from a corresponding negative curvature anomaly across the hanging wall. This "curved" appearance is commonly observed in 3D seismic volumes of carbonate terrains associated with conjugate faults, which are below seismic resolution and are morphologically similar to those described by Ferrill and Morris (2008). The dip magnitude and coherence anomalies fall between the two curvature anomalies. In this image (figure 4.13), the bowl shaped collapse features express a negative value and appear as blue ellipses (yellow and green arrows). The rugose surface (orange arrows) is a product of a shorter wavelength and indicates less deformation. Yellow polygons enclose an area where large collapse features are coincident with high-angle normal faults. The dissolutional caves zone is coincident with through-going faults that tip-out in the such-and-such Formation. The fault damage zone consist of fractures and small scale faults shown as small red lines on most positive curvature and blue channels crossed between faults and karst. In order to visualize the relation between karst and faults, we co-render most positive and most negative curvature with dip magnitude (Figures 4.13c and d). The dip magnitude attribute accurately maps the location of faults and karst boundary while the shape of karst features and more-subtle faults are confidently mapped using curvature attributes. Examining figures 4.13c and d, note that the large karst features appear fault-controlled and are cut by smaller faults or joints. These smaller-scale features may record compaction-induced fracturing across paleocavern roofs similar to that described by Kerans (1989 and 1990). Additionally, reflector rotation and convergence computed from the curvature dip

components (Marfurt and Rich, 2010). Reflector rotation (figure 4.14a) shows a strong NW-SE succession of lineaments, which are strongly aligned and nearly perpendicular to NE-SW trending faults. Co-rendering reflector rotation with dip azimuth as shown in Figure 4.14a reveals a strong correlation between rotation and inferred karst anomalies. We cannot say without further analysis and outcrop analogues whether this "rotation" is a cause or an effect of the karst features. Interpretations based solely on reflector-vector convergence attributes provides ambiguous results. However, when co-rendered with dip magnitude (Figure 4.14b) we recognize that strongly convergent areas correspond to areas characterized by a greater density of faults and karst features. The varying strike of the faults and the elliptical nature of the karst give rise to a complex, but easy to interpret image.

Amplitude gradients

If we use a lateral 3 by 3 trace by *n* sample analysis window, a principal-component (Structure-Oriented) filter produces a lateral pattern (or 3 by 3 eigenmap) that best represents the lateral variation seen in each of the *n* vertical amplitude slices. Such filters were used in the structure-oriented filtering described in Figure 4.3 and Figure 4.4. Figure 4.15 is the coherent energy attribute which it the energy map of the filtered data. Computing the energy with an analysis window (±10ms), we show in Figure 4.16 the display gradient of coherent energy at 0°, 45°, 90° and 135°. The amplitude gradient is simply the derivative of this eigenmap, weighted by its energy. Coherent energy gradient maps can be quite effective for identifying faults and fractures, and can provide constrains for mapping channels which can be emphasized using lateral changes in tuning (Marfurt, 2006). Like apparent dip, amplitude gradients can be calculated at any azimuth (Figure

4.6a-d). Overlaying amplitude gradient maps with the coherent energy gives results in a suite of images that simulates shaded illumination, but of energy, not of time-structure. For example, note the shorter wavelength variation of the amplitude gradient images in Figure 4.16 compared to the structural dip images in Figure 4.8a. Yellow arrows on figure 4.8a indicate high dip anomalies which are well-defined on gradient maps of coherent energy (Figure 4.16). Lateral variations related to lithologic changes are generally greater identified than those in dip. Large faults and karst are seen in both amplitude gradient and structural dip images. Amplitude gradients are computed along dip, which eliminates dip variability. Such correlation provides independently derived and mutually supportive evidence that the imaged features are likely karst and faults. For Figure 4.16, the green arrows mark small-scale karst and the blue arrows indicates channel-like dissolutional features, these dissolution illuminate as caves and eroded zones on gradient of coherent energy (Figure 4.16), but show as points and discontinuities on coherence (Figure 4.10).

Amplitude curvature

Whereas structural curvature is a derivative of structural dip, amplitude curvature is computed by calculating the derivative of varying amplitude gradients. Figures 4.17a and b show the most-positive and most-negative amplitude curvature derived from high-resolution amplitude gradients. With the exception of the dip compensation in the structural curvature computation, the size and the values of both curvature operators are exactly the same. On Figure 4.17a and b, the yellow dashed lines zones indicated complex fault-controlled karst features with fracture system. Fewer fractures and karst are developed in the areas far away from fault zones. Figure 4.17c and d are the same

way co-rendered with dip magnitude to highlight karst and better show the relationship between faults, joints, and karst.

Compared with structural curvature, amplitude curvature delineates several previously overlooked, small circular features in the southern part of the survey where the time slice cuts below the top Ellenburger Dolomite (Figure 4.18a). Zooming in (Figure 4.18b) we draw several vertical lines through the seismic amplitude map and display them in Figures 18c-f map. The small radius amplitude curvature anomalies appear as bright spot anomalies on the seismic section. Several of them exhibit the "string of pearls" pattern (green arrows on Figure 4.18c-e) suggesting they are fault controlled. Those vertical karst anomalies within the Ellenburger have a nearly identical appearance to infilled karst collapse features widely seen in the Tarim Basin, China (Feng .et. al., 2012, Liu et. al., 2012, and Chen et. al., 2011). In the Tarim Basin, the collapse features are filled with Aeolian sands, and form excellent oil and gas reservoirs. These subtle karst collapse features within the Ellenburger have a very different morphology from those that cut the Ellenburger and continue into the overlying Barnett Shale and Marble Falls Formations seen in Figures 4.9 and 4.18d. These subtle karst caves appear to be restricted within the Ellenburger and do not significantly alter the base of the Barnett Shale.

Figure 4.18f shows a subtle collapse-caused fault in seismic section view. The left blue arrow indicates a curved, but continuous feature, while the right blue arrow indicates finite displacement along a small fault. Figures 4.19a-d show the subtle faults on different attributes. Notice that dip magnitude, most-positive and most-negative amplitude curvature can detect two kinds of anomalies (blue arrows) at the edges of this subtle

collapse-caused faults; however coherence can only detect the discontinuity associated with the faulted edge.

KARST ON ATTRIBUTE HORIZON SLICES

Conventional interpretation is based on mapping faults and horizons. While faulted horizon are difficult and time consuming to interpret, karst surfaces are particularly tedious for the interpreter, because of their discontinuous character, high rugosity, etc. As with any unconformity, auto-trackers fail when the overlying strata juxtapose lateral changes in impedance. Interpreting karst topography is exceedingly difficult as the unconformity frequency cross-cuts strata with different and admixed lithologies characterized by highly variable impedance. Where conventional 3D interpretation fails, incorporation of horizon slices from attribute volumes provide an increasingly valuable alternative method for interpreting complex stratigraphic features, such as karst.

Figure 4.20 shows the time-structure map at the top Ellenburger Group co-rendered with a representative vertical slice through the seismic amplitude volume. The structure map shows increased rugosity of the surface towards the south. Figures 4.21a and b show a horizon slice through the most-positive and most-negative curvature volumes. Dashed yellow lines indicate fault-controlled karst within the Ellenburger Group. Figures 4.21c and d show the same horizon slices through the curvature column co-rendered with a horizon slice through the coherence volume shown previously in Figure 4.10. Black anomalies indicate discontinuities (faults, joints, and karst), the latter of which correlate to red most-positive curvature and blue most negative structural curvature anomalies.

Figure 4.22 shows similar horizon slices, but now through the amplitude curvature volume. As seen previously on the time slices, the amplitude curvature varies more

rapidly laterally, likely indicating changes in impedance interpreted as variations in diagenetic alteration. Figures 4.22a and b show most-positive and most-negative amplitude curvature. Although these images are similar to Figures 4.21a and b, they indicate different concepts. The blue in the structural curvature indicates anomalously low structure, while the blue in the amplitude curvature indicates anomalously low amplitude. Thus, we observe lower reflectivity inside the structurally low collapse features, which likely results from anomalous attenuation and/or scattering.

CONCLUSIONS

Karst, faults, and joints are known form geologic hazards for most Barnett Shale wells in the Fort Worth Basin. In the best cases, these drilling-related "geohazards" from conductive features that draw off expensive hydraulic fracturing fluid from the targeted shale formation. In the worst cases, the completed wells are hydraulically connected to the underlying Ellenburger aquifer and produces large amounts of water with little hydrocarbon. 3D seismic data are routinely acquired to map such geohazards prior to spudding. Such information should be presented during interdisciplinary, pre-spud meeting to alert the drilling and completion engineer of potential difficulties before finalization of the drilling and completion program.

Karst collapse generate a distinct morphologic pattern on 3D seismic data. When plotted using a gray scale, karst dolines appear on coherence and dip magnitude time slices as characteristically circular to elliptical features, which provide a karst "fingerprint". In this and many other surveys in the Fort Worth Basin, the karst are strongly correlated with fractures and joints, which in turn are clearly rendered on coherence and most negative curvature images. The chaotic nature of reflectors internal

to the karst features, such as paleocavern fill, often result in low frequency anomalies. The loss of higher frequencies has two possible causes: the existence of fluid filled fractures and cracks within the karst collapse features giving rise to intrinsic attenuation, and scattering from the chaotic infill giving rise to geometric attenuation. In this survey area, and throughout much of the Fort Worth Basin, wells that penetrate karst features or coincident fault and fracture system will produce water from the Ellenburger Group and thus, are not intentionally drilled.

Reflectors dip into the collapse features giving an inward radial display when dip azimuth is plotted against a cyclical-color bar. Vector convergence shows the complementary image, with reflectors converging outward towards the collapse edges. Reflectors at shallower levels in the Barnett Shale and Marble Falls intervals also show down warping into the karst but with parallel (nonconvergent) bedding and near constant thickness, implying that the actual collapse took place long after these formations were deposited. At the shallow Pennsylvanian Age Caddo horizon the reflectors show strong negative curvature and dip magnitude anomalies, but no coherence anomalies, suggesting either delayed collapse or continued diagenetic alteration of the Ellenburger from below. Solution-enlarged joints and faults may remain partially open, or be filled with impermeable clays or preferentially cemented (Hardage et al., 1996). In either case, they will give rise to lateral changes in amplitude measured by amplitude gradients and amplitude curvature. Karst-related architectural elements dolines, paleocaverns, karst towers, solution-enlarged joints, and rugose topography can be inferred from attributes by integrating modern and ancient analog, thereby providing mutually supportive lines of evidence for a compelling interpretation.

Time slices through seismic attributes provide a rapid yet quantitative delineation of karst terrains, delaying and perhaps circumventing the need to carefully pick the top of the difficult-to-pick Ellenburger unconformity. Indeed, many areas covered by 3D seismic data in the Fort Worth Basin have few wells, where the engineers turn to less intensely karst areas to complete.

Interpreters often wish to know which attribute is “best” to delineate a given geologic feature of interest. We propose using mathematically independent attributes, coupled through the underlying geology, to provide a means of confirming or rejecting a given interpretation hypothesis.

ACKOWLEDGEMENTS

The authors would like to thank Marathon Oil for providing the data and key insight in the data analysis of this region. We also thank Mr. Jason Rush, Dr. Yonghe Sun, Dr. Sergio Chavez-Perez, and Don Herron for reviewing manuscript and providing supportive comments. Financial support and most attribute computation was supported by the OU Attribute-Assisted Seismic Processing and Interpretation (Consortium). Data display was done using Petrel software provided to OU for use in research and education.

a)

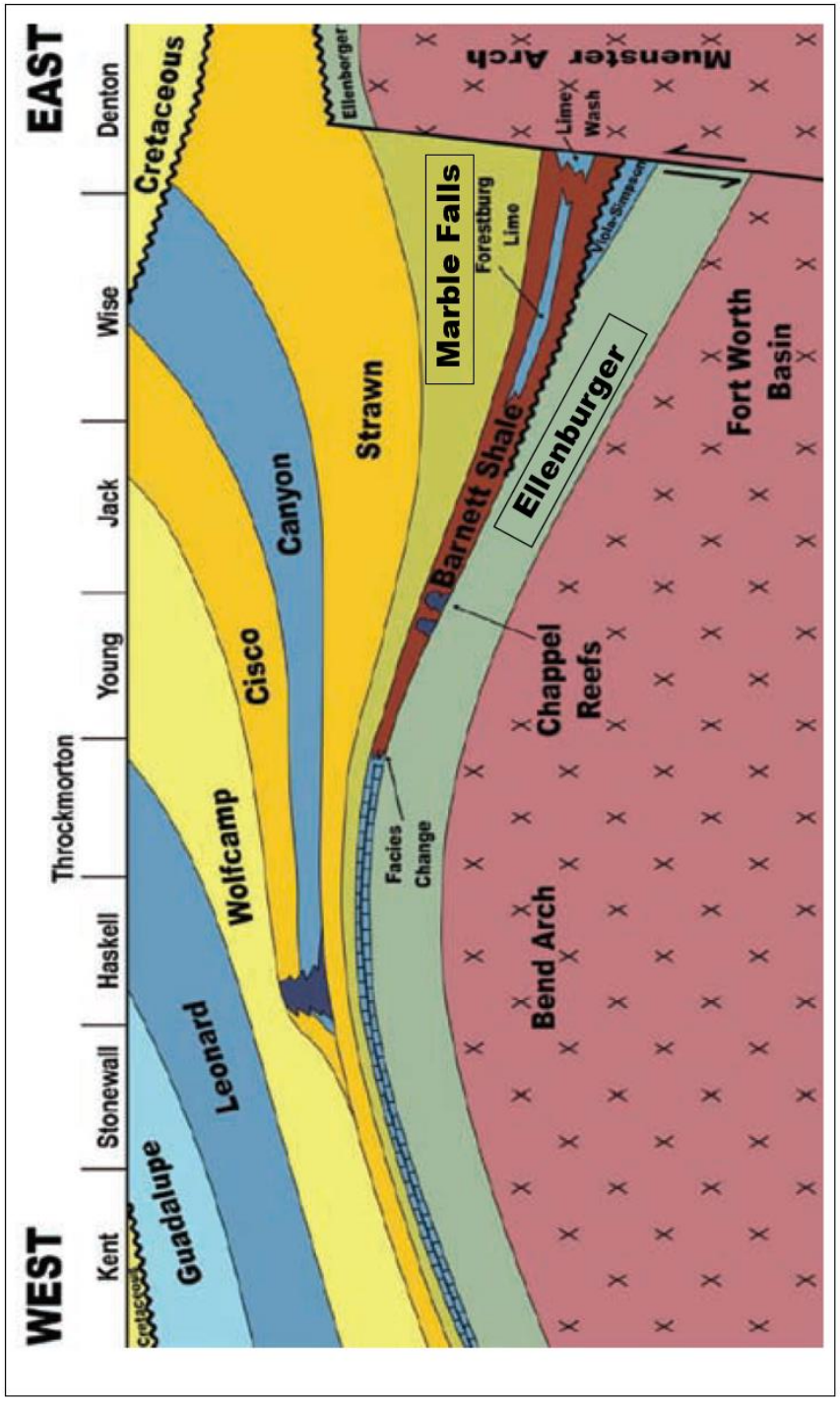
WEST
EAST
Kent
Stonewall
Haskell
Throckmorton
Young
Jack
Wise
Denton
Cretaceous
Guadalupe
Leonard
Wolfcamp
Cisco
Canyon
Strawn
Ellenburger
Marble Falls
Forestburg Lime
Barnett Shale
Ellenburger
Facies Change
Chappel Reefs
Bend Arch
Fort Worth Basin
Lime Wash
Viola-Simpson
Muenster Arch

b)

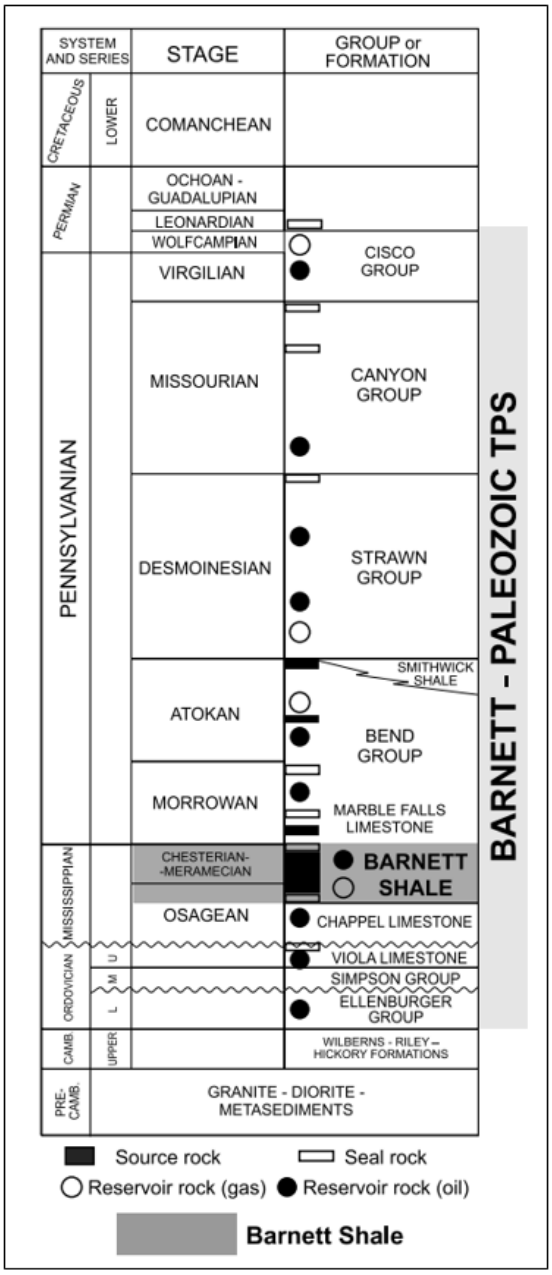

Figure 4.1 (a) Stratigraphic cross section and (b) stratigraphic column of the Fort Worth Basin. In the "core" study area of Wise and Denton Counties to the East, the Barnett Shale is subdivided into Upper and Lower units by the intervening Forestburg Lime. The calcite-rich geomechanical ductile Marble Falls and Viola Limestones from hydraulic fracture barriers. The Viola fracture barrier pinches out to the west, such that the Barnett Shale lies unconformably on top of the more brittle, dolomitic Ellenburger Group. The survey in the following figures is on strike with the area of Young County in this image (After Pollastro et al., 2009).

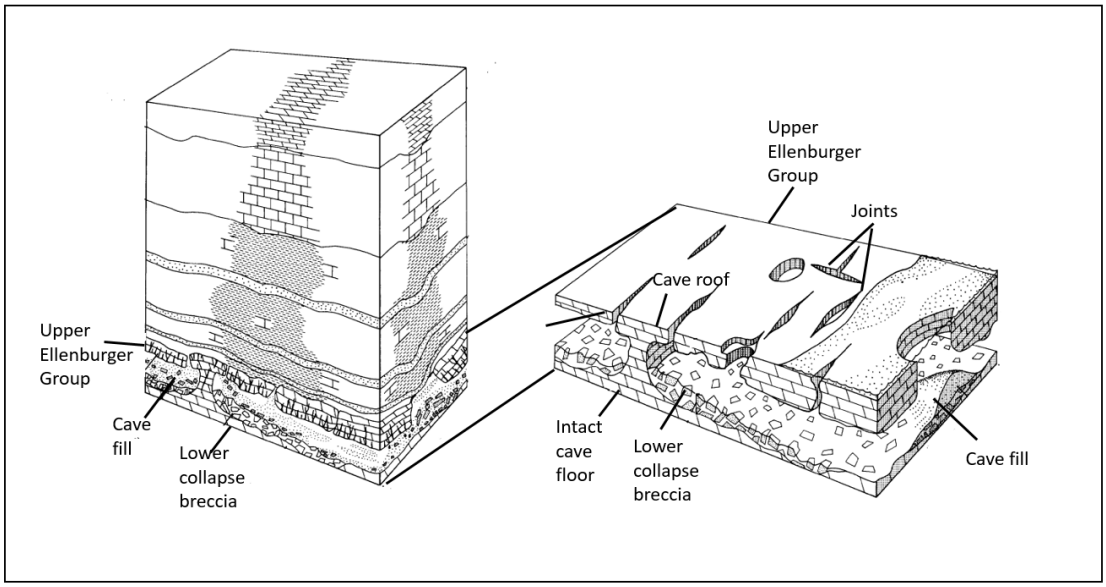

Figure 4.2 Genetic paleocave model for the Lower Ordovician of West Texas showing cave floor, cave roof, and collapsed breccia (modified after Kerans, 1988, 1989).

a)

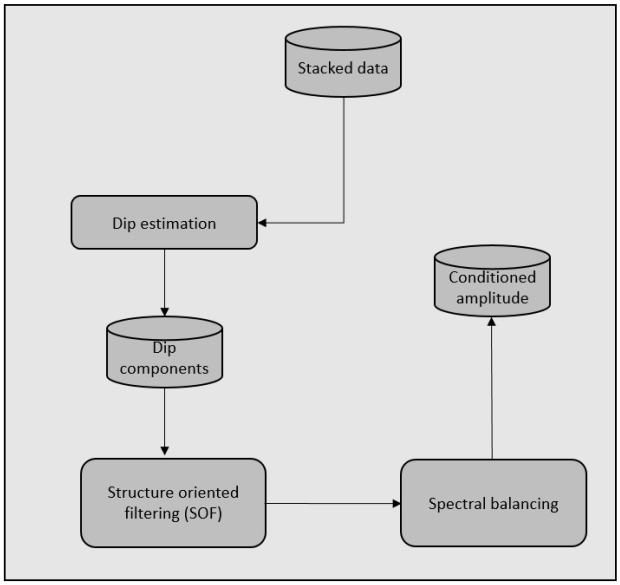

b)

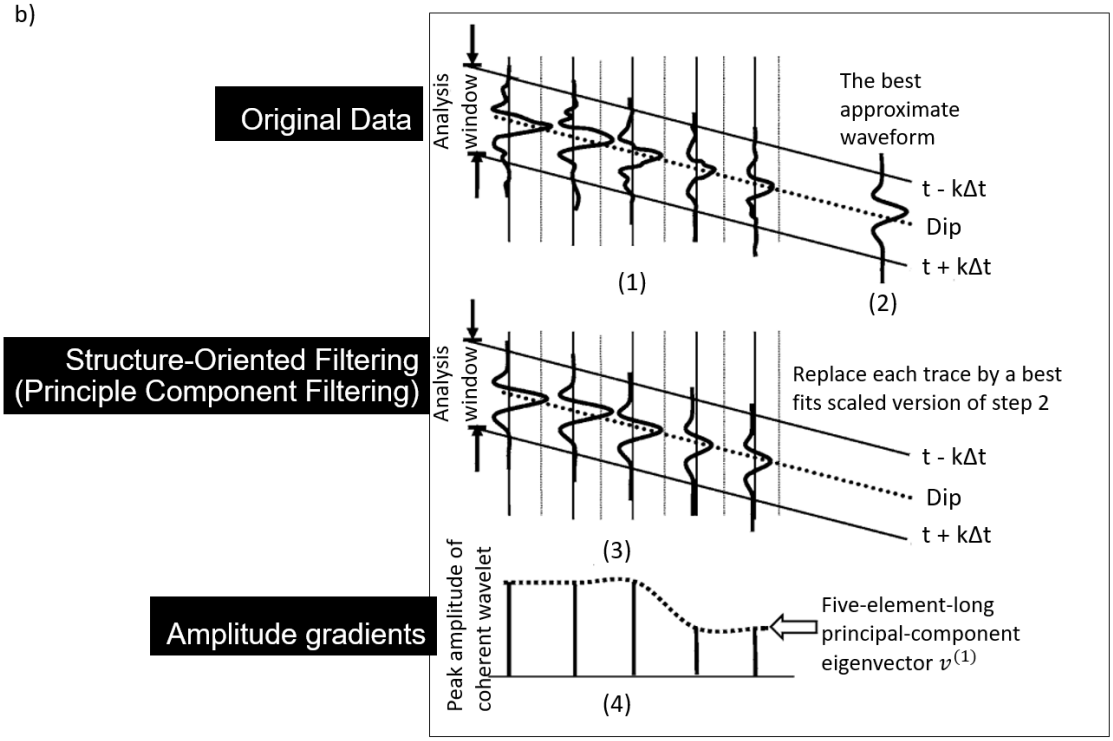

Figure 4.3 Workflow (a) to precondition the seismic data prior to attribute computation and (b) illustrating the steps for structure oriented filtering (SOF) based on principal component analysis (modified after Marfurt, 2006). The filtered seismic amplitude is then spectrally balanced using the average time-frequency distribution computed using a matching-pursuit spectral decomposition algorithm described by Liu et al. (2007).

a)

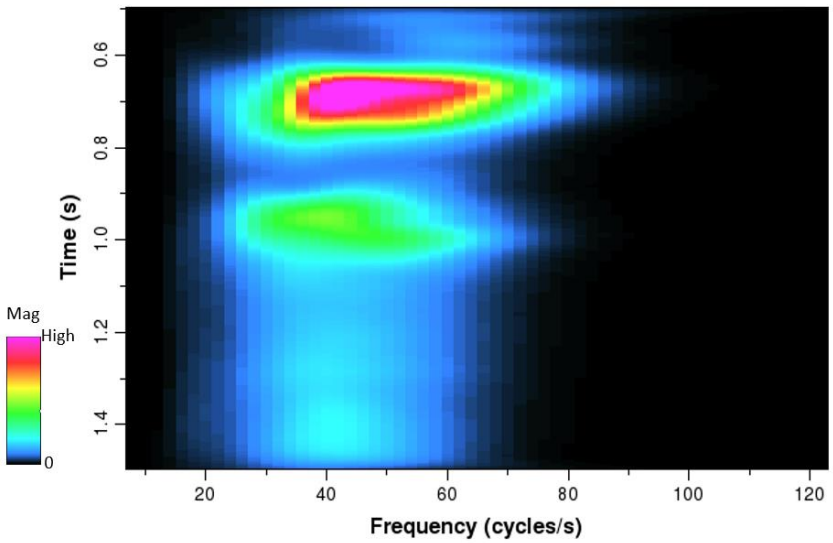
Time (s)
0.6
0.8
1.0
1.2
1.4
Mag
High
0
20
40
60
80
100
120
Frequency (cycles/s)

b)

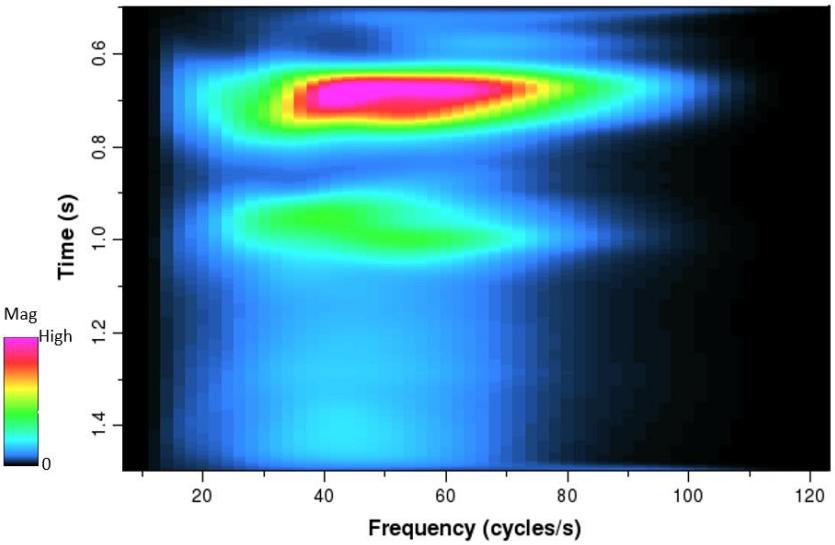
Time (s)
0.6
0.8
1.0
1.2
1.4
Mag
High
0
20
40
60
80
100
120
Frequency (cycles/s)

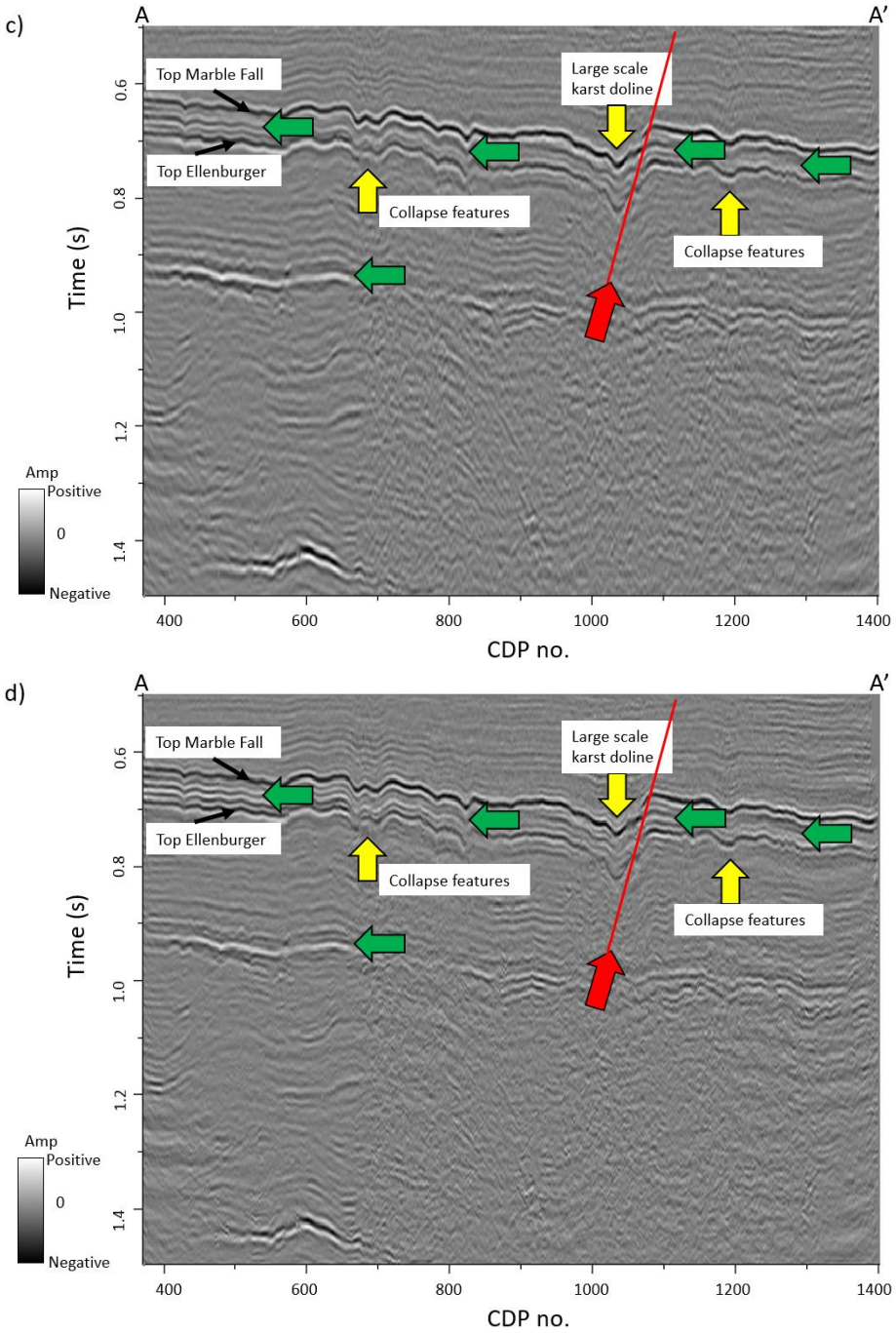

Figure 4.4 Average time-frequency spectrum for the entire survey (a) before and (b) after spectral balancing using a bluing factor of eβf where β=0.3. Note the increase in frequency content between t=0.6 and t=0.8 s. Line AA' (c) before and (d) after time-variant spectral balancing. Note the increase in frequency content within the target Barnett Shale interval between t=0.6 and t=0.8 s as well as the interval above top basement (green arrows). Red arrow indicates one normal fault, and yellow arrows indicate large scale karst dolines, collapse features.

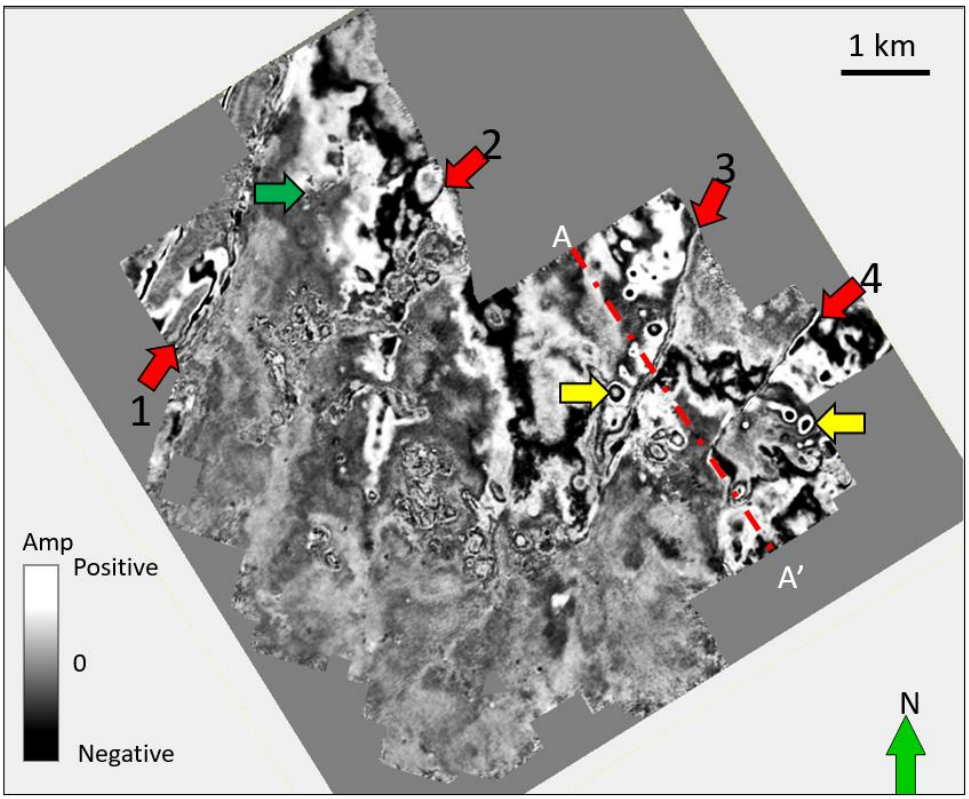

Figure 4.5 Time slice at t=0.750 s through the seismic amplitude volume at the approximate top Ellenburger horizon. Faults are indicated by red arrows. Large karst appears as circular features (yellow arrows). Smaller karst (green arrow) are less obvious but can also be seen. The location of line AA' shown in the previous image is indicated by the red dashed line.

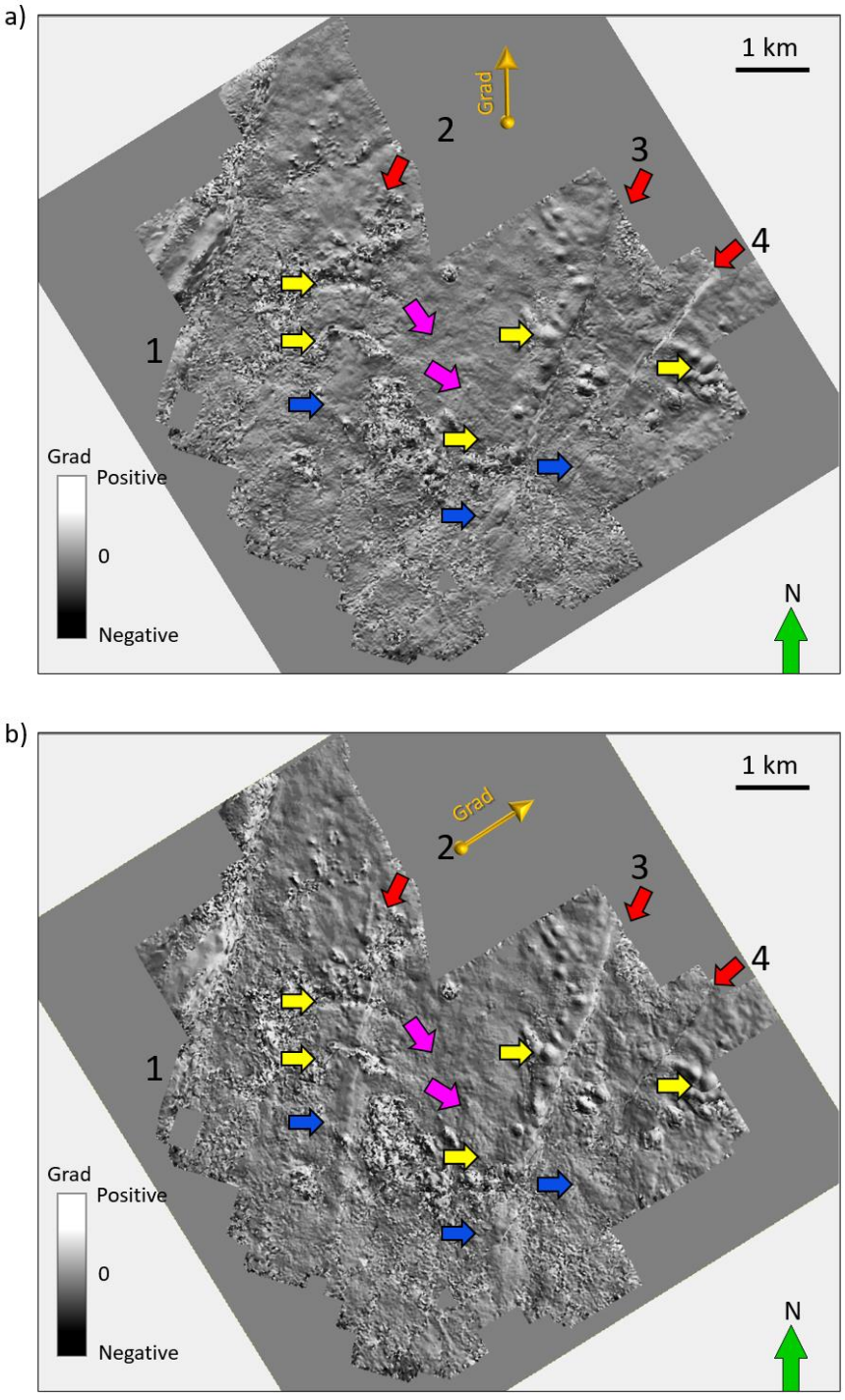
a)
1 km
Grad
2
3
4
1
Grad
Positive
0
Negative
N
b)
1 km
Grad
2
3
4
1
Grad
Positive
0
Negative
N

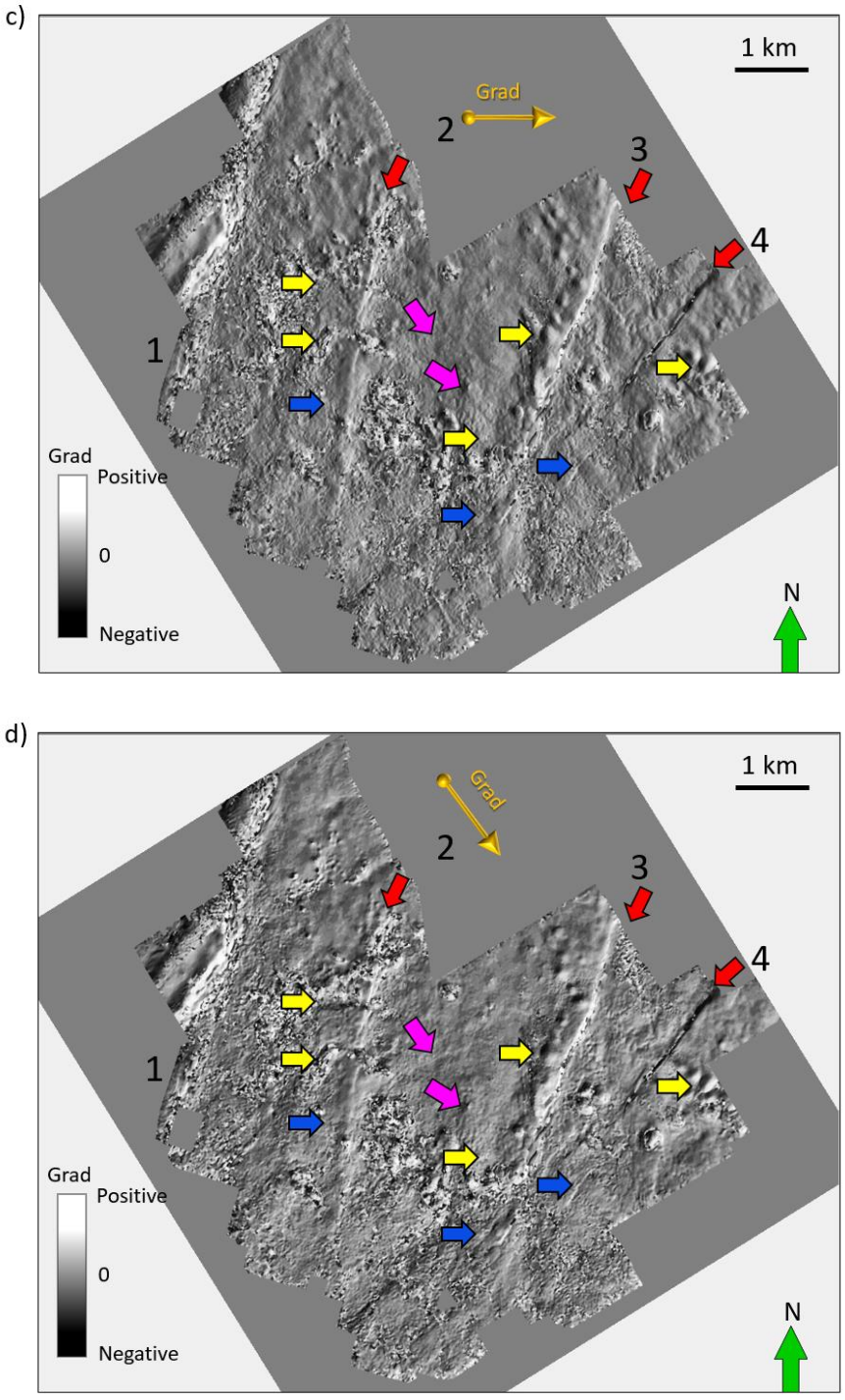

Figure 4.6 Time slices at t=0.75 s through apparent dip volumes at (a) 0˚, (b) 45˚, (c) 90˚, and (d) 135˚ from North. Yellow arrows indicate channels or cave collapse. Red arrows indicate major faults, while pink arrows indicate minor flexures and blue arrows indicate joints.

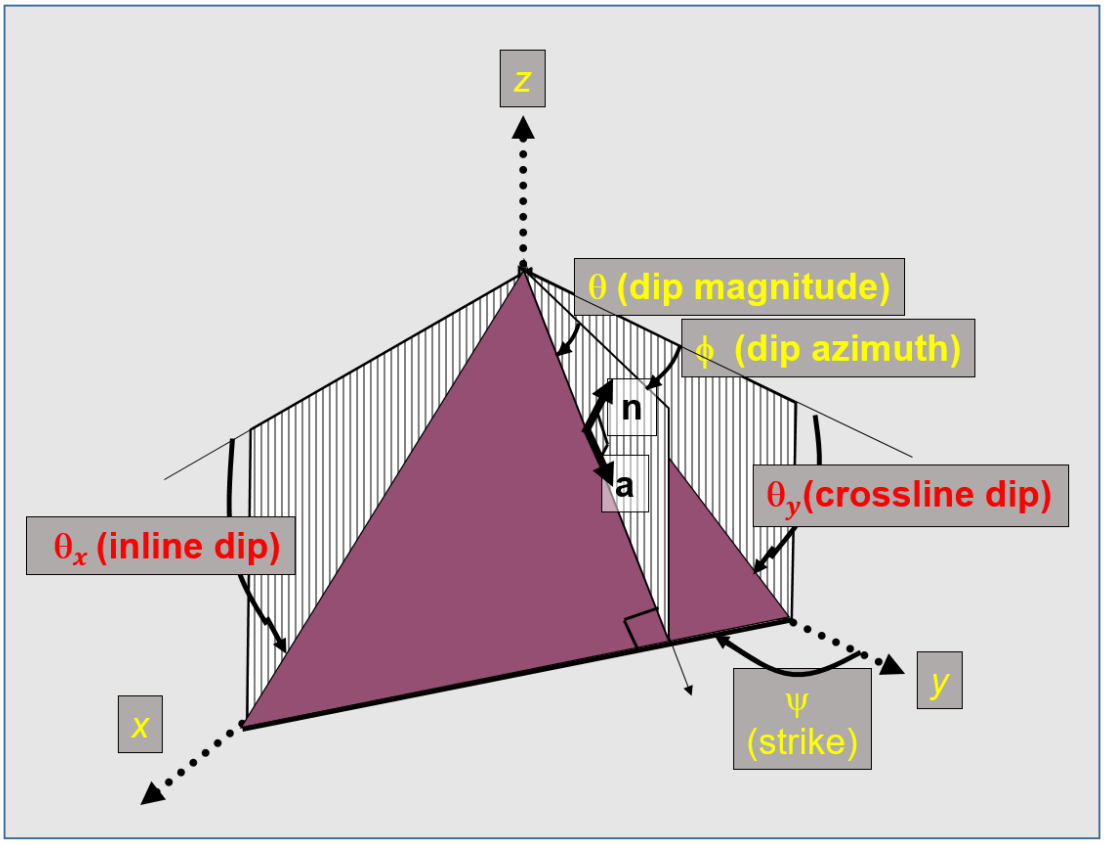

Figure 4.7 Mathematical model in defining reflector dip (modified after Marfurt, 2006). By convention, n = unit vector normal to the reflector; a = unit vector dip along the reflector; θ = dip magnitude; ϕ = dip azimuth; ψ = strike; θ_x = the apparent dip in the *xz* plane; and θ_y = the apparent dip in the *yz* plane.

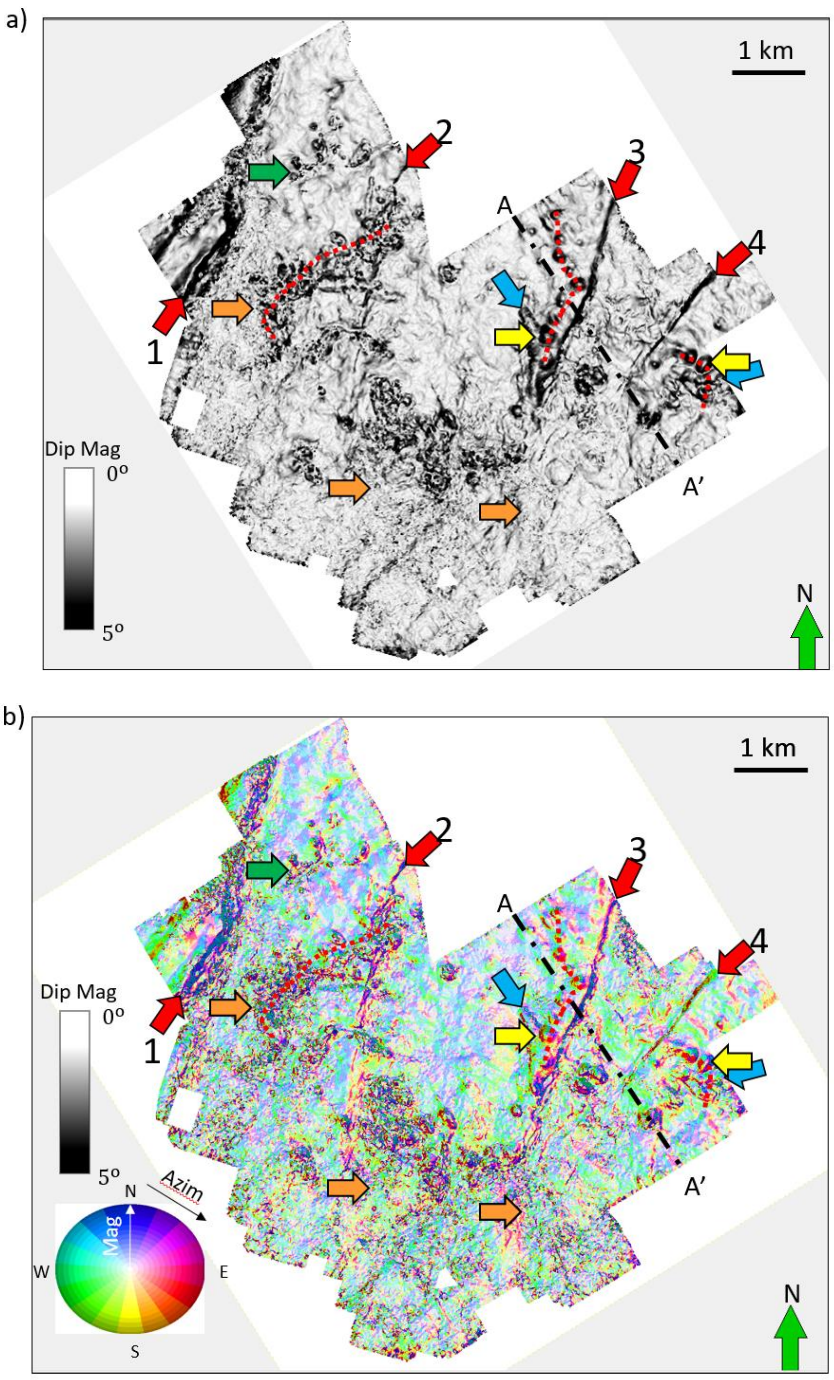

Figure 4.8 Time slice at t=0.750 s through (a) volumetric dip and (b) the dip azimuth modulated by dip magnitude using a 2D color bar. Red arrows indicate faults that control many of the larger collapse features. Dashed red lines show a "string of pearls" features which when correlated with most negative curvature indicates their control by diagenetically altered joints or faults with little vertical offset. We interpret the feature indicated by the blue arrows to be a valley or cave collapse, or channel-like collapse features. Green arrow indicates small scale karst that are far from major fault zones. Orange arrows indicate a relatively rugose surface that are free of large collapse features.

a)

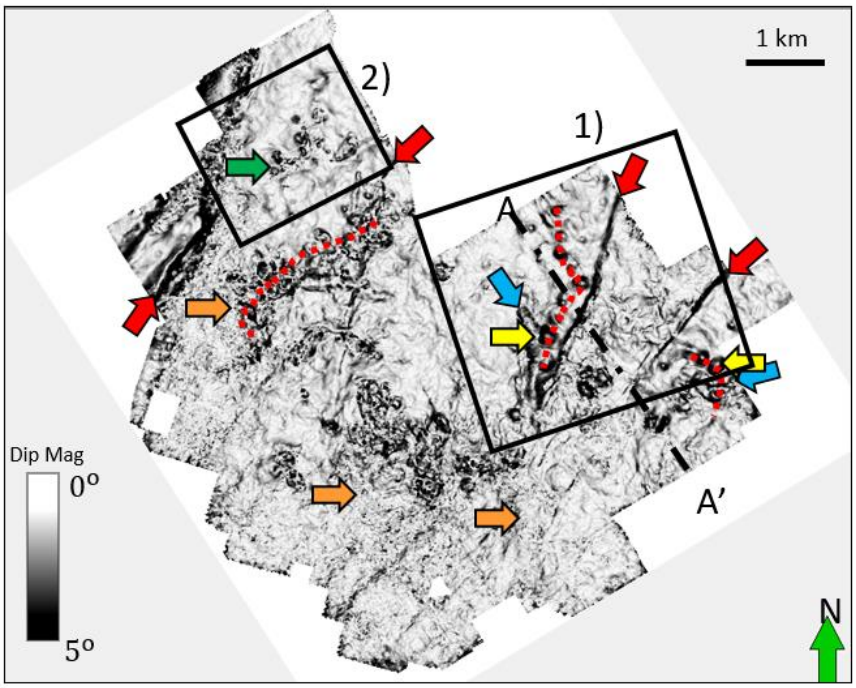

b)

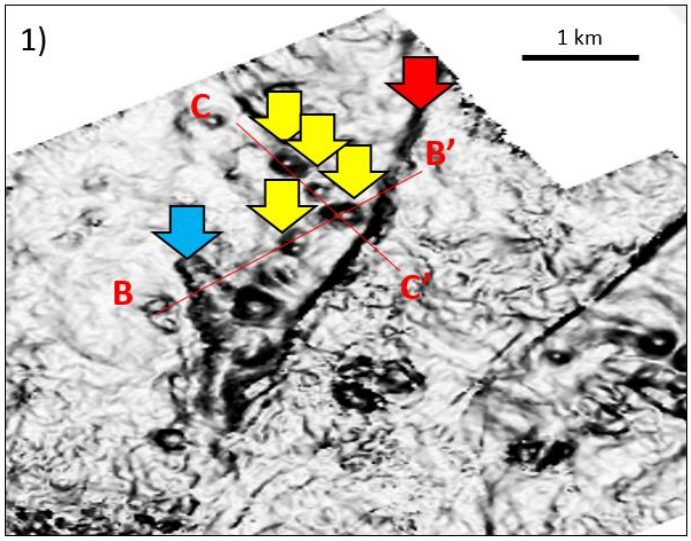

c)

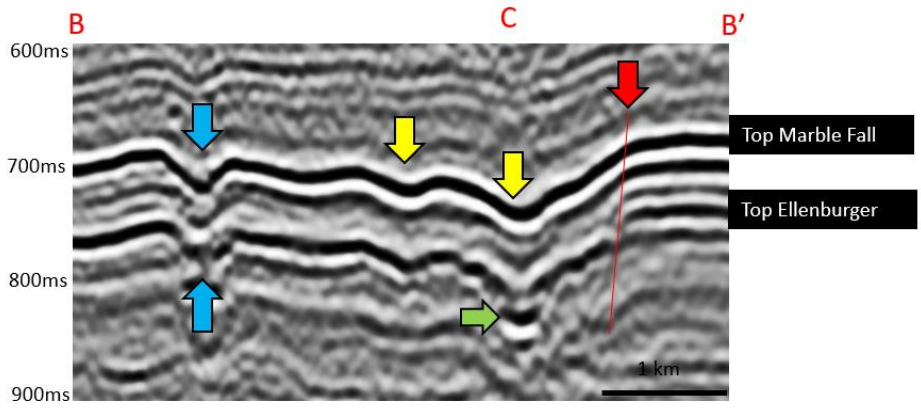
B
C
B′
600ms
700ms
800ms
900ms
Top Marble Fall
Top Ellenburger
1 km

d)

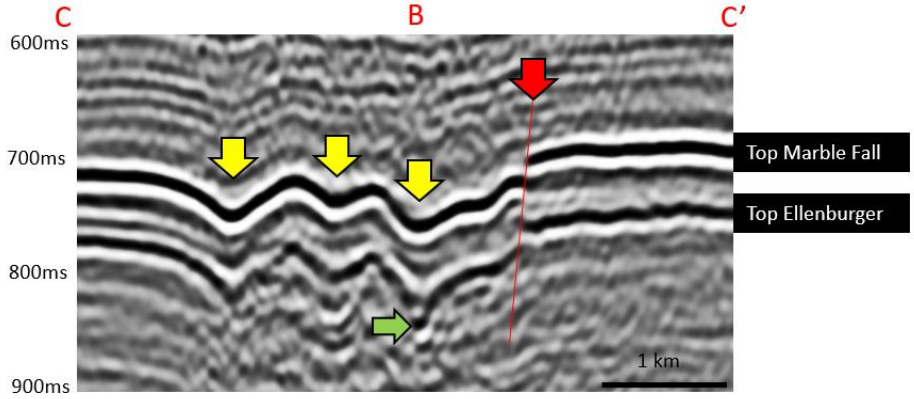
C
B
C′
600ms
700ms
800ms
900ms
Top Marble Fall
Top Ellenburger
1 km

e)

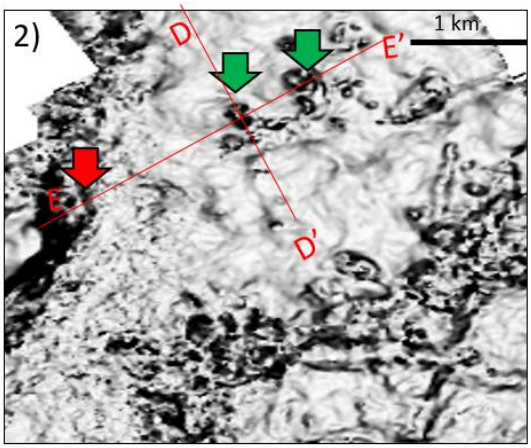
2)
1 km
D
E′
E
D′

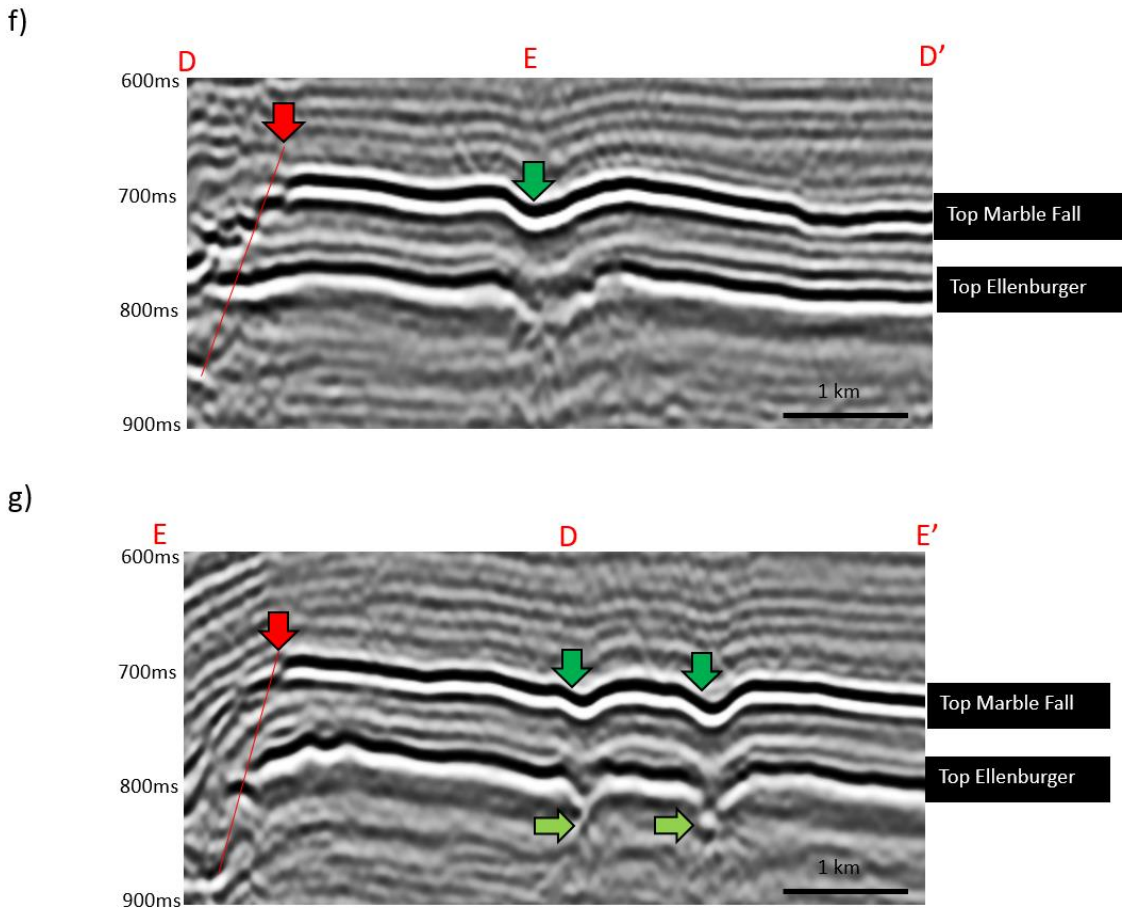

Figure 4.9 Time slice at t=0.750s through (a) volumetric dip, and (b) and (e) zoomed in zones. (c), (d), (f), and (g) are seismic section view of lines BB', CC', DD', and EE' show large scale karst collapse features (yellow arrows), major faults (red arrows), channel-like collapse features (blue arrows), and small scale karst collapse features. Notice that not all karst collapse features exhibit bright bottom reflections, suggesting heterogeneity in their fill.

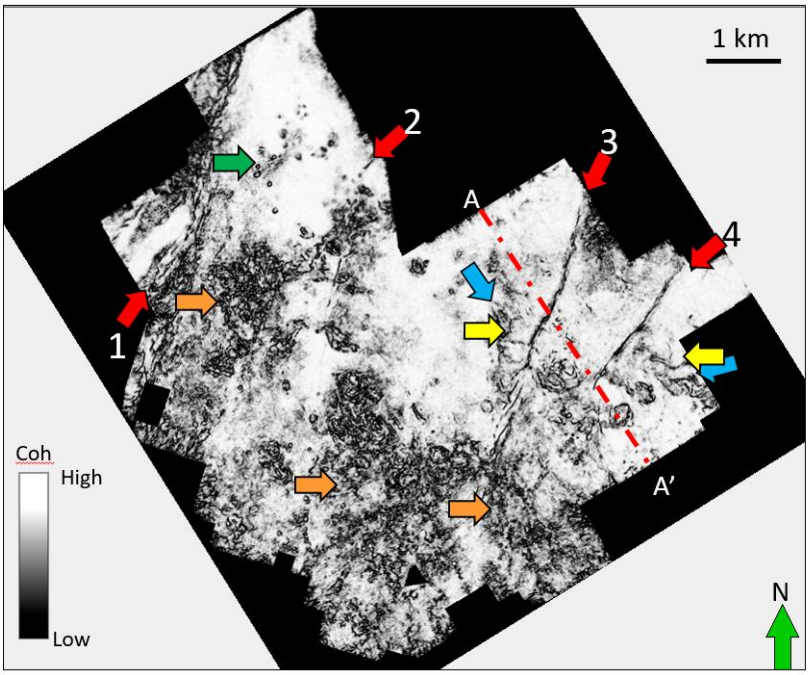

Figure 4.10 Time slice at t=0.750 s through eigenstructure-based coherence. Note that the faults (red arrows), channel-like collapse features (blue arrows) and large collapse features (yellow arrows) do not appear as strong as in the dip magnitude image. Orange arrows indicate incoherent, rugose surfaces that are free of large collapse features.

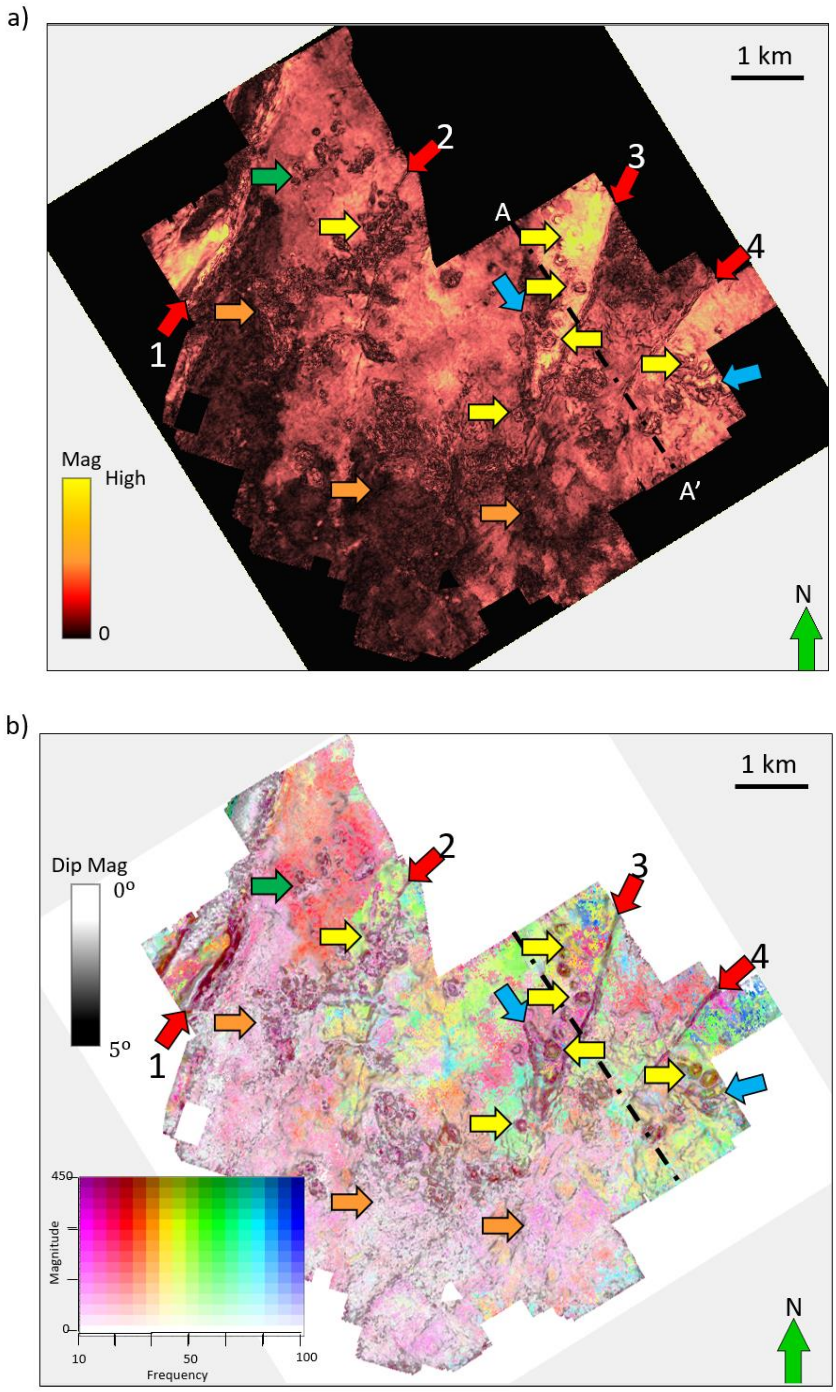

Figure 4.11 Time slice at t=0.750 s through (a) the peak spectral magnitude volumes computed using a matching pursuit algorithm described by Liu et al. (2007) and (b) peak magnitude and frequency modulated images co-rendered with dip magnitude image. Yellow arrows indicate large scale karst features. Red arrows indicate faults, blue arrows channel-like collapse and green arrow small karst shown on the previous image. Orange arrows indicate a relatively rugose surface that are free of large collapse features.

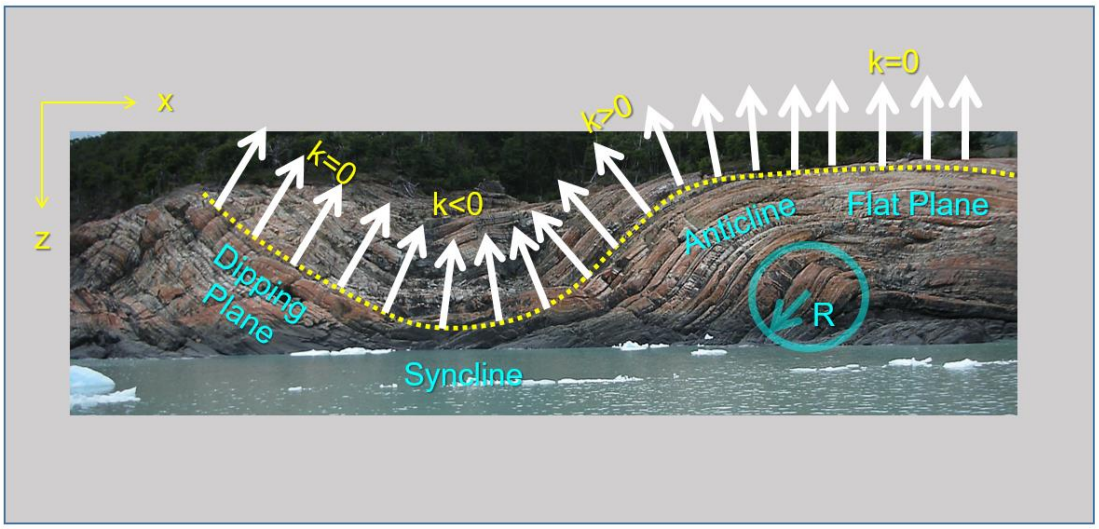

Figure 4.12 Curvature model shows curvature value change based on plane angle (modified after Marfurt, 2010).

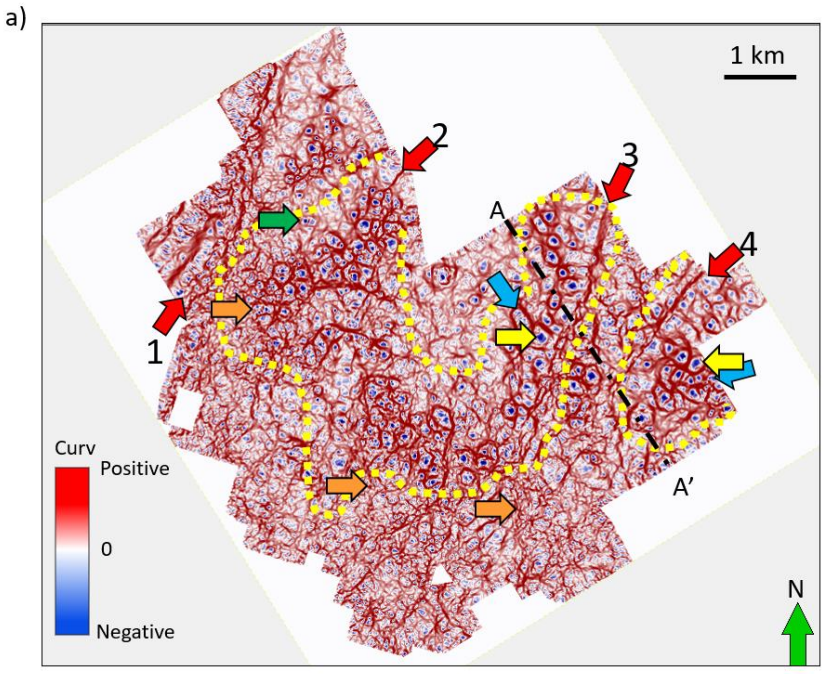

b)

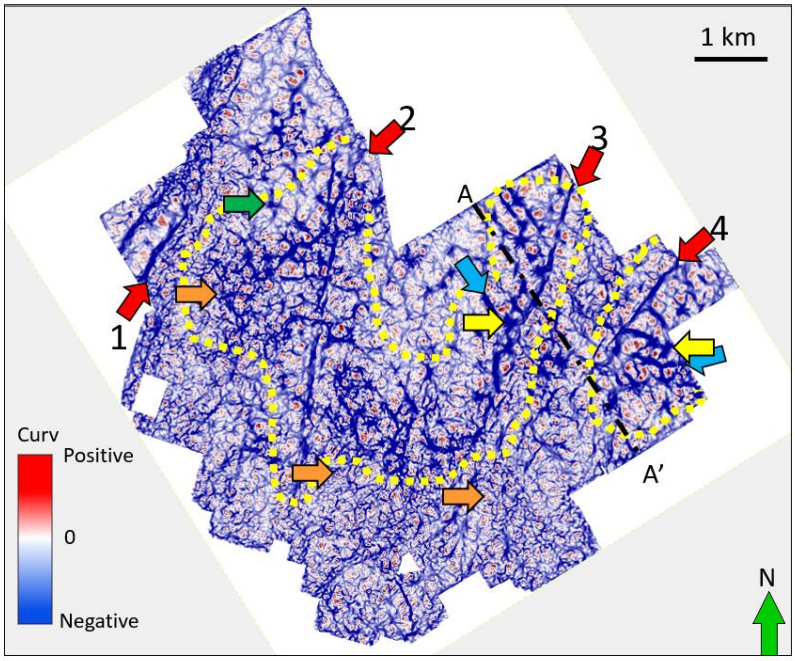
1 km
1
2
3
4
A
A'
Curv
Positive
0
Negative
N

c)

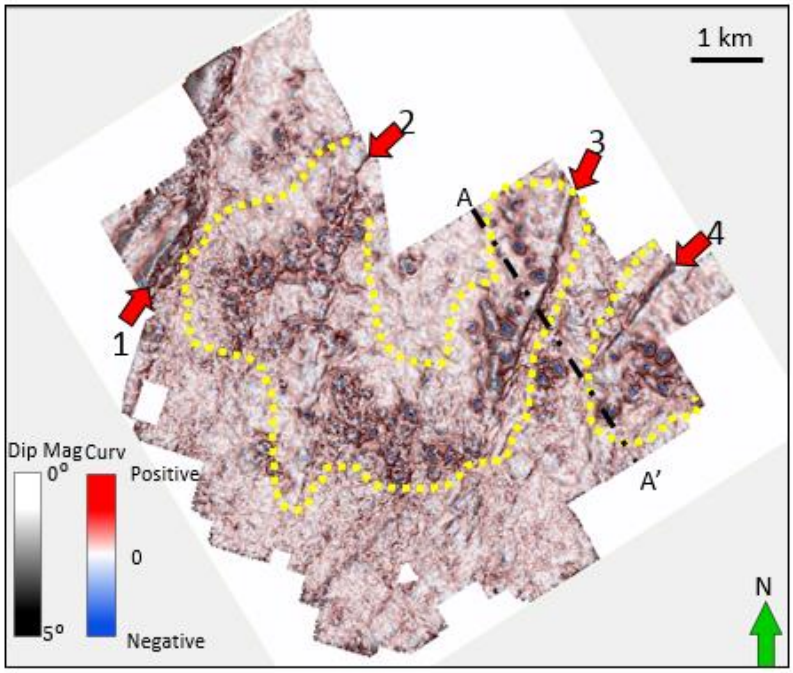
1 km
1
2
3
4
A
A'
Dip Mag Curv
0°
5°
Positive
0
Negative
N

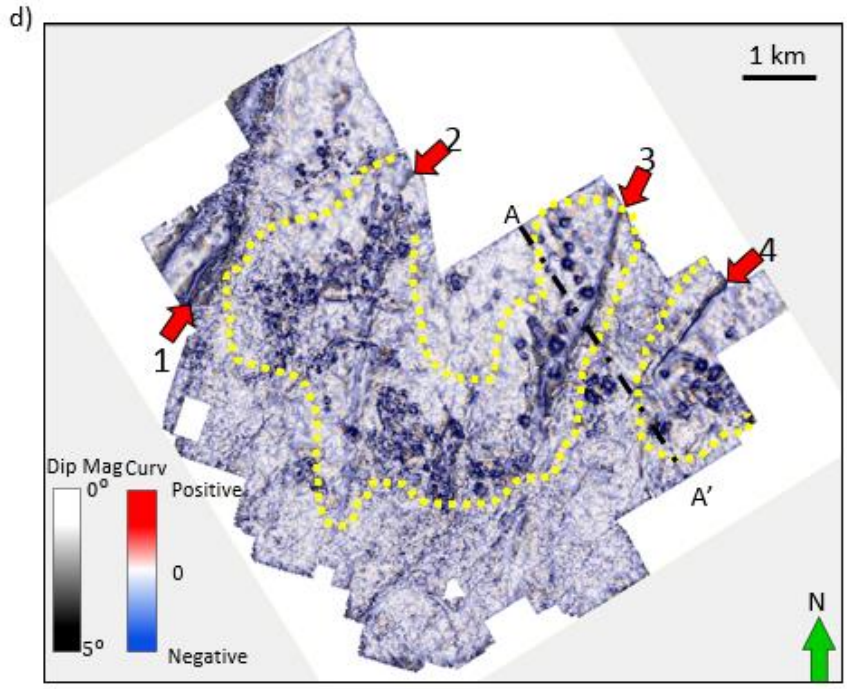

Figure 4.13 Time slice at t=0.750 s through (a) most-positive and (b) most-negative structural curvature, and (c) most-positive and (b) most-negative structural curvature co-rendered with dip magnitude. In this survey, the major faults are expressed by a positive curvature anomaly on the footwall which laterally offset from a corresponding a negative curvature anomaly on the hanging wall. The dip magnitude and coherence anomalies fall between the two curvature anomalies. In this image, the bowl shaped collapse features express a negative value and appear as blue ellipses (yellow and green arrows). The rugose surface (orange arrows) is represented by a shorter wavelength, lower deformation pattern. Yellow polygons indicate the area where large collapse features are controlled by faults. Blue arrows indicate channel-like collapse features as red anomalies.

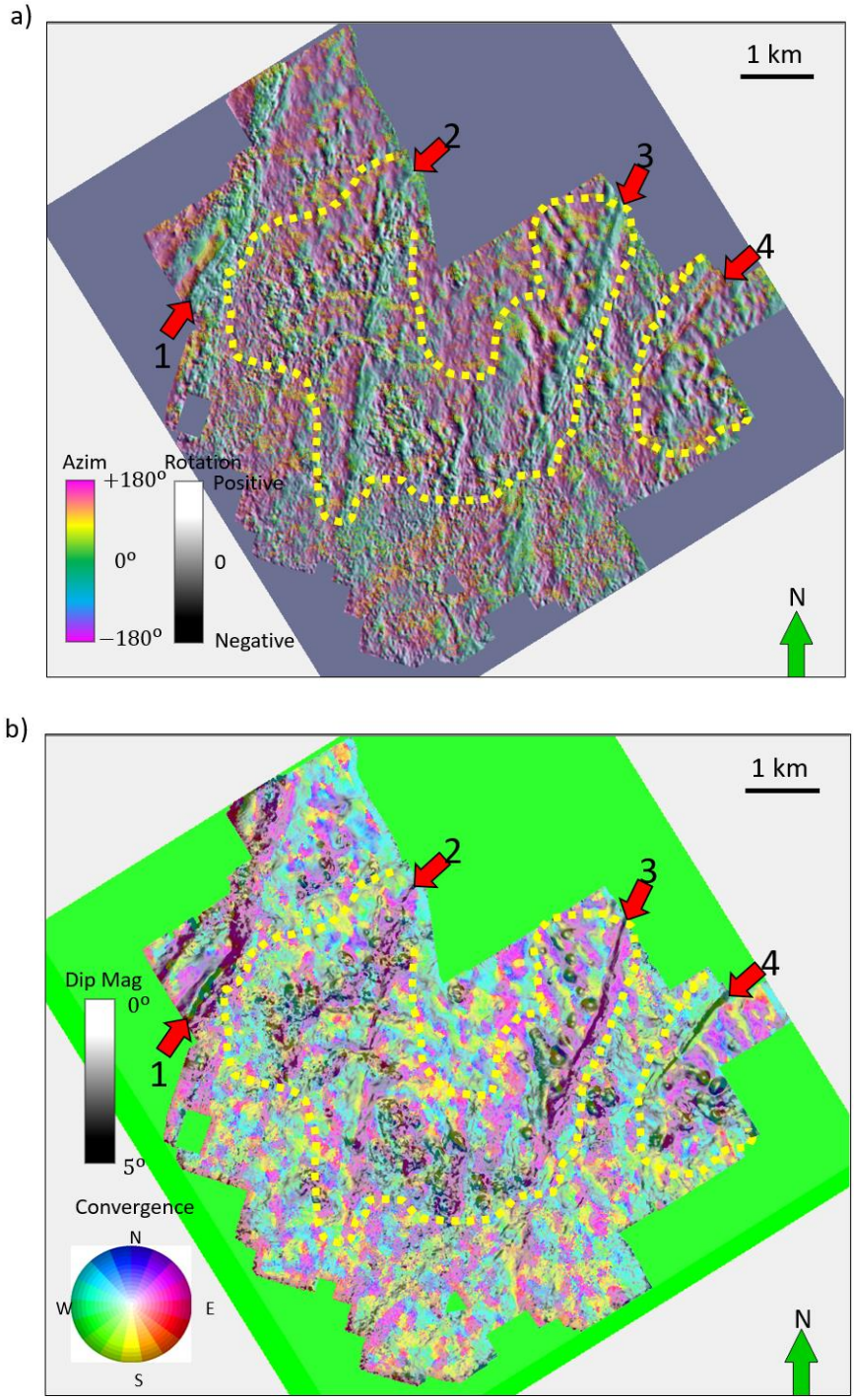

Figure 4.14 Time slice at t=0.750 s through (a) rotation co-rendered with dip azimuth and (b) vector convergence co-rendered with dip magnitude. Note the red arrows indicate major faults, and yellow polygon (14a) and white polygon indicates fault-controlled karst features.

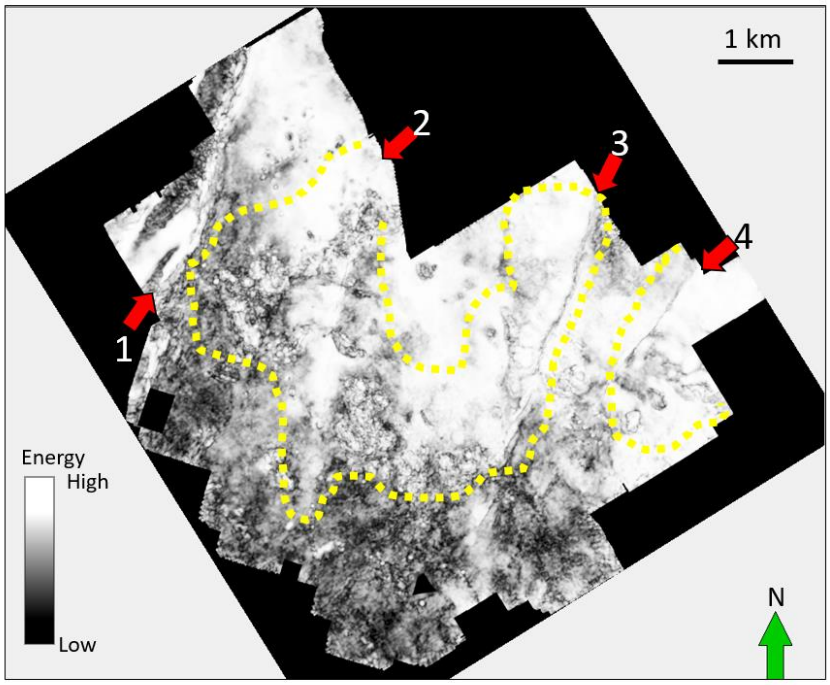

Figure 4.15 Time slice at t=0.750 s through coherent energy attributes. Note the red arrows indicate major faults, and yellow polygon indicates fault-controlled karst features.

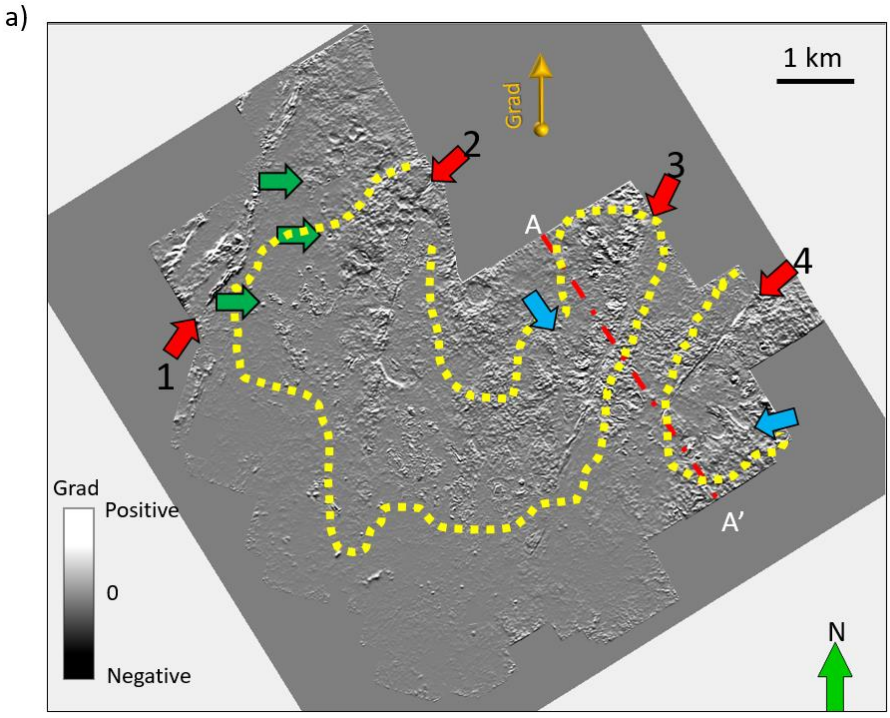

b)

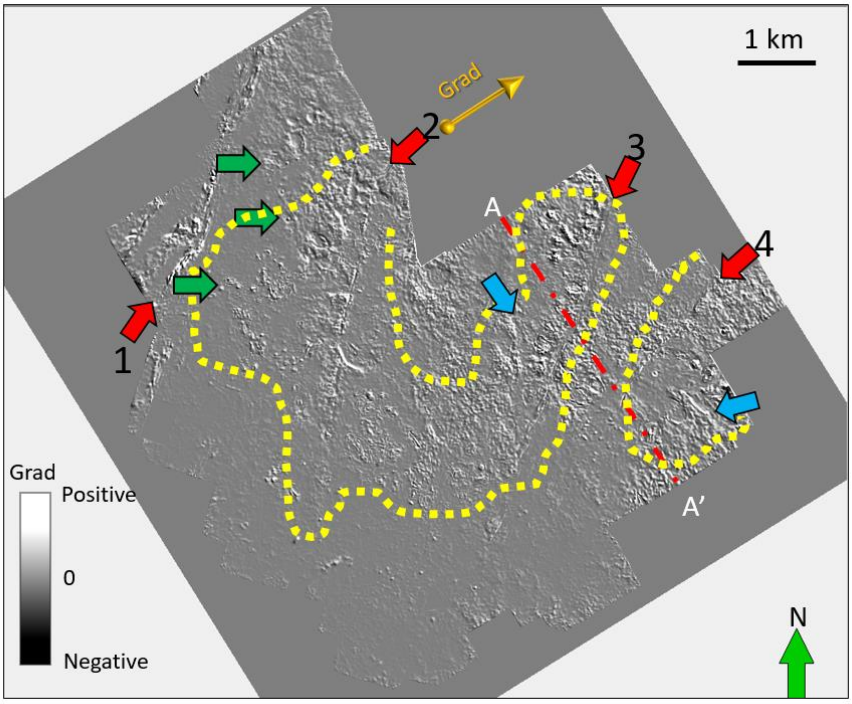
1 km
Grad
2
3
4
1
A
A'
Grad
Positive
0
Negative
N

c)

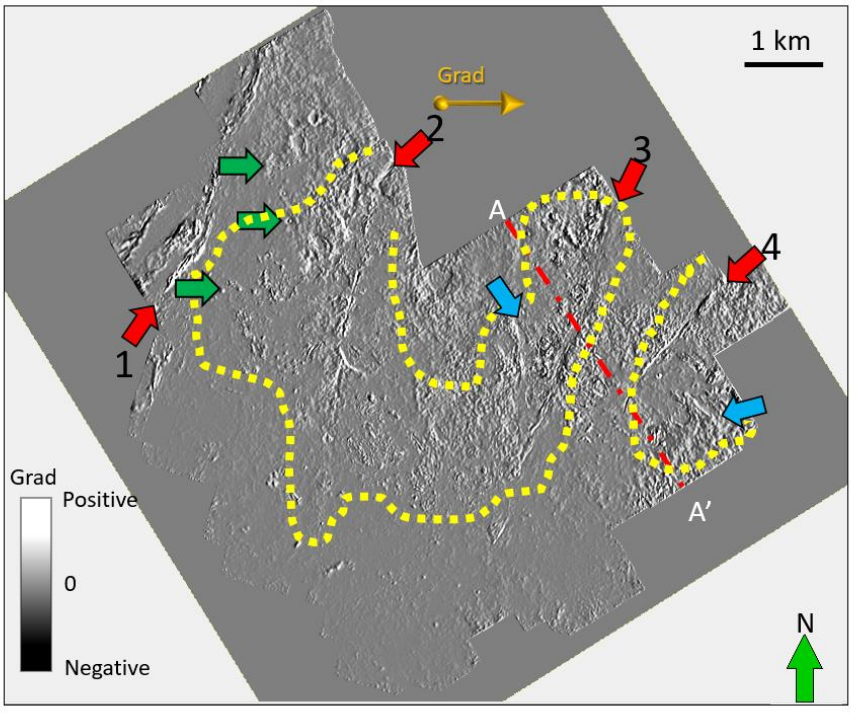
1 km
Grad
2
3
4
1
A
A'
Grad
Positive
0
Negative
N

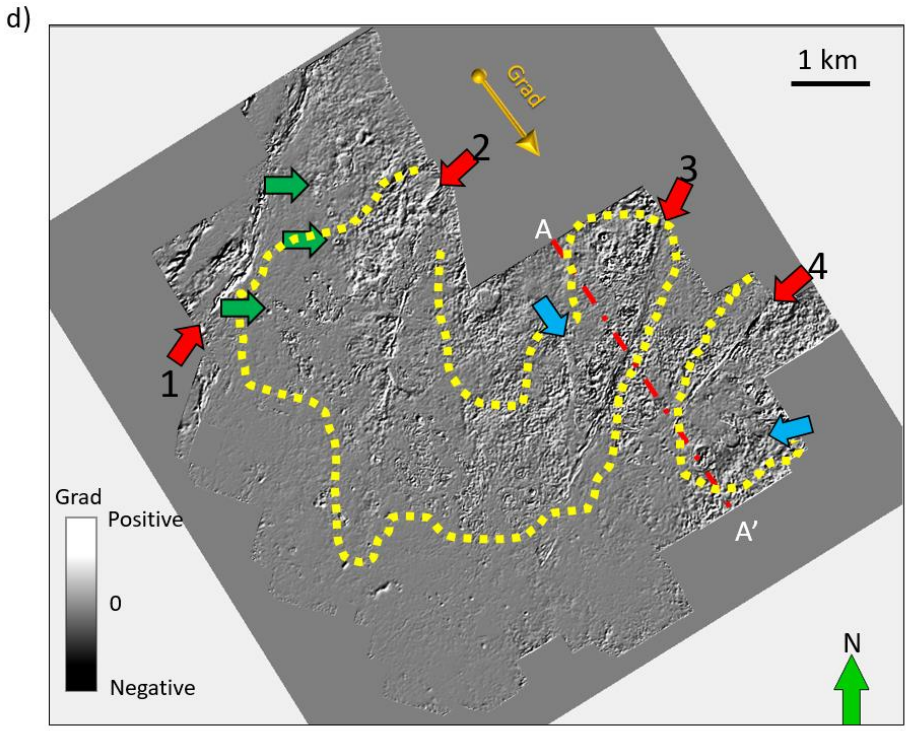

Figure 4.16 Time slices at t=0.750 s through at (a) 0˚, (b) 45˚, (c) 90˚, and (d) 135˚ from North amplitude gradients computed along structural dip. Large karst do not appear to give a strong amplitude anomaly, although small karst (green arrow) do. There does not appear to be significant acquisition footprint in either of the gradient images. Faults (red arrows) and channel-like collapse features (blue arrows) appear differently on each degree amplitude gradients.

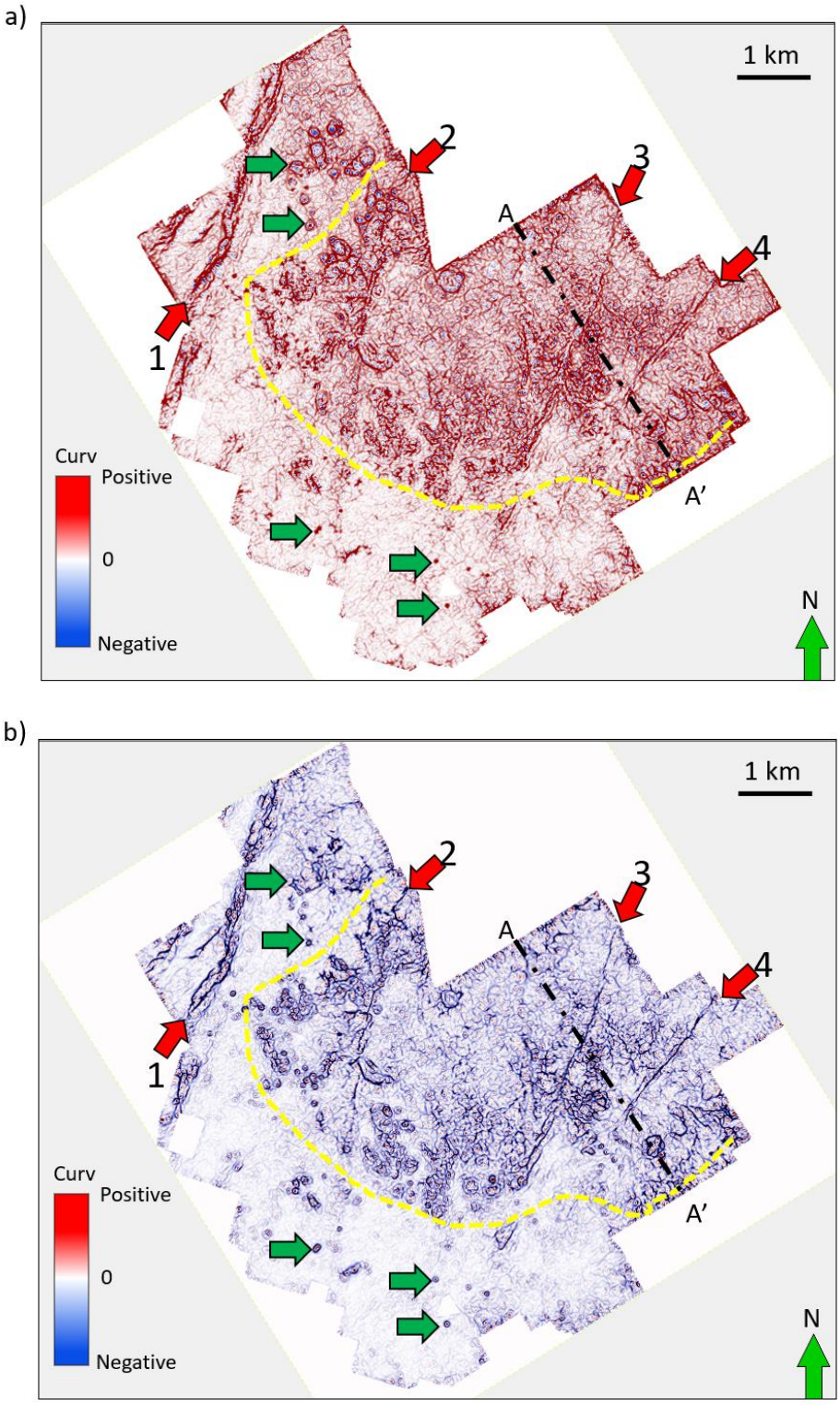
a)
1 km
1
2
3
4
A
A'
Curv
Positive
0
Negative
N
b)
1 km
1
2
3
4
A
A'
Curv
Positive
0
Negative
N

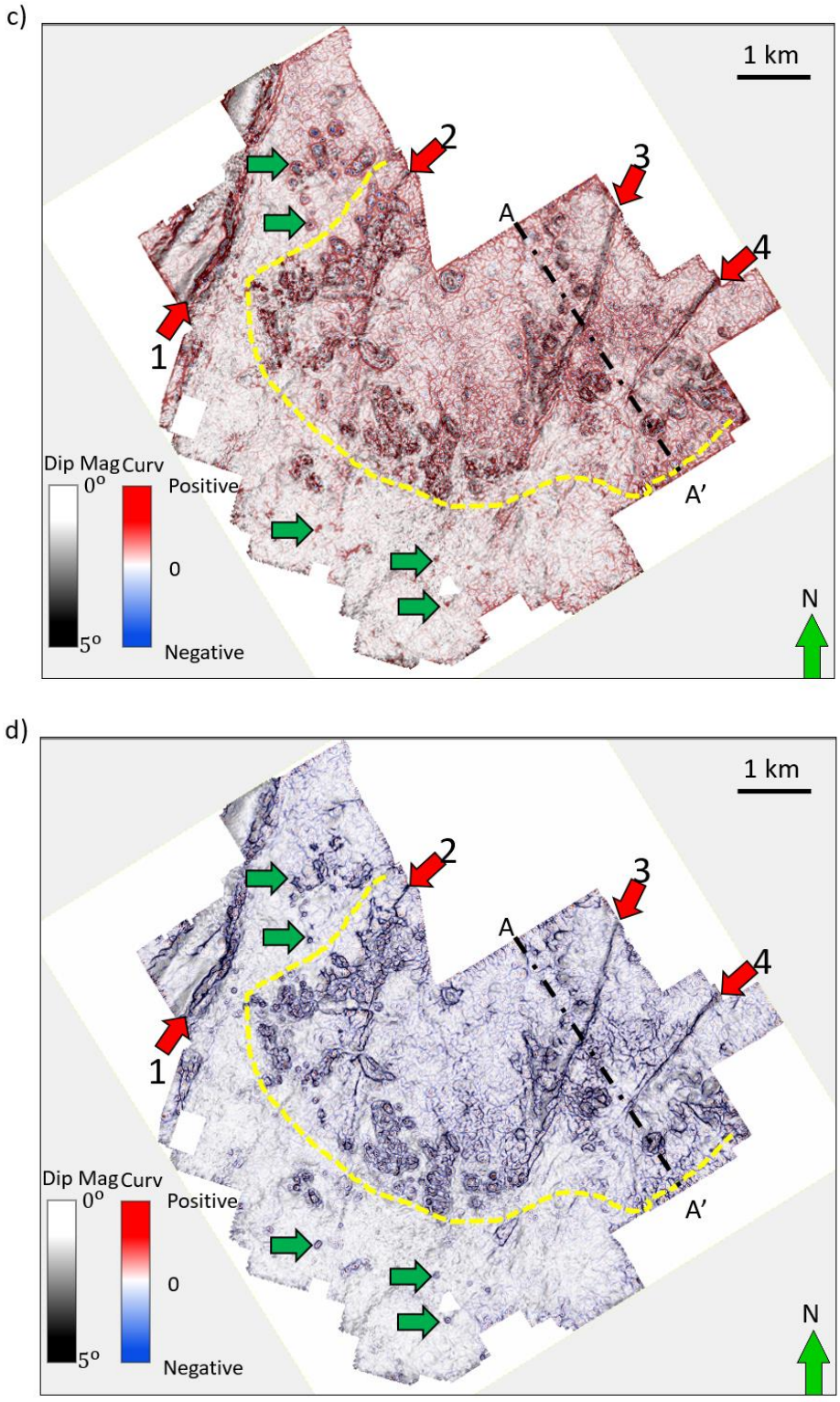

Figure 4.17 Time slices at t=0.750 s through (a) most-positive and (b) most-negative amplitude curvature, and (c) most-positive and (d) most-negative amplitude curvature volumes co-rendered with dip magnitude volumes. Dashed yellow polygons indicate areas of fault-controlled karst. While structural curvature is computed by taking the

derivative of the inline and crossline dip components, amplitude curvature is computed by taking the derivative of the inline and crossline amplitude gradients shown in the previous image. Yellow dashed line indicates zone dominated by fault controlled karst. Although NW-SE and NE-SW lineaments could be acquisition footprint, we interpret lineaments at other azimuths to indicate diagenetically altered joints giving rise to laterally variable reflectivity. Green arrows indicate small karst. Some of those can only be highlighted by amplitude gradient and amplitude curvature.

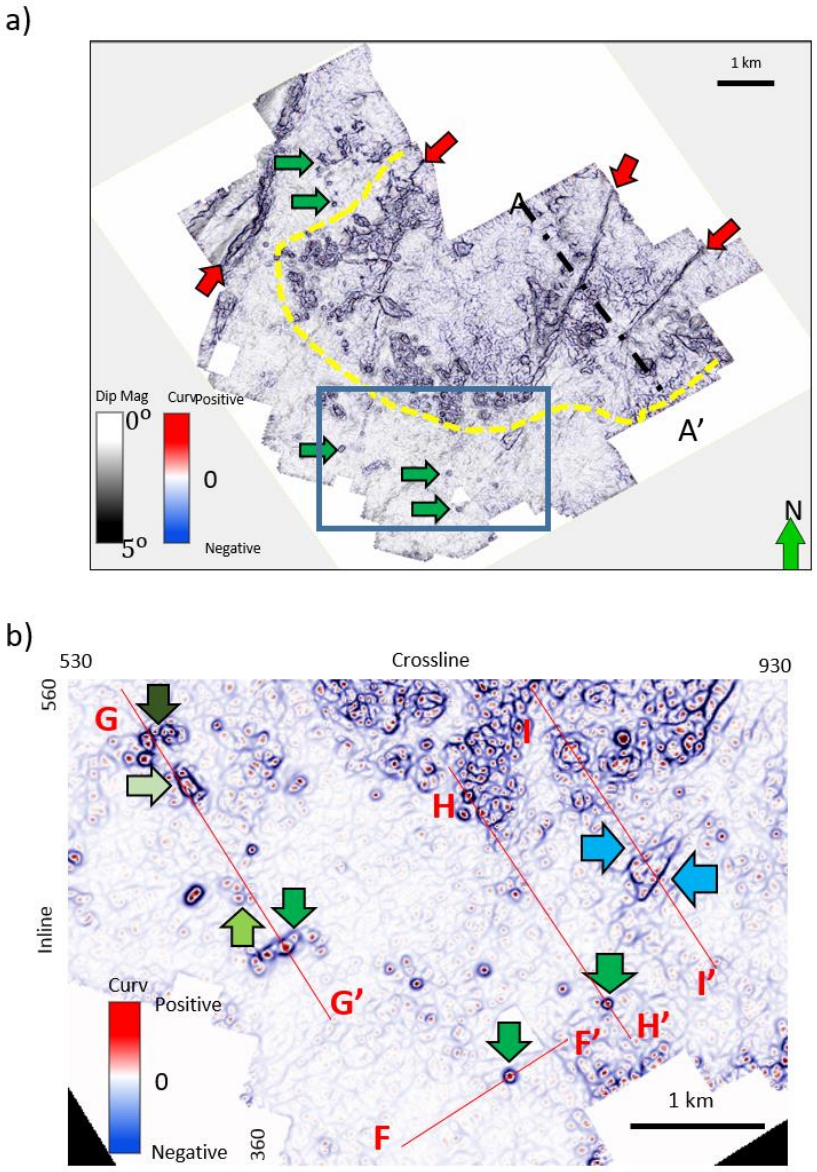

c)

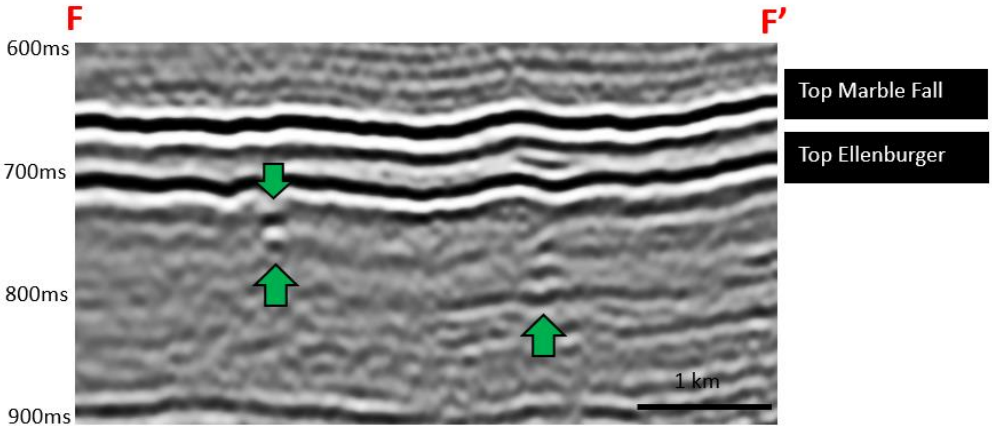
F
F'
600ms
700ms
800ms
900ms
Top Marble Fall
Top Ellenburger
1 km

d)

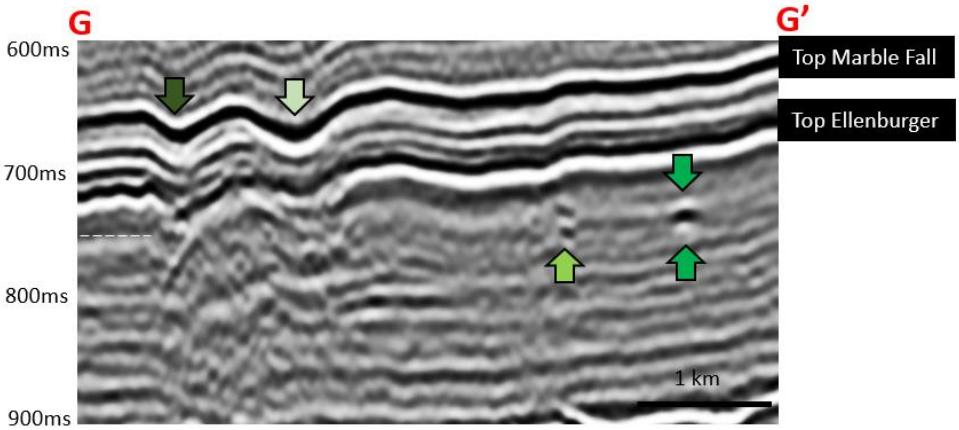
G
G'
600ms
700ms
800ms
900ms
Top Marble Fall
Top Ellenburger
1 km

e)

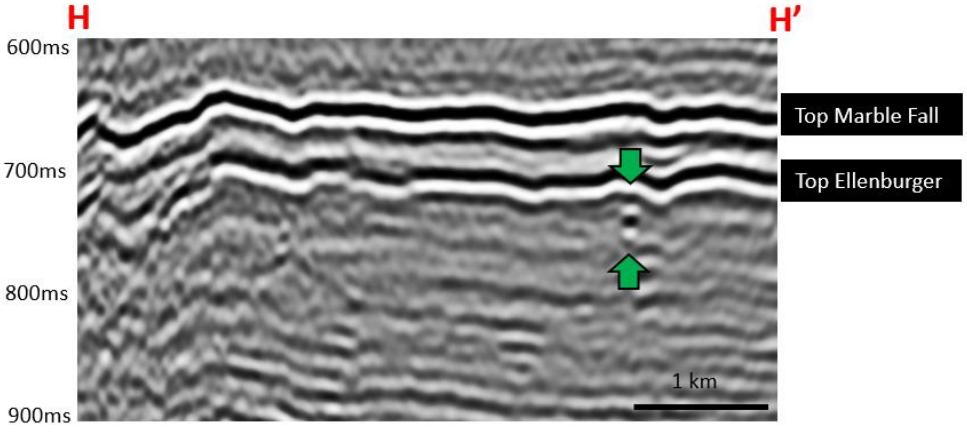
H
H'
600ms
700ms
800ms
900ms
Top Marble Fall
Top Ellenburger
1 km

f)

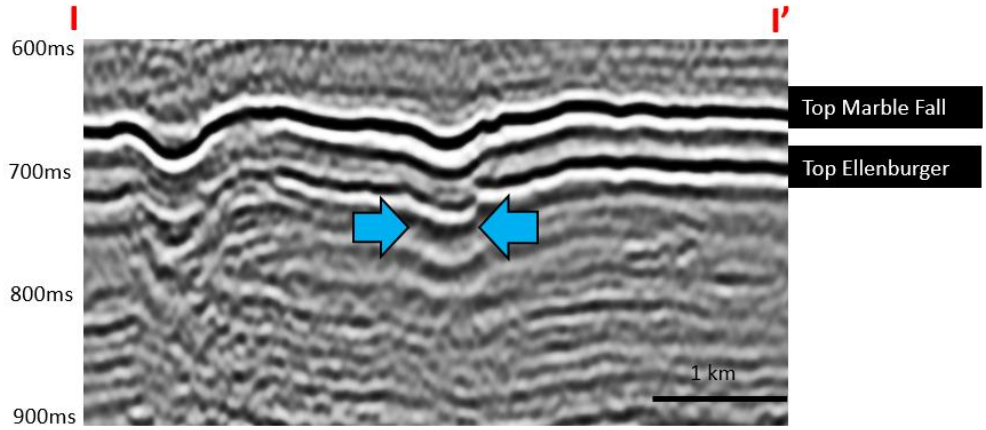

Figure 4.18 Time slice at t=0.750s through (a) most-negative amplitude curvature, and (b) zoomed in zone. (c), (d), (e), and (f) are seismic section view of lines FF', GG', HH', and II'. Circular collapse features are contained entirely within the Ellenburger Dolomite formation and do not propagate shallower. Several of exhibit the "string of pearls" pattern, suggesting that they are controlled by faults or joints.

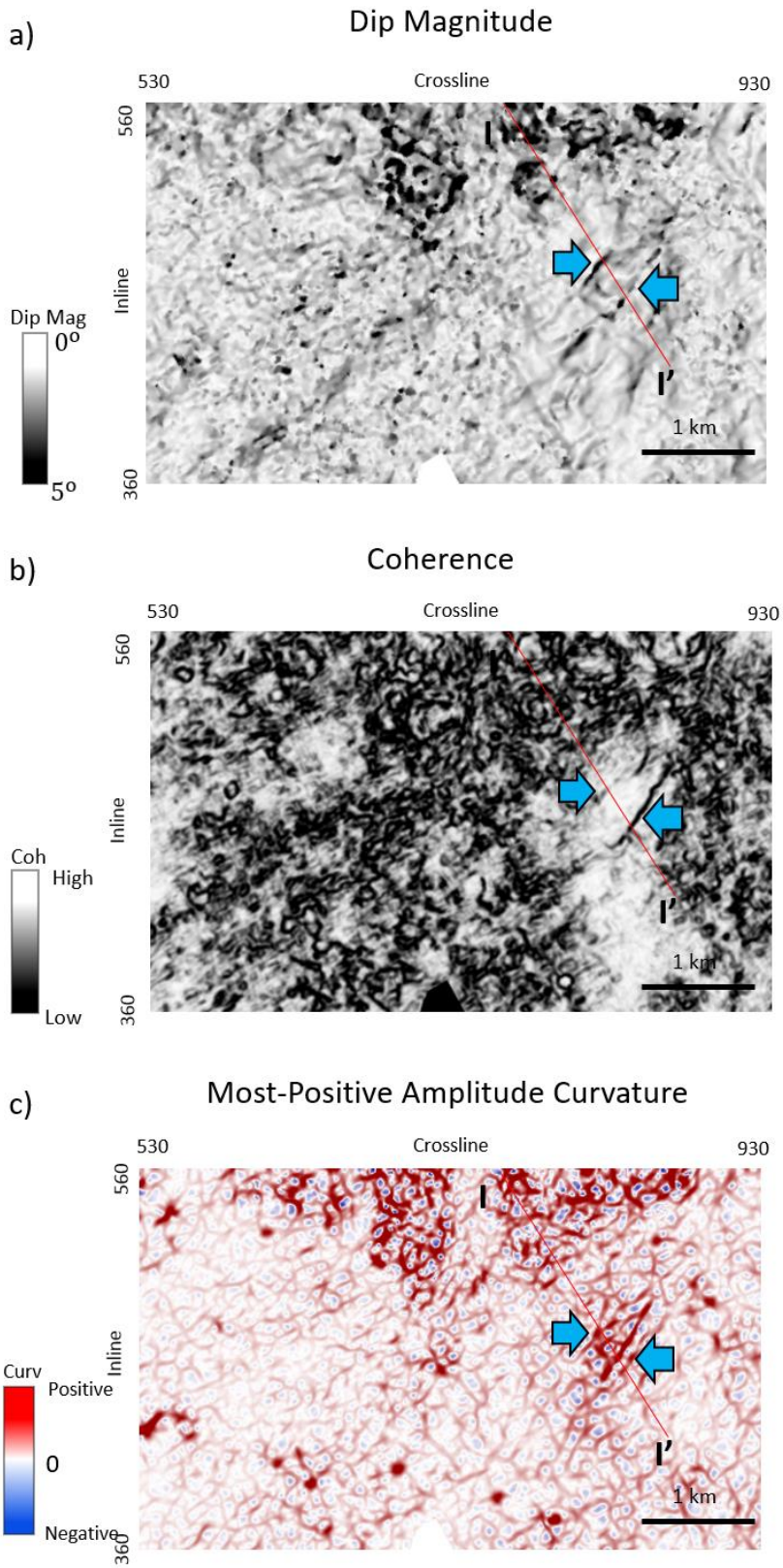
a)
Dip Magnitude
530
Crossline
930
560
Inline
360
I
I'
Dip Mag
0°
5°
1 km
b)
Coherence
530
Crossline
930
560
Inline
360
I
I'
Coh
High
Low
1 km
c)
Most-Positive Amplitude Curvature
530
Crossline
930
560
Inline
360
I
I'
Curv
Positive
0
Negative
1 km

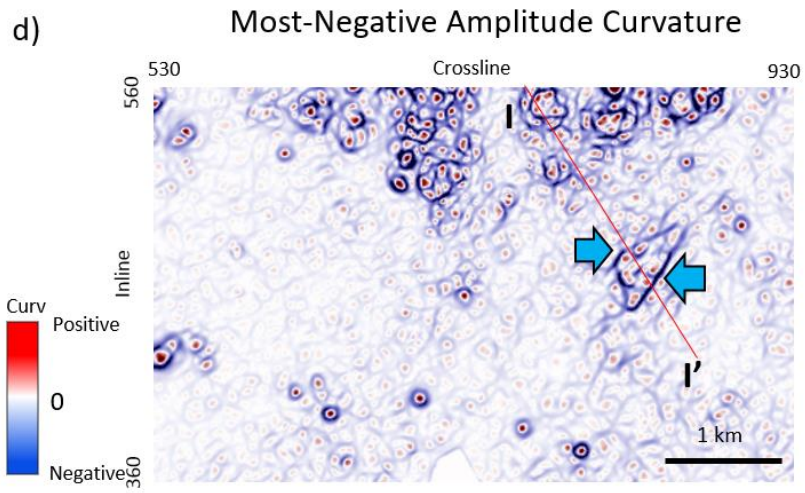

Figure 4.19 Time slice of zoomed in area at t=0.750s through (a) dip magnitude, (b) coherence, (c) most-positive amplitude curvature, and (d) most-negative amplitude curvature. Notice that blue arrows indicate subtle collapse-caused fault.

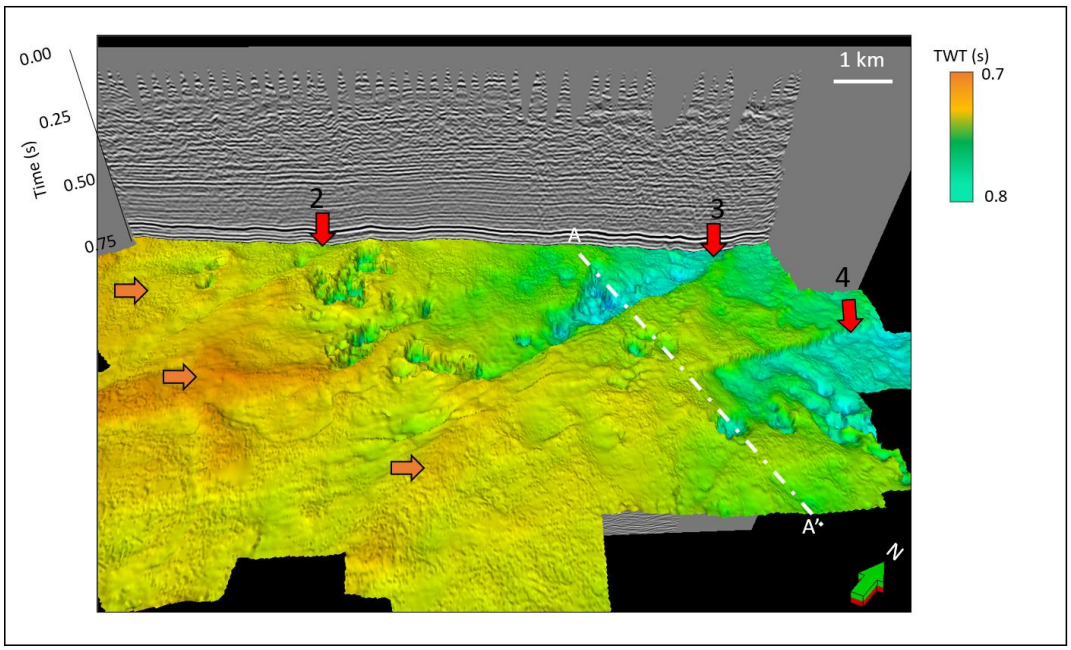

Figure 4.20 Time structure map of the top Ellenburger Group horizon. Karst collapse and three major faults are clearly seen. Note the increased rugosity of the surface towards the south, and increased karst collapse towards the north. Orange arrows indicate rugose surface. Red arrows indicate major faults.

a)

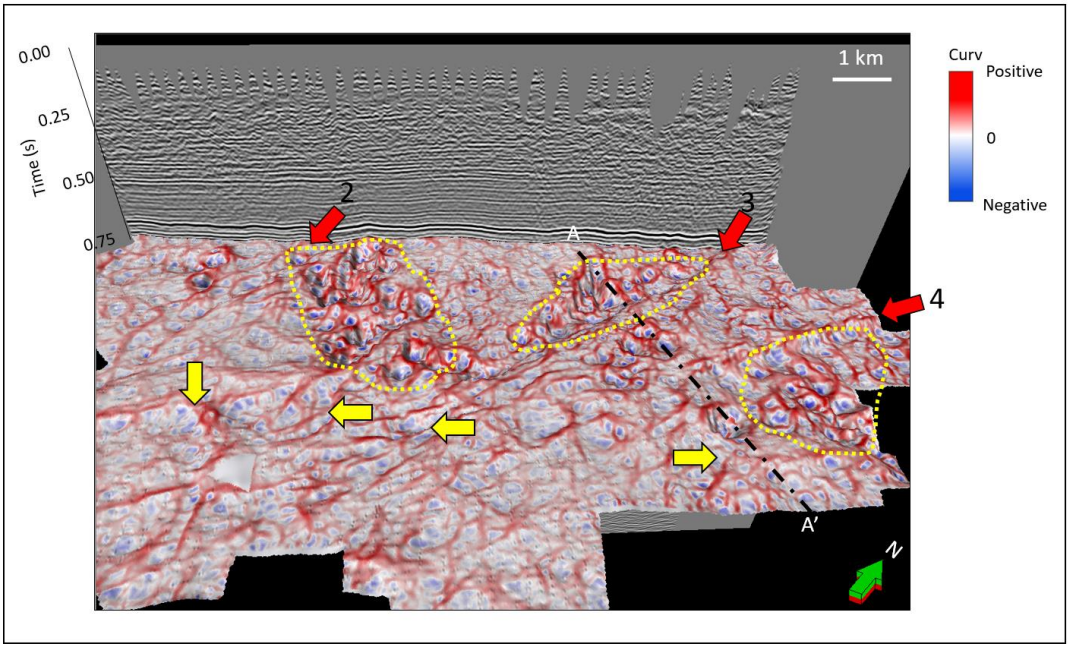
0.00
0.25
0.50
0.75
Time (s)
1 km
Curv
Positive
0
Negative
2
3
4
A
A'
N

b)

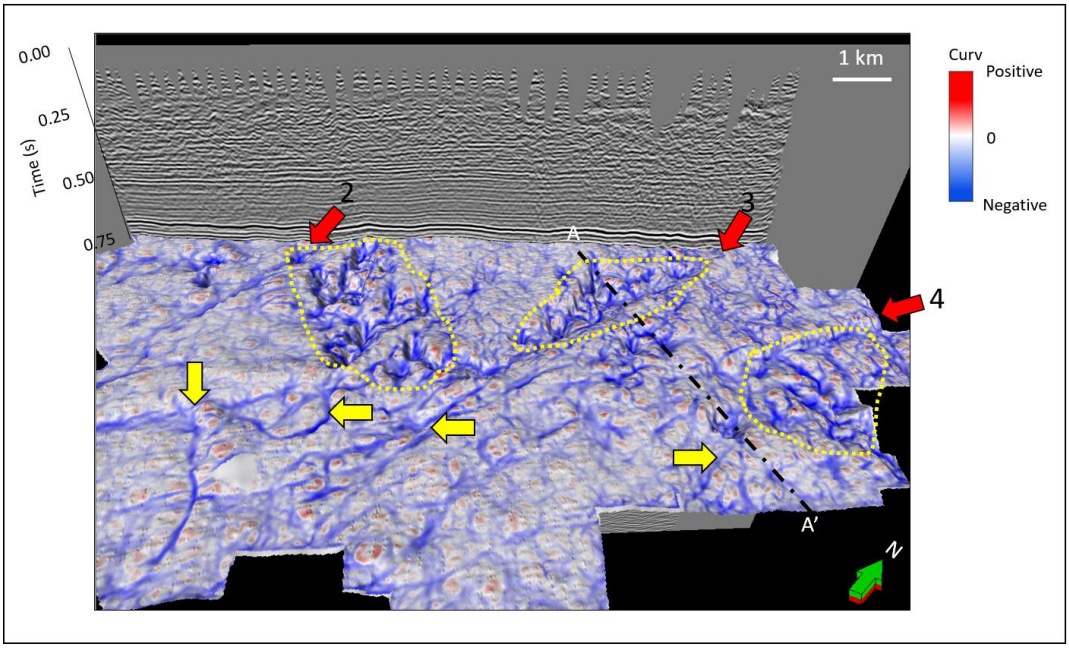
0.00
0.25
0.50
0.75
Time (s)
1 km
Curv
Positive
0
Negative
2
3
4
A
A'
N

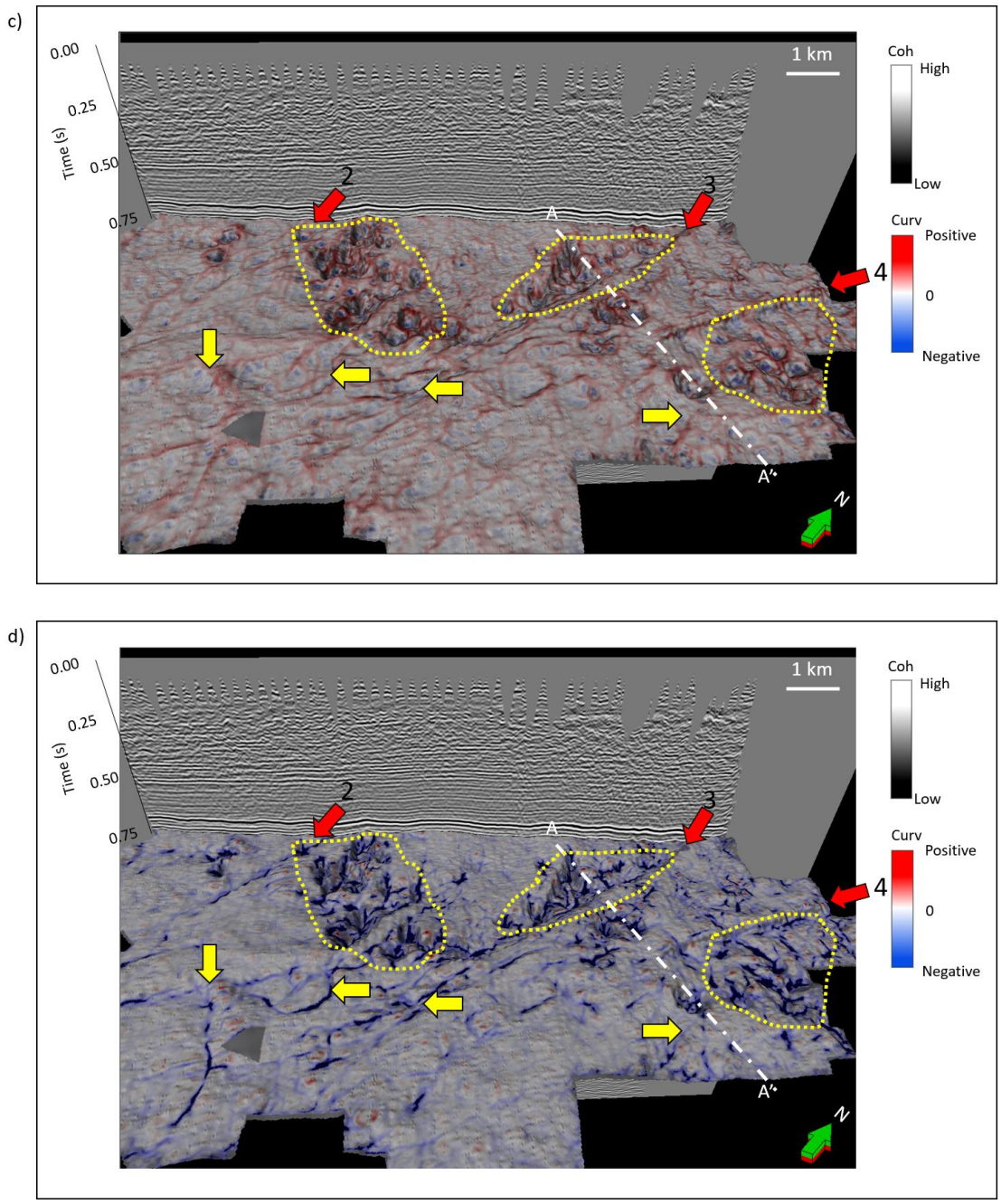

Figure 4.21 Vertical slice through seismic amplitude and horizon slices along the top Ellenburger Group horizon though the (a) most-positive and (b) most-negative structural curvature and (c) most-positive and (d) most-negative structural curvature co-rendered with coherence. Red arrows indicate major faults, yellow dashed lines indicate where karst is developed and larger than other area where there is no major faults. Yellow arrows indicate surface folds and joints.

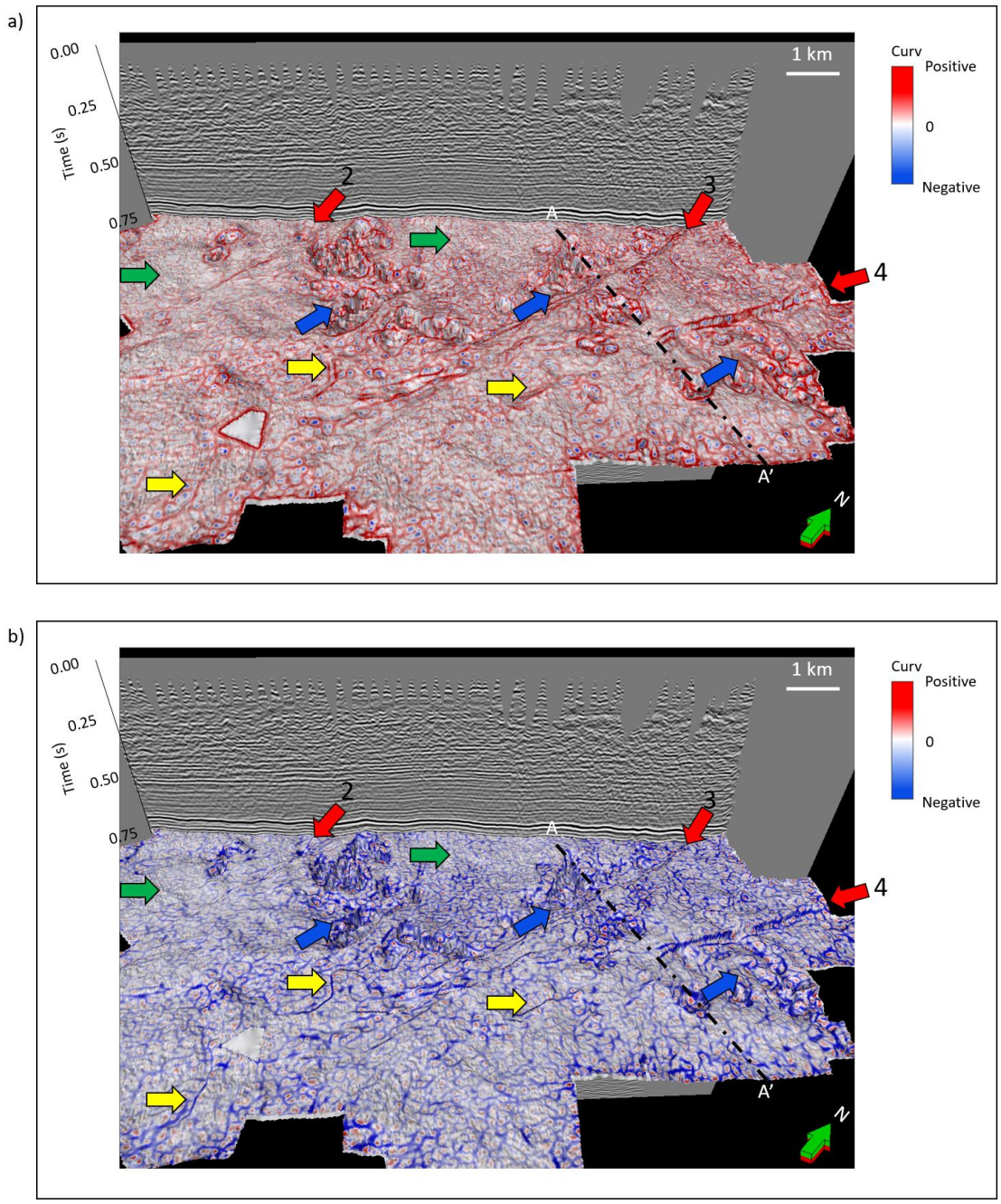

Figure 4.22 Vertical slice through seismic amplitude and horizon slices along the top Ellenburger Group horizon though the (a) most-positive and (b) most-negative amplitude curvature. Red arrows indicate major faults. Blue arrows indicate fault-controlled karst. Yellow arrows indicate surface folds and joints. The fractures are developed in zones where faults and karst are also developed. Green arrows indicate the zones have no faults effects, so that fractures are not developed.

REFERENCES

Al-Dossary, S., and K. J. Marfurt, 2006, 3D volumetric multispectral estimates of reflector curvature and rotation: Geophysics, **71**, P41-P51.

Bahorich, M. S., and S. L. Farmer, 1995, 3D seismic discontinuity for faults and stratigraphic features: The coherence cube: 65th Annual International Meeting, SEG, Expanded Abstracts, 93-96.

Bruner, K. R., and R. Smosna, 2011, A comparative study of the Mississippian Barnett Shale, Fort Worth basin, and Devonian Marcellus Shale, Appalachian basin: Technical Report DOE/NETL/2011/1478, National Energy Technology Laboratory for The United States Department of Energy.

Chen, M., S. Zhan, Z. Wan, H. Zhang, and L. Li, 2010, Detecting carbonate-karst reservoir using the directional amplitude gradient difference technique: 81th Annual International Meeting, SEG, Expanded Abstracts, 1845-1849.

Chopra, S., and K. J. Marfurt, 2007, Volumetric curvature attributes add value to 3D seismic data interpretation: The Leading Edge, **27**, 856-867.

Duo Q., Y. Sun, C. Sullivan, and H. Guo, 2011, Paleokarst system development in the San Andres Formation, Permian Basin, revealed by seismic characterization: Journal of Applied Geophysics, **75,** 379-389.

Elebiju, O. O., G. R. Keller, and K. J. Marfurt, 2010, Case history investigation of links between Precambrian basement structure and Paleozoic strata in the Fort Worth basin, Texas, USA, using high-resolution aeromagnetic, HRAM data and seismic attributes: Geophysics, **75**, 157–168.

Feng, X., Y. Wang, X. Wang, N. Wang, G. Gao and X. Zhu, 2012, The application of high-resolution 3D seismic acquisition techniques for carbonate reservoir characterization in China: The Leading Edge, **31**, 168–179.

Ferrill, D. A., and A. P. Morris, 2008, Fault zone deformation controlled by carbonate mechanical stratigraphy, Balcones fault system, Texas, AAPG Bulletin, **92**, 359-380.

Gale, J. F. W., R. M. Reed, and J. Holder, 2007, Natural fractures in the Barnett Shale and their importance for hydraulic fracture treatments: American Association Petroleum Geologists Bulletin, v 91, p. 603–622.

Hardage, B., D. Carr, D. Lancaster, J. Simmons, Jr, R. Elphick, V. Pendleton, and R. Johns, 1996, 3D seismic evidence of the effects of carbonate karst collapse on overlying clastic stratigraphy and reservoir compartmentalization: Geophysics, **61**, 1336 –1350.

Holtz, M. H., and C., Kerans, 1992, Characterization and categorization of West Texas Ellenburger reservoirs, in Candelaria, M. P., and Reed, C. L., eds., Paleokarst, karst related diagenesis and reservoir development: examples from Ordovician-

Devonian age strata of West Texas and the Mid-Continent: Permian Basin Section SEPM Publication No. 92-33, 31–44.

Kerans, C., 1988, Karst-controlled reservoir heterogeneity in Ellenburger Group carbonates of West Texas: reply: AAPG Bulletin, v. 72, p. 1160–1183.

Kerans, C., 1989, Karst-controlled reservoir heterogeneity and an example from the Ellenburger Group (Lower Ordovician) of West Texas: The University of Texas at Austin, Bureau of Economic Geology Report of Investigations No. 186, 40 p.

Kerans, C., 1990, Depositional systems and karst geology of the Ellenburger Group (Lower Ordovician), subsurface West Texas: The University of Texas at Austin, Bureau of Economic Geology Report of Investigations No. 193, 63 p., 6 pl.

Khatamadi, M., G. R. Keller, and K. J. Marfurt, 2013, A window into the Proterozoic: Integrating 3D seismic, gravity and magnetic data to image subbasement structures in the southeast Fort Worth basin: Interpretation, **1**, T125-T142.

Leach, D.L., and Sangster, D.F., 1993, Mississippi Valley-type lead-zinc deposits: Geological Association of Canada Special Paper 40, p. 289–314.

Liu, J. and K. J. Marfurt, 2007, Instantaneous spectral attributes to detect channels: Geophysics, **72**, 23-31.

Liu, Y., X. Liang, and Y. Zhou, 2011, A method of acquiring full azimuth data for carbonate reservoirs exploration in Tarim basin, western China: 82nd Annual International Meeting, SEG, Expanded Abstracts, 1-5.

Loucks, R. G., 2003, Understanding the development of breccias and fractures in Ordovician carbonate reservoirs, in Hunt, T. J., and Lufholm, P. H., The Permian Basin: back to basics: West Texas Geological Society Fall Symposium: West Texas Geological Society Publication No. 03-112, 231–252.

Loucks, R. G., 2008, Review of the Lower Ordovician Ellenburger Group of the Permian Basin, west Texas.

Lucia, F. J., 1995, Lower Paleozoic cavern development, collapse, and dolomitization, Franklin Mountains, El Paso, Texas, *in* Budd, D. A., Saller, A. H., and Harris, P. M., eds., Unconformities and porosity in carbonate strata: AAPG Memoir 63, p. 279–300.

Marfurt, K. J., and R. L. Kirlin, 2000, 3-D broad-band estimates of reflector dip and amplitude: Geophysics, 65, 304–320.

Marfurt, K. J., 2006, Robust estimates of 3D reflector dip and azimuth: Geophysics, **71**, 29-40.

Marfurt, K. J., and J. R. Rich, 2010, Beyond curvature-Volumetric estimates of reflector rotation and convergence: 80th Annual International Meeting, SEG, Expanded Abstracts, 1467–1472.

McDonnell, A., R. G. Loucks, and T. Dooley, 2007, Quantifying the origin and geometry of circular sag structures in northern Fort Worth Basin, Texas: paleocave collapse, pull-apart fault systems, or hydrothermal alteration? AAPG Bulletin, **91**, 1295–1318.

Neep, J. P., 2007, Time-Variant colored inversion and spectral blueing: 69th Conference and Exhibition, EAGE, Expanded Abstract, E044.

Partyka, G. A., J. A. Gridley, and J. A. Lopez, 1999, Interpretational applications of spectral decomposition in reservoir characterization: The Leading Edge, **18**, 353–360.

Pollastro, R. M., D. M. Jarvie, R. J. Hill, and C. W. Adams, 2007, Geologic framework of the Mississippian Barnett shale, Barnett-paleozoic total petroleum system, Bend arch – Fort Worth basin, Texas: AAPG Bulletin, **91**, 405-436.

Qi, J., and J. P. Castagna, 2013, Application of a PCA fault-attribute and spectral decomposition in Barnett Shale fault detection: 83rd Annual International Meeting, SEG, Expanded Abstracts, 1421-1425.

Roende, H., C. Meeder, J. Allen, S. Peterson, and D. Eubanks, 2008, Estimating subsurface stress direction and intensity from subsurface full azimuth land data: 78th Annual International Meeting, SEG, Expanded Abstracts, 217-220.

Roth, M., and A. Thompson, 2009, Fracture interpretation in the Barnett Shale using macro and microseismic data: First Break, **27**, 61-65.

Schuelke, J. S., 2011, Overview of seismic attribute analysis in shale play: Attributes: New views on seismic imaging-Their use in exploration and production, Presented at 31st Annual GCSSEPM Foundation Bob F. Perkins Research Conference.

Sullivan, E., K. Marfurt, and M. Ammerman, , 2003, Bottoms up karst: New 3D seismic attributes shed light on the Ellenburger (Ordovician) carbonates in the Fort Worth Basin (north Texas, USA), 73rd Annual International Meeting, Society of Exploration Geophysicists Expanded Abstracts, 482-485.

Sullivan, E. C., K. J. Marfurt, A. Lacazette, and M. Ammerman, 2006, Application of new seismic attributes to collapse chimneys in the Fort Worth basin: Geophysics, **71**, 111-119.

Wang, F.P., and J. F. W. Gale, 2009, Screening criteria for shale-gas systems: GCAGS Transactions, **59**, 779 – 793

APPENDIX A

In this appendix, we summarize several of the seismic attributes used in the paper. Several of these definitions are extracted from the glossary in Chopra and Marfurt (2007) which in turn were adapted from definition in Sheriff (2002). Much greater detail can be found under geology.ou.edu/aaspi/documentation.

Apparent inline dip

For time-migrated data, the apparent dip is the change in reflector time from with respect to distance in a given direction and is measured in units of s/m. Using the SEGY convention, where the y-axis is North and the x-axis East, the apparent north component of dip, p_y, and east component of dip, p_x, are given by

$$p_x = \frac{\partial t}{\partial x}, \text{ and} \tag{A-1}$$

$$p_y = \frac{\partial t}{\partial y}. \tag{A-2}$$

In our examples, we computed the inline and crossline components of dip using a multi-window Kuwahara semblance search technique described by Marfurt (2006). The apparent dip in the ξ direction (in this paper 0°, 45°, 90°, and 135° from North) is simply

$$p_\xi = \frac{\partial t}{\partial \xi} = (\cos\xi) p_y + (\sin\xi) p_x. \tag{A-3}$$

Dip magnitude and dip azimuth

The dip magnitude measured in s/m, $|\mathbf{p}|$, is simply the magnitude of the vector dip $\mathbf{p}$ given by

$$|\mathbf{p}| = \left(p_x^2 + p_y^2\right)^{1/2}. \tag{A-4}$$

Conversion to angular dip, θ, requires the use of a velocity, v_P, which we set to 15000 ft/s, representative of the Barnett Shale and Ellenburger Dolomite, and is given by

$$\theta = \tan^{-1}\left[\frac{v_P}{2}\left(p_x^2 + p_y^2\right)^{1/2}\right]. \tag{A-5}$$

Dip azimuth from North is simply

$$\theta = \text{ATAN2}\left(p_y, p_x\right), \tag{A-6}$$

where ATAN2 produces a result that ranges between -180^0 and $+180^0$.

Coherence

Coherence is a measure of waveform similarity. In our examples, we estimate the coherence of J traces within a $\pm K$ sample analysis window as the ratio between the coherent energy within an analysis window to the total energy within the analysis window

$$c = \frac{\sum_{k=-K}^{+K}\left[\sum_{j=1}^{J}\left(d_j^{coh}\right)^2\right]}{\sum_{k=-K}^{+K}\left[\sum_{j=1}^{J}\left(d_j^{orig}\right)^2\right]}. \tag{A-7}$$

Semblance-based coherence estimates the coherent part of the data by the average trace within the analysis window. In the examples we show here, we estimate the coherent part of data using a Karhunen-Loeve filter. We always compute coherence along structural dip.

Structure-oriented filter

As the name implies, structure-oriented filtering is computed along structural dip as estimated by equations A-1 and A-2. Our implementation builds on other previously computed components. First, we examine the centered and examine its coherence. If the coherence is below a given threshold (e.g. c<0.6) we do not filter the data in an attempt

to preserve a potential "edge". If the coherence is above the threshold, we compare this value to the coherence of all non-centered analysis windows that includes the voxel of interest and choose the one with the highest coherence value. Within this window, we apply a Karhunen-Loeve filter and output the filtered sample value.

Spectral components

In this paper, we computed spectral components using a matching pursuit algorithm described by Liu and Marfurt (2007). We begin by computing a library of complex Ricker wavelets. Then we compute the instantaneous envelope and frequency of a given trace. Then using a user-defined threshold (in our examples r=0.8), we extract the time and instantaneous frequency of all envelopes that exceed r times the largest envelope. Wavelets of unknown complex amplitude, α, (or alternatively, unknown magnitude and phase) for the given instantaneous (average) frequency are then extracted from the dictionary. The values of α are computed using least-squares, scaled complex spectra from the dictionary are accumulated and the residual trace is generated. This process iterates until the residual energy is small percentage of the energy of the original trace. The result is a time-frequency spectral decomposition with a spectrum at each time sample.

The peak magnitude is the maximum magnitude at a given voxel and the peak frequency the corresponding frequency of the spectrum.

Spectral balancing and spectral bluing

Given the spectra at every voxel, we compute the average time-frequency spectra for the entire survey. After some vertical smoothing (±0.2 s in our example), we balance the spectra using

$$a_j^{blue}(t,f)=\left[\frac{P_{peak}(t)}{P_{avg}(t,f)+\varepsilon P_{peak}(t)}\right]^{1/2} f^{\beta} a_j(t,f) \tag{A-8}$$

where $a_j(t,f)$ is the magnitude spectrum of the jth trace computed using spectral decomposition, $P_{avg}(t,f)$ is the smoothed, average power spectrum for the entire survey, $P_{peak}(t)$ is the peak power of the smoothed average power spectrum at time t, ε=0.01 is a prewhitening factor, and β=0.3 is a bluing factor described by Neep (2007). After balancing and bluing the magnitude spectra, the balanced and blued output trace is reconstructed by adding its complex (modified magnitude and unchanged phase) components.

Structural curvature

There is considerable confusion in terms of curvature definitions. Mathematically, the curvature is based on eigenvector analysis. In this definition, the maximum curvature is that curvature that best represents the deformation at a given voxel. If that best representation is a syncline, the maximum curvature happens to be negative and the corresponding minimum curvature that represents the least deformation at a voxel will have a larger signed value. Since most geophysicists don't live in eigenvector space, this nomenclature is not used by about 50% of the commercial curvature software implementations, who propose that the maximum curvature should have a greater than or equal signed value than the minimum curvature. We avoid this confusion by explicitly defining the most-positive and most-negative principal (i.e. eigenvector) curvatures, where $k_1 \geq k_2$. We compute volumetric curvature as the first derivatives of the volumetric north and east apparent components of dip. The long-wavelength versions we compute are simply band-passed filtered versions of the curvature results, though using the

associative law of linear operators, it is computationally more convenient to band pass filter the derivative operators rather than the output curvature result. Details of this implementation can be found in Chopra and Marfurt (2007).

Amplitude gradients

Mathematically, amplitude gradients are like time-structure gradients. Within an analysis window we compute the Karhunen-Loeve filtered version of the data which has an associated eigenvalue, λ, and eigenvector (actually, in 2D, an eigenmap), $v(x,y)$ which has a magnitude of 1.0. The east and north components of the energy-weighted (i.e. the eigenvalue weighted) amplitude gradient **g** are then

$$g_x = \lambda \frac{\partial v}{\partial x}, \text{ and} \tag{A-9}$$

$$g_y = \lambda \frac{\partial v}{\partial y}. \tag{A-10}$$

Amplitude gradients always need to be computed along structural dip. One can also compute impedance gradients.

Amplitude curvature

While structural curvature is computed by taking the first derivatives of structural dip, amplitude curvature is computed by taking the first derivatives of the amplitude gradient. In our implementation, we apply the same long wavelength filter operators as we do in structural curvature. The major difference is that the vertical dimension is different in amplitude curvature, such that we compute the mathematically simpler most-positive and most-negative amplitude curvatures (without the word principal). This simple calculation delineates zones that have extreme values of energy and in our

examples shows joints and collapse features. Amplitude curvature can also be computed from impedances or any other gradient attribute.

Structure rotation and convergence

Geophysicists familiar with fluid mechanics and electromagnetics are comfortable with taking the divergence and curl of vectors. The divergence of the structural dip vector is twice the mean curvature. The curl of vector dip is in turn a vector. Computationally, it is convenient to convert from the dip vector, **p**, to the normal vector, **n**. Marfurt and Rich (2010) then define the structural rotation (the *z*-component of the curl vector) as:

$$r = n_x\left(\frac{\partial n_y}{\partial z} - \frac{\partial n_z}{\partial y}\right) - n_y\left(\frac{\partial n_z}{\partial x} - \frac{\partial n_x}{\partial z}\right) - n_z\left(\frac{\partial n_x}{\partial y} - \frac{\partial n_y}{\partial x}\right) \quad \text{(A-11)}$$

and the structural convergence (the *x*- and *y*- components of the curl vector)

$$\begin{aligned}\mathbf{C} = \hat{x}[n_x\left(\frac{\partial n_x}{\partial y} - \frac{\partial n_y}{\partial x}\right) - n_z\left(\frac{\partial n_y}{\partial z} - \frac{\partial n_z}{\partial y}\right)] \\ +\hat{y}[n_z\left(\frac{\partial n_y}{\partial z} - \frac{\partial n_z}{\partial y}\right) - n_x\left(\frac{\partial n_x}{\partial y} - \frac{\partial n_y}{\partial x}\right)] \\ +\hat{z}[n_x\left(\frac{\partial n_z}{\partial x} - \frac{\partial n_x}{\partial z}\right) - n_y\left(\frac{\partial n_y}{\partial z} - \frac{\partial n_z}{\partial y}\right)]\end{aligned} \quad \text{(A-12)}$$

where the "^" denotes the unit normal. As with curvature, we have chosen to apply a long-wavelength filter to these derivative operators. Furthermore, the components of curl are best projected along axes perpendicular the average local dip rather than to the vertical. Rotation enhances measures the rotation of reflector dip rotation fault planes, but is also sensitive to lateral changes in accommodation space and lateral changes in angular unconformities. Convergence is a 2D vector and shows the magnitude and azimuth of convergence, such as occurs with pinch outs and angular unconformities.

Conclusions

In the dissertation, I have developed and applied a suite of algorithms that help both accelerate and quantify conventional interpretation workflows. Seismic attributes are powerful tools in delineating seismic texture and facies, structural anomalies, and geomorphologic patterns. For data with a low signal-to-noise ratio, attributes often provide increased confidence in the interpretation. By multiattribute analyzing, mathematically independent attributes into clustering techniques, one can accelerate the definition of seismic facies.

In chapter 1, I developed software and workflows with image processing techniques to exploit the attribute expression of different seismic facies to provide a semi-automatically volumetric interpretation.

In chapter 2, I developed software and a 3D workflow to enhance fault and stratigraphic discontinuities. Multiattribute display of the skeletonized faults accurately shows interfault relationships.

In chapter 3, I developed a new multi-azimuth coherence algorithm and applied it to two datasets from the Fort Worth Basin. Compared to traditional coherence of the stacked azimuthal coherence, the multi-azimuth coherence displays higher lateral resolution, and delineates karst collapse features and subtle faults as well as the major faults.

In chapter 4, I evaluated the expression of a suite of mathematically independent attributes to karst collapse and erosion surfaces. Interpreters often wish to know which attribute is “best” to delineate a given geologic feature of interest. I find that using

mathematically independent attributes, coupled through the underlying geology, allows one to confirm or reject a given interpretation hypothesis.